Ludwig-Maximilians-Universität München

The Clump Mass Function of the Dense Clouds in the Carina Nebula

PhD Thesis of the Faculty of Physics
of the Ludwig-Maximilians-Universität München

presented by
Stephanie Pekruhl
from Munich, Germany

Submitted May 28th, 2013

Zusammenfassung

Sterne entstehen in dichten, kalten Regionen aus Staub und Gas, die Molekülwolken genannt werden. Wie die Anfangsbedingungen in diesen Sternentstehungsregionen die sich ergebende Massenfunktion für die sich bildenden Sterne beeinflussen, ist eine der grundlegenden offenen Fragestellungen in der Theorie der Sternentstehung. Daher wollen wir in dieser Arbeit die Eigenschaften der kalten Wolkenstrukturen im Carina Nebel (NGC 3372) beschreiben. Der Carina Nebel ist mit einer Entfernung von 2.3 kpc und mindestens 65 O-Sternen eine der nächsten galaktischen Sternentstehungsregionen in der sich massereiche Sterne bilden. Er ist daher die beste Region um die Physik der Sternentstehung unter dem Einfluss massereicher Sterne zu untersuchen. Das Feedback der zahlreichen heißen Sterne treibt die ursprüngliche Wolke auseinander, löst aber auch die Entstehung einer neuen Generation von Sternen aus.

Wir verwenden eine $1.25° \times 1.25°$ große sub-Millimeter Karte des Carina Nebels, die wir aus Beobachtungen mit LABOCA (870μm) am APEX Teleskop erhalten haben, um die Klumpen-Massenfunktion (engl.: Clump Mass Function, ClMF) zu untersuchen. Neue tiefere LABOCA Karten zweier ausgewählter Regionen, die einen unterschiedlichen Grad an stellaren Feedback erfahren, werden, aufgrund ihrer höheren Sensitivität, einen vollständigeren Blick auf die Wolkenstrukturen und den Einfluss der heißen Sterne erlauben.

Um die ClMF des Carina Nebels zu bestimmen, verwenden wir die drei gebräuchlichen Suchalgorithmen für Klumpen CLUMPFIND, GAUSSCLUMPS und SExtractor. Jedes dieser Programme liefert ein Sample von Klumpen und berechnet deren Positionen, Größen und Intensitäten. Für eine verlässliche Massenbestimmung ist es außerdem sehr wichtig die Temperaturen der Klumpen zu kennen. Zusätzlich zu dem häufig genutzten Ansatz eine "typische" Temperatur für alle Wolken anzunehmen, leiten wir eine empirische Relation zwischen den Säulendichten der Wolken und deren Temperaturen her, um eine Temperaturabschätzung für die einzelnen Klumpen zu erhalten. In allen drei Samples finden wir für die Klumpen Temperaturen zwischen 8.5 K und 18.5 K. Mit

diesen Temperaturen ist es uns möglich die Massen der einzelnen Klumpen zu bestimmen.

Für Massen über $\sim 50\,M_\odot$ finden wir für alle drei ClMFs ein Potenzgesetz mit Exponent $\alpha \approx 1.9$. Dies stimmt gut mit ClMFs in anderen Sternentstehungsregionen überein. Nimmt man konstante Temperaturen für alle Klumpen an, wird die Steigung des Potenzgesetzes größer. Die GAUSSCLUMPS- und SExtractor-Samples können jedoch auch sehr gut mit einer Log-Normalverteilung beschrieben werden. Theoretische Modelle sagen für turbulente, prästellare Wolken eine ClMF mit Log-Normalverteilung voraus, während die ClMFs von Regionen mit Sternentstehung einem Potenzgesetz folgen sollten. Da wir jedoch feststellen, dass die Form der ClMF stark von der angewendeten Extraktionsmethode abhängt, sind solche Interpretationen aufgrund der ClMF-Form mit Vorsicht zu betrachten, solange keine zusätzlichen Informationen vorhanden sind.

Abstract

Stars form in dense, cold regions of dust and gas, called Molecular Clouds. The question how the initial conditions in these star-forming regions affect the resulting mass function of the forming stars is one of the most fundamental open problems in the theory of star formation. Therefore in this work we want to characterize the properties of the cold cloud structures in the Carina Nebula (NGC 3372). The Carina Nebula represents with a distance of 2.3 kpc one of the nearest massive Galactic star forming regions, hosting at least 65 O-type stars. Therefore it is the best site to study in detail the physics of violent massive star formation. The feedback of the numerous hot stars disperses the parental cloud but also triggers the formation of new generations of stars.

We use a $1.25° × 1.25°$ wide-field sub-millimetre map of the Carina Nebula obtained with LABOCA (870μm) at the APEX telescope to investigate its Clump Mass Function (ClMF). New deeper LABOCA maps of two selected regions experiencing different levels of stellar feedback will allow, due to their higher sensitivity, a more complete look on the cloud structures and the influence of the hot stars.

To determine the ClMF of the Carina Nebula we use the three common clump-finding algorithms CLUMPFIND, GAUSSCLUMPS, and SExtractor. Each of these programs leads to a sample of clumps, whose positions, sizes, and intensities are calculated. For a reliable mass estimate the knowledge about the temperatures within the clumps is very important. In addition to the commonly used approach to assume a "typical" temperature for all clouds, we derive an empirical relation between cloud column density and temperature to determine an estimate of the individual clump temperatures. For all three samples we find clump temperatures between 8.5 K and 18.5 K. With these temperatures we are able to determine the individual clump masses.

For masses above $\sim 50\,M_\odot$ we find a power-law for all three ClMFs, with a power-law index α of about 1.9. This is in good agreement with observations of ClMFs in other star-forming regions. For an assumed constant temperature for all clumps the power-law

slope steepens. However, the GAUSSCLUMPS and SExtractor samples can also be well described by a log-normal function. Theoretical models predict a log-normal shaped ClMF for turbulent pre-stellar clouds, whereas the ClMFs of star-forming clouds should follow a power-law. But as we find that the resulting ClMF shape depends highly on the employed extraction method, such interpretations based on the shape of the ClMF may be taken with care if no additional information is available.

Contents

List of Figures

List of Tables

Chapter 1

Motivation

After the Big Bang the baryonic universe consisted mainly of hydrogen and helium. All other elements which form our known universe were bred inside stars (e.g. Wallerstein et al., 1997). But even if the stars are constitutive for galaxy formation and evolution, as well as for the chemistry and structure of the interstellar medium and planet formation, only little is understood about the formation process of the stars themselves.

In general star formation takes place in Molecular Clouds. These are dense regions of dust and gas, which are located mainly within the spiral arms of galaxies (Roman-Duval et al., 2010). We can see them as dark patches in front of the starry band of the Milky Way as the dust is dense enough to shield the visible light from the stars behind. The dust makes the clouds opaque also for ultraviolet radiation. So the molecular hydrogen, of which the molecular clouds mainly consist (Usuda & Goto, 2005; Weinreb et al., 1963), can form and is protected against dissociation by the radiation. Turbulences and density fluctuations within the molecular clouds can produce even denser structures. When a certain density is reached the cloud core, from which stars eventually form, becomes self-gravitating and collapses (e.g. McKee & Ostriker, 2007).

But the process of star formation occurs in a wide variety of different environments and the herewith corresponding physical conditions. Most of the star forming regions in the neighbourhood of our Sun ($d \lesssim 300$ pc) contain only low density clusters or associations in which low- and intermediate-mass stars form (see Kauffmann et al., 2010, and references therein). The interaction between the young stars in such regions is minimal and they can thus be considered as forming essentially in isolation. The majority of stars in the Galaxy, however, are born in clusters within massive star forming regions (e.g. Briceño et al., 2007). These contain also high-mass stars ($M \gtrsim 20\,M_\odot$), which

profoundly influence their environments by ionising the surrounding molecular hydrogen and creating hot HII regions. Their stellar winds generate wind-blown bubbles, and finally, when they reach the end of their lives, the massive stars explode as supernovae, enriching their surrounding and releasing high amounts of energy. This massive star feedback on the one hand disperses the natal molecular clouds (Freyer et al., 2003), but on the other hand the ionisation fronts and expanding superbubbles can also compress nearby clouds, and may thereby trigger the formation of new generations of stars (Gritschneder et al., 2009; Dale et al., 2012). Despite these differences in the formation environment, the mass distribution of the forming stars, i.e. the final result of the star formation process, appears to be remarkably uniform (see Bastian et al., 2010, and references therein).

One of the most fundamental open questions in star formation theory is where this universality originates from, and how this Initial Mass Function of stars is related to the molecular cloud density structure. The aim of this work is to describe the dense cloud structures within the Carina Nebula (see Fig. 1.1) and to reveal its Clump Mass Function. The clouds within the Carina Nebula are already dispersed and shaped by the feedback of the high mass stars that have already formed in this region. In the densest regions, however, the formation of a new generation of stars is triggered. The Carina Nebula is therefore the best site to investigate the physics of star formation under the influence of massive star feedback. In the last years sub-mm instruments that are capable to determine the column densities for also large areas became available. Since then sub-mm observations have become an important tool to investigate the cool cloud structures of Molecular Clouds.

In this work I will first discuss the appearance of Molecular Clouds and the theories concerning the mass functions, that are observed. I will also give a short overview of what is already known about the Carina Nebula (Chap. 2). In Chapter 3 I describe the instruments we used for our observations and the data processing to create the final maps. The data analysis and the determination and discussion of the Clump Mass Function in the Carina Nebula is done in Chapter 4. A short summary of our results follows in Chapter 5.

Figure 1.1: A view of the inner region of the Carina Nebula, with η Car and the Keyhole Nebula at the bottom and the star cluster Tr 14 on the top. The Hubble ASC image in the Hα lines (neutral hydrogen) gives the intensities and is colour-coded with ground-based observations obtained with the MOSAIC camera at the Cerro-Tololo Inter-American Observatory. The [OIII] (501 nm) lines are shown in blue, the Hα (658 nm) in green, and the [SII] (672+673 nm) in red (Smith et al., 2010a). (*Credit:* NASA, ESA, N. Smith (U. California, Berkeley) et al., and The Hubble Heritage Team (STScI/AURA))

Chapter 2

Introduction

2.1 Molecular Clouds

Our sun is one of 10^{11} stars in our host galaxy, the Milky Way, and orbits the center of the Galaxy in a distance of ~ 8 kpc (1 pc = 206 264.81 AU = 3.086×10^{18} cm). Most of the stars lie in a flattened disc with a radius of about 10 kpc. Thereby one can distinguish between a thick disc (height: 900 pc), whose population is more metal-poor and therefore older, and a thin disc (height: 300 pc) (Jurić et al., 2008). The disc of the Milky way shows a spiral structure. Recent studies (Churchwell et al., 2009) indicate that there are two major arms (Scutum-Centaurus and Perseus) with high densities of young as well as old stars. Between the major arms two less distinct minor arms (Norma and Sagittarius) are situated. These are mainly filled with gas and very active star forming regions (Fig. 2.1, left panel). In the centre the Milky Way is dominated by a barred bulge, which is thicker than the disc. Its stellar population appears to be from the time of the formation of the Galaxy. Within a 50 kpc wide stellar halo that surrounds the Milky Way only about 1% of the stellar mass is situated. Here only very old stars can be found distributed in several globular clusters (Binney & Tremaine, 2008). A schematic view on the components of disc galaxies is shown in the right panel of Fig. 2.1.

But also the space between the stars of our Galaxy is not empty. Within the disc of the Milky Way one finds about $10^9 M_\odot$ of gas and dust (Stahler & Palla, 2005). The dust, consisting of carbon and silicate compounds, amounts only 1% in mass of this Interstellar Medium (ISM). The grains have typical sizes of few 10 nm and contain about 10^9 atoms. However, the dust plays an important role for the cooling of interstellar gas. Through
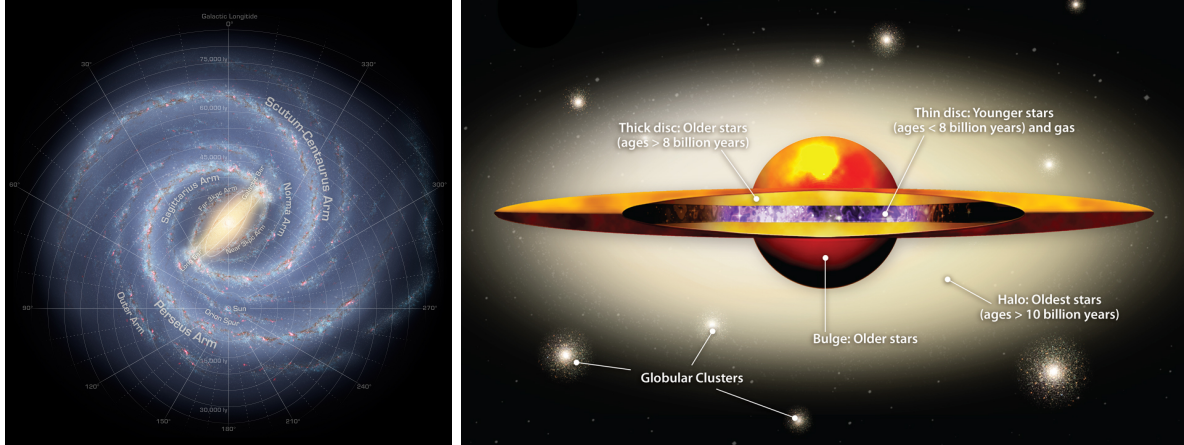
Figure 2.1: *Left:* **The spiral structure of the Milky Way. (***Credit:*** NASA/JPL-Caltech).** *Right:* **The components of a disc galaxy (thick and thin disc, bulge and halo). (***Credit:*** Amanda Smith - Institute of Astronomy, University of Cambridge.)**

Table 2.1: Phases of the Interstellar Medium adapted from Smith (2004). The mass is the total mass of the constituent in our Galaxy.

Phase	Particle density (cm^{-3})	Temperature (K)	Mass $(10^9 M_\odot)$	Fraction of volume
hot ionised	3×10^{-3}	$3 - 20 \times 10^5$	0.003	$0.4 - 0.7$
warm ionised	0.3	10×10^3	0.05	$0.15 - 0.4$
warm neutral	0.4	8×10^3	0.2	$0.2 - 0.6$
cold neutral	60	$40 - 100$	3	$0.1 - 0.4$
molecular	300	$3 - 20$	3	0.01

inelastic collisions with the gas the atomic structure of the dust begins to vibrate. The energy is then released as infrared emission (Stahler & Palla, 2005). On the surface of the cold dust grains also new molecules can form.

The gaseous part of the ISM is composed of mainly hydrogen (90%), which determines the phase of the ISM (see Table 2.1), as well as helium (9%), and a small amount of heavier elements in atomic and molecular form (e.g. C, O, N, Smith, 2004). The hydrogen appears in the atomic (HI), molecular (H_2), and ionized (HII) form. The HII is the rarest form and plays only a role around massive stars which heat and ionize the surrounding hydrogen gas. Most of the hydrogen is in the atomic form and is distributed in discrete HI clouds with diameters from 1 to 100 pc. Considering the heating and cooling processes within the gas, it is found to separate in two components. There is the warm phase ($n = 0.4$ cm^{-3}, $T = 7000$ K), which is mainly cooled by Lyα emission, and the cold neutral medium ($n = 60$ cm^{-3}, $T = 50$ K), in which the HI is distributed in discrete clouds with diameters from 1 to 100 pc. At the densities and temperatures of the cold neutral phase the hydrogen does not provide to the cooling process any more. Instead the gas is cooled by atoms that are still exited at this temperatures (e.g. CII, OI) (Stahler & Palla, 2005; Smith, 2004).

Within the spiral arms of the Galaxy, which are caused by density waves, the HI clouds can get accumulated and compressed (see Fig. 2.2). If the cloud is large enough the central parts are well shielded against the background radiation and can cool down ($T \approx$ 20 K). In the presence of dust grains, the H_2 forms from the atomic hydrogen (Smith, 2004) and is protected against dissociation through external radiation. Such a formation mechanism for Molecular Clouds (MC) and Giant Molecular Clouds (GMC) is well indicated as they are mostly concentrated within the spiral arms of galaxies (Ballesteros-Paredes et al., 2007; Stark & Lee, 2005). On smaller scales molecular material can be swept together by photoionisation, stellar winds, and supernova explosions (see Fig. 2.3, Ntormousi et al., 2011; Heitsch et al., 2005). Such MCs have sizes between 2 and 20 pc and contain $10^2 - 10^3 M_\odot$ (Table 2.2).

At the same time of the transition of the gas to the molecular form the cloud also becomes gravitational contracting (Vázquez-Semadeni, 2010). Supersonic turbulence can prevent the cloud from collapse and stabilize it. These supersonic turbulences and thermal instabilities can lead to density fluctuations. Some parts of the cloud will then exceed the critical mass which was first approximated by Jeans (1902) to

$$ M_{Jeans} \approx 1\, M_\odot \left[\frac{T}{10\,\mathrm{K}} \right]^{\frac{3}{2}} \left[\frac{n_{H_2}}{10^4\,\mathrm{cm}^{-3}} \right]^{-\frac{1}{2}}, \tag{2.1} $$
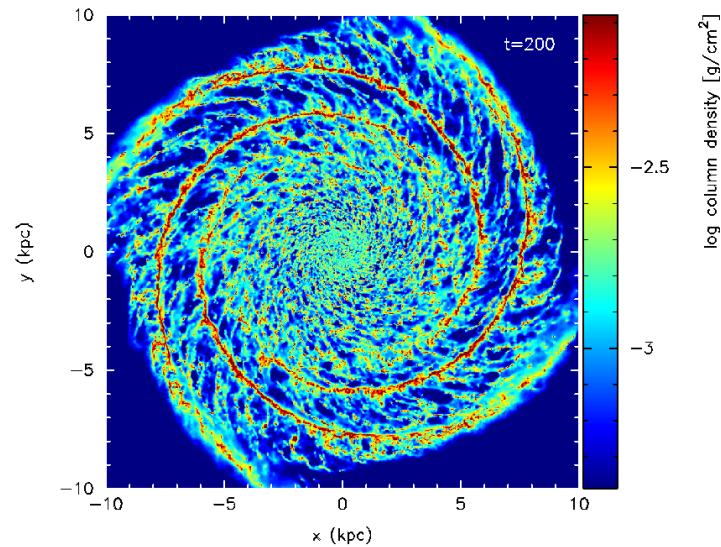
Figure 2.2: **The image of a simulated galaxy shows the gas column density distribution of initially randomly distributed gas particles after 200 Myr evolution in the galaxie's gravitational potential. (*Image:* From Dobbs et al. (2011))**
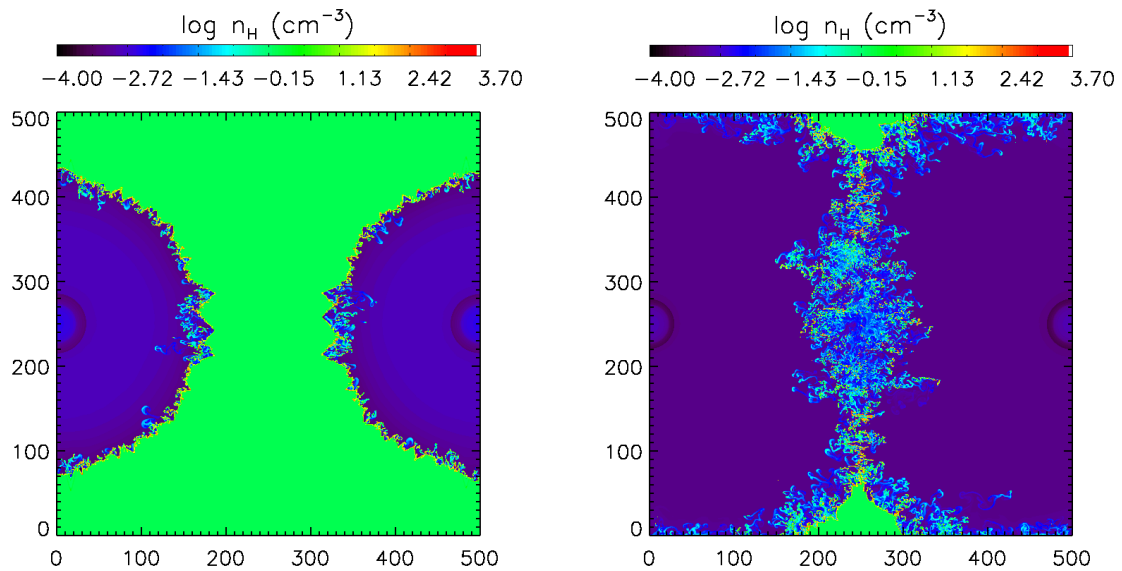
Figure 2.3: **Snapshots of the hydrogen number density structure of a superbubble collision in a uniform diffuse medium 3 Myrs (*left*) and 7 Myrs (*right*) after the stars, wich are located in the centres of the bubbles, have formed. (*Image:* From Ntormousi et al. (2011))**

Table 2.2: From Klessen (2011): Physical properties of molecular cloud structures adapted from Cernicharo (1991) and Bergin & Tafalla (2007)

	molecular cloud	cluster-forming clumps	protostellar cores
Size (pc)	$2 - 20$	$0.1 - 2$	$\lesssim 0.1$
Mean density (H_2 cm^{-3})	$10^2 - 10^3$	$10^3 - 10^5$	$> 10^5$
Mass ($M_\odot$)	$10^2 - 10^6$	$10 - 10^3$	$0.1 - 10$
Temperature (K)	$10 - 30$	$10 - 20$	$7 - 12$
Line width (km s^{-1})	$1 - 10$	$0.5 - 3$	$0.2 - 0.5$
RMS Mach number	$5 - 50$	$2 - 15$	$0 - 2$
Column density (g cm^{-2})	0.03	$0.03 - 1.0$	$0.3 - 3$
Crossing time (Myr)	$2 - 10$	$\lesssim 1$	$0.1 - 0.5$
Free-fall time (Myr)	$0.3 - 3$	$0.1 - 1$	$\lesssim 0.1$

and become gravitational unstable and collapse. Thereby the particle density n_{H_2} in these clumps increases ($10^2 - 10^3$ cm^{-3}) and star formation may start. In presence of the turbulence the 0.1-2 pc large clumps can fragment into multiple cloud cores ($\lesssim 0.1$ pc). This process is called gravoturbulent fragmentation (Klessen, 2011; Klessen et al., 2005). The clumps are expected to be the sites at which whole star clusters can form, while the denser cores are supposed to form single or multiple stellar systems (Williams et al., 2000). The properties of molecular clouds and their substructures are summarized in Table 2.2.

Observing Molecular Clouds

While the HI can be observed relatively well in the 21-cm transition line in the radio regime (Fig. 2.4, 1st row), the homonuclear H_2, with its vanishing dipole momentum, radiates only exceedingly weak. A direct detection is therefore difficult. Hence, to study the properties and structures of MCs, observations of the dust (Fig. 2.4, 3rd row) and several tracer gas molecules (e.g CO, Fig. 2.4, 2nd row), that reside also within the MC, are used. In the following I will give a short overview about the observing methods of MCs.
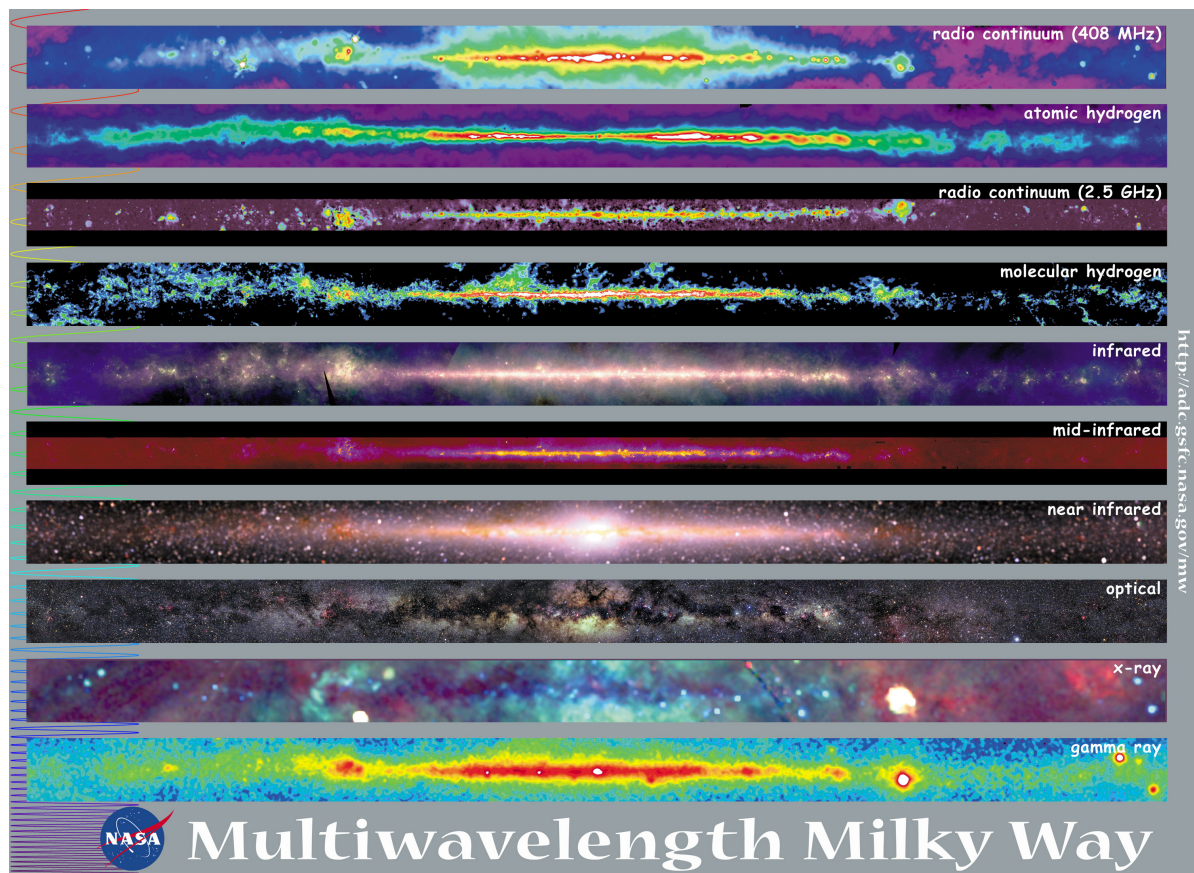
Figure 2.4: The Milky Way mapped in different wavelength regimes. The *radio continuum emission (408 MHz)* is produced by high energetic charged particles that move through the galactic magnetic field with nearly the speed of light. The *atomic hydrogen* can be traced by the radio emission from the 21-cm transition of hydrogen. This line traces the cold and warm ISM. The *radio continuum emission (2.5 GHz)* results from hot, ionized gas and high-energy electrons in the Galaxy. As the *molecular hydrogen* can not be observed directly, the CO (J=1–0) emission line is often used as a tracer of the cold and dense parts of the ISM. The composite *infrared* image is obtained with IRAS in the 12 μm (blue), 60 μm (green), and 100 μm (red) wavelength bands and shows thermal dust emission. It is assumed, that the diffuse *mid-infrared* emission originates from complex molecules. The *near-infrared* image has been observed with COBE in the 1.25 μm (blue), 2.2 μm (green), and 3.5 μm (red) bands. Most of the emission comes from cool stars. In the *optical* image the molecular clouds are only visible as dark patches, where the dust obscures the background stars. Extended soft *X-ray* emission, as shown here, is caused by hot, shocked gas. Cold clouds can absorb the emission and appear as shadows. *Gamma rays* mostly result from collisions of cosmic rays with the nuclei of hydrogen within interstellar clouds. (*Credit:* NASA Multiwavelength Milky Way project (http://mwmw.gsfc.nasa.gov/))

Molecular Line Emission

One important tool for the observation of MCs are molecular lines emissions of several tracer molecules, like e.g. CO, $C^{18}O$, N_2H^+, NH_3, CS, C_2S, which are also hosted within the molecular material of MCs (Caselli et al., 2002). These lines can give additional spectral information and informations about the velocities of the gas and its temperature. One of the standard tracer is the CO spectral line (Fig. 2.4, 4th row). Thereby a constant proportionality between the H_2 and CO density (mass conversion factor $X = 1.8 \cdot 10^{20}$ cm^{-2} K^{-1} km^{-1} s, Dame et al., 2001) is assumed.

The emission lines result from the de-excitation radiation of molecules in the cloud, which have been exited by collisions with other particles (e.g. H_2). To reach a lower energetic state these molecules emit photons of discrete frequencies in the mm and sub-mm regime.

Thereby the different molecules also trace different regions within the cloud. While e.g. NH_3 (1,1) inversion transition lines are prominent only in the densest structures, $C^{18}O$ (1-0) rotational transition emission traces the whole molecular gas in the line of sight (Rathborne et al., 2008). Again, while dominant isotopes (e.g. ^{12}CO) become optically thick even at low column densities, i.e. their column density can not be determined any more, less abundant isotopes (e.g. ^{13}CO) stay optically thin. The molecule abundances can also tell something about the evolutionary state of the cloud cores. Prestellar cores show an 'early-type' pure gas-phase chemistry with high abundances of long carbon-chain molecules (e.g. CS, C_3H_2, HCN), while other molecules (e.g. N_2H^+, $H^{13}CO^+$) form only at later stages (Frau et al., 2010; Kontinen et al., 2000).

Extinction Maps

As the dust absorbs the light of the background stars MCs appear as dark spots in the visual light (Fig. 2.4, 4th row, Fig. 2.5). The extinction of light, however, decreases with increasing wavelength from the optical to the infrared. Therefore the reddened background stars can be observed again in the longer wavelengths (Fig. 2.5). By measuring their reddening the dust distribution can be reproduced, as a higher colour excess corresponds to higher dust column densities.

The colour excess of a stars can be calculated via

$$E(H - K) = (H - K)_{\text{observed}} - (H - K)_{\text{intrinsic}}, \tag{2.2}$$

where H and K represent the H (1.65 μm) and K (2.2 μm) band magnitude. $(H - K)_{\text{observed}}$

is the colour index of the observed star, while its intrinsic colour $(H - K)_{\text{intrinsic}}$ is assumed to be equal to the average colour of the stars observed in a control field. This control field has to be near to the observed MC and should only show a nearly negligible extinction (Lombardi & Alves, 2001; Lada et al., 1994).

By calculating the colour excess for all accessible background stars, a extinction map for the region can be derived, as the colour excess can be expressed as extinction

$$A_\lambda = r_\lambda^{H,K} E(H - K) \tag{2.3}$$

where $r_\lambda^{H,K}$ is a constant of proportionality depending on the assumed extinction law (Lada et al., 2007). From these so obtained extinction data several quantities and structural information of the MCs can be determined. Their mass M, e.g. can be calculated by integrating over the extinction A_λ,

$$M = d^2 \mu \beta_\lambda \int_\Omega A_\lambda d^2 x, \tag{2.4}$$

where d is the distance of the cloud, μ the molecular weight, and $\beta_\lambda = \frac{N(HI) + N(H_2)}{A_\lambda}$ (Lombardi et al., 2006).

Thermal Dust Emission

From the radiation, which the dust absorbs from the surrounding stars, it gets heated. During the cooling process the dust releases the energy in form of thermal emission in the infrared and sub-mm (Hildebrand, 1983). This emission is dependent on the dust temperature T_d and the observed flux density is determined by

$$S[\text{Jy}] = \Omega \left(1 - \text{e}^{-\tau}\right) B_\nu(T_d). \tag{2.5}$$

Ω is the solid angle of the observed emission, τ the optical depth, and $B_\nu(T_d)$ is the Planck function for a dust temperature T_d. As the flux densities of astronomical sources are generally very weak they are often expressed in Jansky (Jy), whereby 1 Jy$= 10^{-26}$Wm^{-2}Hz^{-1}. The knowledge of the dust temperature is crucial for an interpretation of the sub-mm emission. Conclusions on the gas density can than be made, as the gas-to-dust ratio ($R = 100$) appears to be constant (Schuller et al., 2009).

To be able to determine the column density of MC structures from the measured flux the dust has to be optically thin ($\tau < 1$), as for the optically thick case only emission from the surface is observable. In this work we use thermal dust emission, observed
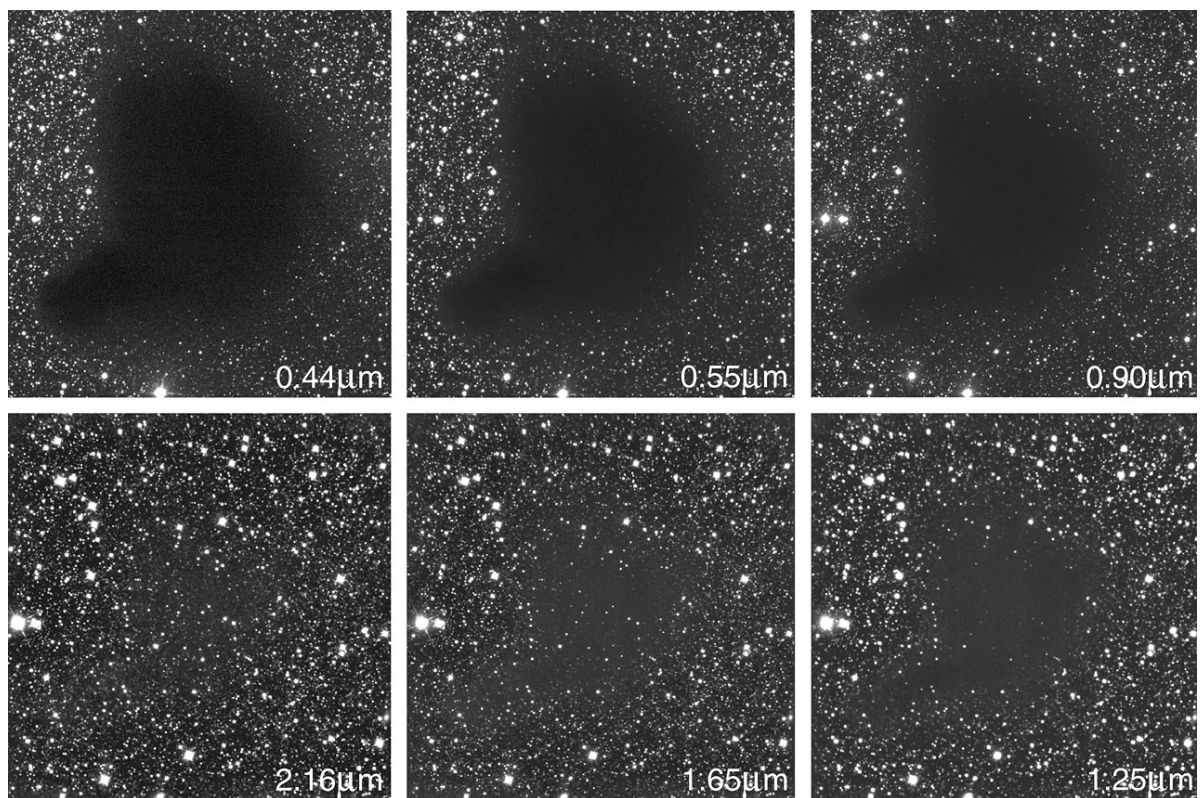
Figure 2.5: The Dark Cloud Bernard 68 observed at six different wavelengths. The wavelengths shift clockwise from the blue (0.44 μm) to the near-infrared (Ks-band, 2.16 μm). As the cloud is less dense at the edges, the cloud there becomes more transparent already at shorter wavelengths. (*Credit:* ESO)

in the sub-mm (870 μm), to determine the masses of the clumps in the Carina Nebula (Chap. 4). For the clouds in our map we find a optical depth $\tau_{870\mu m} \ll 0.01$. That means the observed cloud emission is optically thin (Preibisch et al., 2011d).

2.2 Mass Functions[1]

The stars form with a wide range in mass, starting with Brown Dwarfs, which are not able to fuse hydrogen, with masses below 0.08 $M_\odot$ over low-mass stars ($M = 0.08-1\,M_\odot$) and intermediate stars ($M = 1 - 8\,M_\odot$) to massive stars with masses above $8M_\odot$. The most massive stars known have masses about 120 $M_\odot$. However, the mass of stars can not always be determined directly, but by measuring their luminosity and evolutionary state. It has been found that the distribution of masses, of which the stars form (i.e. start the fusing process), appears roughly uniform independent of the surrounding star-formation conditions (e.g. metallicity, MC mass). Salpeter (1955) first showed that this distribution of initial stellar masses can be described by a power-law of the form

$$\frac{dN}{dM} \propto M^{-\alpha} \tag{2.6}$$

with a power-law index $\alpha = 2.35$ for stellar masses between $0.4 - 10 M_\odot$. This can be also written in the form

$$\frac{dN}{d\log M} \propto M^{-\overline{\alpha}} \text{ with } \overline{\alpha} = \alpha - 1. \tag{2.7}$$

Further studies confirmed the power-law shape of the Initial Mass Function (IMF) with a power-law index α between 2.1 and 2.5 for the whole mass rage above $\sim 1\,M_\odot$ (e.g. Kennicutt, 1983; Kroupa, 2001; Baldry & Glazebrook, 2003), but showed a shallower slope and a turn-over for lower masses (Fig. 2.6). Chabrier (2003) eventually described the IMF by a log-normal distribution.

Studies of various star forming regions found that the dense Core Mass Function (CMF) resembles the shape of the IMF, but is shifted to higher masses by a factor of $\sim 4 - 6$ (Fig. 2.7, Könyves et al., 2010; André et al., 2010; Alves et al., 2007; Nutter & Ward-Thompson, 2007). This could suggest that the IMF, assuming a constant star formation efficiency, is a direct consequence of the initial cloud structure. So far this relation of the CMF and the IMF has only been seen in star forming regions, where low-mass stars form.

---

[1]This section is adapted from Pekruhl et al. (2013)
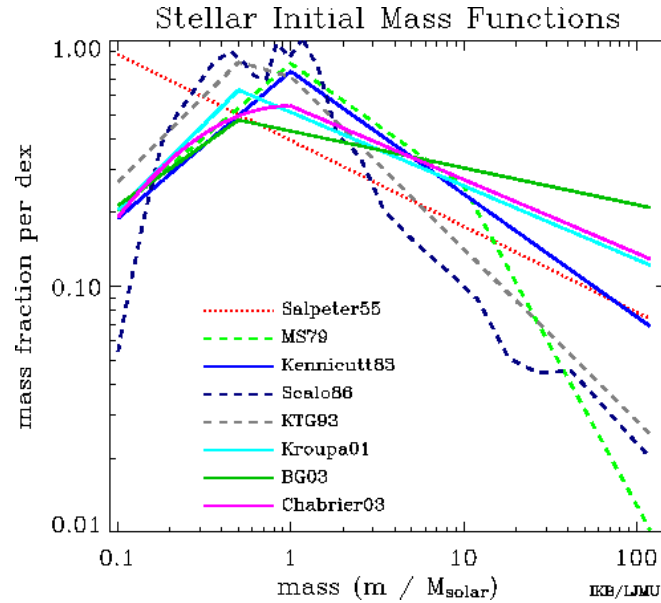
Figure 2.6: A comparison of some common IMFs (Salpeter (1955), MS79 Miller & Scalo (1979), Kennicutt (1983), Scalo (1986), KTG Kroupa et al. (1993), Kroupa (2001), BG03 Baldry & Glazebrook (2003), Chabrier (2003)). The mass fraction (per logarithmic mass bin) is plotted against the mass. (*Credit:* Ivan Baldry (http://www.astro.ljmu.ac.uk/~ikb/research/imf-use-in-cosmology.html))
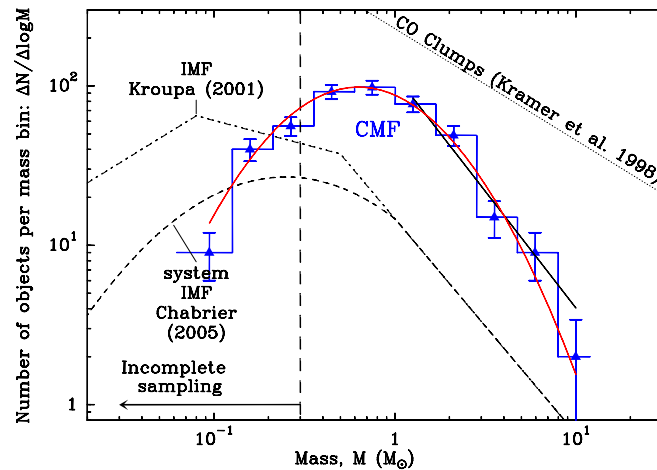
Figure 2.7: The CMF in Aquila approximated with a log-normal fit (red curve). Its high mass end is fitted by a power-law with power-law index $\alpha = -2.5 \pm 0.2$ The IMFs from Kroupa (2001) and Chabrier (2005) are shown as dash-dotted and dashed lines, respectively. The dotted line shows the power-law, which is typically found for clumps (see Kramer et al., 1998). (*Image:* from Könyves et al. (2010))

Observations of more distant massive star forming regions at sub-mm or radio wavelengths can usually not resolve the individual cloud cores. Indeed this observations are an important tool to study the MC clumps and their corresponding Clump Mass Function (ClMF). Molecular line (Kramer et al., 1998; Wong et al., 2008) and dust continuum emission (Johnstone & Bally, 2006; Muñoz et al., 2007) observations of several star forming regions show that the ClMF also can be described by a power-law distribution. With a power-law index of $\alpha \sim 1.4 - 2.0$ (Elmegreen & Falgarone, 1996; Kramer et al., 1998), the ClMF is typically shallower than the CMF and the stellar IMF (Fig. 2.8). Thus, while the IMF is dominated by low-mass stars, most of the mass of the ClMF is contained in massive clumps (Bergin & Tafalla, 2007). However, the slope of the ClMF power-law tail is similar to that found for cluster mass functions ($\alpha \sim 2$, McCrady & Graham, 2007; Bik et al., 2003; Zhang & Fall, 1999)

Recent studies of molecular cloud structure suggest that the ClMF or the distribution function of the column density (N-PDF) can be used as an indicator for the evolutionary state of a molecular cloud (Kainulainen et al., 2009, 2011; Ballesteros-Paredes et al., 2011). Peretto & Fuller (2010) found, for a sample of gravitationally bound Infrared Dark Clouds (IRDC), a power-law index $\alpha \sim 1.8$, while the slope of the mass spectra of unbound fragments steepens at the high mass end and can be well described also by a log-normal distribution (Fig. 2.9). In clouds in which the star formation process has not yet started, therefore turbulence is expected to lead to a log-normal distribution. As soon as the star formation process starts, the denser structures get dominated by gravity. This should result in a power-law distribution of the masses (or column densities) in the upper mass (density) range. These results are in agreement with the theoretical work of Hennebelle & Chabrier (2008), and with studies of the probability distribution function of the column density (N-PDF) within MCs which displays log-normal shapes for turbulent structures and power-law behaviour for gravitationally dominated clouds (Kainulainen et al., 2011; Ballesteros-Paredes et al., 2011). Therefore, the shape of the observed ClMF or density distribution function is sometimes considered as an indicator for the physical status of a cloud. One problem with such an interpretation is that different observing and analysis techniques sometimes yield different ClMF shapes for the same cloud (see Reid & Wilson, 2006; Reid et al., 2010). We also find for our observations in the Carina Nebula that the shape of the resulting ClMF is highly dependant on the analysis techniques, as we will discuss in Sect. 4.3.
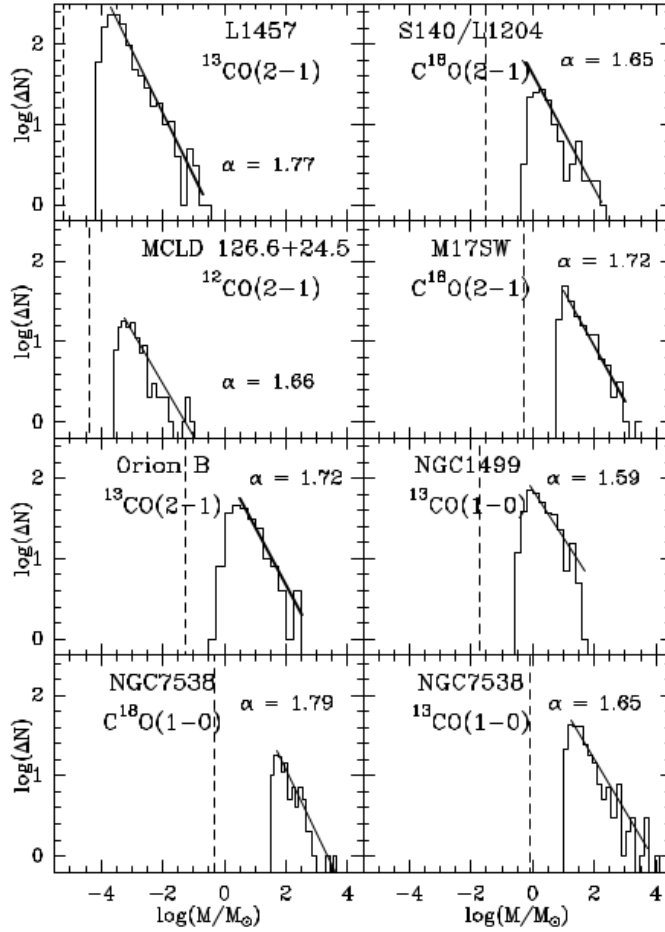
Figure 2.8: ClMF of eight different regions. The best linear fits over the range of masses overdrawn by the lines indicate power-law indices $\alpha = 1.59 - 1.79$. The dashed line shows the minimum mass given by the resolution limits and the rms noise. (*Image:* from Kramer et al. (1998))
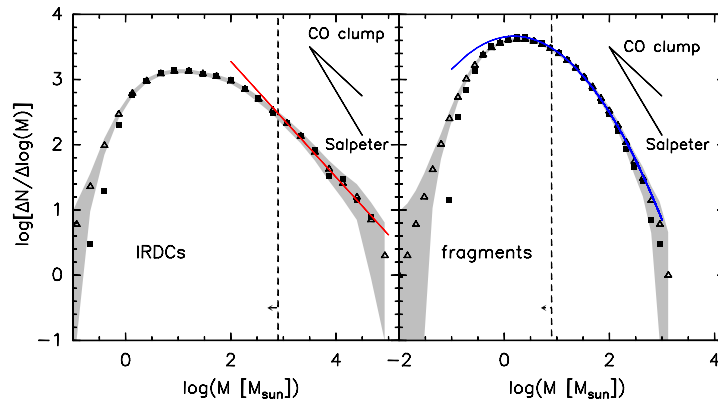
Figure 2.9: The mass distribution of gravitationally bound IRDCs (*left*) is best fitted by a power-law (red line) while the best fit for the mass distribution of unbound fragments (*right*) is a log-normal function (blue line). The vertical dashed lines show the completeness limits. (*Image:* from Peretto & Fuller (2010))
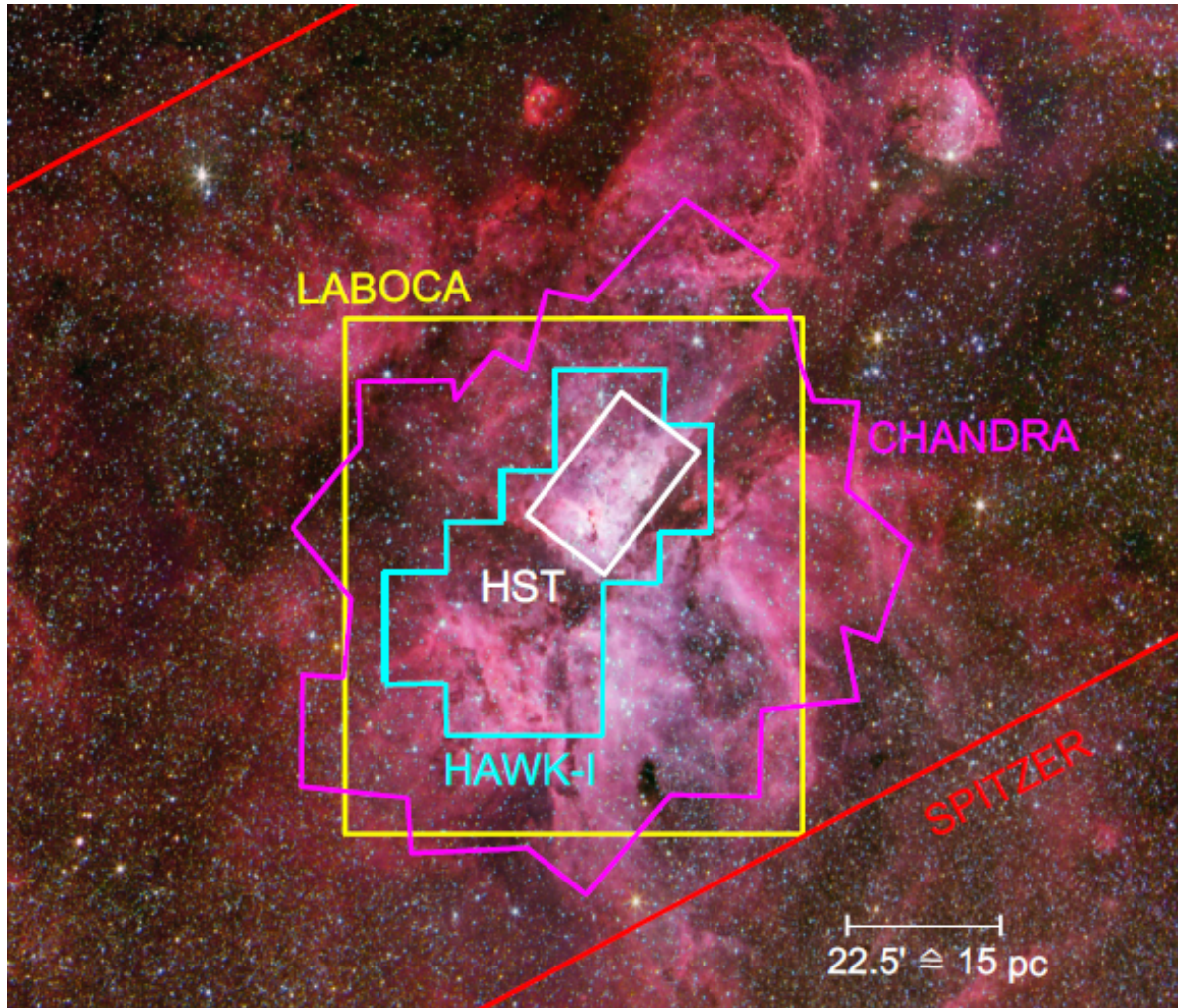
Figure 2.10: Detail of an image of the Carina Nebula taken in Hα (*Credit:* Robert Gendler and Stephane Guisard (www.robgendlerastropics.com/Etacarinaewide.html)). The FoV of several instruments, the Carina Nebula has been observed with, are overplotted in different colours. In white the image of the HST, shown in Fig. 1.1, is marked. The turquoise line shows the FoV of the near-infrared camera HAWK-I at the VLT. The purple line marks the *Chandra* image, also shown in Fig. 2.12. In yellow the FoV of our LABOCA wide-field observations are marked.

2.3   The Carina Nebula

The Carina Nebula Complex (NGC3372) represents one of the most massive ($M_{*,total} \gtrsim$ $25\,000\,M_\odot$) star forming regions in our Galaxy. It is located in the Sagittarius-Carina spiral arm at a distance of 2.3 kpc, and is, with a total infrared luminosity of $1.2 \times 10^7\,L_\odot$ and an extent of about 50 pc, the apparently brightest and largest nebula observable on the southern sky. An overview over the region is given by Smith & Brooks (2008).

Within the Carina Nebula at least 65 O stars with masses up to $\sim 100 M_\odot$ (including a number of O3 stars) and several Wolf-Rayet stars are hosted, as well as the Luminous Blue Variable η Carinae (η Car, Smith, 2006). The variability of η Car has been known and observed for over 300 years (Frew, 2004), however, it is not yet understood completely. A variability with a period of 5.53-yrs results from a close binary companion (Damineli et al., 2000) but the reason for η Car's nova-like outburst in the mid 1800s is still unknown. Until this "Great Eruption" the UV radiation of η Car was the dominating contribution of the massive star feedback in the central region, and formed several very prominent dust pillars. However, during the event the star ejected material with a total mass of about $10\,M_\odot$, which today builds the "Homunculus Nebula" (Fig.2.11, left) and now absorbs the radiation from the star. η Car is still the most massive ($\approx 120 M_\odot$) and luminous star known in our Galaxy, and is expected to explode as a Supernova within the next Myr. It is situated within the loose star cluster Tr 16, which also hosts most of the other O-type stars of the Carina Nebula. The stars of Tr 16, whose ages range between 3 to 4 Myrs (Preibisch et al., 2011a), are widely distributed over a large area, so no clear center can be determined. Tr 16 appears divided due to a dark lane of shading dust in front of the cluster. A slightly younger (1-2 Myr) but much more compact star cluster is Tr 14, which shows a circular shape with a radius of 3.5 pc (see Fig. 2.12, left panel). As well as for the four times more massive cluster Tr 16, the extinction effects due to the gas and dust material within the cluster varies considerably in this 10 O-type stars containing cluster. These two star clusters, Tr 16 and Tr 14, dominate the energy input to the surrounding material, while the older (5-10 Myrs, Wang et al., 2011) Tr 15 star cluster in the north-east influences only its immediate environment (see Tapia et al., 2003).

The indication of a slightly older stellar population (up to 10 Myrs) within the Carina Nebula Complex gives reason to the assumption that the region already faced at least one supernova event. Discoveries of diffuse X-ray emission that may originate from supernova remnants, which enrich the surrounding ISM (Hamaguchi et al., 2007), and a $\sim 10^6$ year old neutron star somewhat in the south-east of η Car (Hamaguchi et al.,
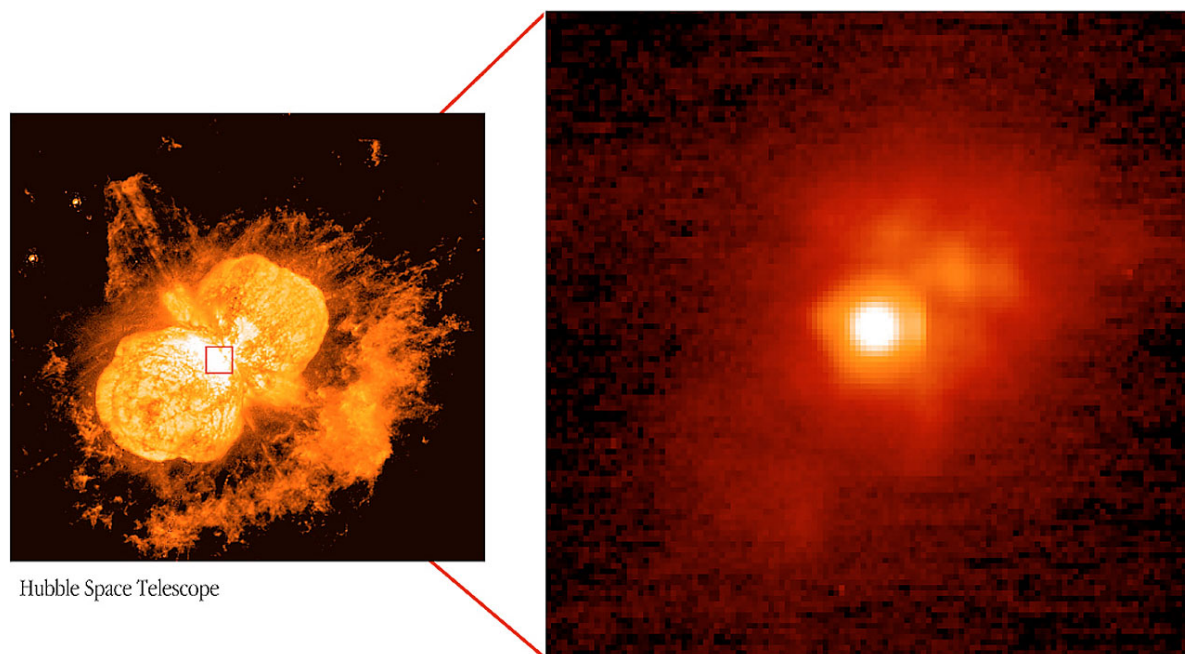
Figure 2.11: *Left:* **The Homunculus Nebula, which formed from the mass that was ejected from η Car during the "Great Eruption" in the 19th century, observed with the Hubble Space telescope. (*Credit*: NASA/ESA HST).** *Right:* **A zoom in to the proximate environment of the blue variable η Car. The image is obtained with the near-infrared adaptive-optics camera NACO at the VLT (*Credit*: ESO)**

2009) reinforce this suggestion (Fig. 2.12, left panel).

The ionizing winds and feedback of the hot and luminous O-type stars within the Carina Nebula have already dispersed large parts of the primordial clouds in the central region around η Car and the T 16 star cluster. In south-eastern and north-western direction numerous giant dust pillars (South Pillars, see Smith, 2006; Rathborne et al., 2004) arose, eroded and shaped by the UV radiation and stellar winds. Several studies found clear indications for the ongoing and triggered formation of a new generation of stars within the tips of these pillars, where the gas is most compressed by the stellar wind feedback (Megeath et al., 1996; Smith & Brooks, 2008; Smith et al., 2010b) (Fig. 2.13).

These conditions make the Carina Nebula a perfect site to study young ongoing star formation in the vicinity of massive stars and their stellar feedback. This feedback is much stronger as e.g. in the closer and prominent Orion Nebula with only two O-type stars. Due to the higher number of massive stars the Carina Nebula is our best comparison to the more denser and much more massive star forming regions like 30 Doradus in
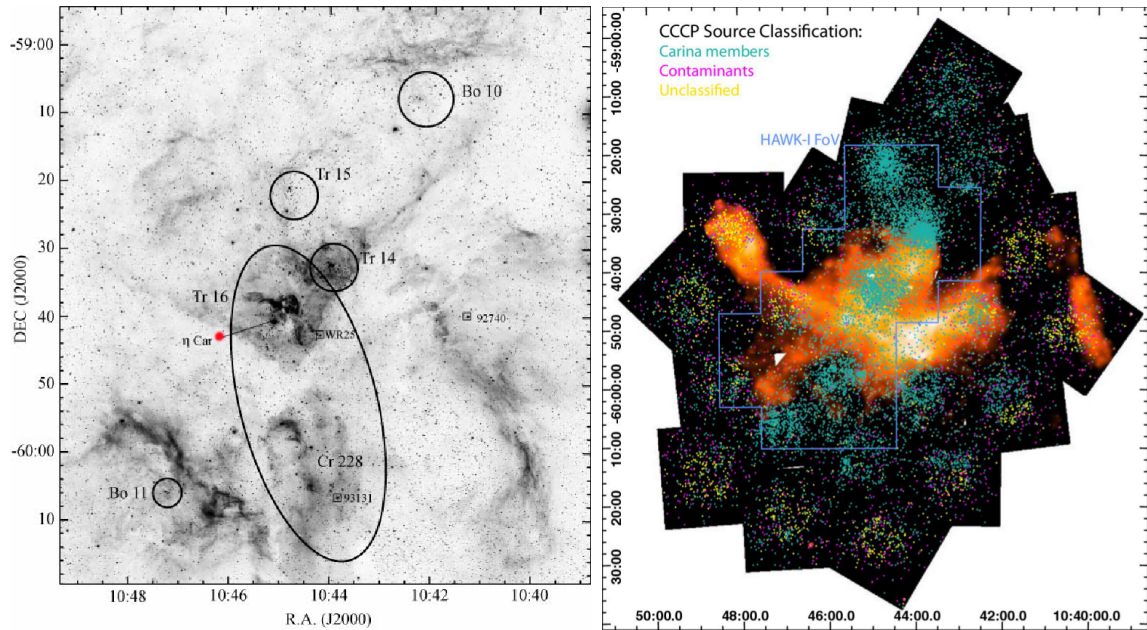
Figure 2.12: *Left:* [SII] image of the Carina Nebula from Smith & Brooks (2008) showing the approximate positions of the star clusters in the Carina Nebula. The red dot marks approximately the position of the neutron star. *Right:* The Chandra Carina Complex Project (CCCP) mosaic from Townsley et al. (2011). In the back (in orange) the diffuse X-ray emission is shown, overlaid with the classification of the point-sources. The young stars belonging to Carina are shown in cyan, fore- and background stars, as well as extragalactic sources in magenta, and unclassified sources in yellow. The HAWK-I field of view from Preibisch et al. (2011c) is marked in blue.

the Large Magellanic Cloud. But while these regions are much more distant, the Carina Nebula is close enough to also investigate small-scale structures, like protoplanetary discs and jets (Preibisch et al., 2011b; Ohlendorf et al., 2012). Therefore the Carina Nebula has been subject of several observations in the last years (Fig. 2.10).

If the stellar population within the Carina Nebula Complex follows the usual IMF (see Sect. 2.2) one would expect about 10^4 intermediate and low-mass stars in this region. They have indeed recently been systematically identified and studied in detail in the context of comprehensive multi-wavelength surveys. Within the framework of the *Chandra* Carina Complex Project (CCCP, Townsley et al., 2011) a 1.4 square-degree ($2300 \, \mathrm{pc^2}$) X-ray survey has been performed (see Fig.2.10), using the Advanced CCD Imaging Spectrometer (ACIS). In the obtained data, besides the diffuse emission, 14 368

point-sources could be identified, from which 10 714 appear to be young stars within the Carina Nebula Complex (Fig. 2.12, right panel). The other point-sources are fore- and background stars, as well as extragalactic sources. The stellar X-ray emission originates from magnetic activity in the hot plasma ($\sim 10^6$ K) in the stellar corona of stars up to $2 M_\odot$ or from shocks in stellar winds of very massive stars. Due to the limited sensitivity this survey only has detected the brightest $10\% - 20\%$ of Carina's young stars. However, this results show that the low-mass stars are in number consistent with the expectations drawn from extrapolating the standard IMF at least down to stellar masses of $\sim 0.5 - 1\, M_\odot$.

Together with the data of a very deep near-infrared survey of the central region obtained with HAWK-I at the ESO Very Large Telescope (Preibisch et al., 2011c, see Fig. 2.10 and blue line in Fig.2.12, right panel), the ages and masses of the X-ray selected young stars could be determined (Preibisch et al., 2011a; Wang et al., 2011; Wolk et al., 2011) using colour-magnitude diagrams. The strong X-ray emission of the young stars helped to discern their near-infrared counterparts from those of older field stars in the background. This is especially important for young stars which have already accreted or blown away their circumstellar discs, and therefore cannot be identified by their infrared-excess any more. The HAWK-I data finally are deep enough to detect the full sample of low-mass stars in the Carina Nebula down to $\approx 0.1\, M_\odot$, and provides a statistically complete sample of the whole young stellar population, which has formed at the same time as the high mass stars. Only four new star clusters are identified in the HAWK-I field. About half of the young stellar population is scattered over the region and not dominantly clustered (Preibisch et al., 2011c).

Additional information about the recent star formation processes came from the Hα observations with the Advanced Camera for Surveys (ACS) at the *Hubble* Space Telescope (HST) (Fig. 1.1, Fig. 2.10) of proto-stellar jets, which implies a large population of accreting young proto-stars and Young Stellar Objects (YSOs) in the region (Smith et al., 2010a). From *Spitzer* infrared imaging (Fig. 2.13, right panel) of the South Pillars region Smith et al. (2010b) found about 900 YSOs. In their analysis of jet driving sources Ohlendorf et al. (2012) found that the presently forming stars lie close to the edges of the clouds, what implies the scenario of triggered star formation (Fig. 2.13, left panel).

With all these observations the stellar component of the Carina Nebula is meanwhile well investigated, but little has been done to understand the effects of the massive star feedback on the surrounding MCs themselves. MC observations in the Carina Nebula Complex were rather limited until recently. The most extensive existing data set of
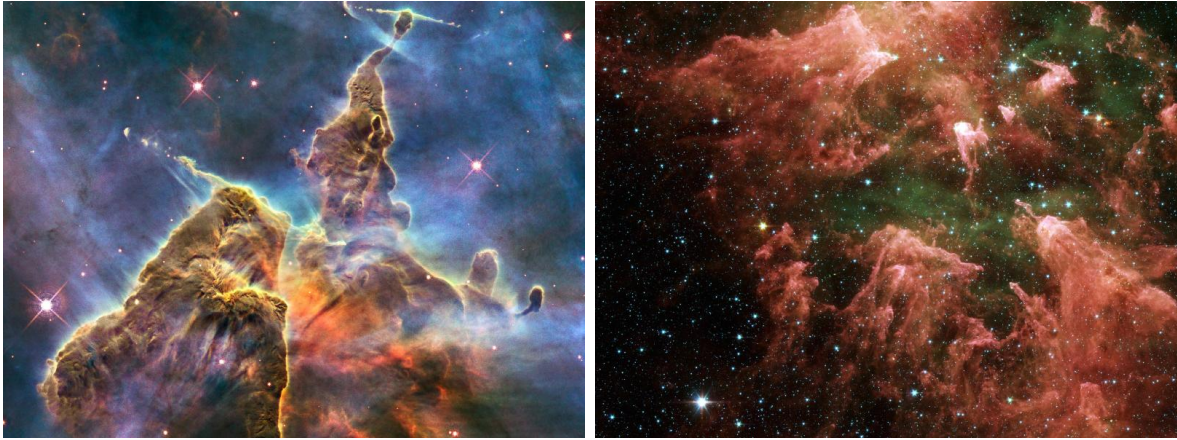
Figure 2.13: *Left:* **A dust pillar north of η Car shaped from stellar feedback. The image from the HST shows also two Herbig Haro jets (HH 901/902) on the edges and tips of the pillar. The [OIII] (502 nm) lines are shown in blue, the Hα (657 nm) in green, and the [SII] (673 nm) in red. (*Credit:* NASA, ESA, and M. Livio and the Hubble 20th Anniversary Team (STScI))** *Right:* **The "South Pillar" region observed with the Infrared Array Camera (IRAC) at** *Spitzer.* **The different wavelengths are represented with different colours (3.6 μm: blue, 4.5 μm: green, 5.8 μm: orange, 8.0 μm: red) (*Credit:* NASA, SSC, JPL, Caltech, Nathan Smith (Univ. of Colorado), et al.)**

the Carina Nebula Complex at radio wavelengths is a NANTEN survey in several CO lines by Yonekura et al. (2005). They covered a $4° \times 2°$ area with a half-power beam-width of $2.7'$, which corresponds at the distance of the Carina Nebula to ~ 2 pc. In the C^{18}O (1–0) line they detected 15 massive cloud structures ($\sim 10^3 \, M_\odot$), from which 6 have already experienced star formation and two are currently involved in massive star formation. Brooks et al. (1998) observed a smaller part of the central region of the Carina Nebula in the ^{12}CO (1–0) line with the MOPRA antenna, which provides a better spatial resolution ($43''$). These data give evidence on the clumpy structure of the molecular gas (see Schneider & Brooks, 2004).

This work is based on data we obtained from large-scale ($1.25° \times 1.25°$) sub-mm observations of the Carina Nebula Complex with LABOCA at the APEX telescope (see Fig. 2.14) with much better resolution. These new data contain detailed information on the structure of the cold dusty clouds (Preibisch et al., 2011d) in the region. With this we derived for the first time a reliable ClMF for the Carina Nebula.
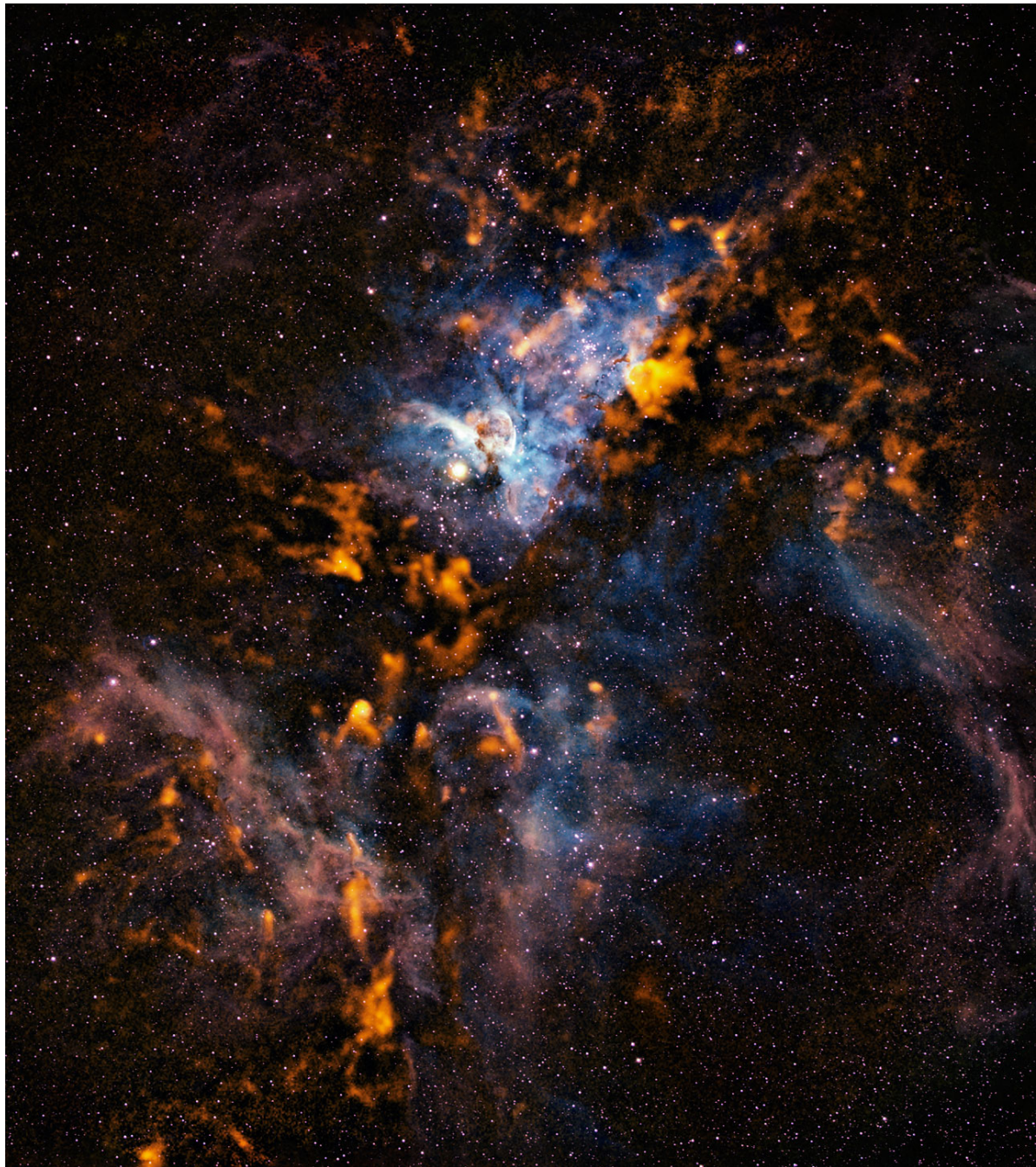
Figure 2.14: Our LABOCA observations in orange, combined with a visible light image from the Curtis Schmidt telescope at the Cerro Tololo Inter-American Observatory. (*Credit:* ESO/APEX/T. Preibisch et al. (Submillimetre); N. Smith, University of Minnesota/NOAO/AURA/NSF (Optical))

Chapter 3

Observations and Data Reduction

This chapter gives an overview of the APEX telescope (Sect. 3.1) and its instruments, especially LABOCA (Sect. 3.2). These are well suited for large scale observations of the cold gas and dust in star forming MCs. These sections follow mainly the descriptions of Güsten et al. (2006), Siringo et al. (2009), Schuller et al. (2009) and the official APEX website[1]. In Sect. 3.3 the reduction process for bolometric data, as from LABOCA, is described.

The observations, data reduction, and first results of our wide field LABOCA map are depicted in Sect. 3.4.1, based on the results from Preibisch et al. (2011d). A detailed description of the data reduction of two deeper LABOCA observations of a strongly irradiated pillar in the south east of η Car and the Giant Pillar in the south, is given in Sect. 3.4.2. In Sect. 3.4.3 we give an overview of recently obtained additional sub-mm and molecular line data we observed at the APEX telescope.

3.1 The APEX Telescope

Most of the radiation that reaches the Earth is absorbed in the atmosphere. The opacity of the atmosphere depends highly on the wavelength (see Fig. 3.1). In the gamma-ray, X-ray, and ultraviolet regime all of the the radiation is absorbed in the upper atmosphere by atoms and molecules of oxygen, nitrogen, and other gases. In this wavelength regime observations can only be done by satellite telescopes (e.g. *Chandra*) from space. However, there are several atmospheric windows at higher wavelengths where most of

---

[1]http://www.apex-telescope.org
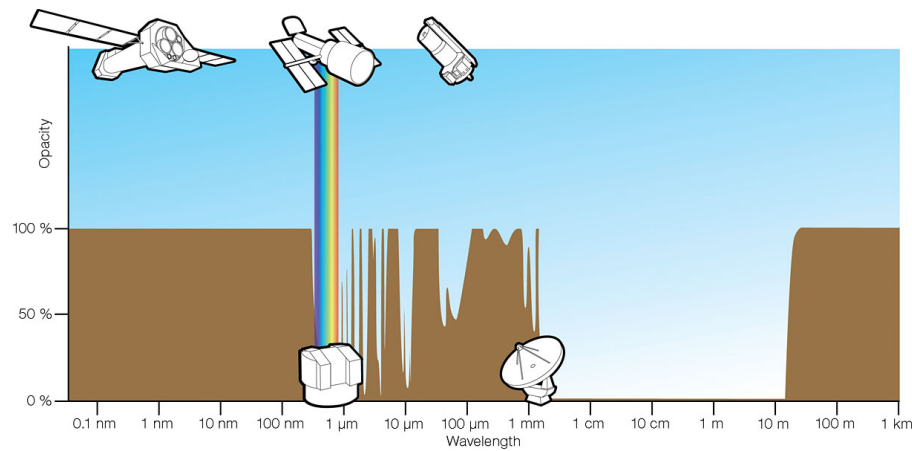
Figure 3.1: This plot shows the opacity of the atmosphere as a function of wavelength. The atmospheric window in the optical is indicated by the rainbow. The sketches of the observation instruments show how best to observe in the different wavelength regimes. The antenna on the right shows the operation regime of APEX. (*Credit:* ESA/Hubble (F. Granato))

the radiation can pervade the atmosphere and reach ground-based telescopes. The most prominent one is the optical window of the visible light from 300 nm to 1100 nm. In the infrared, especially the mid-, and far-infrared, the observations suffer from the thermal background radiation of the earth's atmosphere and absorption effects, mostly due to water vapour in the atmosphere. An important observation tool in this wavelength regime is therefore the *Spitzer* space telescope. A second large atmospheric window opens in the radio regime, from around 1 mm to 11 m.

The APEX (Atacama Pathfinder EXperiment) telescope (Güsten et al., 2006) operates at millimetre and sub-mm wavelengths on the borderline between infrared light and radio waves. To avoid the absorption and diminishing effects of the water vapour, the telescope is located on the Llano de Chajnantor at 5107 m altitude in the Atacama Desert. This is one of the driest places on Earth and therefore an excellent site for sub-mm observations. The amount of perceptible water vapour (PWV) is in the mean about 1.2 mm, and drops to 0.7 mm up to 25% of the time (Fig.3.2). APEX is the precursor of the Atacama Large Millimeter Array (ALMA), which is currently built at the same site. While APEX is modified for the single dish use, ALMA will consist of 54 antennas with a 12 m diameter, like APEX, and 12 smaller dishes (7 m), which can be combined to reach a unprecedented resolution. APEX is a collaboration between the Max Planck Institut für Radioastronomie (MPIfR, 50%), the European Southern Observatory (ESO,
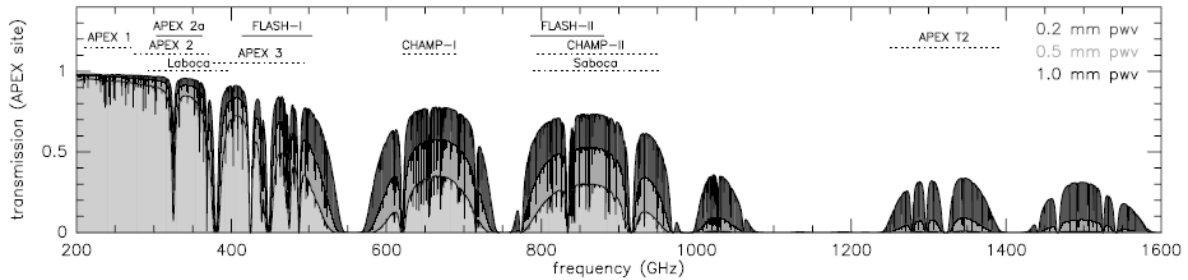
Figure 3.2: This plot by Güsten et al. (2006) shows the zenith transmission of the atmosphere for different amounts of perceptible water vapour. The bars above mark the atmospheric windows in which the APEX instruments operate.

27%) and the Onsala Space Observatory (OSO, 23%), who also share the observing time with the Chilean host nation.

Construction and design of the telescope has been assigned to VERTEX Antennentechnik in Duisburg, Germany, in summer 2001 from the MPIfR. Two years later, in spring 2003, the on-site construction began. Finally in July 2005 the APEX telescope saw first light.

The APEX telescope is a 12 m antenna (Fig. 3.3). The main dish consists of 264 adjustable aluminium panels that are arranged in 8 concentric rings. The panels have been chemically etched to scatter visible and infrared radiation. Thus also observations during daytime are possible. The telescope is built in a Cassegrain configuration. This means the radiation is reflected over the paraboloidal main reflector to a hyperboloidal secondary reflector in the primary focus (focal length 4.8 m), which leads the radiation through a hole in the primary reflector into the Cassegrain cabin (see Fig. 3.3). The APEX aluminium secondary reflector has a diameter of 0.75 m and a final focal ratio of f/D=8.

This assembly permits wide field bolometer arrays in the Cassegrain cabin (e.g LABOCA, SABOCA) as well as the operation of heterodyne receivers in two additional Nasmyth cabins (e.g. APEX-2, CHAMP+), which can be fed by light with the help of an rotational Gaussian tertiary mirror.

Figure 3.3: The APEX 12-m telescope on the Chajnantor plateau (5107 m) in the Atacama Desert (Chile). *Credit:* **ESO**

3.2 LABOCA

The LArge BOlometer CAmera (LABOCA, Siringo et al., 2009) operates in the atmospheric window at $870\,\mu$m (345 GHz, see Fig. 3.2). The sub-mm continuum emission is an effective tool to study the cool dust (10-40 K) of MCs. With its angular resolution of $18.6''$ and a total field of view (FoV) of $11.4'$ LABOCA allows to sample large regions with high sensitivity (single pixel sensitivity of 40-70 mJy $s^{1/2}$, Schuller et al., 2009).

As described in Sect. 3.1, LABOCA is situated in the Cassegrain cabin of the APEX telescope. To reach the instrument's focal plane the beam of the incoming radiation has to pass a complex tertiary optics system (Fig. 3.4) of tree concave mirrors (M3, M5, M7) and two plane mirrors (M4, M6). Finally the radiation passes an aspherical lens into the cryostat, in which the bolometers are mounted. This optical path is necessary to transform the focal ratio from the Cassegrain focus f/D=8 to the focus f/D=1.5 of the conical horn antennas, which collect the radiation and lead it to the bolometers.

The bolometers measure the power of incoming radiation. They consist of a thin layer of metal as absorber on a semiconducting temperature sensor. To achieve higher sensitivity the titanium absorber is cooled down to a temperature of about 280 mK using liquid nitrogen and helium. The arriving radiation heats the absorber, which leads to a change
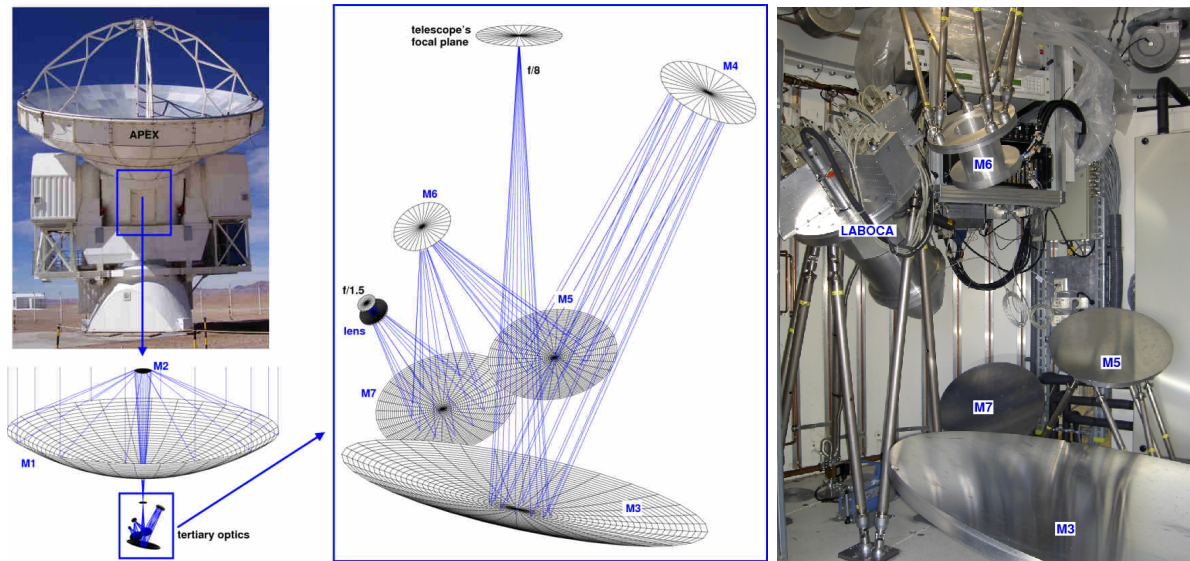
Figure 3.4: The optical path of the radiation, which reaches the APEX telescope in zenith position (*left*), through the tertiary optics within the Cassegrain cabin (*middle*). *Right:* A photo of the tertiary optics. (*Images:* From Siringo et al. (2009))

of voltage in the temperature dependent resistor below. The voltage change corresponds then to the intensity of the radiation.

As the sub-mm thermal dust emission is only very weak, in the last decades much efforts were made to develop more sensitive instruments with a large FoV. The construction of bolometer arrays, where multiple single bolometers are collocated in the focal plane, allow the mapping of large areas by simultaneous multi-beam coverage. The bolometer group of the MPIfR in Bonn, developed LABOCA for the APEX telescope. LABOCA consists of 295 bolometers, which are arranged in 9 concentric hexagons around the central channel (see Fig. 3.5, left panel).

To handle the sky noise LABOCA uses a fast scanning technique (Reichertz et al., 2001). This method employs that every single detector of the array is receiving atmospheric noise while scanning across a source. The noise is highly correlated in the detector pixels and can therefore be removed in the offline data reduction (see Sect. 3.3). At the APEX telescope there are two possible scanning modes available. In the spiral mode the beam array moves outwards along a spiral pattern with a constant angular speed. This produces a fully sampled map of the total FoV of LABOCA with sensitivities down to a few Jy. For higher sensitivities the basic pattern can be combined with a raster
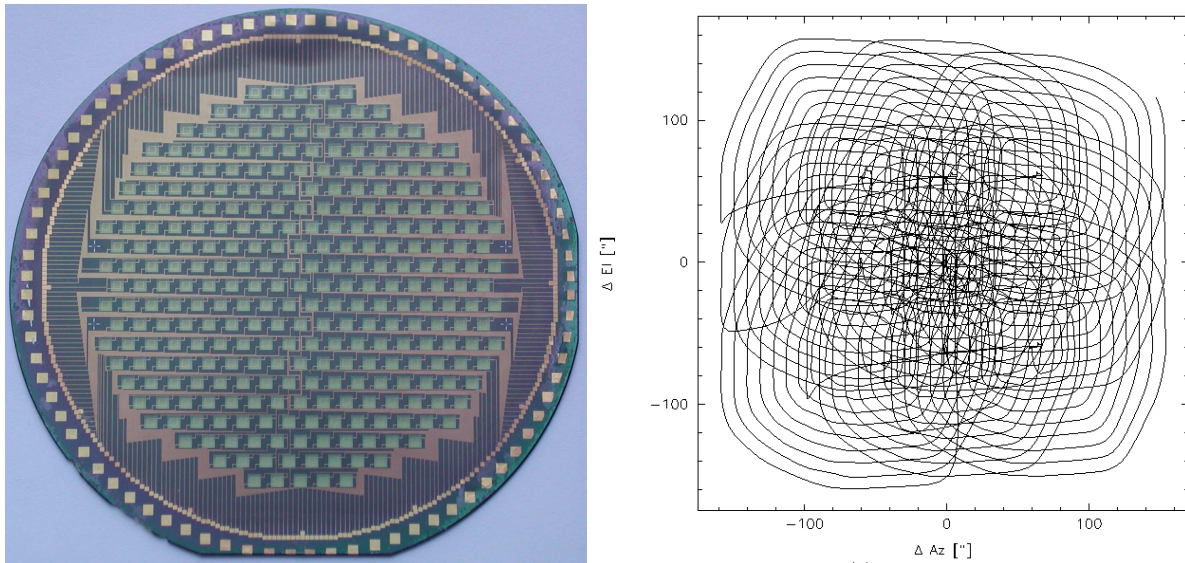
Figure 3.5: *Left:* **The LABOCA bolometer array consisting of 295 bolometers (green squares).** *Right:* **Raster-spiral scanning pattern of the central bolometer (***Images:* **From Siringo et al. (2009))**

pattern (Fig. 3.5, right panel). This results in an even denser sampling of the map and an increase of the integration time. The spiral mode provides a uniform coverage with only small overheads. Another scanning mode is to produce on-the-fly maps (OTF). Here the beam array scans continuously back and forth in rows, accelerating only at the turning points, finally producing a rectangular map. For a homogeneous mapping the spacings between the rows should be less than one third of the beam size. This scanning method produces larger overheads than the spiral mode, but for larger maps the overhead fraction of the map depletes.

3.3   BOA

For the data reduction of our LABOCA observations the Bolometer array Analysis (BoA) software package[2] has been used. This program has been designed for visualisation during the observations with LABOCA as well as for post-processing data reduction, but can also be used on data obtained with similar bolometer array instruments. BoA is mainly written in Python in a collaborative project of the MPIfR, the

---

[2]ftp://ftp.eso.org/web/sci/activities/apexsv/labocasv/boaman_v4.1.pdf

Table 3.1: Some basic commands for BoA

bash shell commands	
source ∼/.boarc.sh	initialize the startup script
boa	starts BoA
BoA commands	
op()	opens graphic window (pgplot)
close()	closes graphic window
indir('/home/user/data')	sets the input directory
ils()	lists the content of the input directory
proj('projectID')	if set, the filenames can be described with only the observation numbers
read('filename')	reads the input data file
execfile('filename')	executes program files (*.boa, *.py)
print command.__doc__	prints help to a command
crtl+d	ends BoA session

Argelander Institut für Astronomie (Bonn, AIfA), and the Astronomisches Institut der Ruhr-Universität Bochum (AIRUB). Its latest version (June 2010) is free available from the ESO LABOCA web page[3]. Some first basic commands to start and handle the software are summarised in Table 3.1.

For the reduction of LABOCA data, there are already several example scripts available, which can be used and adapted by the user. In the following I will describe the scripts, that are used to generate our LABOCA maps.

From an observation run with LABOCA one obtains three different kinds of data. The skydip, calibrator measurements, and the scientific data. The skydip consist of two runs. The first one is the so called hot-sky scan, from which the zenith sky temperature is determined for calibration. In the second scan the telescope dips down vertically from the zenith to the horizon. From this scan the observed sky temperature can be calculated as a function of the elevation (Fig. 3.6), and the opacity τ can be determined. Such scans are made typically every two hours (Siringo et al., 2009). The reduction of

---

[3]http://www.eso.org/sci/activities/apexsv/labocasv.html
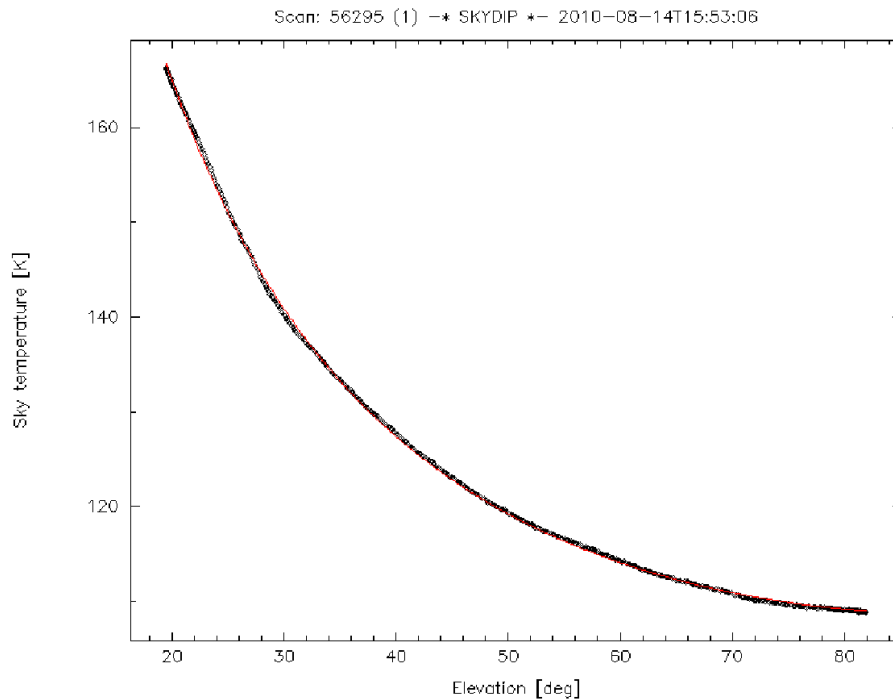
Figure 3.6: Skydip measurement from our deeper LABOCA observations discussed in Sect. 3.4.2.

the skydip can be done with the script `reduce-skydip.boa`. Therefore first the scan number of the hot-sky scan has to be assigned to the program (`scannr=`*'scan number'*). As in every reduction step, in the beginning the channels from broken or unreliable bolometers are flagged and excluded from the data processing. After the program has also corrected the data for temperature drifts, due to the immense mechanical movement the telescope is exposed during the skydip scan, it finally calculates the sky temperature and the opacity τ of the atmosphere. With `reduce-skydip-loop.boa` this can be repeated for all skydips during the observation run. The opacities are stored together with the observation time in a data file. With the function `getTau()` the opacity can be determined for each scientific data scan, using the opacity value stored in the data file which is closest in time or a linear interpolated opacity.

The opacities are checked against primary calibrators (planets: Uranus, Neptun, Mars, Saturn, Jupiter, Venus) and secondary calibrators (bright galactic sources: e.g. B13134, η Car, CW-Leo, IRAS16293, G10.62, G5.89). In the program `reduce-calibrator.boa` the observed fluxes in calibrator measurements are compared to the expected ones, and a calibration correction factor is calculated. To process many scans at once the script

`reduce-calib-loop.boa` can be used. This stores the calibration correction factors in a data file, and they can be addressed with the function `getCalCorr()`.

To reduce LABOCA observations of thermal dust emission from MCs the script `reduce-map-weaksource.boa` is well suited (Schuller et al., 2009). Every single scan is processed and calibrated separately, and afterwards all scans of the observation run are added together using the function `mapsumfast()`. During the reduction process, as mentioned above, first all bad pixels are flagged, as well as data affected by the movement and acceleration of the telescope. Afterwards, the data is corrected for correlated noise, which results from the variable atmospheric emission (see Sect. 3.2). Therefore, the median of the normalized signal is first calculated and removed for the whole bolometer array (`medianNoiseRemoval()`) and then for channels sharing parts of the electronics, as the amplifier box (up to 80 channels, `correlbox()`) or the read-out cable (up to 25 channels, `correlgroup()`). Unfortunately uniform extended emission can not be distinguished from the sky noise and any emission on scales larger than $\sim 2.5'$ is filtered out. In a next step very noisy channels are flagged (`data.flagFractionRMS`) as well as data above or below a given number of times the channel rms (e.g spikes from high energetic particles, `despike()`). In the end a low frequency filtering is performed (`data.flattenFreq()`), to correct for the effects of instrumental offsets and a first order baseline is removed (`base(order=1, subscan=0)`) before a natural weighting $(1/\text{rms}^2)$ is applied to the data (`weight()`).

This method of data reduction generates overcorrections on the border of bright sources, which leads to dark voids around them (see left top panel in Fig. 3.7). To avoid this an iteration with source models is applied. Therefore, the final sources weighted with the rms are subtracted from the original data (`data.addSource(model=`*'source model'*`, factor=-1)`) before the reduction process is executed once more. Afterwards, the source model is added again (`data.addSource(model=`*'source model'*`, factor=1)`). This procedure can be repeated until the artefacts around the sources have vanished (bottom right panel in Fig.3.7) and the final map is accomplished.
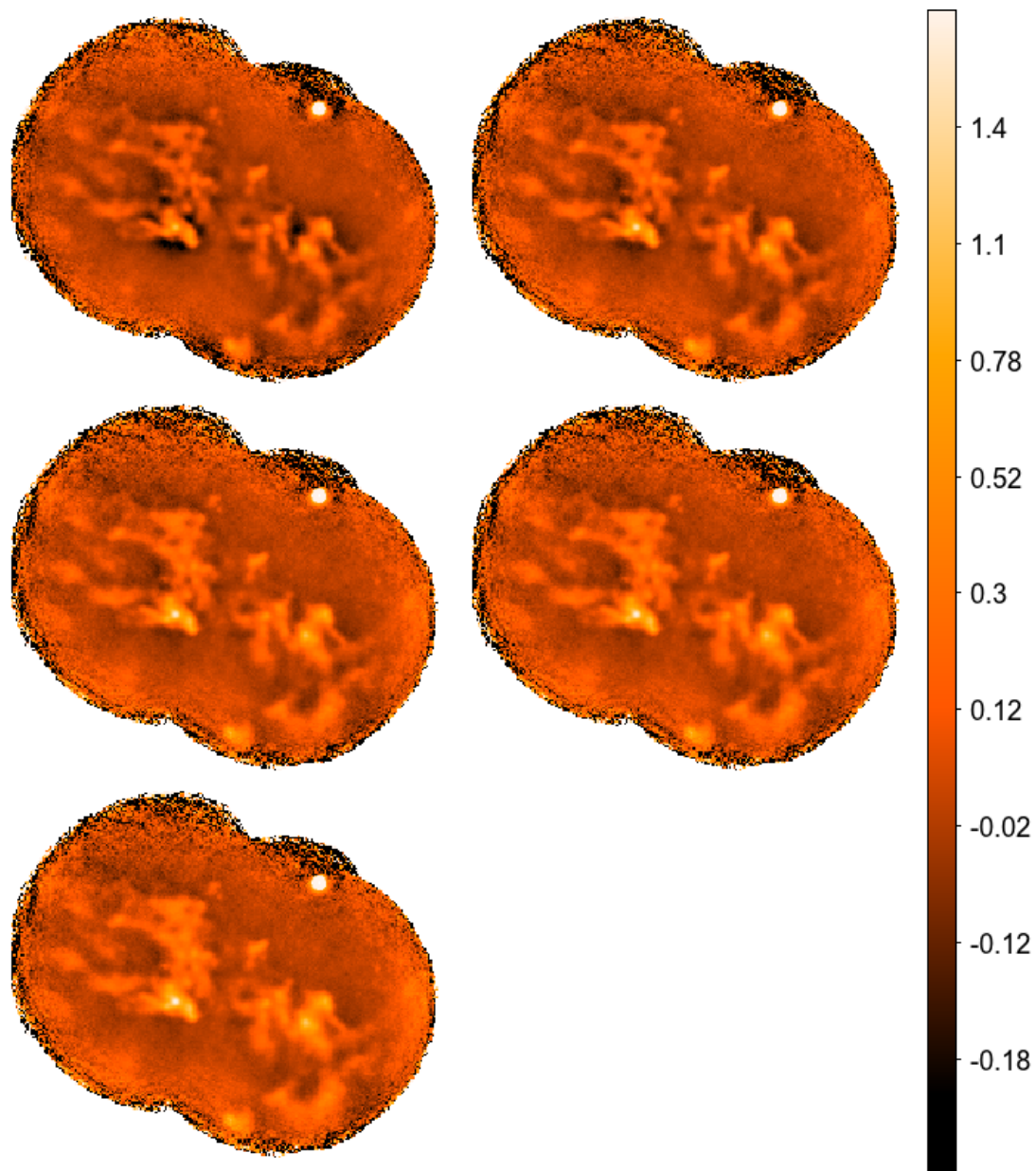
Figure 3.7: The iteration steps with a source model we performed for our deeper LABOCA observations of a highly irradiated cloud pillar. The scale bar on the right shows the intensities in Jy/beam in logarithmic scale.

3.4   Observations

3.4.1   The Wide Field LABOCA Map

With LABOCA we obtained a wide-field ($1.25° \times 1.25°$) map (Fig. 3.8) of the Carina Nebula Complex which is discussed in detail in Preibisch et al. (2011d). The total area has been covered by a raster of pointings, at which fully sampled maps of the total FoV have been achieved. Thereby we used the "raster map in spiral mode" as described in Sect. 3.2. The total on-source integration time amounts about 10 hours. The observations were made on 22th, 24th, and 26th of December 2007 under good observing conditions, with a PWV of less than 2 mm.

The so obtained map was reduced by F. Schuller (MPIfR) using the BoA software (Sect. 3.3). The total calibration error should be below 15% as the data were calibrated by applying an opacity correction which is received, as explained above, from the skydip observations and checked against primary and secondary calibrators. Because of the correlated noise removal during the data reduction the final map is not sensitive to structures larger than the FoV and can only partly recover emission on scales larger than $\approx 2.5'$. As uniform emission of angular scales above $\approx 2.5'$ is filtered out, the measured fluxes in the map have to be seen as lower limits.

To transform the surface brightness to integrated fluxes it has to be multiplied with the pixel-to-beam-size ratio. Our final map has a pixel size of $6.07''$ (i.e. ~ 3 pixels per beam). The beam area can be calculated as integral over the Gaussian

$$A = \int e^{-\frac{1}{2}(\frac{x-x_0}{\sigma_x})^2} dx \stackrel{2D}{=} 2\pi\sigma_x\sigma_y. \tag{3.1}$$

With a FWHM$= 2\sqrt{2\ln 2}\sigma = 18,6''$ we find a LABOCA beam area of 395 arcsec^2 and a pixel-to-beam-size ratio of 0.0941 beams/pixel. The average rms noise level for the map is about 20 mJy/beam, which corresponds for isolated compact clumps with estimated temperatures of $T \approx 20 - 30$ K to a sensitivity limit in mass of about $2\,M_\odot$. For the clouds we measure intensities up to around 4 Jy/beam. The total flux measured in the map above a $3\,\sigma$ noise level amounts to 1147 Jy.
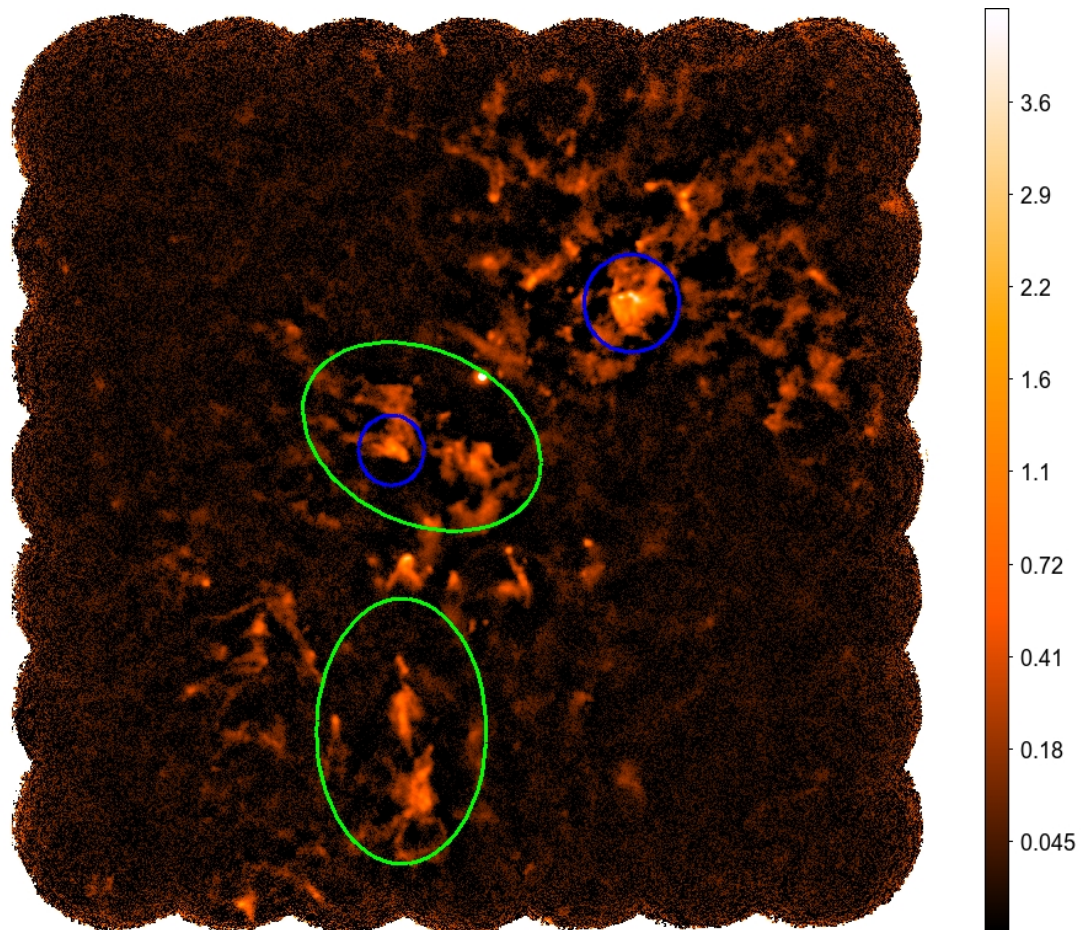
Figure 3.8: The wide-field LABOCA map of the Carina Nebula Complex. The scale bar on the right shows the intensities in Jy/beam in logarithmic scale. The green and blue ellipses mark the regions we observed again with LABOCA and SABOCA respectively.

3.4.2 Deeper LABOCA Maps

In a following observation we obtained deeper LABOCA maps of two selected regions of the Carina Nebula. With the higher sensitivity it is possible to determine a reliable ClMF for also the low-mass population of the clumps. The two regions are experiencing very different levels of feedback, which could affect the resulting ClMF. The stellar feedback on the one hand disperses the surrounding clouds but also compresses other parts of the gas, triggering further star formation. Highly affected clouds are therefore expected to inclose a larger fraction of their gas within their denser structures as more isolated clouds and therefore tend to form more massive stars with higher efficiency (Whitworth et al., 1994). A relation between the star formation activity within bright-rimmed clouds and the strength of the external irradiation was found by Morgan et al. (2008).

Both of the regions are located in the South Pillar region. Our first target was a small pillar in the south-east of η Car (in the following "LABOCA north"). This pillar is highly affected by the stellar feedback and UV radiation from the numerous nearby massive stars of Tr 16, as well as from the X-ray irradiation from the numerous highly X-ray active young stars surrounding the pillar. Additionally it is embedded in strong diffuse X-ray emitting plasma. In the near-infrared the pillar shows remarkable substructures due to this feedback effects. We again used the "raster spiral mode" to map $13' \times 8'$ (104 square-arcmin) around the pillar, with a total on-source integration time of about 8 hours. The observations were made on 20th of April, 17th to 19th and 21st to 22nd of June, as well as 13th and 14th of August in 2010. The observing conditions have been good. The PWV was less than 2 mm, except for the first day where it had also values up to 2.2 mm.

Furthermore we obtained a $8' \times 16'$ (128 square-arcmin) raster spiral map of the "Giant Pillar" (Smith et al., 2010b; Rathborne et al., 2008) ("LABOCA south"). The Giant Pillar is a symmetric and large-scaled (~ 10 pc) cloud pillar, which is located far in the south of the Carina Complex, at a projected distance of ~ 15 pc from η Car. Its elongated structure is pointing towards η Car and Tr 16 star cluster, indicating that it is affected by their radiation and stellar wind feedback. A YSO detected at the tip of the pillar confirms that there is still ongoing triggered star formation (Rathborne et al., 2004). However, due to its distance to the massive stars in the region, the irradiation and stellar feedback effects should be much less than for our small pillar. We requested a total on-source integration time of 8 hours for the Giant Pillar. The observations have been gained from 3rd to 6th May 2010 under very good observing conditions, with a

PWV of less than 1 mm.

I reduced the data obtained in these observations with BoA, following the procedures described in Sect. 3.3. From the skydip measurements the zenith opacities τ during the observations can be calculated (see Table 3.2). As the `reduce-skydip.boa` procedure is usually underestimating the actual zenithal τ they have to be checked against primary and secondary calibrators. For the LABOCA north region Mars and Venus have been used as primary calibrators. As secondary calibrators IRAS 16293, B13134, G5.89, G10.62, CW-LEO and, η Car have been observed. However, due to their variability CW-LEO and η Car led to differing correction factors than all, at the same time observed calibrators. Therefore we decided not take them into account, as well as two other bad calibrator observations. For LABOCA south we used calibrator observations of Mars (primary), B13134 and IRAS 16293 (secondary). Calibrator observations of η Car again have been omitted, except for one case, where no other reliable calibrator observation is available.

After the calibration corrections were achieved the maps are reduced, using the `reduce-map-weaksource.boa` script and four iterations with the source model. The final maps again have a pixel size of $6.07''$ and are therefore well comparable to the large map (Fig. 3.9).

In both maps we find an average noise level of 10 mJy/beam. For isolated clumps with temperatures of $\approx 20 - 30$ K this correspond to a sensitivity limit in mass of $\approx 0.8 - 0.5\,M_\odot$ respectively. Clumps with masses in this range will typically generate stars with initial masses around $\sim 0.1\,M_\odot$, assuming a constant star formation efficiency (Alves et al., 2007; Nutter & Ward-Thompson, 2007). This corresponds to the detection limit of the existing infrared data.

For the LABOCA north region we find a total flux above a $3\,\sigma$ noise level of 194 Jy. The clouds have intensities up to 1.8 Jy/beam. The brightest clouds in the LABOCA south region have lower intensities of about 1 Jy/beam. The total flux above the noise level can be measured to 106 Jy.

3.4.3   New SABOCA and Molecular Line Data

In March 2010 the Submillimetre APEX Bolometer Camera (SABOCA, Siringo et al., 2010) was approved for use at the APEX telescope. It operates in the atmospheric window at 350 μm (852 GHz, see Fig. 3.2) and consists of an array of operational 37 composite superconducting bolometers on a hexagonal grid and two blind additional

Table 3.2: Opacities derived with `reduce-skydip-loop.boa` for the individual observations

LABOCA north			LABOCA south		
scannr	date	τ	scannr	date	τ
18944	2010-04-20T03:43:41	0.430	21964	2010-05-03T22:41:23	0.288
18960	2010-04-20T04:21:53	0.465	21998	2010-05-03T23:56:33	0.246
18973	2010-04-20T04:49:40	0.481	22017	2010-05-04T00:38:21	0.268
36650	2010-06-17T21:33:36	0.302	22349	2010-05-04T21:16:23	0.214
36679	2010-06-17T22:44:40	0.294	22404	2010-05-04T22:34:37	0.250
37319	2010-06-19T18:12:33	0.330	22425	2010-05-04T23:30:19	0.273
37356	2010-06-19T19:42:17	0.361	22457	2010-05-05T01:38:12	0.198
37949	2010-06-21T23:19:30	0.290	22835	2010-05-05T22:22:26	0.262
37973	2010-06-22T00:18:25	0.309	22869	2010-05-05T23:48:20	0.262
55934	2010-08-13T19:55:48	0.175	22887	2010-05-06T01:01:23	0.220
55954	2010-08-13T20:44:19	0.177	22904	2010-05-06T02:11:12	0.204
56289	2010-08-14T15:46:25	0.210			
56294	2010-08-14T15:53:06	0.217			
56319	2010-08-14T16:45:37	0.230			
56339	2010-08-14T17:31:04	0.230			
56363	2010-08-14T18:24:25	0.235			
56409	2010-08-14T20:14:55	0.224			
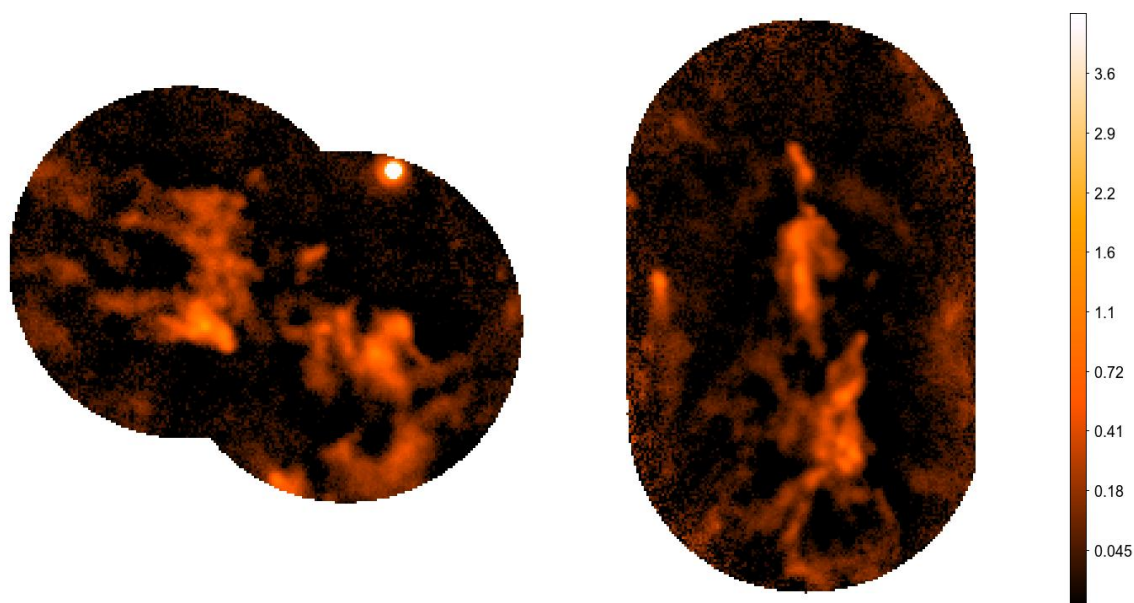
Figure 3.9: The deeper LABOCA maps of the Carina Nebula Complex. The scale bar on the right shows the intensities in Jy/beam in logarithmic scale.

bolometers positioned at diametrically opposite sides for monitoring purpose. SABOCA was built by the MPIfR together with the Institute of Photonic Technology (IPHT).

SABOCA's FoV of 1.5' makes its large-scale sensitivity comparable to similar bolometer arrays in this wavelength regime. However, to acquire a reasonable on source integration time we selected only few arcmin wide fields within the Carina Nebula Complex for our observations. With a beam size of 7.8" SABOCA provides a spatial resolution that is 2.5 times better compared to LABOCA (see Fig. 3.10). In the distance of the Carina nebula this will even allow us to resolve small molecular cloud structures with physical scales of 0.08 pc, and to separate the individual cloud cores from the surrounding diffuse emission.

With SABOCA we obtained observations of two selected regions. First we mapped a 12.5 square-arcmin wide field of the small, highly irradiated pillar, from which we already gained some additional deeper LABOCA data, in the "LABOCA north" region (see Sect. 3.4.2, Fig. 3.8). The observations have been made under very good conditions. Furthermore we observed a cloud in the west of Tr 14 (28 square-arcmin). Especially the western edge of this cloud has been highly irradiated by the numerous massive stars in Tr 14. Only a few deeply embedded protostellar objects can be detected in this cloud (Tapia et al., 2006), so the star formation activity has been found to be very low. But
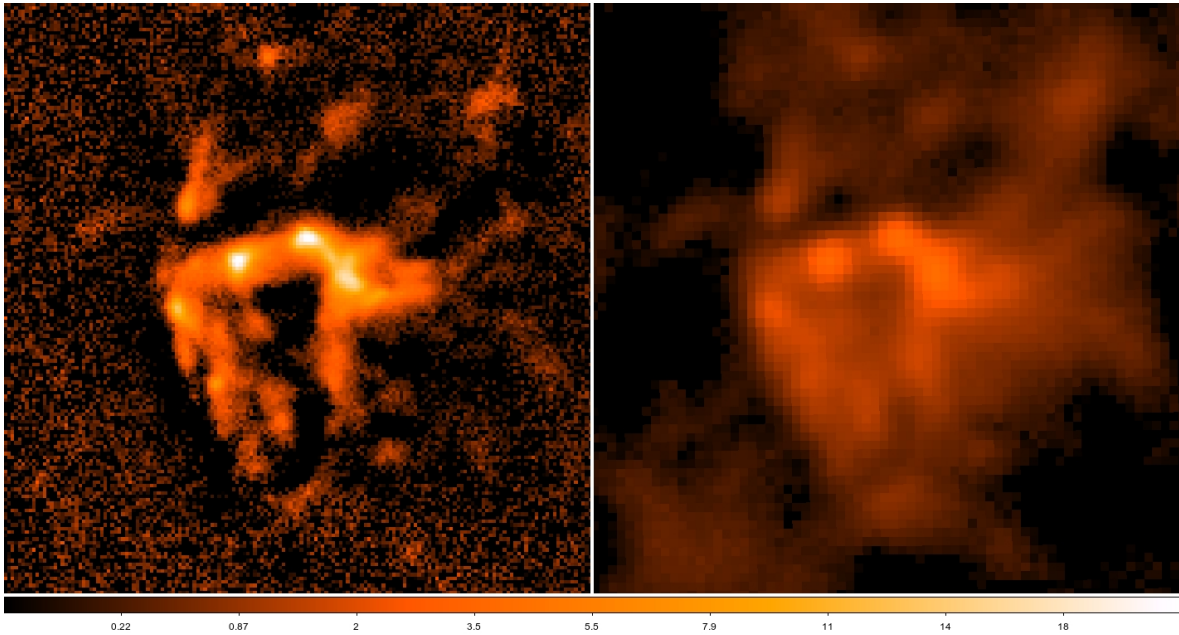
Figure 3.10: *Left:* **A preliminary SABOCA map of the cloud in the west of Tr 14, produced by F. Schuller.** *Right:* **The same region in our wide field LABOCA map. The scale bar shows the intensities in Jy/beam in logarithmic scale.**

in the near future the strong stellar feedback that compresses the cloud in this region is assumed to trigger new star formation.

Fig. 3.10 shows the cloud near Tr 14. The map on the right is from our wide-field LABOCA observations, where only the brightest sources can be distinguished from the diffuse emission around them. On the preliminary SABOCA map already much more detailed cloud structures are apparent. With this data we hope, that we will be able to extract also the molecular cloud cores in this region.

We also used several heterodyne receivers (e.g. SHFI, CAMP+, FLASH), that are mounted in the Nasmyth cabins of the APEX telescope, to obtain molecular line data. We achieved $4' \times 4'$ maps of the "LABOCA north" pillar in several CO transition lines (CO (J=3–2), (J=7–6) and (J=6–5)). A future analysis of these data will reveal the kinematics, the molecular excitation, and the temperature distribution in this region. Additionally we did 15 pointings aligned to the pillars axis and a few in orthogonal direction in the much fainter ^{13}CO (J=3–2) line and simultaneously in the CO (J=4–3) line. As the ^{12}CO lines are optically thick, these observations in the optically thin ^{13}CO line are crucial to determine the column densities in the cloud (see Sect. 2.1).

For these data no further analysis has been done yet. However, in the future they will help to improve our knowledge about the molecular dust structures in this region and how it is influenced by the massive star feedback. The high angular resolution of this data will make it also possible to compare our results with numerical observations and learn more about the formation and evolution of such structures.

Chapter 4

The Clump Mass Function in the Carina Nebula

To investigate the clumpy dust structures and to determine the ClMF in the Carina Nebula we analysed the sub-mm emission in our large-field LABOCA map (see 3.4.1). In this map structures down to 0.2 pc can be resolved. The map thus is suitable to resolve the molecular clumps, but the individual cores can not be resolved. The clumps are expected to be the sites at which star clusters can form, contrary to the smaller cores which are supposed to form single or gravitationally bound multiple protostars (Williams et al., 2000).

To identify the clumps, we used three common source extraction algorithms, which are described in Sect. 4.1. The masses of the clumps are then calculated, applying two different temperature approximations (Sect. 4.2). The resulting ClMF is discussed in Sect. 4.3. The here described analysis and results have been published in Pekruhl et al. (2013).

4.1   The Clump-finding Algorithms

In the past several techniques to extract the cores and clumps of MCs in an automated and consistent way have been developed. These algorithms mostly work directly on the two-dimensional maps or three-dimensional data cubes obtained during the observations. In the three-dimensional case the third dimension is the velocity, which can be determined from molecular line data. Here I describe three commonly used routines, we
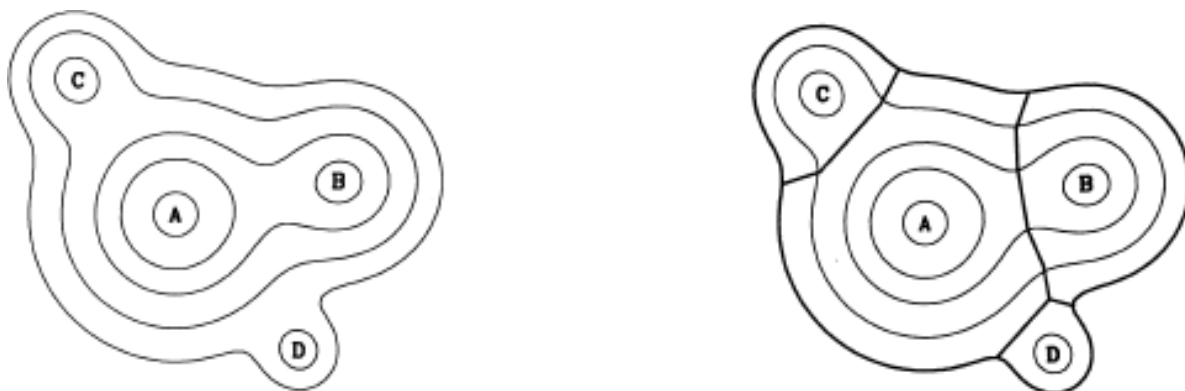
Figure 4.1: From Williams et al. (1994): A two-dimensional sample contour map (left), with the clumps found by the CLUMPFIND algorithm (right).

applied on our LABOCA data.

4.1.1 CLUMPFIND

The CLUMPFIND (CF) algorithm from Williams et al. (1994) is designed similar to the way the eye would analyse the data. The IDL[1] (Landsman, 1993) coded program contours the data in linear, user-defined steps while reading it. Tests on simulated data performed by Williams et al. (1994) showed that the best results can be achieved by using a stepsize of twice the rms noise level σ. Then the algorithm identifies the peaks of emission which locate the clumps. Afterwards CLUMPFIND starts at the highest level and follows the contours down to the detection threshold, a second user-defined parameter, e.g. 3σ. Every isolated contour is defined as a new clump, others are extensions of previously found clumps. Contours that surround only one peak can be easily assigned, while contours around several peaks have to be distributed. CLUMPFIND therefore uses a "friends-of-friends" algorithm. Thereby the pixels next to the unblended contours (clump) and their direct neighbours will be assigned to this clump. Only few pixels in the middle may be connected to more than one clump, and will then be completely assigned to the nearer peak (Fig 4.1). No specific clump profile is assumed.

As we find an rms noise level of about 20 mJy/beam for our data we start contouring at an intensity level of 60 mJy/beam and go in steps of 40 mJy/beam up to 4.5 Jy/beam, below which all the emission of the clouds is found. CLUMPFIND extracts 687 molecular clumps with a total flux of 720 Jy from the LABOCA map. This is about 63% of the total

---

[1]http://www.exelisvis.com/ProductsServices/IDL.aspx

flux in the map. The remaining flux is distributed in diffuse emission. A section of the central region around the star cluster Tr 14, with the clumps detected by CLUMPFIND marked as blue circles, is shown in the left panel of Fig. 4.3. The bright, point-like source η Car has been excluded from this and the following samples.

4.1.2   GAUSSCLUMPS

GAUSSCLUMPS (GC) (Stutzki & Guesten, 1990) is an iterative procedure, assuming a Gaussian-shaped density distribution for all clumps. The algorithm works directly on the continuous intensity distribution of the data and searches for the absolute intensity maximum in the map. There it fits a Gaussian-shaped clump. Therefore a least-squares fitting method is used, i.e. χ^2 is minimised by varying the clump parameters (position of the peak, peak intensity F_{max}, size and orientation of the principal axes, linewidth) under certain constraints, specified by a weighting function ω and three stiffness parameters s_0, s_a, and s_c (Kramer et al., 1998). Afterwards the clump is subtracted from the original map and a residual map is created on which the algorithm continues with the next iteration step.

We used the GAUSSCLUMPS algorithm as it is implemented in the "Starlink" package CUPID[2]. As an rms noise level of 22 mJy/beam has been calculated by the program, we define a detection threshold of $3\,\sigma$. This is similar to the threshold we used for the CLUMPFIND sample, so the resulting ClMFs are comparable. Kramer et al. (1998) showed that the best fit is achieved for the stiffness parameter combination $s_0 = s_a = s_c = 1$. For all other parameters we used also the default values. With this configuration 371 clumps have been detected (see Fig. 4.3, middle panel). This is only about half the number found by CLUMPFIND. Nevertheless, the total flux of 728 Jy within these clumps is nearly the same as for the CLUMPFIND sample.

4.1.3   SExtractor

The third algorithm we used to analyse the data is the SExtractor (SE, short hand for 'Source Extractor') software by Bertin & Arnouts (1996), which originally was developed to detect stars and galaxies in large surveys. However the algorithm has also been used to extract sources in sub-mm observations of MC structures (Schuller et al., 2009; Coppin et al., 2000). Like the CLUMPFIND algorithm it uses the thresholding method. It first

---

[2]http://starlink.jach.hawaii.edu/starlink/CUPID
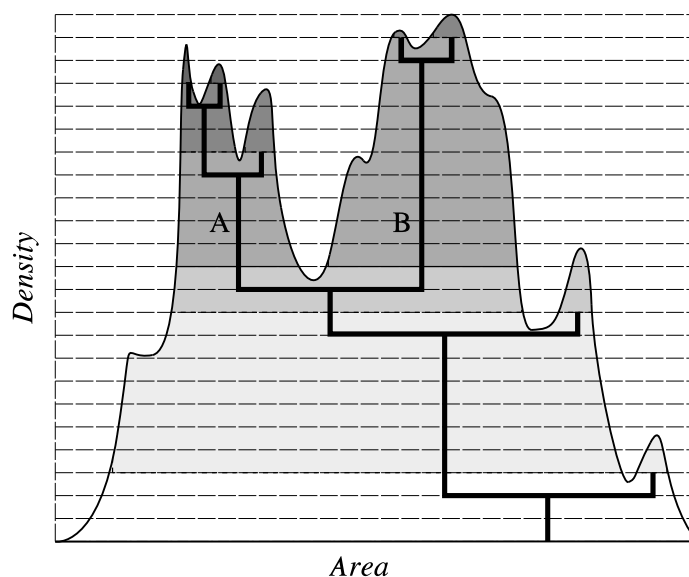
Figure 4.2: A representation of the deblending procedure used by the SExtractor algorithm. *Credit:* **Bertin & Arnouts (1996)**

contours the data at the detection threshold. Nearby sources are blended in this step. To deblend them, each set of so connected pixel is then contoured at 30 exponentially spaced levels between the peak value and the detection threshold (see Fig. 4.2). Afterwards the program follows the structures from the peak downwards. At each contour level it tests if there is another peak, with an intensity exceeding a certain fraction of the total intensity, included. If this is the case, it extracts a new source. For each pixel between these maxima, SExtractor calculates its contribution to each source. Therefore it assumes a Gaussian profile for the sources and converts this into a probability for the pixel to be assigned to a certain object.

The SExtractor software is included in the GAIA ("Graphical Astronomy and Image Analysis tool") software[3]. As the program calculated an rms noise level of about 30 mJy/beam we used a detection threshold of 2σ to make our results comparable to the other algorithms. Corresponding to our resolution we defined the minimal area of a detected clump to 10 pixel. SExtractor finds 432 sources (see Fig. 4.3, right panel) with a total flux of 823 Jy, 72% of the total flux in the map. This is slightly higher than the results of the other algorithms.

All the extracted sources of the SExtractor sample, as well as the clumps identified by

---

[3]http://star-www.dur.ac.uk/ pdraper/gaia/gaia.html
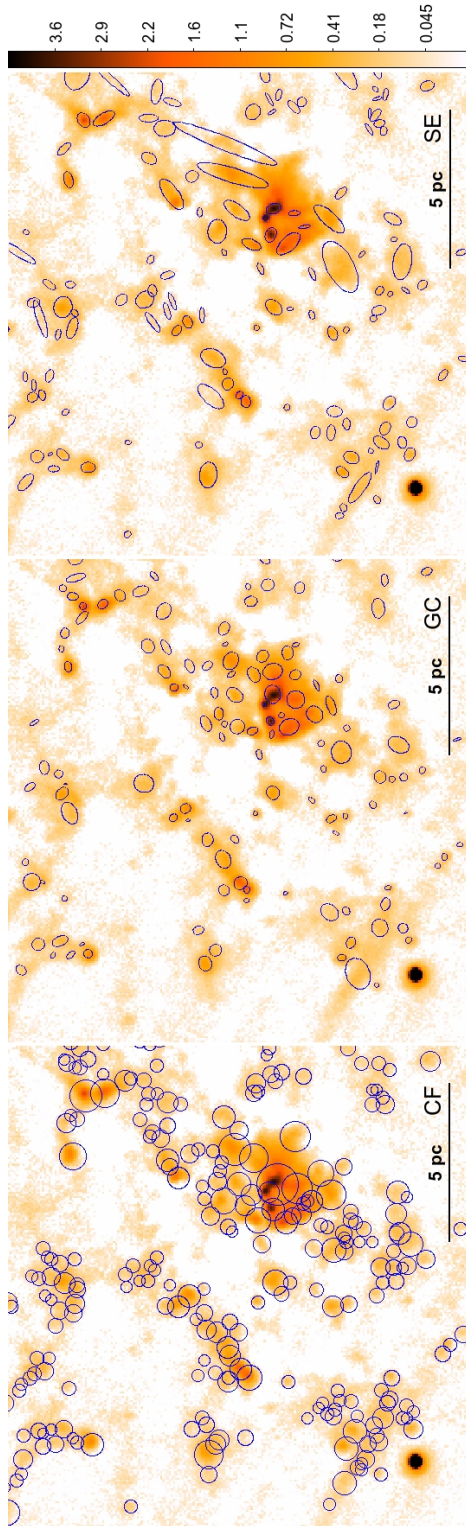
Figure 4.3: A section of our LABOCA map at $870\,\mu m$ of the central region around Tr 14 in the Carina Nebula Complex. The units of the scale bar on the right are Jy/beam in logarithmic scale. In the left panel the positions of the clumps found with CLUMPFIND are shown with circles of the effective radial size of the clumps. The **GAUSSCLUMPS** (middle panel) and **SExtractor** (right panel) samples are shown as ellipses. The sizes of their axes correspond to the rms deviations. The bright source in the lower left corner is the Luminous Blue Variable η Car.
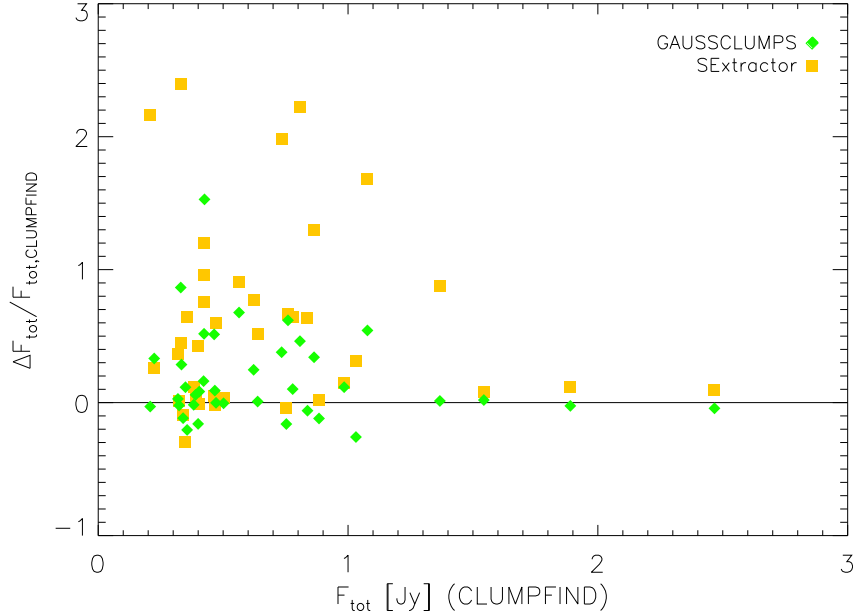
Figure 4.4: The relative difference of the total GAUSSCLUMPS (green) and SExtractor (yellow) fluxes F_{tot} with respect to the CLUMPFIND fluxes of the 38 commonly identified clumps.

the algorithms introduced before, have fluxes above 0.15 Jy, except 18 of them that we considered artefacts and do not further take into account in our analysis.

4.1.4   Common Sources

The three used extraction algorithms are working along different principles. While CLUMPFIND assumes no specific clump profile, the other two algorithms presume a Gaussian shape. Furthermore, the CLUMPFIND and SExtractor algorithms use thresholding methods, while the GAUSSCLUMPS algorithm works on residual maps.

In order to check how well the extraction results of the different algorithms agree, we searched for clumps that are detected by all three algorithms. Within the crowded and filamentary regions, which dominate the Carina Nebula, a direct one-to-one correlation of single clumps proves difficult, as most of the clumps are blended. In this cases the different algorithms produce often quite different decomposition results.

However, in the less crowded parts of our map, we could identify 38 rather isolated
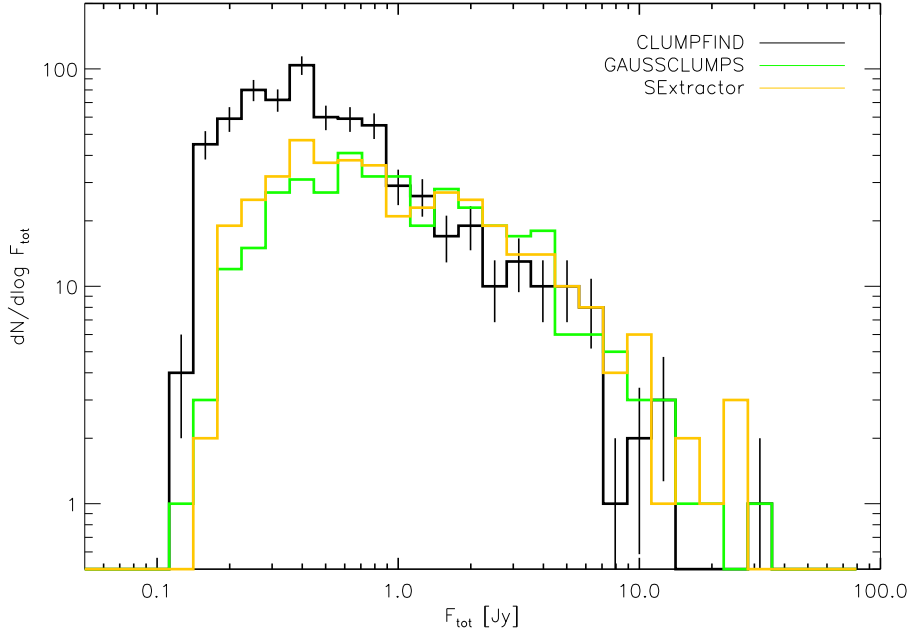
Figure 4.5: The flux distribution for the three different clump-finding algorithms with a statistical error $\sqrt{\frac{dN}{d\log F}}$ for the CLUMPFIND sample.

clumps which are detected by all three algorithms. The derived total fluxes yielded from the different algorithms are all below 3 Jy, what corresponds to $\sim 80 M_\odot$ for an assumed temperature of 20 K. In Fig. 4.4 we plot the relative difference of the GAUSSCLUMPS and SExtractor total fluxes with respect to the CLUMPFIND fluxes. The plot shows reasonable agreement, although differences by factors up to $\sim 2 - 3$ are seen in the total fluxes for some of the faintest clumps in this commonly found sample. For the majority of the clumps the deviations are less than 50%, and for most of the brighter clumps a very good agreement, with deviations of less than 10%, is found. From this we conclude that for sufficiently bright isolated clumps the three extraction algorithms yield consistent total fluxes and thus masses.

4.2 Mass Calculation

From the clump-finding algorithms we obtain the position and the peak intensity of each clump as well as the total flux F_{tot} (Fig. 4.5) over the whole area assigned to it (see Appendix A). These fluxes correspond to thermal dust emission and are in general

optically thin in the sub-mm continuum (Sect. 2.1). The total masses of the clumps can therefore be calculated via

$$M = \frac{d^2 \, F_{\nu,\,\text{tot}} \, R}{B_\nu(T_d) \, \kappa_\nu} \quad , \tag{4.1}$$

where $F_{\nu,\,\text{tot}}$ is the observed intensity integrated over the source and d is the distance of the MC (see Hildebrand, 1983). For the dust emissivity $\kappa_\nu = 1.85\,\text{cm}^2\,\text{g}^{-1}$ we use, as again for the gas-to-dust mass ratio $R = 100$, values from Schuller et al. (2009). As the Planck function $B_\nu(T_d)$ is highly dependent on the dust temperature T_d, a good estimate for the temperature is of particular importance. Only a few degrees difference in the relevant temperature regime can change the derived masses of the clumps by a factor of $2-3$. This can therefore strongly affect the derived ClMF of the region (Stamatellos et al., 2007).

Constant Temperature Profile

For single-wavelength data sets, such as our LABOCA map, a direct determination of the cloud temperature is not possible. In many investigations it is assumed that all clouds in a map have a common temperature (e.g. Mookerjea et al., 2004; Kirk et al., 2006). So, our first approach was to assume isothermal cloud and we considered two different values for the dust temperature, 10 K and 20 K. These values are typical and often used in sub-mm studies of molecular clouds (e.g. Johnstone et al., 2000; Schuller et al., 2009).

For an assumption of 20 K the total flux measured in our LABOCA map (1 147 Jy; see Sect. 3.4.1) corresponds to a total mass of $33.4 \cdot 10^3 \, M_\odot$. The 687 clumps detected by the CLUMPFIND algorithm have a total mass of $21.0 \cdot 10^3 \, M_\odot$. The remaining mass is distributed in diffuse structures. The individual clumps have masses between $4.5 \, M_\odot$ and $1024.4 \, M_\odot$. GAUSSCLUMPS detected 371 clumps with a total mass of $21.3 \cdot 10^3 \, M_\odot$. The clump with the lowest mass has a mass of $4.1 \, M_\odot$, while the most massive one has a mass of $981.6 \, M_\odot$. The total mass detected by SExtractor is $24.0 \cdot 10^3 \, M_\odot$, distributed over 411 clumps with masses between $4.7 \, M_\odot$ and $814.6 \, M_\odot$. If we halve the temperature, the mass rises by a factor of ≈ 3.3, so there is a high temperature dependency. These results are summarized in Table 4.1.

Individual Clump Temperatures

The assumption of a common temperature for all clumps may be a good approximation for more or less isolated clouds in a quiescent environment. The Carina Nebula, however, hosts several high-mass stars, which influence their surrounding clouds by stellar winds and ionizing radiation (see Sect. 2.3). The clumps in different parts of the complex will therefore be affected by strongly different levels of irradiation, depending on the exact distance from the nearest massive stars. This should lead to considerable differences in the temperatures of the clouds.

In general, clouds with high column density should be cooler than low-column density clouds, because their interior is better shielded from the external radiation field. Such a relation between column density and cloud temperature has been observed in several cases, and can provide us important information for an estimation of cloud masses. Peretto et al. (2010) investigated a sample of 22 IRDCs from the Hi-GAL plane survey (see Molinari et al., 2010), a open time key project to observe the inner part ($|l| \leq 60°$; $|b| \leq 1°$) of the Galactic plane with Herschel. They determined the column densities and temperatures within these clouds in great detail, by analysing the spectral energy distribution. Indeed they found a temperature gradient from the edges to the cooler inner regions, while the temperature minima are strongly correlated to the peaks of column densities. Their Fig. 6 (see Fig. 4.6) shows the expected anti-correlation between column density and temperature. We used the column density peak data (red circles) to quantify this relation, by performing an Ordinary Least Squares (OLS) Bisector (Isobe et al., 1990) fit and found the relation

$$\log N_{\mathrm{H_2}}[\mathrm{cm}^{-2}] = 25.6 - 0.22 \log T_d[\mathrm{K}] \tag{4.2}$$

The intensities of our LABOCA map can be converted to the column density via the formula

$$N_{\mathrm{H_2}} = \frac{F_{\nu,\,\mathrm{max}}\,R}{B_\nu(T_d)\,\Omega\,\kappa_\nu\,\mu\,m_{\mathrm{H}}} \quad, \tag{4.3}$$

where $F_{\nu,\,\mathrm{max}}$ is the peak intensity, Ω is the beam solid angle, and μ is the mean molecular weight. This gives us two equations relating the observed intensity, column density, and temperature. We solve these by calculating the column densities for the extracted clouds for temperatures between 0.1 K and 100 K in steps of $\Delta T = 0.1$ K and determined for
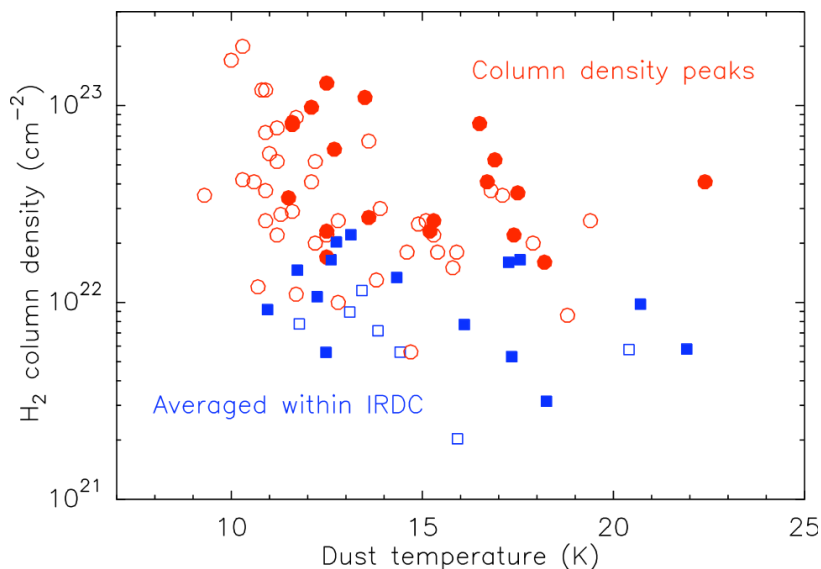
Figure 4.6: From Peretto et al. (2010): The red circles show column densities and temperatures at the column density peaks within the **22 IRDCs**. We used these data to derive the relation presented as Eq. (4.2). For the IRDCs represented by the filled symbols at least one 70μm point-like source has been found.
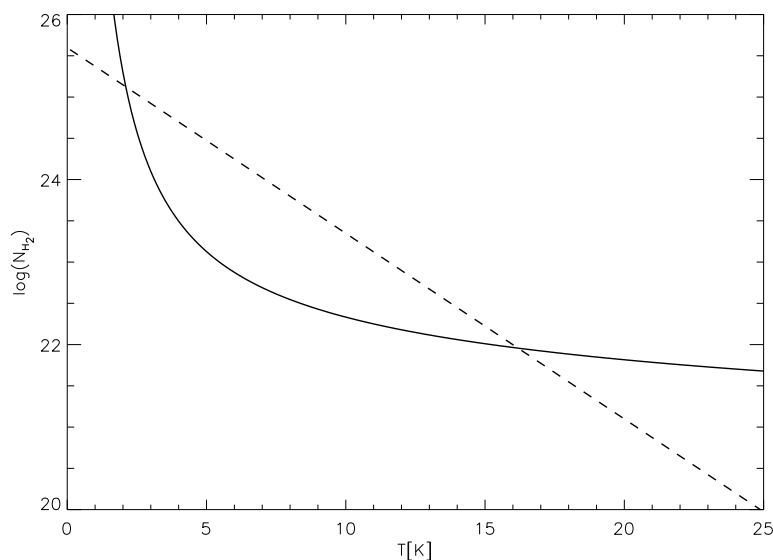
Figure 4.7: The temperature-density relation of a clump with a total flux $\mathbf{F}_{tot} = 0.52$ **Jy** and a peak intensity $\mathbf{F}_{max} = 0.26$ **Jy/beam**. There are two intersections $(T_1 = 2.2$ **K**, $T_2 = 16.1$ **K**) with the relation we found from the data from Peretto et al. (2010)(dashed line).

which values

$$|\log(Eq.\ (4.3)) - Eq.\ (4.2)| = min. \tag{4.4}$$

This gives us two solutions for the estimated temperatures (see Fig. 4.7), from which we can reject the first one as it leads to temperatures below 4 K. The second solution gives us, for all samples, temperatures between $8.5 - 18.5$ K, which are typical temperatures of MCs and clumps (Bergin & Tafalla, 2007). Fig. 4.8 shows the derived temperature and column density distributions for the different samples. Most of the clumps (CF: 92 %, GC: 86 %, SE: 87 %) have temperatures above 14 K, while the temperature peak lies around 16 K.

In Fig. 4.9 we show the location and the temperature of the clumps extracted with CLUMPFIND. The clump temperatures are shown by the color while the size of the circles increases with the measured flux $F_{\nu,\text{tot}}$. The clumps are assembled along filamentary structures and pillars. These pillars show cold dense clumps on their tips, within which star formation occurs. The pillars in the south-east of η Car and the Tr 16 cluster also show a temperature gradient and appear to be warmer nearer to the ionizing stars and cooler at their far end. Most of the brightest clumps are located within the structures a few arcminutes to the west of the Tr 14 cluster, where the clouds are dense and massive. So the ionizing radiation of the nearby cluster can only affect the cloud surfaces and does not reach the cool center of the cloud.

With these individual clump temperature estimates we now can derive the masses of individual clumps via Eq. (4.1). For the CLUMPFIND sample we find masses between $5.2\,M_\odot$ and $4\,652.2\,M_\odot$. The total mass extracted in clumps is about $42.2 \cdot 10^3\,M_\odot$. The GAUSSCLUMPS algorithm finds a total mass of $42.6 \cdot 10^3\,M_\odot$. The clump with the lowest mass has a mass of $8.2\,M_\odot$, while the heaviest one again has a mass of $4\,458.2\,M_\odot$. SExtractor finds clumps between $5.7\,M_\odot$ and $2\,972.8\,M_\odot$. The total mass detected is $48.2 \cdot 10^3\,M_\odot$ (see Table 4.1).

4.3 The Clump Mass Function (ClMF)

In Fig. 4.11 we plotted the ClMF of the three clump samples, derived by the different extraction algorithms, assuming individual and constant temperatures respectively. For the two constant temperatures the shape of the ClMF does not change, but is shifted to lower masses for the higher temperature. Below $\sim 10\,M_\odot$ our sample is not complete due to the mass sensitivity limit and the wide range of background levels at different locations in our map. For clump masses above $\sim 10 - 20\,M_\odot$ one can see the expected
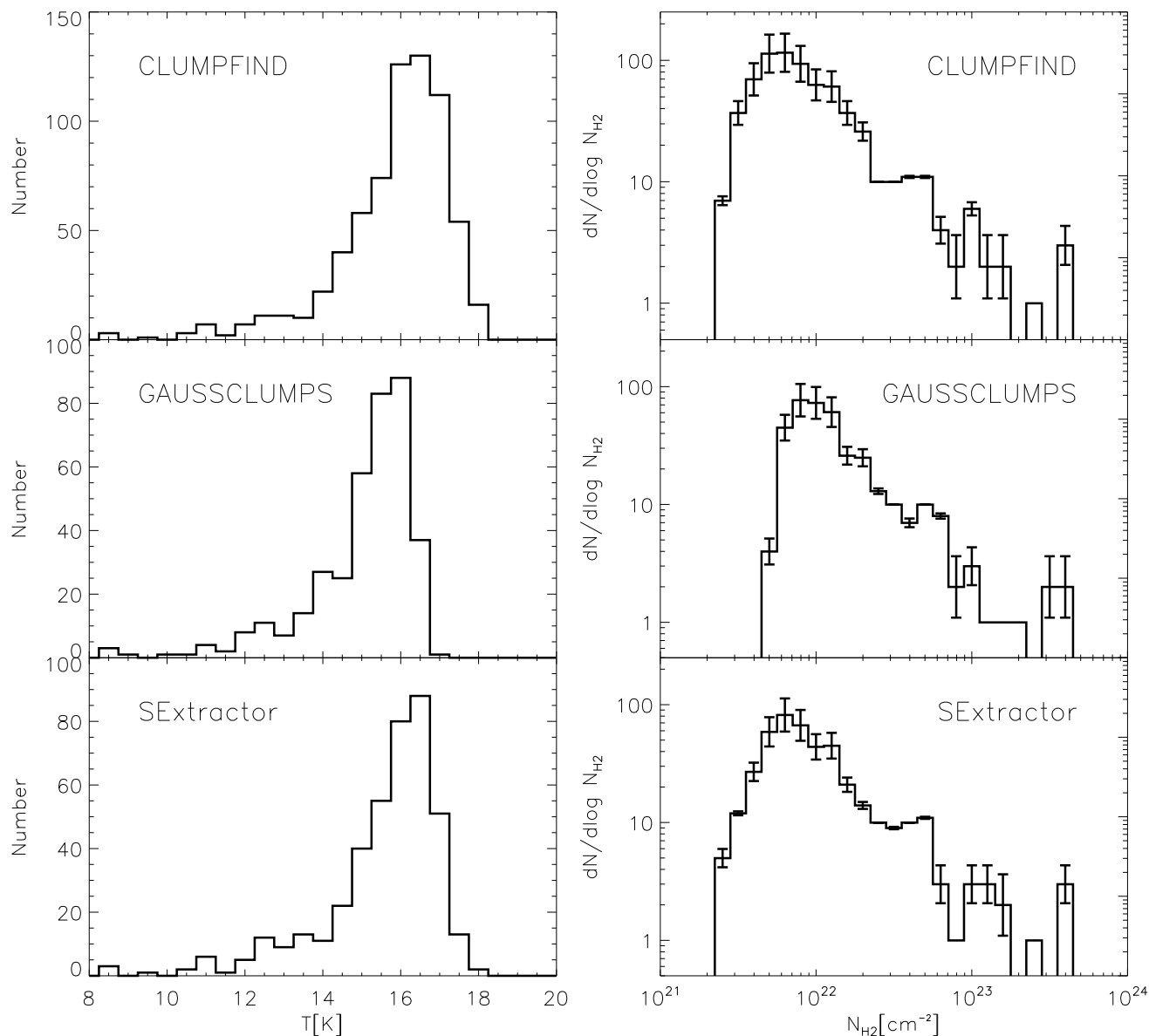
Figure 4.8: The distribution of individual clump temperatures (left) and column densities, with statistical errors $\sqrt{\frac{dN}{d\log N_{H2}}}$ **(right), as found from Eq. (4.3) and Eq. (4.2) for the three different clump-finding algorithms.**
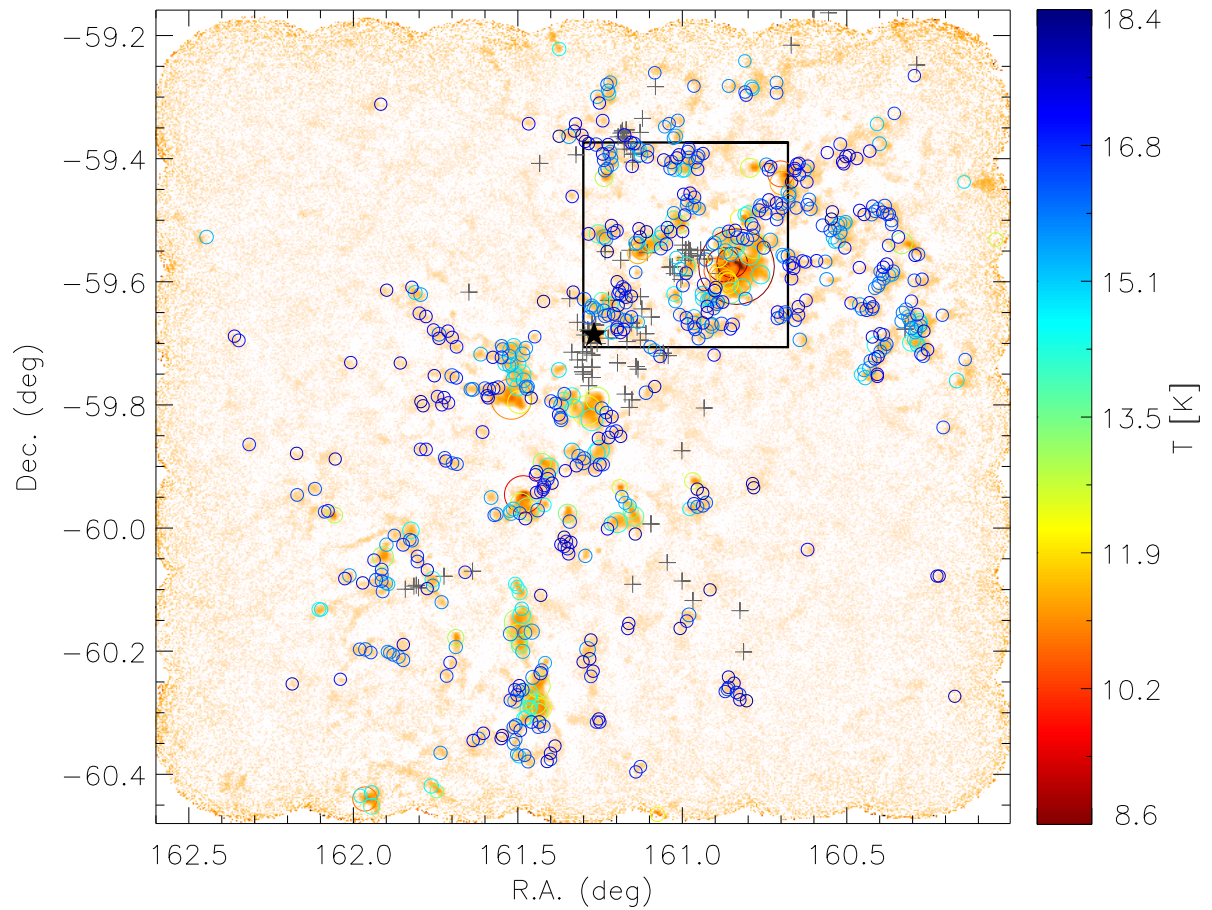
Figure 4.9: The temperatures and fluxes of the CLUMPFIND sample overplotted on the LABOCA map. The colour of the circles corresponds to the calculated temperatures and the size of the circles to the measured total flux ($\sim 0.15 - 35$ **Jy**). The grey crosses show the massive stars in the region (**Smith, 2006**). The position of η **Car** is marked by the black star. The black box represents the region shown in **Fig. 4.3.**
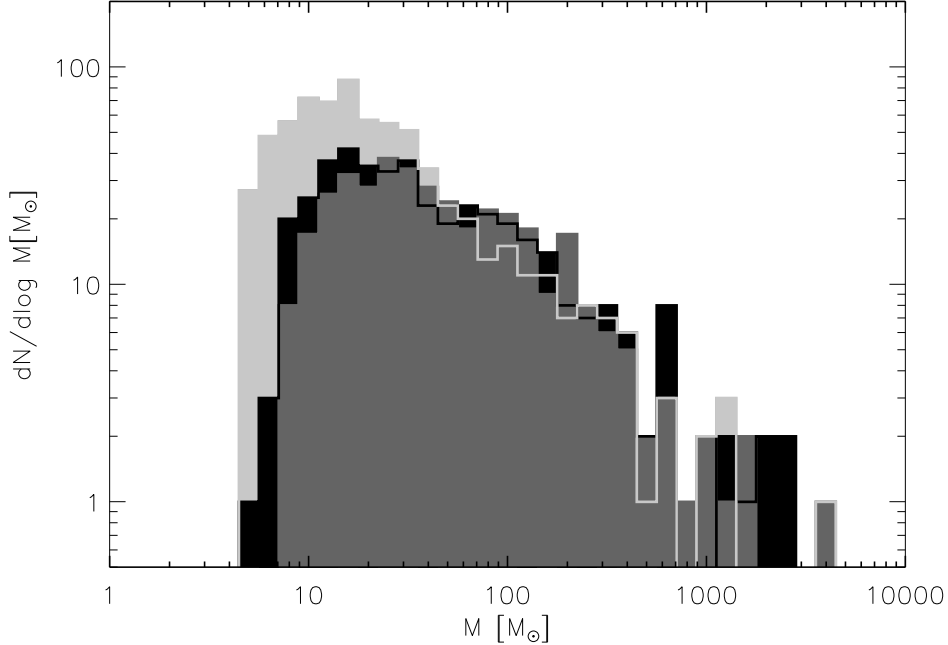
Figure 4.10: The CLUMPFIND ClMF (light gray), with the GAUSSCLUMPS CMF (dark gray) and the SExtractor CMF (black) overplotted. We derived the clump masses with the individual clump temperatures.

decrease in the number of clumps for rising clump masses, which roughly follows a power-law as defined in Eq. (2.6). To derive the slope of the power-law tail of the mass spectra, we use the method of Maschberger & Kroupa (2009) to fit the distribution. They use a bias-free Maximum Likelihood (ML) estimator to determine the power-law exponent without binning. This method takes into account only data above a given lower cut-off limit to calculate the power-law index.

For comparison we overplotted the histograms derived with the individual temperatures (Fig. 4.10). For masses below $50\,M_\odot$ CLUMPFIND finds, with 416 clumps, much more clumps than GAUSSCLUMPS and SExtractor, which find only 110 and 145 clumps respectively. Above $50\,M_\odot$ all three algorithms find almost the same amount of clumps and follow a power-law. In order to make sure that our power-law fit is not affected by incompleteness effects at lower masses, we use a conservative lower cut-off limit at $50\,M_\odot$ (gray dashed line in Fig. 4.11). For the power-law index we find $\alpha_{CF} = 1.95 \pm 0.07$, $\alpha_{GC} = 1.95 \pm 0.06$ and $\alpha_{SE} = 1.89 \pm 0.06$ for the CLUMPFIND, GAUSSCLUMPS, and SExtractor sample, respectively (see Table 4.1).
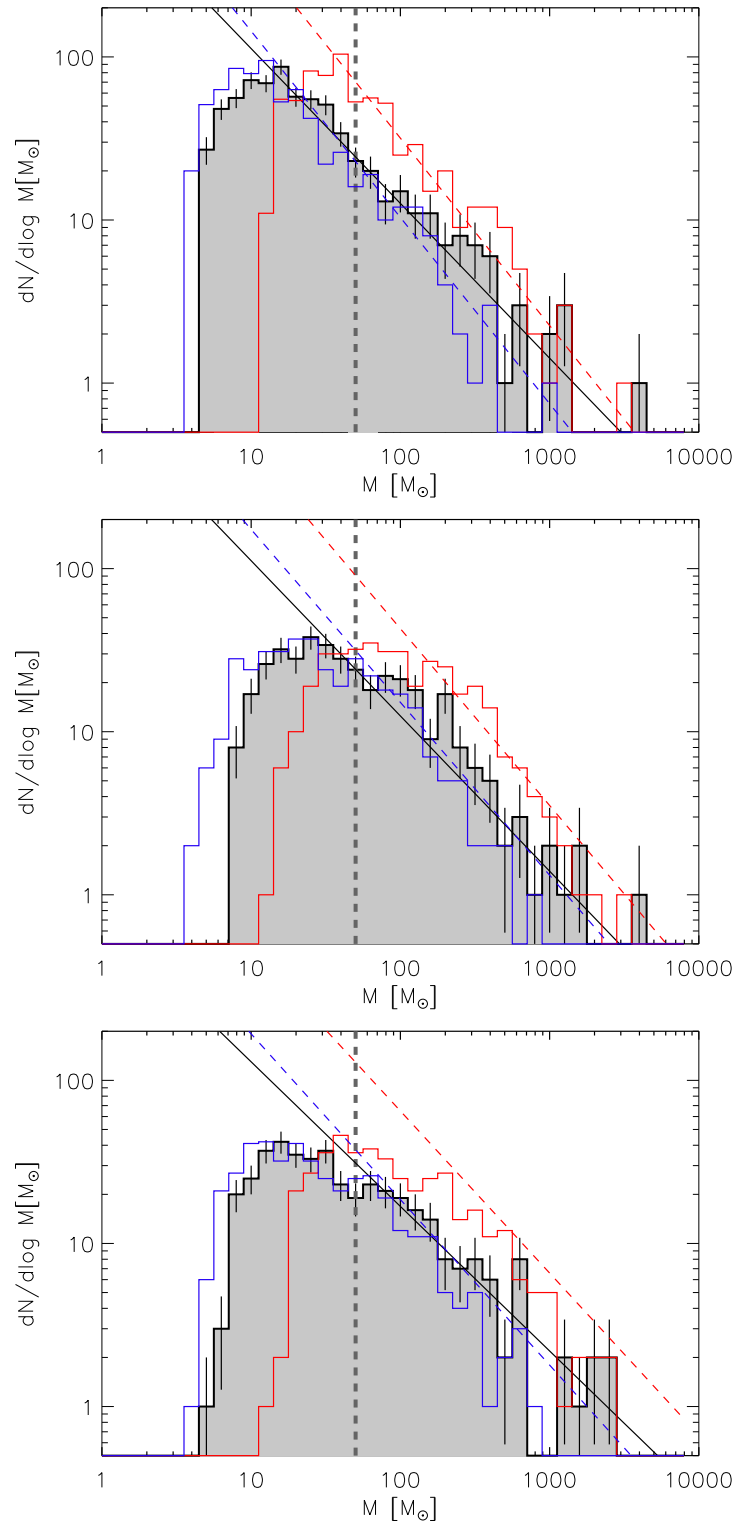
Figure 4.11: The ClMFs derived with the three different clump-finding algorithms CLUMPFIND (top), GAUSSCLUMPS (middle) and SExtractor (bottom). The black lines show the samples and their power-law slopes with the masses derived with the individual temperatures. The dashed gray line shows the used lower cut-off limit of $50\,M_\odot$. For the red/blue line we assumed a constant temperature of 10 K/20 K for all clumps.
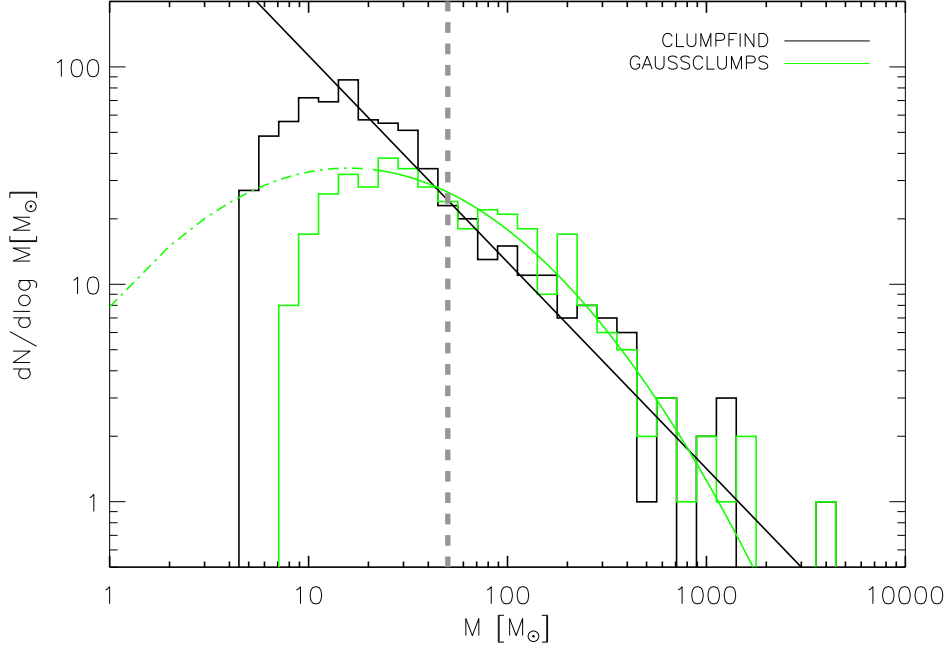
Figure 4.12: The mass distribution of the CLUMPFIND sample with its power-law slope ($\alpha = 1.95$) in black. In green the GAUSSCLUMPS sample is over plotted with its log-normal fit. The grey dashed line shows the lower-cutoff limit.

If we assume constant temperatures for all clumps the overall shape of the ClMFs keeps the same, but we derive a steeper power-law slope (e.g. for 10 K $\alpha_{CF} = 2.15 \pm 0.08$, $\alpha_{GC} = 2.08 \pm 0.06$ and $\alpha_{SE} = 1.99 \pm 0.06$ for a lower cut-off limit of $100 M_{\odot}$). The slopes for the two different constant temperatures stay the same within their errors, as a change of temperature corresponds to a constant shift in mass (Fig. 4.11). The results are summarized in Table 4.1.

Power-law versus Log-normal

In Sect. 2.2 we described observational and theoretical results, which find log-normal shapes for turbulent structures and power-law behavior for gravitationally dominated clouds (Kainulainen et al., 2011; Peretto & Fuller, 2010). When we calculate the power-law slope for different lower cut-off limits, starting from the peak mass to higher masses, we find that the power-law index for our CLUMPFIND sample is quite robust, within the errors, for both temperature profile cases. The slopes of the other two samples, however, become continuously steeper while shifting the cut-off point to higher masses.

Our analysis shows that the GAUSSCLUMPS and SExtractor samples can therefore also be well described by a log-normal function, while the CLUMPFIND sample shows a clear power-law behavior (Fig. 4.12). We thus find that the results of the above mentioned studies have to be used with caution while drawing conclusions on the physical state of a single molecular cloud, because the shape of the ClMF is highly dependent on the clump extracting method. Whether the clumps are gravitationally bound or dominated by turbulence has to be confirmed otherwise, e.g. by determining their viral parameter $\alpha_{\mathrm{vir}} = 5\sigma^2 R/M$ (Bertoldi & McKee, 1992).

Table 4.1: The resulting masses and power-law indices for the CLUMPFIND, GAUSS-CLUMPS and SExtractor samples, with individual clump temperatures and the two constant temperature cases.

	#	M_{tot}	M_{max}	M_{min}	M_{peak}	α
		$[10^3\ M_\odot]$	$[M_\odot]$	$[M_\odot]$	$[M_\odot]$	
individual clump temperatures; lower cut-off limit: $50 M_\odot$						
CF	687	42.2	4 652.2	5.2	15.8	1.95 ± 0.07
GC	371	42.6	4 458.2	8.2	25.1	1.95 ± 0.06
SE	414	48.2	2 972.8	5.7	15.8	1.89 ± 0.06
T=10K; lower cut-off limit: $100 M_\odot$						
CF		69.1	3 366.2	14.7	39.8	2.15 ± 0.08
GC		69.9	3 225.9	14.6	63.1	2.08 ± 0.06
SE		78.8	2 676.9	15.4	39.8	1.99 ± 0.06
T=20K; lower cut-off limit: $32 M_\odot$						
CF		21.0	1 024.4	4.5	12.6	2.14 ± 0.08
GC		21.3	981.6	4.5	20.0	2.06 ± 0.06
SE		24.0	814.6	4.7	12.6	2.02 ± 0.06

4.4   The Clumpy Structures in the Deeper LABOCA Maps

To analyse the MC structures in our deeper LABOCA maps we used again the CLUMPFIND algorithm to extract clump samples. For both maps we found an rms noise level of 10 mJy/beam, which is only half the rms of the large map. Therefore we used a $3\,\sigma$ detection threshold of 30 mJy/beam and a stepsize for the contouring of 20 mJy/beam. This approach is the same as in the analysis of the large LABOCA map. Depending on the highest intensities measured in the maps we contoured the data up to 2 Jy/beam and 1.2 Jy/beam for the LABOCA north and LABOCA south region, respectively. The observations and the data reduction is described in Sect. 3.4.2.

With a total flux above the $3\,\sigma$ noise level of 194 Jy in the LABOCA north map (Fig. 4.13) we can measure slightly more flux as for the same region in the large LABOCA map (171 Jy) with its higher noise level. To avoid any boundary effects we extracted only the clumps in the inner part of the map (black circles in Fig. 4.13). The clumps found have total fluxes between 0.1 Jy and 14.4 Jy (Fig. 4.15), which correspond to masses between about $3\,M_{\odot}$ and $420\,M_{\odot}$ for a constant temperature of 20 K. For the deeper LABOCA north map we find a maximum peak intensity of 1.8 Jy/beam. The peak intensities of the large map slightly exceed the peak intensities of the deeper LABOCA maps as the maps differ in calibration and observation conditions. The calibration errors, however, stay below 10%.

This is also true for the LABOCA south map (Fig. 4.14), which has a maximum peak intensity of 1.0 Jy/beam. The total flux that can be measured in the map above a $3\,\sigma$ noise level is 107 Jy and is nearly the same as measured in the large LABOCA map for this region (101 Jy). The total fluxes of the clumps range from about 0.1 Jy to 8.3 Jy. This corresponds for a constant temperature of 20 K to masses between about $3\,M_{\odot}$ and $232\,M_{\odot}$. Again we excluded clumps at the edges of the map.

By reducing the noise with the new observations we find, as expected, several new filamentary structures, that are to faint to appear in the large LABOCA map. Two new filaments in the LABOCA south structures are marked with an **A**. Equally marked we see a new ring-like structure in the LABOCA north region. These clumps are less dense and applying the temperature-density relation from Eq. (4.2) to the new sample leads to slightly higher temperatures of up to 19 K. Isolated clumps that are detected in the new as well as in the large map have the same peak intensities within the calibration uncertainties and identical or higher total fluxes. Examples of such isolated clumps are
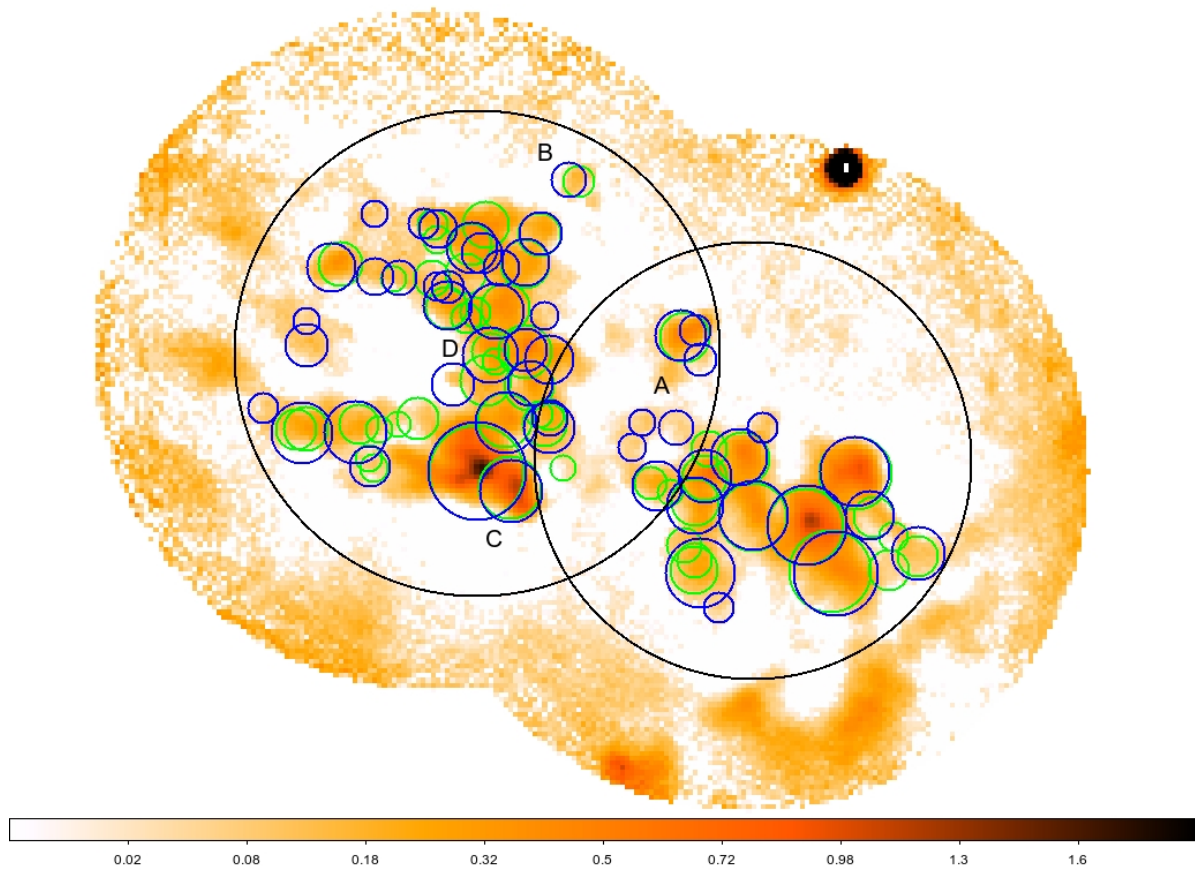
Figure 4.13: The deeper LABOCA map of the highly irradiated pillar in the west of η Car. The black circles indicate the region in which we searched for clumps with the CLUMPFIND algorithm. The blue circles show the clumps found on the deeper LABOCA map. In green the clumps found from the CLUMPFIND sample on the large map are shown. With A-D some interesting regions are marked (for details see Sect. 4.4). The scale bar on the bottom shows the intensities in Jy/beam in logarithmic scale.
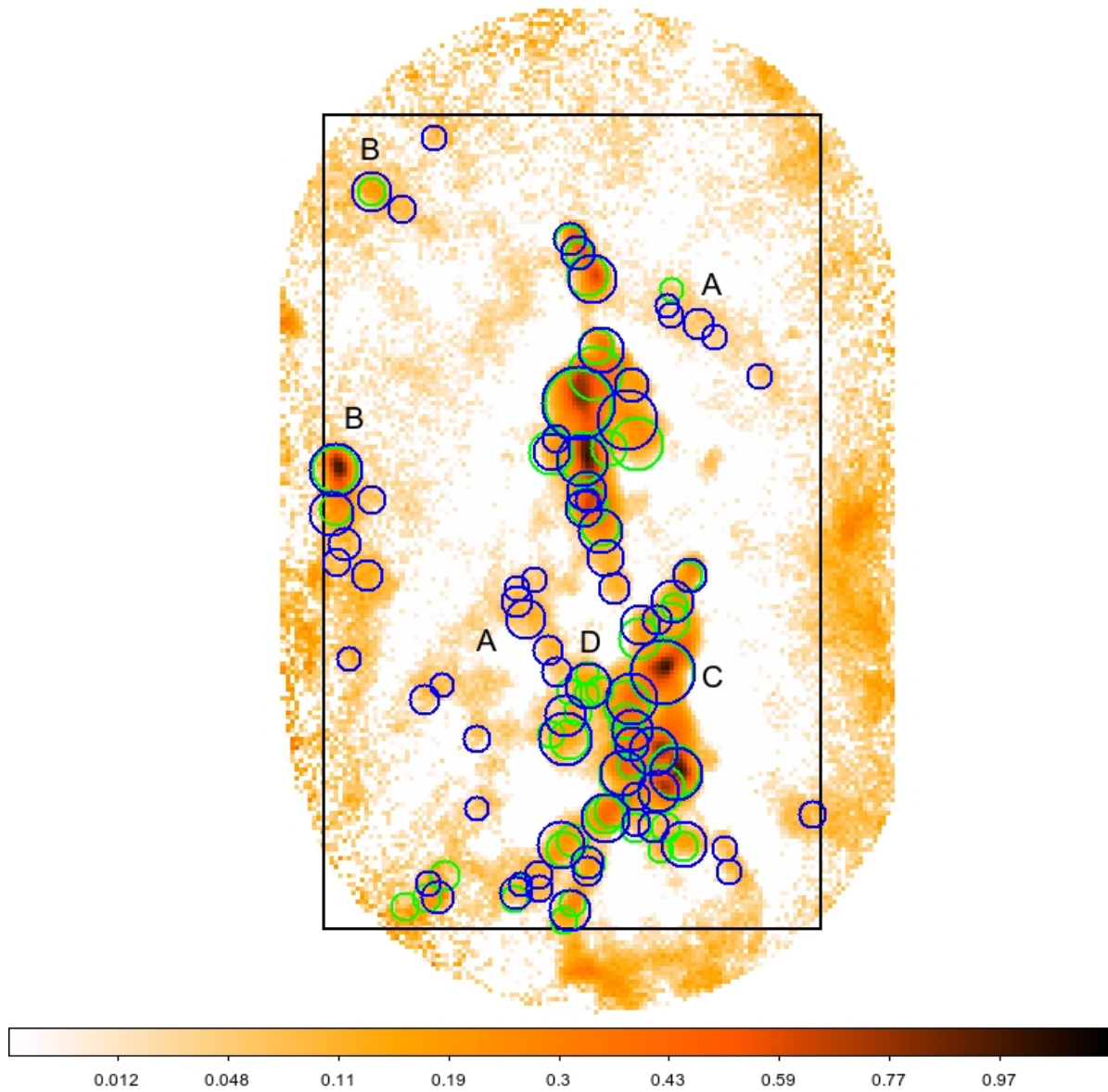
Figure 4.14: The deeper LABOCA map of the Giant Pillar. The black rectangle indicates the region in which we searched for clumps with the CLUMPFIND algorithm. The blue circles show the clumps found on the deeper LABOCA map. In green the clumps found from the CLUMPFIND sample on the large map are shown. With A-D some interesting regions are marked (for details see Sect. 4.4). The scale bar on the bottom shows the intensities in Jy/beam in logarithmic scale.

marked with a **B** in both maps.

Clumps detected in both maps within more crowded regions (marked with a **C**), however, can also have lower total fluxes in the deeper LABOCA maps, as the fluxes are differently distributed over different clumps in those regions. In the most crowded regions, where the contrast between the single clumps is very low CLUMPFIND potentially identifies spurious clumps if the noise fluctuations on the sources exceeds over the next contour defined by the stepsize. The algorithm then separates clumps into multiple sources (Pineda et al., 2009). Such false clumps are now merged in our samples on the deeper LABOCA maps due to the better rms. Two prominent examples are indicated with a **D** in the maps.

In general we find that the pillars in the LABOCA south region are all orientated in north-south direction, as the irradiation of the massive stars comes dominantly from the massive star clusters around η Car. For the LABOCA north region no such clear alignment can be seen. The clouds in this region are irradiated from the different sides, not only from the star clusters in the central region, but also from massive stars in the direct surrounding.

The clumps with the highest intensities and fluxes and therefore the more denser and more massive ones can be found in the LABOCA north region. Their intensities are twice as high as those which can be found in the LABOCA south region. This was already indicated in the results we find for the sample of the large LABOCA map, where the coldest clumps are also found in regions that are highly irradiated (see Fig. 4.9). The higher fraction of clumps with low total fluxes in the LABOCA south region, in comparison to the LABOCA north region, that can be seen in Fig. 4.15 may result from our selection of clumps. Due to to the small samples a power-law fitting is not meaningful.
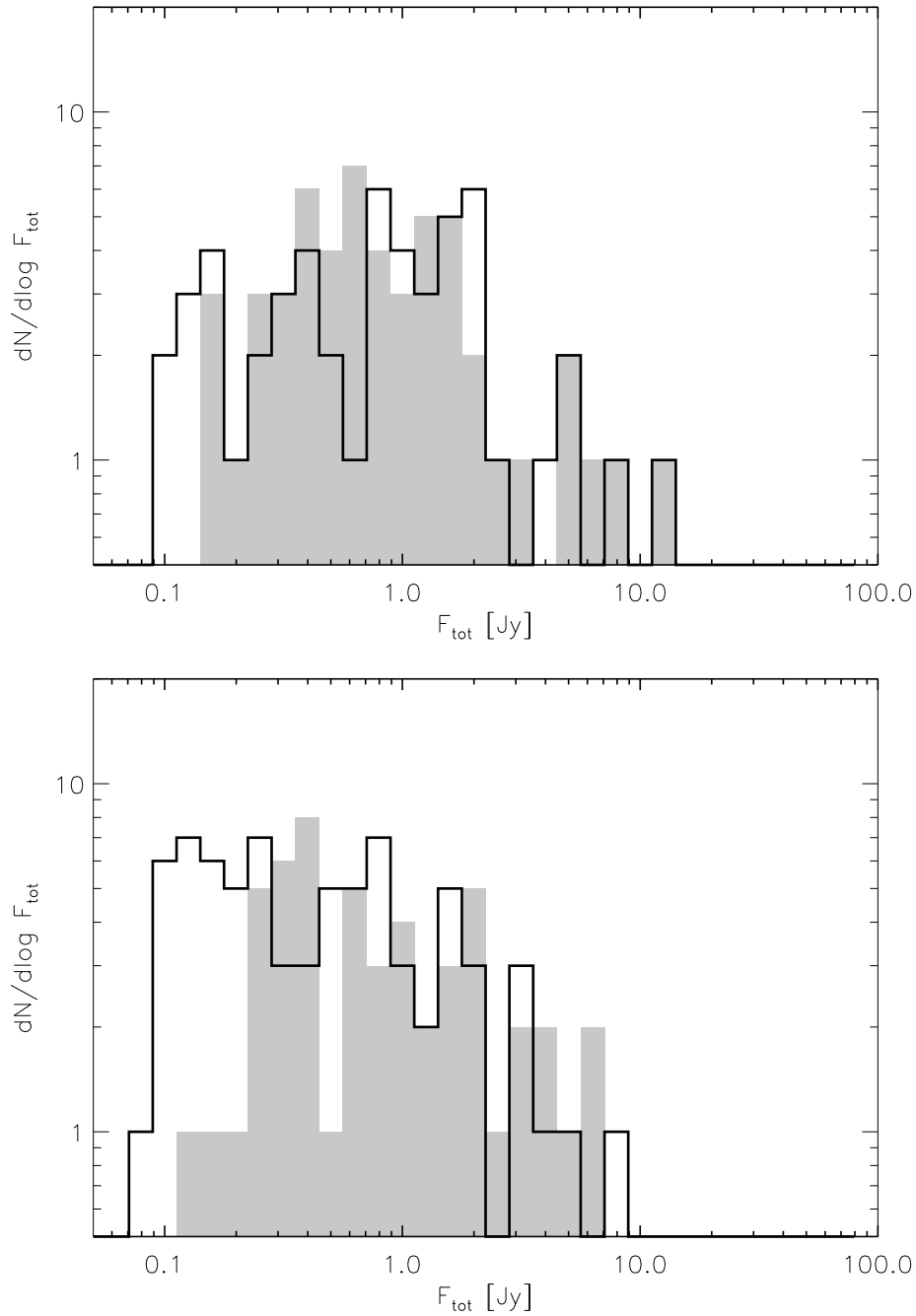
Figure 4.15: Distribution of the total fluxes for the clumps of the LABOCA north (*top*) and LABOCA south (*bottom*) regions (black lines). Shaded in grey are the clumps of the CLUMPFIND sample of the large map found in this regions.

Chapter 5

Summary[1]

The aim of this work was to analyse the clumpy structures in the Carina Nebula Complex and derive the ClMF of this region. One first question was how the ClMF is affected by the extraction method and the assumed temperatures. The different regions within the Carina Nebula, however, are exposed to highly different levels of irradiation and massive star feedback. We also looked at the effects that varying environments could have on the molecular structures.

We used three common clump-finding algorithms (CLUMPFIND, GAUSSCLUMPS, and SExtractor) to extract the clumps from our large-scale LABOCA map, so we are able to characterize the differences in the resulting ClMFS caused by the different extraction methods. To calculate the masses of the detected clumps we first used constant temperatures of 10 K and 20 K for all clumps. But such an assumption of a uniform temperature in the whole area disregards the variable amount of feedback the different regions are affected by. Hence, we used also an empirical calibration of the relation between column density and temperature, which we calculated from data of Peretto et al. (2010), to estimate the temperatures and masses of the individual clumps. With this relation we find clump temperatures between $8.5 - 18.5$ K for all three extracted samples.

From the calculated clump masses of the samples we derived the ClMFs of the Carina Nebula. For masses above $50\,M_\odot$ all samples can be described by a power-law with index α around 1.9. This is in good agreement with the results of other studies of clump mass distributions in molecular clouds (Elmegreen & Falgarone, 1996; Kramer et al., 1998; Schneider & Brooks, 2004). The slope of the power-law we determined is also very

---

[1]This chapter is partly adapted from Pekruhl et al. (2013)

similar to the slopes that have been found for mass functions of stellar clusters (e.g. Lada & Lada, 2003). For a assumed constant temperature for all clumps (10 K / 20 K) the power-law slope steepens.

At the low-mass end of the clump mass distribution the GAUSSCLUMPS and SExtractor samples show a lack of clumps, while the CLUMPFIND algorithm finds for this mass regime at least twice the number of clumps as the other algorithms. So even when the high mass end of the found ClMFs of the GAUSSCLUMPS and SExtractor samples show a power-law behaviour their overall shapes are better described by a log-normal function. The CLUMPFIND sample, however, clearly follows a power-law. Hence we find that the shape of the ClMF is highly dependent on the method used to extract the clumps.

Theoretical models predict that unbound turbulent clouds should have a log-normal ClMF, whereas clouds containing gravitationally bound clumps develop a power-law tail (Kainulainen et al., 2011; Peretto & Fuller, 2010). In this sense, the shape of the ClMF contains very important information of the evolutionary state of a molecular cloud. However, our results show that a reliable determination of the shape of the ClMF (log-normal or power-law) is often difficult as it can depend on the specific source extraction algorithm. Therefore, conclusions drawn from a ClMF derived from a single extraction algorithm should be taken with care to avoid an over-interpretation.

In our deeper LABOCA maps of two selected regions, which are experiencing very different levels of feedback, we were able to detect fainter clumps as in the large map. These are located on filamentary structures and have masses down to $3\,M_\odot$. This is the first step of a more detailed analysis. Our further sub-mm and molecular line data, will in future steps give even more insight to the kinematics and structures of the clumps and cores in this regions.

Bibliography

Alves, J., Lombardi, M., & Lada, C. J. (2007). The mass function of dense molecular cores and the origin of the IMF. A&A, 462, L17–L21.

André, P., Men'shchikov, A., Bontemps, S., Könyves, V., Motte, F., Schneider, N., Didelon, P., Minier, V., Saraceno, P., Ward-Thompson, D., di Francesco, J., White, G., Molinari, S., Testi, L., Abergel, A., Griffin, M., Henning, T., Royer, P., Merín, B., Vavrek, R., Attard, M., Arzoumanian, D., Wilson, C. D., Ade, P., Aussel, H., Baluteau, J.-P., Benedettini, M., Bernard, J.-P., Blommaert, J. A. D. L., Cambrésy, L., Cox, P., di Giorgio, A., Hargrave, P., Hennemann, M., Huang, M., Kirk, J., Krause, O., Launhardt, R., Leeks, S., Le Pennec, J., Li, J. Z., Martin, P. G., Maury, A., Olofsson, G., Omont, A., Peretto, N., Pezzuto, S., Prusti, T., Roussel, H., Russeil, D., Sauvage, M., Sibthorpe, B., Sicilia-Aguilar, A., Spinoglio, L., Waelkens, C., Woodcraft, A., & Zavagno, A. (2010). From filamentary clouds to prestellar cores to the stellar IMF: Initial highlights from the Herschel Gould Belt Survey. A&A, 518, L102+.

Baldry, I. K. & Glazebrook, K. (2003). Constraints on a Universal Stellar Initial Mass Function from Ultraviolet to Near-Infrared Galaxy Luminosity Densities. ApJ, 593, 258–271.

Ballesteros-Paredes, J., Klessen, R. S., Mac Low, M.-M., & Vazquez-Semadeni, E. (2007). Molecular Cloud Turbulence and Star Formation. In B. Reipurth, D. Jewitt, & K. Keil (Eds.), *Protostars and Planets V* (pp. 63–80).

Ballesteros-Paredes, J., Vázquez-Semadeni, E., Gazol, A., Hartmann, L. W., Heitsch, F., & Colín, P. (2011). Gravity or turbulence? - II. Evolving column density probability distribution functions in molecular clouds. MNRAS, 416, 1436–1442.

Bastian, N., Covey, K. R., & Meyer, M. R. (2010). A Universal Stellar Initial Mass Function? A Critical Look at Variations. ARA&A, 48, 339–389.

Bergin, E. A. & Tafalla, M. (2007). Cold Dark Clouds: The Initial Conditions for Star Formation. ARA&A, 45, 339–396.

Bertin, E. & Arnouts, S. (1996). SExtractor: Software for source extraction. A&AS, 117, 393–404.

Bertoldi, F. & McKee, C. F. (1992). Pressure-confined clumps in magnetized molecular clouds. ApJ, 395, 140–157.

Bik, A., Lamers, H. J. G. L. M., Bastian, N., Panagia, N., & Romaniello, M. (2003). Clusters in the inner spiral arms of M 51: The cluster IMF and the formation history. A&A, 397, 473–486.

Binney, J. & Tremaine, S. (2008). *Galactic Dynamics: Second Edition*. Princeton University Press.

Briceño, C., Preibisch, T., Sherry, W. H., Mamajek, E. A., Mathieu, R. D., Walter, F. M., & Zinnecker, H. (2007). The Low-Mass Populations in OB Associations. *Protostars and Planets V*, (pp. 345–360).

Brooks, K. J., Whiteoak, J. B., & Storey, J. W. V. (1998). An investigation of the molecular clouds of the Carina HII region/molecular cloud complex - First results. PASA, 15, 202–207.

Caselli, P., Benson, P. J., Myers, P. C., & Tafalla, M. (2002). Dense Cores in Dark Clouds. XIV. N_2H^+ (1-0) Maps of Dense Cloud Cores. ApJ, 572, 238–263.

Cernicharo, J. (1991). The Physical Conditions of Low Mass Star Forming Regions. In C. J. Lada & N. D. Kylafis (Eds.), *NATO ASIC Proc. 342: The Physics of Star Formation and Early Stellar Evolution* (pp. 287).

Chabrier, G. (2003). Galactic Stellar and Substellar Initial Mass Function. PASP, 115, 763–795.

Chabrier, G. (2005). The Initial Mass Function: from Salpeter 1955 to 2005. In E. Corbelli, F. Palla, & H. Zinnecker (Eds.), *The Initial Mass Function 50 Years Later*, volume 327 of *Astrophysics and Space Science Library* (pp.41).

Churchwell, E., Babler, B. L., Meade, M. R., Whitney, B. A., Benjamin, R., Indebetouw, R., Cyganowski, C., Robitaille, T. P., Povich, M., Watson, C., & Bracker, S. (2009). The Spitzer/GLIMPSE Surveys: A New View of the Milky Way. PASP, 121, 213–230.

Coppin, K. E. K., Greaves, J. S., Jenness, T., & Holland, W. S. (2000). Structure, star formation and magnetic fields in the OMC1 region. A&A, 356, 1031–1038.

Dale, J. E., Ercolano, B., & Bonnell, I. A. (2012). Ionization–induced star formation IV: Triggering in bound clusters. *ArXiv e-prints*.

Dame, T. M., Hartmann, D., & Thaddeus, P. (2001). The Milky Way in Molecular Clouds: A New Complete CO Survey. ApJ, 547, 792–813.

Damineli, A., Kaufer, A., Wolf, B., Stahl, O., Lopes, D. F., & de Araújo, F. X. (2000). η Carinae: Binarity Confirmed. ApJ, 528, L101–L104.

Dobbs, C. L., Burkert, A., & Pringle, J. E. (2011). Why are most molecular clouds not gravitationally bound? MNRAS, 413, 2935–2942.

Elmegreen, B. G. & Falgarone, E. (1996). A Fractal Origin for the Mass Spectrum of Interstellar Clouds. ApJ, 471, 816–+.

Frau, P., Girart, J. M., Beltrán, M. T., Morata, O., Masqué, J. M., Busquet, G., Alves, F. O., Sánchez-Monge, Á., Estalella, R., & Franco, G. A. P. (2010). Young Starless Cores Embedded in the Magnetically Dominated Pipe Nebula. ApJ, 723, 1665–1677.

Frew, D. J. (2004). The Historical Record of η Carinae I. The Visual Light Curve, 1595-2000. *Journal of Astronomical Data*, 10, 6.

Freyer, T., Hensler, G., & Yorke, H. W. (2003). Massive Stars and the Energy Balance of the Interstellar Medium. I. The Impact of an Isolated 60 M$_{solar}$ Star. ApJ, 594, 888–910.

Gritschneder, M., Naab, T., Walch, S., Burkert, A., & Heitsch, F. (2009). Driving Turbulence and Triggering Star Formation by Ionizing Radiation. ApJ, 694, L26–L30.

Güsten, R., Nyman, L. Å., Schilke, P., Menten, K., Cesarsky, C., & Booth, R. (2006). The Atacama Pathfinder EXperiment (APEX) - a new submillimeter facility for southern skies -. A&A, 454, L13–L16.

Hamaguchi, K., Corcoran, M. F., Ezoe, Y., Townsley, L., Broos, P., Gruendl, R., Vaidya, K., White, S. M., Strohmayer, T., Petre, R., & Chu, Y.-H. (2009). A Smoking Gun in the Carina Nebula. ApJ, 695, L4–L9.

Hamaguchi, K., Petre, R., Matsumoto, H., Tsujimoto, M., Holt, S. S., Ezoe, Y., Ozawa, H., Tsuboi, Y., Soong, Y., Kitamoto, S., Sekiguchi, A., & Kokubun, M. (2007). Suzaku Observation of Diffuse X-Ray Emission from the Carina Nebula. PASJ, 59, 151–161.

Heitsch, F., Burkert, A., Hartmann, L. W., Slyz, A. D., & Devriendt, J. E. G. (2005). Formation of Structure in Molecular Clouds: A Case Study. ApJ, 633, L113–L116.

Hennebelle, P. & Chabrier, G. (2008). Analytical Theory for the Initial Mass Function: CO Clumps and Prestellar Cores. ApJ, 684, 395–410.

Hildebrand, R. H. (1983). The Determination of Cloud Masses and Dust Characteristics from Submillimetre Thermal Emission. QJRAS, 24, 267–+.

Isobe, T., Feigelson, E. D., Akritas, M. G., & Babu, G. J. (1990). Linear regression in astronomy. ApJ, 364, 104–113.

Jeans, J. H. (1902). The Stability of a Spherical Nebula. *Royal Society of London Philosophical Transactions Series A*, 199, 1–53.

Johnstone, D. & Bally, J. (2006). Large-Area Mapping at 850 μm. V. Analysis of the Clump Distribution in the Orion A South Molecular Cloud. ApJ, 653, 383–397.

Johnstone, D., Wilson, C. D., Moriarty-Schieven, G., Joncas, G., Smith, G., Gregersen, E., & Fich, M. (2000). Large-Area Mapping at 850 Microns. II. Analysis of the Clump Distribution in the ρ Ophiuchi Molecular Cloud. ApJ, 545, 327–339.

Jurić, M., Ivezić, Ž., Brooks, A., Lupton, R. H., Schlegel, D., Finkbeiner, D., Padmanabhan, N., Bond, N., Sesar, B., Rockosi, C. M., Knapp, G. R., Gunn, J. E., Sumi, T., Schneider, D. P., Barentine, J. C., Brewington, H. J., Brinkmann, J., Fukugita, M., Harvanek, M., Kleinman, S. J., Krzesinski, J., Long, D., Neilsen, Jr., E. H., Nitta, A., Snedden, S. A., & York, D. G. (2008). The Milky Way Tomography with SDSS. I. Stellar Number Density Distribution. ApJ, 673, 864–914.

Kainulainen, J., Beuther, H., Banerjee, R., Federrath, C., & Henning, T. (2011). Probing the evolution of molecular cloud structure. II. From chaos to confinement. A&A, 530, A64.

Kainulainen, J., Beuther, H., Henning, T., & Plume, R. (2009). Probing the evolution of molecular cloud structure. From quiescence to birth. A&A, 508, L35–L38.

Kauffmann, J., Pillai, T., Shetty, R., Myers, P. C., & Goodman, A. A. (2010). The Mass-size Relation from Clouds to Cores. II. Solar Neighborhood Clouds. ApJ, 716, 433–445.

Kennicutt, Jr., R. C. (1983). The rate of star formation in normal disk galaxies. ApJ, 272, 54–67.

Kirk, H., Johnstone, D., & Di Francesco, J. (2006). The Large- and Small-Scale Structures of Dust in the Star-forming Perseus Molecular Cloud. ApJ, 646, 1009–1023.

Klessen, R. S. (2011). Star Formation in Molecular Clouds. In C. Charbonnel & T. Montmerle (Eds.), *EAS Publications Series*, volume 51 of *EAS Publications Series* (pp. 133–167).

Klessen, R. S., Spaans, M., & Jappsen, A.-K. (2005). Gravoturbulent star formation: Effects of the equation of state on stellar masses. In R. Cesaroni, M. Felli, E. Churchwell, & M. Walmsley (Ed.), *Massive Star Birth: A Crossroads of Astrophysics*, volume 227 of *IAU Symposium* (pp. 337–345).

Kontinen, S., Harju, J., Heikkilä, A., & Haikala, L. K. (2000). Molecular line study of evolution in protostellar cloud cores. A&A, 361, 704–718.

Könyves, V., André, P., Men'shchikov, A., Schneider, N., Arzoumanian, D., Bontemps, S., Attard, M., Motte, F., Didelon, P., Maury, A., Abergel, A., Ali, B., Baluteau, J.-P., Bernard, J.-P., Cambrésy, L., Cox, P., di Francesco, J., di Giorgio, A. M., Griffin, M. J., Hargrave, P., Huang, M., Kirk, J., Li, J. Z., Martin, P., Minier, V., Molinari, S., Olofsson, G., Pezzuto, S., Russeil, D., Roussel, H., Saraceno, P., Sauvage, M., Sibthorpe, B., Spinoglio, L., Testi, L., Ward-Thompson, D., White, G., Wilson, C. D., Woodcraft, A., & Zavagno, A. (2010). The Aquila prestellar core population revealed by Herschel. A&A, 518, L106.

Kramer, C., Stutzki, J., Rohrig, R., & Corneliussen, U. (1998). Clump mass spectra of molecular clouds. A&A, 329, 249–264.

Kroupa, P. (2001). On the variation of the initial mass function. MNRAS, 322, 231–246.

Kroupa, P., Tout, C. A., & Gilmore, G. (1993). The distribution of low-mass stars in the Galactic disc. MNRAS, 262, 545–587.

Lada, C. J., Alves, J. F., & Lombardi, M. (2007). Near-Infrared Extinction and Molecular Cloud Structure. *Protostars and Planets V*, (pp. 3–15).

Lada, C. J. & Lada, E. A. (2003). Embedded Clusters in Molecular Clouds. ARA&A, 41, 57–115.

Lada, C. J., Lada, E. A., Clemens, D. P., & Bally, J. (1994). Dust extinction and molecular gas in the dark cloud IC 5146. ApJ, 429, 694–709.

Landsman, W. B. (1993). The IDL Astronomy User's Library. In R. J. Hanisch, R. J. V. Brissenden, & J. Barnes (Eds.), *Astronomical Data Analysis Software and Systems II*, volume 52 of *Astronomical Society of the Pacific Conference Series* (pp. 246).

Lombardi, M. & Alves, J. (2001). Mapping the interstellar dust with near-infrared observations: An optimized multi-band technique. A&A, 377, 1023–1034.

Lombardi, M., Alves, J., & Lada, C. J. (2006). 2MASS wide field extinction maps. I. The Pipe nebula. A&A, 454, 781–796.

Maschberger, T. & Kroupa, P. (2009). Estimators for the exponent and upper limit, and goodness-of-fit tests for (truncated) power-law distributions. MNRAS, 395, 931–942.

McCrady, N. & Graham, J. R. (2007). Super Star Cluster Velocity Dispersions and Virial Masses in the M82 Nuclear Starburst. ApJ, 663, 844–856.

McKee, C. F. & Ostriker, E. C. (2007). Theory of Star Formation. ARA&A, 45, 565–687.

Megeath, S. T., Cox, P., Bronfman, L., & Roelfsema, P. R. (1996). Evidence for ongoing star formation in the Carina nebula. A&A, 305, 296–+.

Miller, G. E. & Scalo, J. M. (1979). The initial mass function and stellar birthrate in the solar neighborhood. ApJS, 41, 513–547.

Molinari, S., Swinyard, B., Bally, J., Barlow, M., Bernard, J.-P., Martin, P., Moore, T., Noriega-Crespo, A., Plume, R., Testi, L., Zavagno, A., Abergel, A., Ali, B., André, P., Baluteau, J.-P., Benedettini, M., Berné, O., Billot, N. P., Blommaert, J., Bontemps, S., Boulanger, F., Brand, J., Brunt, C., Burton, M., Campeggio, L., Carey, S., Caselli, P., Cesaroni, R., Cernicharo, J., Chakrabarti, S., Chrysostomou, A., Codella, C., Cohen, M., Compiegne, M., Davis, C. J., de Bernardis, P., de Gasperis, G., Di Francesco, J., di Giorgio, A. M., Elia, D., Faustini, F., Fischera, J. F., Fukui, Y., Fuller, G. A., Ganga, K., Garcia-Lario, P., Giard, M., Giardino, G., Glenn, J. ., Goldsmith, P., Griffin, M., Hoare, M., Huang, M., Jiang, B., Joblin, C., Joncas, G., Juvela, M., Kirk, J., Lagache, G., Li, J. Z., Lim, T. L., Lord, S. D., Lucas, P. W., Maiolo, B., Marengo, M., Marshall, D., Masi, S., Massi, F., Matsuura, M., Meny, C., Minier, V., Miville-Deschênes, M.-A., Montier, L., Motte, F., Müller, T. G., Natoli, P., Neves, J., Olmi, L., Paladini, R., Paradis, D., Pestalozzi, M., Pezzuto, S., Piacentini, F., Pomarès, M., Popescu, C. C., Reach, W. T., Richer, J., Ristorcelli, I., Roy, A., Royer, P., Russeil, D., Saraceno, P., Sauvage, M., Schilke, P., Schneider-Bontemps, N., Schuller, F., Schultz, B., Shepherd, D. S., Sibthorpe, B., Smith, H. A., Smith, M. D., Spinoglio, L., Stamatellos, D., Strafella, F., Stringfellow, G., Sturm, E., Taylor, R., Thompson, M. A., Tuffs, R. J., Umana, G., Valenziano, L., Vavrek, R., Viti, S., Waelkens, C., Ward-Thompson, D., White, G., Wyrowski, F., Yorke, H. W., & Zhang, Q. (2010). Hi-GAL: The Herschel Infrared Galactic Plane Survey. PASP, 122, 314–325.

Mookerjea, B., Kramer, C., Nielbock, M., & Nyman, L.-Å. (2004). The Giant Molecular Cloud associated with RCW 106. A 1.2 mm continuum mapping study. A&A, 426, 119–129.

Morgan, L. K., Thompson, M. A., Urquhart, J. S., & White, G. J. (2008). A SCUBA survey of bright-rimmed clouds. A&A, 477, 557–571.

Muñoz, D. J., Mardones, D., Garay, G., Rebolledo, D., Brooks, K., & Bontemps, S. (2007). Massive Clumps in the NGC 6334 Star-forming Region. ApJ, 668, 906–917.

Ntormousi, E., Burkert, A., Fierlinger, K., & Heitsch, F. (2011). Formation of Cold Filamentary Structure from Wind-blown Superbubbles. ApJ, 731, 13.

Nutter, D. & Ward-Thompson, D. (2007). A SCUBA survey of Orion - the low-mass end of the core mass function. MNRAS, 374, 1413–1420.

Ohlendorf, H., Preibisch, T., Gaczkowski, B., Ratzka, T., Grellmann, R., & McLeod, A. F. (2012). Jet-driving protostars identified from infrared observations of the Carina Nebula complex. A&A, 540, A81.

Pagels, H. R. (1985). *Perfect symmetry : The search for the beginning of time.*

Pekruhl, S., Preibisch, T., Schuller, F., & Menten, K. (2013). The clump mass function of the dense clouds in the Carina nebula complex. A&A, 550, A29.

Peretto, N. & Fuller, G. A. (2010). A Statistical Study of the Mass and Density Structure of Infrared Dark Clouds. ApJ, 723, 555–562.

Peretto, N., Fuller, G. A., Plume, R., Anderson, L. D., Bally, J., Battersby, C., Beltran, M. T., Bernard, J.-P., Calzoletti, L., Digiorgio, A. M., Faustini, F., Kirk, J. M., Lenfestey, C., Marshall, D., Martin, P., Molinari, S., Montier, L., Motte, F., Ristorcelli, I., Rodón, J. A., Smith, H. A., Traficante, A., Veneziani, M., Ward-Thompson, D., & Wilcock, L. (2010). Mapping the column density and dust temperature structure of IRDCs with Herschel. A&A, 518, L98+.

Pineda, J. E., Rosolowsky, E. W., & Goodman, A. A. (2009). The Perils of Clumpfind: The Mass Spectrum of Substructures in Molecular Clouds. ApJ, 699, L134–L138.

Preibisch, T., Hodgkin, S., Irwin, M., Lewis, J. R., King, R. R., McCaughrean, M. J., Zinnecker, H., Townsley, L., & Broos, P. (2011a). Near-infrared Properties of the X-ray-emitting Young Stellar Objects in the Carina Nebula. ApJS, 194, 10.

Preibisch, T., Ratzka, T., Gehring, T., Ohlendorf, H., Zinnecker, H., King, R. R., McCaughrean, M. J., & Lewis, J. R. (2011b). Detection of a large massive circumstellar disk around a high-mass young stellar object in the Carina Nebula. A&A, 530, A40.

Preibisch, T., Ratzka, T., Kuderna, B., Ohlendorf, H., King, R. R., Hodgkin, S., Irwin, M., Lewis, J. R., McCaughrean, M. J., & Zinnecker, H. (2011c). Deep wide-field near-infrared survey of the Carina Nebula. A&A, 530, A34.

Preibisch, T., Schuller, F., Ohlendorf, H., Pekruhl, S., Menten, K. M., & Zinnecker, H. (2011d). A deep wide-field sub-mm survey of the Carina Nebula complex. A&A, 525, A92+.

Rathborne, J. M., Brooks, K. J., Burton, M. G., Cohen, M., & Bontemps, S. (2004). The giant pillars of the Carina Nebula. A&A, 418, 563–576.

Rathborne, J. M., Lada, C. J., Muench, A. A., Alves, J. F., & Lombardi, M. (2008). The Nature of the Dense Core Population in the Pipe Nebula: A Survey of NH_3, CCS, and HC_5N Molecular Line Emission. ApJS, 174, 396–425.

Reichertz, L. A., Weferling, B., Esch, W., & Kreysa, E. (2001). The fastscanning observing technique for millimeter and submillimeter astronomy. A&A, 379, 735–739.

Reid, M. A., Wadsley, J., Petitclerc, N., & Sills, A. (2010). Measuring the Clump Mass Function in the Age of SCUBA2, Herschel, and ALMA. ApJ, 719, 561–575.

Reid, M. A. & Wilson, C. D. (2006). High-Mass Star Formation. III. The Functional Form of the Submillimeter Clump Mass Function. ApJ, 650, 970–984.

Roman-Duval, J., Jackson, J. M., Heyer, M., Rathborne, J., & Simon, R. (2010). Physical Properties and Galactic Distribution of Molecular Clouds Identified in the Galactic Ring Survey. ApJ, 723, 492–507.

Salpeter, E. E. (1955). The Luminosity Function and Stellar Evolution. ApJ, 121, 161–+.

Scalo, J. M. (1986). The stellar initial mass function. Fund. Cosmic Phys., 11, 1–278.

Schneider, N. & Brooks, K. (2004). The Bias of Molecular Clump Identification Programs: the Example of the Carina Molecular Clouds. PASA, 21, 290–301.

Schuller, F., Menten, K. M., Contreras, Y., Wyrowski, F., Schilke, P., Bronfman, L., Henning, T., Walmsley, C. M., Beuther, H., Bontemps, S., Cesaroni, R., Deharveng, L., Garay, G., Herpin, F., Lefloch, B., Linz, H., Mardones, D., Minier, V., Molinari, S., Motte, F., Nyman, L.-Å., Reveret, V., Risacher, C., Russeil, D., Schneider, N., Testi, L., Troost, T., Vasyunina, T., Wienen, M., Zavagno, A., Kovacs, A., Kreysa, E., Siringo, G., & Weiß, A. (2009). ATLASGAL - The APEX telescope large area survey of the galaxy at 870 μm. A&A, 504, 415–427.

Siringo, G., Kreysa, E., De Breuck, C., Kovacs, A., Lundgren, A., Schuller, F., Stanke, T., Weiss, A., Guesten, R., Jethava, N., May, T., Menten, K. M., Meyer, H.-G., Starkloff, M., & Zakosarenko, V. (2010). A New Facility Receiver on APEX: The Submillimetre APEX Bolometer Camera, SABOCA. *The Messenger*, 139, 20–23.

Siringo, G., Kreysa, E., Kovács, A., Schuller, F., Weiß, A., Esch, W., Gemünd, H.-P., Jethava, N., Lundershausen, G., Colin, A., Güsten, R., Menten, K. M., Beelen, A., Bertoldi, F., Beeman, J. W., & Haller, E. E. (2009). The Large APEX BOlometer CAmera LABOCA. A&A, 497, 945–962.

Smith, M. D. (2004). *The origin of stars.*

Smith, N. (2006). A census of the Carina Nebula - I. Cumulative energy input from massive stars. MNRAS, 367, 763–772.

Smith, N., Bally, J., & Walborn, N. R. (2010a). HST/ACS Hα imaging of the Carina Nebula: outflow activity traced by irradiated Herbig-Haro Jets. MNRAS, 405, 1153–1186.

Smith, N. & Brooks, K. J. (2008). The Carina Nebula: A Laboratory for Feedback and Triggered Star Formation. *Handbook of Star Forming Regions, Volume II*, (pp. 138–+).

Smith, N., Povich, M. S., Whitney, B. A., Churchwell, E., Babler, B. L., Meade, M. R., Bally, J., Gehrz, R. D., Robitaille, T. P., & Stassun, K. G. (2010b). Spitzer Space Telescope observations of the Carina nebula: the steady march of feedback-driven star formation. MNRAS, 406, 952–974.

Stahler, S. W. & Palla, F. (2005). *The Formation of Stars*.

Stamatellos, D., Whitworth, A. P., & Ward-Thompson, D. (2007). The dust temperatures of the prestellar cores in the ρ Oph main cloud and in other star-forming regions: consequences for the core mass function. MNRAS, 379, 1390–1400.

Stark, A. A. & Lee, Y. (2005). The Scale Height of Giant Molecular Clouds Is Less than That of Smaller Clouds. ApJ, 619, L159–L162.

Stutzki, J. & Guesten, R. (1990). High spatial resolution isotopic CO and CS observations of M17 SW - The clumpy structure of the molecular cloud core. ApJ, 356, 513–533.

Tapia, M., Persi, P., Bohigas, J., Roth, M., & Gómez, M. (2006). Imaging study of NGC 3372, the Carina nebula - II. Evidence of activity in the complex Trumpler 14/Car I photodissociation region. MNRAS, 367, 513–526.

Tapia, M., Roth, M., Vázquez, R. A., & Feinstein, A. (2003). Imaging study of NGC 3372, the Carina nebula - I. UBVRIJHK photometry of Tr 14, Tr 15, Tr 16 and Car I. MNRAS, 339, 44–62.

Townsley, L. K., Broos, P. S., Corcoran, M. F., Feigelson, E. D., Gagné, M., Montmerle, T., Oey, M. S., Smith, N., Garmire, G. P., Getman, K. V., Povich, M. S., Remage Evans, N., Nazé, Y., Parkin, E. R., Preibisch, T., Wang, J., Wolk, S. J., Chu, Y.-H., Cohen, D. H., Gruendl, R. A., Hamaguchi, K., King, R. R., Mac Low, M.-M., McCaughrean, M. J., Moffat, A. F. J., Oskinova, L. M., Pittard, J. M., Stassun, K. G., ud-Doula, A., Walborn, N. R., Waldron, W. L., Churchwell, E., Nichols, J. S., Owocki, S. P., & Schulz, N. S. (2011). An Introduction to the Chandra Carina Complex Project. ApJS, 194, 1.

Usuda, T. & Goto, M. (2005). Molecular Hydrogen Absorption Line Detected in Dense Molecular Clouds. In H. U. Käufl, R. Siebenmorgen, & A. Moorwood (Eds.), *High Resolution Infrared Spectroscopy in Astronomy* (pp. 248–251).

Vázquez-Semadeni, E. (2010). Molecular Cloud Evolution. In R. Kothes, T. L. Landecker, & A. G. Willis (Eds.), *Astronomical Society of the Pacific Conference Series*, volume 438 of *Astronomical Society of the Pacific Conference Series* (pp. 83).

Wallerstein, G., Iben, Jr., I., Parker, P., Boesgaard, A. M., Hale, G. M., Champagne, A. E., Barnes, C. A., Käppeler, F., Smith, V. V., Hoffman, R. D., Timmes, F. X., Sneden, C., Boyd, R. N., Meyer, B. S., & Lambert, D. L. (1997). Synthesis of the elements in stars: forty years of progress. *Reviews of Modern Physics*, 69, 995–1084.

Wang, J., Feigelson, E. D., Townsley, L. K., Broos, P. S., Getman, K. V., Wolk, S. J., Preibisch, T., Stassun, K. G., Moffat, A. F. J., Garmire, G., King, R. R., McCaughrean, M. J., & Zinnecker, H. (2011). A Chandra ACIS Study of the Young Star Cluster Trumpler 15 in Carina and Correlation with Near-infrared Sources. ApJS, 194, 11.

Weinreb, S., Barrett, A. H., Meeks, M. L., & Henry, J. C. (1963). Radio Observations of OH in the Interstellar Medium. Nature, 200, 829–831.

Whitworth, A. P., Bhattal, A. S., Chapman, S. J., Disney, M. J., & Turner, J. A. (1994). The Preferential Formation of High-Mass Stars in Shocked Interstellar Gas Layers. MNRAS, 268, 291.

Williams, J. P., Blitz, L., & McKee, C. F. (2000). The Structure and Evolution of Molecular Clouds: from Clumps to Cores to the IMF. *Protostars and Planets IV*, (pp. 97–+).

Williams, J. P., de Geus, E. J., & Blitz, L. (1994). Determining structure in molecular clouds. ApJ, 428, 693–712.

Wolk, S. J., Broos, P. S., Getman, K. V., Feigelson, E. D., Preibisch, T., Townsley, L. K., Wang, J., Stassun, K. G., King, R. R., McCaughrean, M. J., Moffat, A. F. J., & Zinnecker, H. (2011). The Chandra Carina Complex Project View of Trumpler 16. ApJS, 194, 12.

Wong, T., Ladd, E. F., Brisbin, D., Burton, M. G., Bains, I., Cunningham, M. R., Lo, N., Jones, P. A., Thomas, K. L., Longmore, S. N., Vigan, A., Mookerjea, B., Kramer, C., Fukui, Y., & Kawamura, A. (2008). Molecular line mapping of the giant molecular cloud associated with RCW 106 - II. Column density and dynamical state of the clumps. MNRAS, 386, 1069–1084.

Yonekura, Y., Asayama, S., Kimura, K., Ogawa, H., Kanai, Y., Yamaguchi, N., Barnes, P. J., & Fukui, Y. (2005). High-Mass Cloud Cores in the η Carinae Giant Molecular Cloud. ApJ, 634, 476–494.

Zhang, Q. & Fall, S. M. (1999). The Mass Function of Young Star Clusters in the "Antennae" Galaxies. ApJ, 527, L81–L84.

Appendix A

Appendix

Table A.1: Properties of the CLUMPFIND sample

n	R.A. (deg) (J2000)	Dec. (deg) (J2000)	R (")	F_{max} [Jy/beam]	F_{tot} [Jy/beam]	T [K]	N_{H_2} [cm^{-2}]	M [$M_\odot$]	M (10 K) [$M_\odot$]	M (20 K) [$M_\odot$]
2	160.83520	-59.575366	59.0	4.0	373.3	8.6	$4.60 \cdot 10^{23}$	4652.2	3366.2	1024.4
3	160.84862	-59.568664	29.1	3.8	108.6	8.8	$4.14 \cdot 10^{23}$	1285.6	979.3	298.0
4	160.87523	-59.572127	32.9	3.7	128.2	8.8	$4.06 \cdot 10^{23}$	1517.7	1156.0	351.8
5	161.48361	-59.945573	40.7	3.1	150.7	9.5	$2.84 \cdot 10^{23}$	1511.6	1358.8	413.5
6	160.70127	-59.424650	45.7	2.3	82.1	10.5	$1.70 \cdot 10^{23}$	670.7	740.0	225.2
7	160.89510	-59.582314	32.1	2.2	80.5	10.5	$1.67 \cdot 10^{23}$	658.0	726.0	220.9
8	161.96522	-60.440108	31.9	2.0	71.8	10.8	$1.43 \cdot 10^{23}$	554.8	647.1	196.9
9	161.51964	-59.790290	58.6	1.9	168.3	11.0	$1.29 \cdot 10^{23}$	1255.5	1517.4	461.8
10	160.88504	-59.587344	22.5	1.7	57.0	11.3	$1.11 \cdot 10^{23}$	403.8	513.9	156.4
11	160.84166	-59.590574	43.2	1.7	147.3	11.3	$1.10 \cdot 10^{23}$	1043.6	1328.2	404.2
12	160.88162	-59.594083	28.2	1.7	58.6	11.4	$1.07 \cdot 10^{23}$	408.5	528.6	160.9
13	161.12189	-59.547387	29.7	1.7	48.0	11.4	$1.07 \cdot 10^{23}$	334.5	432.9	131.7
14	160.69769	-59.439819	40.3	1.7	68.0	11.4	$1.06 \cdot 10^{23}$	474.1	613.5	186.7
15	161.13518	-59.554153	35.6	1.6	48.8	11.4	$1.06 \cdot 10^{23}$	340.2	440.3	134.0
16	160.86155	-59.599079	17.1	1.4	25.8	11.9	$8.20 \cdot 10^{22}$	166.0	232.8	70.9
17	160.86493	-59.595716	19.7	1.4	37.3	11.9	$8.20 \cdot 10^{22}$	240.0	336.6	102.4
18	160.86151	-59.602453	31.0	1.4	53.5	12.0	$7.84 \cdot 10^{22}$	338.8	482.5	146.8
19	161.07581	-60.465189	16.8	1.3	14.1	12.0	$7.73 \cdot 10^{22}$	89.5	127.5	38.8
20	160.82630	-59.497718	30.2	1.3	36.5	12.0	$7.67 \cdot 10^{22}$	231.2	329.3	100.2
21	161.29161	-59.809033	47.6	1.2	104.4	12.3	$6.72 \cdot 10^{22}$	631.6	941.1	286.4
22	160.89203	-59.560370	35.8	1.1	49.4	12.4	$6.29 \cdot 10^{22}$	294.6	445.6	135.6
23	161.49620	-59.795389	38.9	1.1	64.1	12.4	$6.24 \cdot 10^{22}$	382.2	577.9	175.9
24	161.42768	-60.293215	36.6	1.1	45.3	12.4	$6.24 \cdot 10^{22}$	270.2	408.7	124.4
25	161.19055	-59.933845	27.4	1.1	20.1	12.5	$6.04 \cdot 10^{22}$	118.0	181.1	55.1

n	R.A. (deg)	Dec. (deg)	R (")	F_{max}	F_{tot}	T	N_{H_2}	M	M (10 K)	M (20 K)
26	160.79430	-59.414920	38.4	1.1	41.4	12.6	$5.74 \cdot 10^{22}$	239.7	373.1	113.5
27	161.49845	-60.173333	34.8	1.1	58.4	12.6	$5.74 \cdot 10^{22}$	338.1	526.2	160.1
28	160.96838	-59.923351	31.4	1.1	26.2	12.6	$5.74 \cdot 10^{22}$	151.8	236.3	71.9
29	161.49043	-59.960749	31.6	1.1	55.4	12.6	$5.74 \cdot 10^{22}$	321.2	499.9	152.1
30	161.43774	-60.256085	44.0	1.1	70.0	12.6	$5.64 \cdot 10^{22}$	405.4	631.0	192.0
31	160.04713	-59.531380	15.7	1.0	10.2	12.7	$5.35 \cdot 10^{22}$	58.0	91.5	27.9
32	161.25808	-59.790466	44.7	1.0	68.2	12.8	$5.07 \cdot 10^{22}$	384.1	614.9	187.1
33	161.44467	-60.286449	32.5	1.0	49.5	12.9	$4.95 \cdot 10^{22}$	274.9	446.2	135.8
34	162.05711	-59.978970	31.2	0.9	23.5	12.9	$4.84 \cdot 10^{22}$	130.4	211.7	64.4
35	161.23862	-59.431073	32.1	0.9	32.0	12.9	$4.79 \cdot 10^{22}$	177.8	288.6	87.8
36	161.68848	-60.177976	30.2	0.9	25.3	13.0	$4.63 \cdot 10^{22}$	138.8	228.4	69.5
37	160.33316	-59.537184	45.1	0.9	53.8	13.0	$4.63 \cdot 10^{22}$	295.0	485.5	147.7
38	160.78242	-59.541422	45.2	0.9	78.5	13.0	$4.58 \cdot 10^{22}$	430.4	708.2	215.5
39	161.90998	-60.047222	42.5	0.9	53.3	13.1	$4.47 \cdot 10^{22}$	288.2	480.7	146.3
40	161.00906	-59.506690	32.3	0.9	34.5	13.1	$4.47 \cdot 10^{22}$	186.5	311.0	94.6
41	161.50172	-60.153081	46.1	0.9	82.9	13.1	$4.47 \cdot 10^{22}$	448.4	747.9	227.6
42	161.43792	-60.299954	31.4	0.9	40.4	13.1	$4.37 \cdot 10^{22}$	218.3	364.1	110.8
43	161.42614	-59.893336	36.9	0.9	35.7	13.1	$4.32 \cdot 10^{22}$	192.8	321.6	97.9
44	161.34890	-59.976062	37.1	0.8	37.3	13.4	$3.81 \cdot 10^{22}$	193.9	336.5	102.4
45	161.15670	-59.972619	25.4	0.8	18.4	13.4	$3.72 \cdot 10^{22}$	95.8	166.3	50.6
46	161.74616	-60.427515	16.1	0.8	8.9	13.4	$3.72 \cdot 10^{22}$	46.1	80.1	24.4
47	161.47025	-59.969213	43.4	0.8	60.2	13.5	$3.58 \cdot 10^{22}$	308.7	542.7	165.1
48	160.85130	-59.617605	40.1	0.8	52.3	13.5	$3.58 \cdot 10^{22}$	268.4	471.8	143.6
49	161.49514	-60.186836	27.0	0.7	23.3	13.6	$3.35 \cdot 10^{22}$	118.2	210.5	64.0
50	161.49517	-60.191898	26.8	0.7	23.3	13.7	$3.26 \cdot 10^{22}$	116.6	210.3	64.0
51	161.02575	-59.498289	29.7	0.7	24.4	13.7	$3.26 \cdot 10^{22}$	121.9	219.8	66.9
52	161.14655	-59.981044	43.6	0.7	43.4	13.7	$3.26 \cdot 10^{22}$	216.8	391.0	119.0
53	160.86241	-59.533277	36.4	0.7	34.7	13.7	$3.26 \cdot 10^{22}$	173.6	313.1	95.3
54	160.99001	-59.408784	29.5	0.7	26.1	13.8	$3.08 \cdot 10^{22}$	128.7	235.0	71.5
55	161.25509	-59.522191	39.7	0.7	37.6	13.9	$2.91 \cdot 10^{22}$	183.5	339.2	103.2
56	161.24493	-59.630172	33.2	0.7	22.4	13.9	$2.91 \cdot 10^{22}$	109.4	202.2	61.5
57	161.10197	-59.538922	29.7	0.6	26.9	14.0	$2.79 \cdot 10^{22}$	129.6	242.5	73.8
58	161.94494	-60.452018	25.9	0.6	23.0	14.0	$2.79 \cdot 10^{22}$	110.8	207.3	63.1
59	161.46167	-60.281367	25.2	0.6	23.3	14.0	$2.74 \cdot 10^{22}$	112.1	209.8	63.9
60	160.98848	-59.574133	36.3	0.6	32.9	14.0	$2.70 \cdot 10^{22}$	158.3	296.2	90.1
61	161.36204	-59.792146	27.8	0.6	20.0	14.0	$2.70 \cdot 10^{22}$	96.3	180.3	54.9
62	161.46854	-60.294857	29.9	0.6	25.6	14.1	$2.62 \cdot 10^{22}$	121.7	230.5	70.1
63	161.08867	-59.537213	29.7	0.6	24.1	14.1	$2.58 \cdot 10^{22}$	114.9	217.7	66.2
64	161.46500	-60.267865	31.9	0.6	31.6	14.2	$2.50 \cdot 10^{22}$	148.6	284.9	86.7
65	161.49465	-60.104161	28.1	0.6	18.6	14.2	$2.50 \cdot 10^{22}$	87.5	167.7	51.0
66	161.46504	-60.274614	24.0	0.6	17.8	14.2	$2.46 \cdot 10^{22}$	83.6	160.3	48.8
67	161.19710	-59.991217	43.6	0.6	47.5	14.3	$2.39 \cdot 10^{22}$	221.0	428.7	130.4

n	R.A. (deg)	Dec. (deg)	R (")	F_{max}	F_{tot}	T	N_{H_2}	M	M (10 K)	M (20 K)
68	160.30508	-59.698968	36.6	0.6	28.6	14.3	$2.35 \cdot 10^{22}$	132.8	257.7	78.4
69	160.83562	-59.544996	33.8	0.6	24.0	14.3	$2.35 \cdot 10^{22}$	111.6	216.5	65.9
70	161.48587	-59.748160	32.7	0.5	24.8	14.4	$2.28 \cdot 10^{22}$	113.9	223.5	68.0
71	160.41200	-59.703109	35.5	0.5	31.3	14.4	$2.28 \cdot 10^{22}$	143.8	282.2	85.9
72	161.46172	-60.291491	15.7	0.5	10.2	14.4	$2.28 \cdot 10^{22}$	46.8	91.9	28.0
73	161.27482	-59.824216	51.3	0.5	57.6	14.4	$2.28 \cdot 10^{22}$	264.7	519.6	158.1
74	161.40598	-59.901790	41.9	0.5	42.1	14.4	$2.28 \cdot 10^{22}$	193.2	379.3	115.4
75	161.33520	-59.785407	33.0	0.5	25.2	14.4	$2.23 \cdot 10^{22}$	116.0	227.6	69.3
76	161.75840	-60.083265	32.1	0.5	20.8	14.4	$2.23 \cdot 10^{22}$	95.4	187.3	57.0
77	161.48225	-60.310024	26.1	0.5	15.0	14.4	$2.19 \cdot 10^{22}$	69.0	135.3	41.2
78	160.79983	-59.489183	31.6	0.5	21.2	14.4	$2.19 \cdot 10^{22}$	97.5	191.4	58.3
79	160.79550	-59.556659	40.4	0.5	45.6	14.5	$2.13 \cdot 10^{22}$	206.9	410.8	125.0
80	161.48809	-60.141290	37.1	0.5	33.7	14.5	$2.13 \cdot 10^{22}$	153.0	303.9	92.5
81	161.32852	-59.805655	43.4	0.5	35.7	14.5	$2.08 \cdot 10^{22}$	162.1	321.8	97.9
82	160.80978	-59.490908	22.2	0.5	12.7	14.5	$2.08 \cdot 10^{22}$	57.7	114.6	34.9
83	161.47543	-60.308346	24.5	0.5	15.8	14.5	$2.08 \cdot 10^{22}$	71.7	142.4	43.3
84	161.50137	-60.095714	20.0	0.5	8.3	14.6	$2.02 \cdot 10^{22}$	37.2	74.8	22.7
85	161.82480	-60.003716	36.6	0.5	26.9	14.6	$2.02 \cdot 10^{22}$	121.0	243.0	74.0
86	162.10469	-60.132241	25.0	0.5	11.4	14.6	$2.02 \cdot 10^{22}$	51.4	103.2	31.4
87	161.41966	-59.962519	25.0	0.5	10.8	14.6	$2.02 \cdot 10^{22}$	48.7	97.7	29.7
88	161.50810	-60.090642	20.3	0.5	7.8	14.6	$2.02 \cdot 10^{22}$	35.1	70.6	21.5
89	161.76313	-60.419021	27.2	0.5	14.7	14.6	$2.02 \cdot 10^{22}$	66.0	132.7	40.4
90	161.02476	-59.619771	29.5	0.5	16.6	14.6	$1.98 \cdot 10^{22}$	74.5	149.7	45.6
91	161.37419	-59.221846	21.9	0.5	8.8	14.6	$1.98 \cdot 10^{22}$	39.5	79.3	24.1
92	160.28842	-59.697153	20.8	0.5	10.0	14.6	$1.98 \cdot 10^{22}$	44.8	89.9	27.4
93	161.49941	-59.771762	34.0	0.5	27.7	14.6	$1.98 \cdot 10^{22}$	124.3	249.8	76.0
94	161.97880	-60.434978	19.7	0.5	7.8	14.6	$1.98 \cdot 10^{22}$	35.1	70.5	21.5
95	161.06543	-59.528738	29.1	0.5	19.2	14.7	$1.91 \cdot 10^{22}$	85.3	173.4	52.8
96	161.21822	-59.636907	31.9	0.5	19.7	14.7	$1.91 \cdot 10^{22}$	87.6	177.9	54.1
97	161.50932	-59.748125	23.5	0.5	14.6	14.7	$1.91 \cdot 10^{22}$	64.8	131.6	40.0
98	160.27941	-59.663335	27.2	0.5	15.0	14.7	$1.91 \cdot 10^{22}$	66.5	135.1	41.1
99	160.81806	-59.609050	36.9	0.5	27.8	14.7	$1.91 \cdot 10^{22}$	123.5	250.9	76.4
100	161.25126	-59.873140	46.0	0.5	42.9	14.7	$1.91 \cdot 10^{22}$	190.2	386.5	117.6
101	161.94450	-60.430085	22.7	0.5	13.5	14.8	$1.85 \cdot 10^{22}$	59.2	121.7	37.0
102	160.76169	-59.588583	41.9	0.5	37.1	14.8	$1.85 \cdot 10^{22}$	162.7	334.4	101.8
103	161.49918	-59.732955	29.9	0.5	21.0	14.8	$1.85 \cdot 10^{22}$	92.0	189.1	57.5
104	161.26134	-59.878205	38.1	0.5	33.2	14.8	$1.85 \cdot 10^{22}$	145.9	299.7	91.2
105	161.50599	-59.751505	17.1	0.5	7.5	14.8	$1.85 \cdot 10^{22}$	33.0	67.9	20.7
106	160.92456	-59.629646	17.5	0.5	7.8	14.8	$1.81 \cdot 10^{22}$	34.1	70.2	21.3
107	160.97803	-59.968931	21.9	0.5	9.6	14.8	$1.81 \cdot 10^{22}$	42.2	86.7	26.4
108	160.93793	-59.627996	25.0	0.4	14.2	14.9	$1.75 \cdot 10^{22}$	61.5	127.9	38.9
109	160.16588	-59.760278	28.5	0.4	16.5	14.9	$1.75 \cdot 10^{22}$	71.8	149.2	45.4

n	R.A. (deg)	Dec. (deg)	R (")	F_{max}	F_{tot}	T	N_{H_2}	M	M (10 K)	M (20 K)
110	160.28492	-59.702189	30.2	0.4	17.3	14.9	$1.75 \cdot 10^{22}$	75.2	156.3	47.6
111	160.99986	-59.418930	21.9	0.4	11.8	14.9	$1.75 \cdot 10^{22}$	51.0	106.0	32.3
112	162.09791	-60.132282	23.3	0.4	7.8	14.9	$1.75 \cdot 10^{22}$	34.1	70.8	21.5
113	161.53935	-59.732888	25.9	0.4	13.0	14.9	$1.71 \cdot 10^{22}$	56.6	117.6	35.8
114	160.14352	-59.437768	16.1	0.4	4.4	14.9	$1.71 \cdot 10^{22}$	19.3	40.0	12.2
115	160.45763	-59.750657	17.5	0.4	6.1	14.9	$1.71 \cdot 10^{22}$	26.4	54.9	16.7
116	160.29520	-59.693831	20.0	0.4	9.2	14.9	$1.71 \cdot 10^{22}$	39.8	82.7	25.2
117	161.37534	-59.743208	30.7	0.4	16.4	14.9	$1.71 \cdot 10^{22}$	71.2	147.9	45.0
118	161.21477	-59.682461	26.3	0.4	10.1	14.9	$1.71 \cdot 10^{22}$	43.9	91.2	27.7
119	161.51239	-59.704251	28.7	0.4	17.4	15.0	$1.65 \cdot 10^{22}$	74.7	156.9	47.7
120	160.27597	-59.666683	21.9	0.4	10.4	15.0	$1.65 \cdot 10^{22}$	44.9	94.2	28.7
121	160.99323	-59.418915	21.1	0.4	9.0	15.0	$1.65 \cdot 10^{22}$	38.6	81.2	24.7
122	161.52246	-59.710984	26.1	0.4	19.6	15.0	$1.61 \cdot 10^{22}$	83.9	176.3	53.6
123	161.12937	-59.385419	20.3	0.4	9.0	15.0	$1.61 \cdot 10^{22}$	38.6	81.1	24.7
124	161.81208	-59.617372	25.0	0.4	11.6	15.0	$1.61 \cdot 10^{22}$	49.8	104.7	31.9
125	161.48803	-60.131166	23.7	0.4	8.9	15.0	$1.61 \cdot 10^{22}$	38.1	80.1	24.4
126	160.91791	-59.627939	17.5	0.4	7.9	15.0	$1.61 \cdot 10^{22}$	33.8	71.1	21.6
127	160.40818	-59.343665	23.3	0.4	8.9	15.1	$1.56 \cdot 10^{22}$	37.8	80.3	24.4
128	160.44410	-59.755632	28.5	0.4	14.3	15.2	$1.50 \cdot 10^{22}$	60.1	128.9	39.2
129	161.01858	-59.560703	17.5	0.4	5.3	15.2	$1.50 \cdot 10^{22}$	22.4	48.1	14.6
130	161.23845	-59.527246	27.2	0.4	14.6	15.2	$1.50 \cdot 10^{22}$	61.4	131.8	40.1
131	160.67750	-59.454910	28.5	0.4	16.9	15.2	$1.50 \cdot 10^{22}$	70.9	152.3	46.3
132	161.52422	-59.972507	17.1	0.4	5.0	15.2	$1.50 \cdot 10^{22}$	21.1	45.3	13.8
133	160.93802	-59.619560	33.8	0.4	18.7	15.2	$1.50 \cdot 10^{22}$	78.7	169.0	51.4
134	161.51408	-59.969149	23.5	0.4	11.5	15.2	$1.50 \cdot 10^{22}$	48.4	104.0	31.6
135	161.49624	-60.370746	22.7	0.4	8.9	15.2	$1.50 \cdot 10^{22}$	37.6	80.7	24.6
136	161.89387	-60.091166	18.5	0.4	6.5	15.2	$1.50 \cdot 10^{22}$	27.4	58.8	17.9
137	160.91123	-59.627920	23.5	0.4	10.8	15.2	$1.46 \cdot 10^{22}$	45.4	97.5	29.7
138	160.52629	-59.533407	27.8	0.4	14.2	15.2	$1.46 \cdot 10^{22}$	59.8	128.4	39.1
139	160.53624	-59.535153	18.5	0.4	5.8	15.2	$1.46 \cdot 10^{22}$	24.4	52.5	16.0
140	161.16011	-59.964187	19.7	0.4	7.7	15.2	$1.46 \cdot 10^{22}$	32.3	69.3	21.1
141	160.31301	-59.656842	23.0	0.4	11.2	15.2	$1.46 \cdot 10^{22}$	47.1	101.2	30.8
142	160.78965	-59.283292	23.3	0.4	10.7	15.2	$1.46 \cdot 10^{22}$	45.0	96.7	29.4
143	160.96434	-59.656750	26.8	0.4	13.4	15.2	$1.46 \cdot 10^{22}$	56.4	121.0	36.8
144	160.50697	-59.506293	16.1	0.4	4.8	15.2	$1.46 \cdot 10^{22}$	20.2	43.5	13.2
145	161.22235	-59.294396	20.6	0.4	7.3	15.2	$1.46 \cdot 10^{22}$	30.8	66.2	20.1
146	161.21546	-59.409125	24.7	0.4	11.2	15.3	$1.41 \cdot 10^{22}$	46.4	100.8	30.7
147	161.33530	-59.874831	38.6	0.4	21.9	15.3	$1.41 \cdot 10^{22}$	91.2	197.9	60.2
148	161.12602	-59.393851	24.2	0.4	10.6	15.3	$1.41 \cdot 10^{22}$	44.1	95.7	29.1
149	161.51927	-59.734611	18.8	0.4	7.4	15.3	$1.41 \cdot 10^{22}$	30.6	66.5	20.2
150	161.51273	-59.758243	32.1	0.4	17.4	15.3	$1.41 \cdot 10^{22}$	72.2	156.8	47.7
151	160.88583	-59.523230	25.0	0.4	12.7	15.3	$1.41 \cdot 10^{22}$	52.7	114.3	34.8

n	R.A. (deg)	Dec. (deg)	R (")	F_{max}	F_{tot}	T	N_{H_2}	M	M (10 K)	M (20 K)
152	161.13463	-59.665512	21.9	0.4	6.1	15.3	$1.41 \cdot 10^{22}$	25.3	54.8	16.7
153	161.02309	-59.417295	25.9	0.4	12.3	15.4	$1.36 \cdot 10^{22}$	50.6	110.9	33.8
154	161.17361	-59.959138	18.8	0.4	6.3	15.4	$1.36 \cdot 10^{22}$	25.8	56.6	17.2
155	160.81007	-59.241188	16.1	0.4	3.2	15.4	$1.36 \cdot 10^{22}$	13.2	29.0	8.8
156	161.48503	-60.200348	27.0	0.4	12.4	15.4	$1.36 \cdot 10^{22}$	51.0	111.9	34.1
157	160.43110	-59.740360	24.7	0.4	10.9	15.4	$1.36 \cdot 10^{22}$	44.8	98.3	29.9
158	161.14192	-59.537289	28.7	0.4	11.6	15.4	$1.36 \cdot 10^{22}$	47.7	104.6	31.8
159	161.61285	-59.717549	27.0	0.4	10.6	15.4	$1.36 \cdot 10^{22}$	43.6	95.7	29.1
160	160.28898	-59.678596	16.1	0.4	5.5	15.4	$1.36 \cdot 10^{22}$	22.6	49.6	15.1
161	161.00510	-59.579234	21.1	0.4	8.1	15.4	$1.36 \cdot 10^{22}$	33.1	72.6	22.1
162	160.78630	-59.286653	20.6	0.4	7.4	15.4	$1.36 \cdot 10^{22}$	30.3	66.4	20.2
163	160.96424	-59.666874	22.2	0.4	9.3	15.4	$1.36 \cdot 10^{22}$	38.1	83.7	25.5
164	161.02022	-59.363296	27.2	0.4	11.3	15.4	$1.36 \cdot 10^{22}$	46.6	102.2	31.1
165	160.86885	-59.550172	28.5	0.4	16.3	15.4	$1.36 \cdot 10^{22}$	67.1	147.2	44.8
166	161.52087	-59.975887	29.9	0.4	14.7	15.4	$1.36 \cdot 10^{22}$	60.3	132.4	40.3
167	161.48259	-59.759976	30.7	0.3	16.1	15.4	$1.32 \cdot 10^{22}$	66.2	145.2	44.2
168	161.52598	-59.736287	18.5	0.3	7.1	15.4	$1.32 \cdot 10^{22}$	29.1	63.8	19.4
169	161.90061	-60.089448	20.0	0.3	6.5	15.4	$1.32 \cdot 10^{22}$	26.9	59.1	18.0
170	161.06216	-59.520295	26.5	0.3	13.0	15.4	$1.32 \cdot 10^{22}$	53.4	117.1	35.6
171	160.62841	-59.419232	23.0	0.3	9.2	15.4	$1.32 \cdot 10^{22}$	37.8	82.9	25.2
172	160.37166	-59.589773	20.3	0.3	8.0	15.4	$1.32 \cdot 10^{22}$	32.8	72.0	21.9
173	161.08423	-59.710995	18.2	0.3	5.2	15.4	$1.32 \cdot 10^{22}$	21.2	46.5	14.2
174	162.44624	-59.527296	25.6	0.3	9.6	15.4	$1.32 \cdot 10^{22}$	39.3	86.2	26.2
175	160.40071	-59.375674	29.3	0.3	11.0	15.4	$1.32 \cdot 10^{22}$	45.1	98.8	30.1
176	160.54305	-59.528443	17.5	0.3	5.5	15.4	$1.32 \cdot 10^{22}$	22.6	49.6	15.1
177	161.26828	-59.641990	16.8	0.3	5.5	15.5	$1.27 \cdot 10^{22}$	22.2	49.3	15.0
178	160.46047	-59.637620	30.2	0.3	14.8	15.5	$1.27 \cdot 10^{22}$	60.1	133.2	40.5
179	160.36170	-59.588015	20.8	0.3	7.4	15.5	$1.27 \cdot 10^{22}$	30.2	67.0	20.4
180	161.89947	-60.027022	26.3	0.3	8.6	15.5	$1.27 \cdot 10^{22}$	35.1	77.9	23.7
181	161.36876	-59.800579	29.5	0.3	15.6	15.5	$1.27 \cdot 10^{22}$	63.4	140.5	42.8
182	161.41720	-60.218985	20.3	0.3	5.8	15.5	$1.27 \cdot 10^{22}$	23.4	51.9	15.8
183	160.50372	-59.502899	21.7	0.3	7.1	15.5	$1.27 \cdot 10^{22}$	29.0	64.2	19.5
184	161.25869	-59.299474	24.5	0.3	8.6	15.5	$1.27 \cdot 10^{22}$	34.9	77.4	23.5
185	161.21734	-59.992918	26.8	0.3	10.3	15.5	$1.27 \cdot 10^{22}$	41.8	92.7	28.2
186	161.21909	-59.275834	16.8	0.3	5.1	15.5	$1.27 \cdot 10^{22}$	20.7	45.8	13.9
187	160.52030	-59.504686	23.3	0.3	8.8	15.5	$1.27 \cdot 10^{22}$	35.9	79.5	24.2
188	160.73263	-59.532778	32.5	0.3	15.6	15.6	$1.22 \cdot 10^{22}$	62.8	140.8	42.8
189	161.27496	-59.638617	20.3	0.3	6.9	15.6	$1.22 \cdot 10^{22}$	27.7	62.0	18.9
190	160.96281	-59.476207	16.1	0.3	4.0	15.6	$1.22 \cdot 10^{22}$	16.1	36.2	11.0
191	162.01201	-60.077086	25.9	0.3	9.1	15.6	$1.22 \cdot 10^{22}$	36.7	82.1	25.0
192	161.26160	-59.645363	23.7	0.3	9.9	15.6	$1.22 \cdot 10^{22}$	39.9	89.5	27.2
193	160.91072	-59.671788	30.2	0.3	16.0	15.6	$1.22 \cdot 10^{22}$	64.3	144.1	43.9

n	R.A. (deg)	Dec. (deg)	R (")	F_{max}	F_{tot}	T	N_{H_2}	M	M (10 K)	M (20 K)
194	161.19813	-59.658827	29.3	0.3	15.6	15.6	$1.22 \cdot 10^{22}$	62.8	140.8	42.8
195	160.44775	-59.743844	16.5	0.3	4.6	15.6	$1.22 \cdot 10^{22}$	18.4	41.1	12.5
196	161.79545	-59.620811	26.8	0.3	10.2	15.6	$1.22 \cdot 10^{22}$	41.1	92.1	28.0
197	160.40453	-59.482007	20.0	0.3	7.5	15.6	$1.18 \cdot 10^{22}$	30.0	67.2	20.4
198	160.69561	-59.556235	23.3	0.3	7.2	15.6	$1.18 \cdot 10^{22}$	28.8	64.6	19.6
199	161.34470	-59.363589	34.4	0.3	14.5	15.6	$1.18 \cdot 10^{22}$	58.5	131.0	39.9
200	160.52688	-59.508100	18.5	0.3	6.3	15.6	$1.18 \cdot 10^{22}$	25.3	56.7	17.3
201	161.58135	-59.950463	28.7	0.3	10.5	15.6	$1.18 \cdot 10^{22}$	42.1	94.3	28.7
202	161.13526	-59.537280	17.1	0.3	5.3	15.6	$1.18 \cdot 10^{22}$	21.2	47.4	14.4
203	161.02133	-59.631575	22.7	0.3	7.8	15.6	$1.18 \cdot 10^{22}$	31.3	70.1	21.3
204	161.22566	-59.289336	19.1	0.3	6.5	15.6	$1.18 \cdot 10^{22}$	26.1	58.4	17.8
205	160.96942	-59.479599	17.5	0.3	5.2	15.6	$1.18 \cdot 10^{22}$	20.8	46.5	14.2
206	160.29222	-59.681995	20.6	0.3	7.5	15.6	$1.18 \cdot 10^{22}$	30.2	67.7	20.6
207	161.13602	-59.382053	19.4	0.3	5.4	15.6	$1.18 \cdot 10^{22}$	21.6	48.3	14.7
208	161.50932	-60.281301	27.4	0.3	11.3	15.6	$1.18 \cdot 10^{22}$	45.6	102.1	31.1
209	161.48570	-59.717790	30.1	0.3	15.9	15.7	$1.13 \cdot 10^{22}$	63.5	143.7	43.7
210	161.21882	-59.388880	21.4	0.3	6.8	15.7	$1.13 \cdot 10^{22}$	26.9	61.0	18.6
211	160.85213	-59.555177	28.1	0.3	13.1	15.7	$1.13 \cdot 10^{22}$	52.1	118.0	35.9
212	160.90230	-59.536779	22.7	0.3	8.6	15.7	$1.13 \cdot 10^{22}$	34.3	77.5	23.6
213	160.98608	-59.474578	18.8	0.3	6.8	15.7	$1.13 \cdot 10^{22}$	27.1	61.4	18.7
214	161.05344	-59.348178	17.8	0.3	4.0	15.7	$1.13 \cdot 10^{22}$	15.7	35.6	10.8
215	160.28918	-59.671847	17.1	0.3	5.6	15.7	$1.13 \cdot 10^{22}$	22.5	50.9	15.5
216	161.75855	-60.093389	17.1	0.3	5.1	15.7	$1.13 \cdot 10^{22}$	20.3	45.9	14.0
217	161.52588	-59.721101	25.6	0.3	11.7	15.7	$1.13 \cdot 10^{22}$	46.8	105.9	32.2
218	161.68866	-60.193161	23.0	0.3	8.2	15.7	$1.13 \cdot 10^{22}$	32.6	73.9	22.5
219	160.38515	-59.706300	20.8	0.3	8.4	15.7	$1.13 \cdot 10^{22}$	33.5	75.8	23.1
220	161.45772	-60.168325	35.8	0.3	19.3	15.7	$1.13 \cdot 10^{22}$	76.7	173.7	52.9
221	160.92734	-59.680272	34.1	0.3	17.2	15.7	$1.13 \cdot 10^{22}$	68.4	154.7	47.1
222	160.27582	-59.671744	18.2	0.3	5.1	15.8	$1.09 \cdot 10^{22}$	20.0	45.7	13.9
223	161.27830	-59.641992	18.2	0.3	4.4	15.8	$1.09 \cdot 10^{22}$	17.4	39.8	12.1
224	161.23179	-59.530617	28.1	0.3	10.0	15.8	$1.09 \cdot 10^{22}$	39.3	89.9	27.4
225	160.91076	-59.668413	20.6	0.3	5.8	15.8	$1.09 \cdot 10^{22}$	22.8	52.1	15.9
226	161.02682	-59.366684	17.8	0.3	4.3	15.8	$1.09 \cdot 10^{22}$	17.0	38.8	11.8
227	161.50304	-60.367361	18.5	0.3	4.8	15.8	$1.09 \cdot 10^{22}$	18.8	43.1	13.1
228	160.74464	-59.409656	25.6	0.3	8.2	15.8	$1.09 \cdot 10^{22}$	32.3	73.9	22.5
229	161.56472	-59.977494	26.5	0.3	7.8	15.8	$1.09 \cdot 10^{22}$	30.6	70.0	21.3
230	161.47561	-59.707680	26.1	0.3	9.4	15.8	$1.09 \cdot 10^{22}$	37.3	85.2	25.9
231	160.69222	-59.559594	18.8	0.3	5.3	15.8	$1.09 \cdot 10^{22}$	20.8	47.6	14.5
232	160.30953	-59.661878	22.2	0.3	7.9	15.8	$1.09 \cdot 10^{22}$	31.2	71.3	21.7
233	161.17473	-59.662182	23.3	0.3	8.8	15.8	$1.09 \cdot 10^{22}$	34.7	79.4	24.2
234	160.67408	-59.459956	17.8	0.3	5.4	15.8	$1.09 \cdot 10^{22}$	21.4	48.9	14.9
235	160.56153	-59.596044	27.2	0.3	9.4	15.8	$1.09 \cdot 10^{22}$	37.0	84.7	25.8

n	R.A. (deg)	Dec. (deg)	R (")	F_{max}	F_{tot}	T	N_{H_2}	M	M (10 K)	M (20 K)
236	160.85904	-59.281859	20.6	0.3	6.0	15.8	$1.09 \cdot 10^{22}$	23.6	54.0	16.4
237	161.89586	-60.200833	21.7	0.3	5.2	15.8	$1.09 \cdot 10^{22}$	20.4	46.7	14.2
238	160.64296	-59.694343	27.0	0.3	9.2	15.8	$1.09 \cdot 10^{22}$	36.2	82.8	25.2
239	161.29493	-60.045249	25.2	0.3	8.3	15.8	$1.09 \cdot 10^{22}$	32.6	74.6	22.7
240	161.28812	-60.197102	40.6	0.3	21.7	15.8	$1.09 \cdot 10^{22}$	85.6	195.8	59.6
241	161.86205	-60.209416	20.0	0.3	5.5	15.8	$1.09 \cdot 10^{22}$	21.9	50.0	15.2
242	161.91389	-60.075889	20.8	0.3	6.2	15.9	$1.04 \cdot 10^{22}$	24.0	55.5	16.9
243	161.02583	-59.488166	21.9	0.3	5.7	15.9	$1.04 \cdot 10^{22}$	22.4	51.7	15.7
244	161.73183	-60.120475	23.3	0.3	6.7	15.9	$1.04 \cdot 10^{22}$	26.3	60.7	18.5
245	161.73506	-60.365122	24.0	0.3	7.8	15.9	$1.04 \cdot 10^{22}$	30.4	70.3	21.4
246	161.22213	-59.392257	15.7	0.3	3.5	15.9	$1.04 \cdot 10^{22}$	13.7	31.6	9.6
247	160.32004	-59.645082	24.2	0.3	7.6	15.9	$1.04 \cdot 10^{22}$	29.7	68.6	20.9
248	160.33286	-59.663739	25.4	0.3	10.5	15.9	$1.04 \cdot 10^{22}$	40.9	94.4	28.7
249	160.71379	-59.276222	20.0	0.3	4.9	15.9	$1.04 \cdot 10^{22}$	19.2	44.5	13.5
250	161.21548	-59.399002	16.5	0.3	4.3	15.9	$1.04 \cdot 10^{22}$	16.7	38.7	11.8
251	161.47261	-59.773487	27.2	0.3	10.6	16.0	$9.93 \cdot 10^{21}$	40.9	95.4	29.0
252	160.56549	-59.567381	24.2	0.3	8.1	16.0	$9.93 \cdot 10^{21}$	31.2	72.8	22.1
253	161.16805	-59.663862	22.2	0.3	8.0	16.0	$9.93 \cdot 10^{21}$	31.0	72.4	22.0
254	160.95447	-59.965497	19.1	0.3	6.7	16.0	$9.93 \cdot 10^{21}$	25.7	60.1	18.3
255	161.45468	-60.242569	28.2	0.3	11.6	16.0	$9.93 \cdot 10^{21}$	44.8	104.5	31.8
256	160.98614	-59.467829	15.7	0.3	3.6	16.0	$9.93 \cdot 10^{21}$	14.0	32.6	9.9
257	160.30244	-59.675324	25.4	0.3	8.1	16.0	$9.93 \cdot 10^{21}$	31.2	72.9	22.2
258	160.92863	-59.563853	25.6	0.3	8.0	16.0	$9.93 \cdot 10^{21}$	30.9	72.1	22.0
259	160.40134	-59.601792	23.7	0.3	7.5	16.0	$9.93 \cdot 10^{21}$	29.0	67.7	20.6
260	161.63685	-59.774857	28.1	0.3	11.3	16.0	$9.93 \cdot 10^{21}$	43.7	101.9	31.0
261	160.41445	-59.610318	21.1	0.3	5.5	16.0	$9.93 \cdot 10^{21}$	21.3	49.6	15.1
262	160.71011	-59.488808	27.8	0.3	11.5	16.0	$9.93 \cdot 10^{21}$	44.5	103.9	31.6
263	160.39850	-59.583211	16.5	0.3	3.9	16.0	$9.93 \cdot 10^{21}$	15.1	35.3	10.8
264	161.47808	-60.169987	24.5	0.3	9.1	16.0	$9.93 \cdot 10^{21}$	35.1	82.0	24.9
265	161.88910	-60.202550	16.1	0.3	3.9	16.0	$9.93 \cdot 10^{21}$	14.9	34.7	10.6
266	160.45362	-59.644325	23.5	0.3	7.4	16.0	$9.93 \cdot 10^{21}$	28.6	66.7	20.3
267	161.23823	-59.647042	24.0	0.3	9.5	16.0	$9.58 \cdot 10^{21}$	36.6	85.3	26.0
268	161.64355	-59.774839	24.7	0.3	7.0	16.0	$9.58 \cdot 10^{21}$	27.2	63.6	19.3
269	160.40454	-59.606876	18.8	0.3	5.2	16.0	$9.58 \cdot 10^{21}$	20.1	46.9	14.3
270	160.89115	-59.632920	20.3	0.3	6.1	16.0	$9.58 \cdot 10^{21}$	23.5	54.9	16.7
271	161.52218	-60.171608	30.1	0.3	13.3	16.0	$9.58 \cdot 10^{21}$	51.4	120.0	36.5
272	160.76349	-59.475540	19.1	0.3	4.9	16.0	$9.58 \cdot 10^{21}$	19.1	44.5	13.5
273	160.61418	-59.466404	21.4	0.3	5.7	16.0	$9.58 \cdot 10^{21}$	22.0	51.3	15.6
274	160.38818	-59.594951	19.7	0.3	6.0	16.0	$9.58 \cdot 10^{21}$	23.1	54.0	16.4
275	161.47594	-59.770108	16.5	0.3	5.0	16.0	$9.58 \cdot 10^{21}$	19.2	44.7	13.6
276	160.53674	-59.513220	15.7	0.3	4.5	16.0	$9.58 \cdot 10^{21}$	17.4	40.6	12.3
277	161.01381	-59.337973	18.8	0.3	4.5	16.0	$9.58 \cdot 10^{21}$	17.4	40.6	12.3

n	R.A. (deg)	Dec. (deg)	R (")	F_{max}	F_{tot}	T	N_{H_2}	M	M (10 K)	M (20 K)
278	161.51317	-60.350473	17.5	0.3	3.7	16.0	$9.58 \cdot 10^{21}$	14.3	33.3	10.1
279	160.32991	-59.650218	22.5	0.3	7.2	16.0	$9.58 \cdot 10^{21}$	27.8	64.8	19.7
280	161.61882	-60.341827	19.1	0.3	5.2	16.0	$9.58 \cdot 10^{21}$	20.0	46.7	14.2
281	161.46924	-59.770117	18.8	0.3	4.4	16.0	$9.58 \cdot 10^{21}$	17.1	39.9	12.1
282	160.67722	-59.470095	21.4	0.3	7.0	16.0	$9.58 \cdot 10^{21}$	26.9	62.9	19.1
283	160.70046	-59.657497	18.2	0.3	4.7	16.0	$9.58 \cdot 10^{21}$	18.1	42.3	12.9
284	161.82169	-60.020601	18.5	0.3	3.9	16.1	$9.13 \cdot 10^{21}$	15.0	35.3	10.7
285	161.54918	-59.704187	18.5	0.3	5.0	16.1	$9.13 \cdot 10^{21}$	19.0	44.7	13.6
286	160.89444	-59.636305	18.8	0.3	5.3	16.1	$9.13 \cdot 10^{21}$	20.4	48.2	14.7
287	160.51995	-59.519871	26.1	0.3	9.0	16.1	$9.13 \cdot 10^{21}$	34.5	81.2	24.7
288	161.50631	-60.343735	17.8	0.3	3.6	16.1	$9.13 \cdot 10^{21}$	13.7	32.2	9.8
289	160.98015	-59.398636	25.0	0.3	9.2	16.1	$9.13 \cdot 10^{21}$	35.1	82.8	25.2
290	160.75682	-59.477200	20.6	0.3	6.3	16.1	$9.13 \cdot 10^{21}$	24.1	56.8	17.3
291	160.94947	-59.481234	19.1	0.3	4.8	16.1	$9.13 \cdot 10^{21}$	18.2	42.9	13.1
292	161.42743	-60.230786	18.2	0.3	4.3	16.1	$9.13 \cdot 10^{21}$	16.5	39.0	11.9
293	160.67893	-59.557844	27.6	0.3	10.1	16.1	$9.13 \cdot 10^{21}$	38.6	91.1	27.7
294	161.54587	-59.709255	17.8	0.3	4.2	16.1	$9.13 \cdot 10^{21}$	16.0	37.7	11.5
295	161.96369	-60.197138	27.8	0.3	8.8	16.1	$9.13 \cdot 10^{21}$	33.5	79.0	24.0
296	160.39835	-59.713141	20.6	0.3	5.2	16.1	$9.13 \cdot 10^{21}$	19.9	46.9	14.3
297	160.96020	-59.405335	23.5	0.3	7.0	16.1	$9.13 \cdot 10^{21}$	27.0	63.6	19.3
298	161.18376	-59.949024	17.5	0.3	3.7	16.1	$9.13 \cdot 10^{21}$	14.2	33.5	10.2
299	160.61055	-59.481571	25.4	0.3	8.9	16.1	$9.13 \cdot 10^{21}$	34.0	80.3	24.4
300	160.42806	-59.728528	20.0	0.3	5.9	16.1	$9.13 \cdot 10^{21}$	22.5	52.9	16.1
301	160.36414	-59.500286	21.4	0.3	5.5	16.1	$9.13 \cdot 10^{21}$	21.1	49.8	15.1
302	160.80779	-59.627572	23.3	0.3	6.8	16.1	$9.13 \cdot 10^{21}$	25.9	61.1	18.6
303	160.97974	-60.141037	29.9	0.3	10.8	16.1	$9.13 \cdot 10^{21}$	41.1	96.9	29.5
304	160.42424	-59.490578	23.7	0.3	6.7	16.1	$9.13 \cdot 10^{21}$	25.8	60.8	18.5
305	161.23487	-59.655476	25.2	0.2	8.2	16.2	$8.69 \cdot 10^{21}$	30.9	73.6	22.4
306	161.49560	-60.264449	17.1	0.2	4.8	16.2	$8.69 \cdot 10^{21}$	18.2	43.4	13.2
307	161.17150	-59.633495	19.7	0.2	5.2	16.2	$8.69 \cdot 10^{21}$	19.6	46.7	14.2
308	160.83253	-59.528112	25.0	0.2	8.7	16.2	$8.69 \cdot 10^{21}$	33.0	78.5	23.9
309	161.09764	-59.705954	22.2	0.2	5.5	16.2	$8.69 \cdot 10^{21}$	20.9	49.7	15.1
310	161.46898	-60.379220	20.0	0.2	5.9	16.2	$8.69 \cdot 10^{21}$	22.2	52.9	16.1
311	160.68720	-59.652374	16.5	0.2	3.9	16.2	$8.69 \cdot 10^{21}$	14.8	35.3	10.7
312	161.31513	-59.883271	27.0	0.2	10.0	16.2	$8.69 \cdot 10^{21}$	37.9	90.3	27.5
313	161.69861	-59.894482	17.1	0.2	3.6	16.2	$8.69 \cdot 10^{21}$	13.8	32.7	10.0
314	161.14169	-59.584532	18.2	0.2	3.4	16.2	$8.69 \cdot 10^{21}$	13.0	31.0	9.4
315	161.73957	-59.685127	28.2	0.2	10.6	16.2	$8.69 \cdot 10^{21}$	40.2	95.6	29.1
316	161.87897	-60.205969	17.8	0.2	4.1	16.2	$8.69 \cdot 10^{21}$	15.6	37.2	11.3
317	160.92758	-59.9958675	22.7	0.2	5.8	16.2	$8.69 \cdot 10^{21}$	22.0	52.3	15.9
318	160.86290	-60.262190	17.8	0.2	4.3	16.2	$8.69 \cdot 10^{21}$	16.4	39.0	11.9
319	160.90438	-59.643085	21.1	0.2	6.0	16.2	$8.69 \cdot 10^{21}$	22.9	54.5	16.6

n	R.A. (deg)	Dec. (deg)	R (")	F_{max}	F_{tot}	T	N_{H_2}	M	M (10 K)	M (20 K)
320	160.42358	-59.644128	23.0	0.2	7.0	16.2	$8.69 \cdot 10^{21}$	26.5	63.0	19.2
321	161.23533	-59.419260	19.1	0.2	5.2	16.2	$8.69 \cdot 10^{21}$	19.6	46.6	14.2
322	161.08378	-59.260494	15.7	0.2	3.5	16.3	$8.26 \cdot 10^{21}$	13.0	31.3	9.5
323	161.03313	-59.405505	25.2	0.2	8.3	16.3	$8.26 \cdot 10^{21}$	31.2	74.9	22.8
324	160.14025	-59.726304	17.1	0.2	3.4	16.3	$8.26 \cdot 10^{21}$	12.6	30.4	9.2
325	162.11677	-59.936431	23.5	0.2	6.6	16.3	$8.26 \cdot 10^{21}$	24.8	59.6	18.1
326	160.41440	-59.485450	15.7	0.2	3.3	16.3	$8.26 \cdot 10^{21}$	12.4	29.8	9.1
327	161.59997	-59.773259	24.5	0.2	7.7	16.3	$8.26 \cdot 10^{21}$	28.7	69.1	21.0
328	160.35851	-59.582929	20.0	0.2	4.4	16.3	$8.26 \cdot 10^{21}$	16.5	39.7	12.1
329	161.24465	-59.805647	24.5	0.2	7.3	16.3	$8.26 \cdot 10^{21}$	27.4	65.9	20.1
330	161.87557	-60.011942	15.7	0.2	2.9	16.3	$8.26 \cdot 10^{21}$	10.8	26.0	7.9
331	161.36881	-59.820826	21.7	0.2	5.6	16.3	$8.26 \cdot 10^{21}$	21.0	50.6	15.4
332	161.43802	-60.323575	16.8	0.2	3.0	16.3	$8.26 \cdot 10^{21}$	11.3	27.2	8.3
333	160.96473	-59.282175	15.7	0.2	3.0	16.3	$8.26 \cdot 10^{21}$	11.3	27.2	8.3
334	160.78600	-59.524563	18.2	0.2	4.4	16.3	$8.26 \cdot 10^{21}$	16.6	39.9	12.2
335	161.70027	-59.752744	34.4	0.2	12.9	16.3	$8.26 \cdot 10^{21}$	48.3	116.0	35.3
336	161.42097	-60.321905	19.1	0.2	3.8	16.3	$8.26 \cdot 10^{21}$	14.4	34.6	10.5
337	160.69709	-59.473563	20.0	0.2	4.8	16.3	$8.26 \cdot 10^{21}$	18.0	43.4	13.2
338	160.80935	-59.291804	16.1	0.2	3.1	16.3	$8.26 \cdot 10^{21}$	11.8	28.3	8.6
339	161.00778	-59.653480	20.8	0.2	4.8	16.3	$8.26 \cdot 10^{21}$	18.0	43.3	13.2
340	161.82842	-60.018887	17.1	0.2	3.6	16.3	$8.26 \cdot 10^{21}$	13.7	32.9	10.0
341	160.26763	-59.720616	21.7	0.2	5.6	16.3	$8.26 \cdot 10^{21}$	20.9	50.3	15.3
342	161.84855	-60.214534	24.7	0.2	6.8	16.3	$8.26 \cdot 10^{21}$	25.6	61.6	18.7
343	161.91101	-60.102899	22.2	0.2	5.4	16.3	$8.26 \cdot 10^{21}$	20.4	49.0	14.9
344	161.43992	-59.970936	27.2	0.2	9.0	16.3	$8.26 \cdot 10^{21}$	33.6	80.9	24.6
345	161.48539	-60.262777	19.1	0.2	5.0	16.4	$7.84 \cdot 10^{21}$	18.8	45.5	13.9
346	160.95364	-59.398568	17.5	0.2	3.9	16.4	$7.84 \cdot 10^{21}$	14.4	35.0	10.6
347	160.90892	-59.540174	16.5	0.2	2.9	16.4	$7.84 \cdot 10^{21}$	10.8	26.2	8.0
348	161.28497	-59.657179	18.2	0.2	3.3	16.4	$7.84 \cdot 10^{21}$	12.3	29.8	9.1
349	160.68726	-59.648999	15.7	0.2	2.9	16.4	$7.84 \cdot 10^{21}$	10.6	25.7	7.8
350	161.04024	-59.343090	17.5	0.2	3.6	16.4	$7.84 \cdot 10^{21}$	13.3	32.2	9.8
351	162.17092	-59.946210	21.9	0.2	4.5	16.4	$7.84 \cdot 10^{21}$	16.6	40.4	12.3
352	160.38473	-59.476808	26.8	0.2	8.9	16.4	$7.84 \cdot 10^{21}$	33.1	80.3	24.4
353	160.28269	-59.555363	22.5	0.2	5.8	16.4	$7.84 \cdot 10^{21}$	21.5	52.3	15.9
354	161.29833	-59.628496	32.7	0.2	11.5	16.4	$7.84 \cdot 10^{21}$	42.8	104.0	31.6
355	160.88069	-59.668321	28.7	0.2	8.8	16.4	$7.84 \cdot 10^{21}$	32.8	79.5	24.2
356	161.40602	-59.913600	25.6	0.2	8.7	16.4	$7.84 \cdot 10^{21}$	32.1	78.0	23.7
357	160.54996	-59.516672	20.8	0.2	5.5	16.4	$7.84 \cdot 10^{21}$	20.5	49.9	15.2
358	161.50616	-60.320113	21.4	0.2	4.5	16.4	$7.84 \cdot 10^{21}$	16.6	40.3	12.3
359	161.29832	-59.886647	22.7	0.2	7.2	16.4	$7.84 \cdot 10^{21}$	26.8	65.0	19.8
360	161.26191	-59.377089	27.4	0.2	8.6	16.4	$7.84 \cdot 10^{21}$	32.0	77.7	23.7
361	160.37772	-59.490258	19.4	0.2	4.5	16.4	$7.84 \cdot 10^{21}$	16.8	40.8	12.4

n	R.A. (deg)	Dec. (deg)	R (")	F_{max}	F_{tot}	T	N_{H_2}	M	M (10 K)	M (20 K)
362	161.03637	-59.415635	24.2	0.2	7.0	16.4	$7.84 \cdot 10^{21}$	25.9	62.8	19.1
363	161.57148	-59.979168	21.7	0.2	4.7	16.4	$7.84 \cdot 10^{21}$	17.5	42.4	12.9
364	160.95036	-59.395185	18.2	0.2	3.6	16.4	$7.84 \cdot 10^{21}$	13.3	32.2	9.8
365	161.10617	-59.387074	19.7	0.2	5.3	16.4	$7.84 \cdot 10^{21}$	19.6	47.5	14.5
366	161.22870	-59.415882	16.8	0.2	3.7	16.4	$7.84 \cdot 10^{21}$	13.9	33.7	10.3
367	161.36881	-59.824200	29.9	0.2	9.8	16.4	$7.84 \cdot 10^{21}$	36.6	88.7	27.0
368	160.29475	-59.597642	19.1	0.2	4.7	16.4	$7.84 \cdot 10^{21}$	17.4	42.3	12.9
369	160.96417	-59.673623	16.5	0.2	3.3	16.4	$7.84 \cdot 10^{21}$	12.2	29.7	9.0
370	161.30168	-59.893396	34.1	0.2	16.5	16.4	$7.84 \cdot 10^{21}$	61.3	148.9	45.3
371	161.91408	-60.086012	18.2	0.2	4.8	16.4	$7.84 \cdot 10^{21}$	17.8	43.1	13.1
372	161.98066	-60.197052	19.7	0.2	4.6	16.4	$7.84 \cdot 10^{21}$	17.1	41.5	12.6
373	161.47917	-60.369083	16.1	0.2	3.3	16.4	$7.84 \cdot 10^{21}$	12.3	29.8	9.1
374	161.51299	-60.323477	24.2	0.2	7.0	16.4	$7.84 \cdot 10^{21}$	25.9	62.9	19.1
375	161.22899	-59.279214	16.5	0.2	2.9	16.4	$7.84 \cdot 10^{21}$	10.8	26.2	8.0
376	161.49389	-59.975929	20.3	0.2	5.2	16.4	$7.84 \cdot 10^{21}$	19.4	47.2	14.4
377	160.39170	-59.588226	17.5	0.2	4.0	16.5	$7.43 \cdot 10^{21}$	14.5	35.6	10.8
378	160.98356	-59.388521	19.4	0.2	4.5	16.5	$7.43 \cdot 10^{21}$	16.6	40.7	12.4
379	160.37860	-59.701192	17.5	0.2	3.9	16.5	$7.43 \cdot 10^{21}$	14.4	35.3	10.7
380	160.93763	-59.963765	19.4	0.2	5.0	16.5	$7.43 \cdot 10^{21}$	18.2	44.6	13.6
381	161.34217	-59.989563	26.8	0.2	8.6	16.5	$7.43 \cdot 10^{21}$	31.6	77.4	23.5
382	160.78286	-59.512739	17.8	0.2	4.0	16.5	$7.43 \cdot 10^{21}$	14.8	36.2	11.0
383	161.06531	-59.545610	23.5	0.2	7.2	16.5	$7.43 \cdot 10^{21}$	26.6	65.1	19.8
384	160.95061	-59.692147	24.7	0.2	6.1	16.5	$7.43 \cdot 10^{21}$	22.3	54.7	16.7
385	160.35571	-59.326420	19.4	0.2	3.5	16.5	$7.43 \cdot 10^{21}$	13.0	31.9	9.7
386	161.11060	-59.780213	29.9	0.2	9.0	16.5	$7.43 \cdot 10^{21}$	33.1	81.1	24.7
387	161.18489	-59.621697	18.2	0.2	4.5	16.5	$7.43 \cdot 10^{21}$	16.6	40.7	12.4
388	161.93096	-60.084245	24.5	0.2	7.2	16.5	$7.43 \cdot 10^{21}$	26.5	64.9	19.8
389	161.39893	-59.793810	20.8	0.2	4.8	16.5	$7.43 \cdot 10^{21}$	17.7	43.3	13.2
390	161.35867	-59.782024	22.5	0.2	5.2	16.5	$7.43 \cdot 10^{21}$	19.3	47.3	14.4
391	162.08734	-59.973731	17.1	0.2	3.1	16.5	$7.43 \cdot 10^{21}$	11.3	27.7	8.4
392	160.80254	-59.531376	18.8	0.2	5.0	16.5	$7.43 \cdot 10^{21}$	18.5	45.3	13.8
393	161.22486	-59.653784	20.6	0.2	5.9	16.5	$7.43 \cdot 10^{21}$	21.8	53.5	16.3
394	160.20694	-59.836562	22.7	0.2	5.1	16.5	$7.43 \cdot 10^{21}$	18.7	45.9	14.0
395	161.71641	-60.240322	20.8	0.2	4.3	16.5	$7.43 \cdot 10^{21}$	15.8	38.7	11.8
396	161.23868	-59.402389	22.7	0.2	5.8	16.5	$7.43 \cdot 10^{21}$	21.2	51.9	15.8
397	160.71350	-59.293094	20.3	0.2	4.6	16.5	$7.43 \cdot 10^{21}$	17.0	41.8	12.7
398	161.94681	-60.202283	20.3	0.2	3.5	16.5	$7.43 \cdot 10^{21}$	13.1	32.0	9.7
399	161.68518	-59.896209	21.9	0.2	4.9	16.5	$7.43 \cdot 10^{21}$	18.1	44.4	13.5
400	161.40069	-60.375914	17.1	0.2	3.0	16.5	$7.43 \cdot 10^{21}$	10.9	26.6	8.1
401	160.20955	-59.654335	16.5	0.2	2.5	16.5	$7.43 \cdot 10^{21}$	9.3	22.9	7.0
402	161.72205	-59.885973	20.6	0.2	4.6	16.5	$7.43 \cdot 10^{21}$	16.8	41.2	12.5
403	160.36396	-59.507034	16.5	0.2	2.6	16.6	$7.02 \cdot 10^{21}$	9.4	23.2	7.1

n	R.A. (deg)	Dec. (deg)	R (")	F_{max}	F_{tot}	T	N_{H_2}	M	M (10 K)	M (20 K)
404	161.58657	-59.774976	16.5	0.2	2.9	16.6	$7.02 \cdot 10^{21}$	10.5	25.9	7.9
405	160.62066	-59.474875	18.5	0.2	3.8	16.6	$7.02 \cdot 10^{21}$	13.8	34.1	10.4
406	160.57343	-59.508367	24.2	0.2	6.0	16.6	$7.02 \cdot 10^{21}$	21.9	54.3	16.5
407	161.27790	-60.240969	20.8	0.2	4.4	16.6	$7.02 \cdot 10^{21}$	16.0	39.7	12.1
408	160.75241	-59.544674	25.2	0.2	7.0	16.6	$7.02 \cdot 10^{21}$	25.3	62.7	19.1
409	160.96079	-59.676988	24.0	0.2	6.0	16.6	$7.02 \cdot 10^{21}$	21.9	54.1	16.5
410	161.24113	-59.896757	24.5	0.2	5.6	16.6	$7.02 \cdot 10^{21}$	20.3	50.2	15.3
411	161.44877	-59.689153	19.4	0.2	3.6	16.6	$7.02 \cdot 10^{21}$	13.2	32.6	9.9
412	160.71045	-59.659230	25.0	0.2	6.2	16.6	$7.02 \cdot 10^{21}$	22.7	56.3	17.1
413	160.65695	-59.662353	18.8	0.2	3.7	16.6	$7.02 \cdot 10^{21}$	13.4	33.3	10.1
414	161.80533	-60.054411	21.1	0.2	4.5	16.6	$7.02 \cdot 10^{21}$	16.5	40.8	12.4
415	161.23121	-59.812389	17.8	0.2	3.6	16.6	$7.02 \cdot 10^{21}$	13.3	32.8	10.0
416	161.91374	-60.067453	20.6	0.2	4.0	16.6	$7.02 \cdot 10^{21}$	14.7	36.4	11.1
417	161.26082	-60.315204	18.5	0.2	3.3	16.6	$7.02 \cdot 10^{21}$	12.2	30.1	9.2
418	160.99819	-59.606214	20.3	0.2	4.1	16.6	$7.02 \cdot 10^{21}$	15.1	37.3	11.4
419	160.65378	-59.480105	17.8	0.2	3.1	16.6	$7.02 \cdot 10^{21}$	11.3	27.9	8.5
420	161.12756	-60.387651	19.4	0.2	3.8	16.6	$7.02 \cdot 10^{21}$	14.0	34.6	10.5
421	161.18160	-59.608196	15.7	0.2	2.7	16.6	$7.02 \cdot 10^{21}$	9.9	24.6	7.5
422	160.82536	-60.270499	17.5	0.2	2.8	16.6	$7.02 \cdot 10^{21}$	10.1	25.0	7.6
423	160.38905	-59.686078	17.5	0.2	3.5	16.8	$6.56 \cdot 10^{21}$	12.3	31.1	9.5
424	161.42292	-59.933833	16.1	0.2	2.8	16.8	$6.56 \cdot 10^{21}$	10.2	25.6	7.8
425	160.39912	-59.684460	17.8	0.2	3.5	16.8	$6.56 \cdot 10^{21}$	12.6	31.8	9.7
426	161.19807	-59.677387	15.7	0.2	3.0	16.8	$6.56 \cdot 10^{21}$	10.8	27.2	8.3
427	160.37300	-59.540847	17.8	0.2	2.9	16.8	$6.56 \cdot 10^{21}$	10.3	26.1	7.9
428	160.42033	-59.640731	16.1	0.2	2.8	16.8	$6.56 \cdot 10^{21}$	10.1	25.5	7.8
429	161.66017	-60.071757	19.1	0.2	3.5	16.8	$6.56 \cdot 10^{21}$	12.6	31.7	9.6
430	160.29467	-59.265214	17.1	0.2	2.9	16.8	$6.56 \cdot 10^{21}$	10.3	26.1	7.9
431	160.42127	-59.477059	15.7	0.2	2.3	16.8	$6.56 \cdot 10^{21}$	8.3	20.8	6.3
432	160.37107	-59.490211	18.8	0.2	3.5	16.8	$6.56 \cdot 10^{21}$	12.5	31.5	9.6
433	160.98030	-59.383451	17.1	0.2	2.7	16.8	$6.56 \cdot 10^{21}$	9.8	24.7	7.5
434	161.45843	-60.315116	20.0	0.2	4.1	16.8	$6.56 \cdot 10^{21}$	14.6	36.7	11.2
435	160.83562	-60.267160	18.8	0.2	3.7	16.8	$6.56 \cdot 10^{21}$	13.1	33.0	10.0
436	160.98642	-60.151177	19.4	0.2	4.1	16.8	$6.56 \cdot 10^{21}$	14.7	37.1	11.3
437	160.51994	-59.376444	21.4	0.2	5.5	16.8	$6.56 \cdot 10^{21}$	19.7	49.7	15.1
438	160.66538	-59.569591	21.9	0.2	5.2	16.8	$6.56 \cdot 10^{21}$	18.6	47.0	14.3
439	160.84726	-59.669897	31.4	0.2	10.0	16.8	$6.56 \cdot 10^{21}$	35.7	89.9	27.4
440	162.31666	-59.864172	21.4	0.2	4.1	16.8	$6.56 \cdot 10^{21}$	14.5	36.6	11.1
441	161.21435	-59.844437	18.5	0.2	3.4	16.8	$6.56 \cdot 10^{21}$	12.1	30.4	9.2
442	161.52292	-60.279592	17.1	0.2	3.4	16.8	$6.56 \cdot 10^{21}$	12.0	30.2	9.2
443	160.80597	-59.296854	17.1	0.2	2.8	16.8	$6.56 \cdot 10^{21}$	9.9	25.1	7.6
444	161.84882	-60.027241	21.9	0.2	4.9	16.8	$6.56 \cdot 10^{21}$	17.6	44.5	13.5
445	160.30375	-59.631460	19.7	0.2	3.2	16.8	$6.56 \cdot 10^{21}$	11.6	29.2	8.9

n	R.A. (deg)	Dec. (deg)	R (")	F_{max}	F_{tot}	T	N_{H_2}	M	M (10 K)	M (20 K)
446	161.42969	-59.940575	20.8	0.2	4.5	16.8	$6.56 \cdot 10^{21}$	16.2	40.8	12.4
447	161.50245	-60.271188	18.8	0.2	4.4	16.8	$6.56 \cdot 10^{21}$	15.6	39.3	12.0
448	161.20092	-59.842741	22.7	0.2	5.4	16.8	$6.56 \cdot 10^{21}$	19.5	49.1	14.9
449	161.15471	-59.657099	19.4	0.2	4.0	16.8	$6.56 \cdot 10^{21}$	14.4	36.4	11.1
450	162.07719	-59.972104	21.7	0.2	4.7	16.8	$6.56 \cdot 10^{21}$	16.8	42.4	12.9
451	161.38553	-59.797194	16.1	0.2	2.8	16.8	$6.56 \cdot 10^{21}$	9.9	25.1	7.6
452	160.73787	-59.418063	20.8	0.2	4.7	16.8	$6.56 \cdot 10^{21}$	16.8	42.4	12.9
453	160.81587	-59.529739	17.1	0.2	3.3	16.8	$6.56 \cdot 10^{21}$	11.8	29.8	9.1
454	160.86966	-60.265587	16.5	0.2	2.4	16.8	$6.56 \cdot 10^{21}$	8.7	21.8	6.6
455	160.69697	-59.480312	17.5	0.2	3.4	16.8	$6.56 \cdot 10^{21}$	12.3	31.0	9.4
456	161.49258	-60.328570	21.7	0.2	4.6	16.8	$6.56 \cdot 10^{21}$	16.5	41.7	12.7
457	160.96294	-59.462709	18.2	0.2	3.7	16.8	$6.56 \cdot 10^{21}$	13.1	33.0	10.0
458	160.44022	-59.645925	23.0	0.2	5.7	16.8	$6.56 \cdot 10^{21}$	20.4	51.4	15.6
459	160.61859	-59.412432	21.7	0.2	5.0	16.8	$6.56 \cdot 10^{21}$	18.0	45.4	13.8
460	161.55973	-59.771657	26.3	0.2	7.8	16.8	$6.56 \cdot 10^{21}$	27.9	70.2	21.4
461	161.26467	-59.905202	30.1	0.2	8.8	16.9	$6.18 \cdot 10^{21}$	31.3	79.6	24.2
462	160.71325	-59.498946	19.4	0.2	3.7	16.9	$6.18 \cdot 10^{21}$	13.1	33.3	10.1
463	161.35911	-60.030050	17.1	0.2	3.0	16.9	$6.18 \cdot 10^{21}$	10.6	27.1	8.2
464	160.98837	-59.585944	18.5	0.2	3.8	16.9	$6.18 \cdot 10^{21}$	13.3	33.8	10.3
465	161.68633	-59.705542	20.0	0.2	4.5	16.9	$6.18 \cdot 10^{21}$	16.0	40.8	12.4
466	161.19159	-59.614953	18.5	0.2	2.9	16.9	$6.18 \cdot 10^{21}$	10.1	25.8	7.8
467	161.80520	-60.045975	17.8	0.2	3.0	16.9	$6.18 \cdot 10^{21}$	10.7	27.3	8.3
468	161.04872	-59.538830	22.2	0.2	5.1	16.9	$6.18 \cdot 10^{21}$	18.0	45.9	14.0
469	161.40941	-59.920347	22.7	0.2	6.3	16.9	$6.18 \cdot 10^{21}$	22.2	56.5	17.2
470	160.62419	-59.630129	21.7	0.2	4.6	16.9	$6.18 \cdot 10^{21}$	16.4	41.8	12.7
471	161.19855	-59.517098	19.1	0.2	3.6	16.9	$6.18 \cdot 10^{21}$	12.9	32.8	10.0
472	161.41954	-59.930461	23.5	0.2	6.4	16.9	$6.18 \cdot 10^{21}$	22.5	57.4	17.5
473	160.27146	-59.595774	15.7	0.2	2.8	16.9	$6.18 \cdot 10^{21}$	10.1	25.6	7.8
474	161.35234	-60.021617	18.5	0.2	3.2	16.9	$6.18 \cdot 10^{21}$	11.4	28.9	8.8
475	161.20852	-59.520480	21.7	0.2	5.0	16.9	$6.18 \cdot 10^{21}$	17.8	45.2	13.7
476	161.17153	-59.625059	16.5	0.2	3.3	16.9	$6.18 \cdot 10^{21}$	11.7	29.8	9.1
477	161.19808	-59.674013	19.4	0.2	4.3	16.9	$6.18 \cdot 10^{21}$	15.4	39.1	11.9
478	160.62544	-59.567704	18.2	0.2	3.1	16.9	$6.18 \cdot 10^{21}$	11.0	28.0	8.5
479	160.39110	-59.486977	16.1	0.2	2.6	16.9	$6.18 \cdot 10^{21}$	9.2	23.5	7.2
480	161.14118	-60.396105	16.1	0.2	2.7	16.9	$6.18 \cdot 10^{21}$	9.4	24.0	7.3
481	162.34831	-59.695178	23.0	0.2	5.2	16.9	$6.18 \cdot 10^{21}$	18.3	46.5	14.2
482	160.78961	-59.506016	24.5	0.2	5.5	16.9	$6.18 \cdot 10^{21}$	19.5	49.6	15.1
483	161.14598	-59.375316	17.5	0.2	3.3	16.9	$6.18 \cdot 10^{21}$	11.6	29.5	9.0
484	161.19491	-59.620018	23.5	0.2	4.9	16.9	$6.18 \cdot 10^{21}$	17.4	44.2	13.4
485	160.34343	-59.527135	20.8	0.2	4.4	16.9	$6.18 \cdot 10^{21}$	15.4	39.3	12.0
486	160.98770	-59.658495	18.2	0.2	3.6	16.9	$6.18 \cdot 10^{21}$	12.7	32.4	9.9
487	161.79583	-59.872218	21.4	0.2	4.2	16.9	$6.18 \cdot 10^{21}$	14.8	37.6	11.4

n	R.A. (deg)	Dec. (deg)	R (")	F_{max}	F_{tot}	T	N_{H_2}	M	M (10 K)	M (20 K)
488	161.54932	-59.722746	22.5	0.2	5.5	16.9	$6.18 \cdot 10^{21}$	19.3	49.1	15.0
489	161.93711	-60.052157	20.3	0.2	3.7	16.9	$6.18 \cdot 10^{21}$	13.1	33.3	10.1
490	160.93714	-59.391774	19.7	0.2	3.4	16.9	$6.18 \cdot 10^{21}$	12.1	30.7	9.4
491	160.41476	-59.725064	21.7	0.2	4.8	16.9	$6.18 \cdot 10^{21}$	17.0	43.2	13.1
492	160.65181	-59.409227	23.0	0.2	4.7	16.9	$6.18 \cdot 10^{21}$	16.5	42.1	12.8
493	160.98426	-59.668611	21.9	0.2	4.6	16.9	$6.18 \cdot 10^{21}$	16.2	41.3	12.6
494	161.70594	-60.218419	20.3	0.2	3.8	16.9	$6.18 \cdot 10^{21}$	13.4	34.1	10.4
495	160.65825	-59.419383	20.6	0.2	4.6	16.9	$6.18 \cdot 10^{21}$	16.2	41.2	12.5
496	160.96463	-59.960461	17.8	0.2	3.1	16.9	$6.18 \cdot 10^{21}$	11.0	28.0	8.5
497	161.34898	-60.033429	21.4	0.2	4.5	16.9	$6.18 \cdot 10^{21}$	16.1	40.8	12.4
498	160.28640	-59.653264	21.9	0.2	5.3	16.9	$6.18 \cdot 10^{21}$	18.6	47.4	14.4
499	160.64486	-59.426066	21.1	0.2	4.8	16.9	$6.18 \cdot 10^{21}$	17.0	43.4	13.2
500	160.93485	-59.604366	24.5	0.2	4.8	16.9	$6.18 \cdot 10^{21}$	16.9	43.1	13.1
501	160.85928	-59.518081	19.7	0.2	3.9	16.9	$6.18 \cdot 10^{21}$	13.6	34.7	10.6
502	160.62140	-59.437757	17.8	0.2	3.2	16.9	$6.18 \cdot 10^{21}$	11.3	28.9	8.8
503	161.50920	-60.262741	16.5	0.2	2.8	16.9	$6.18 \cdot 10^{21}$	10.0	25.3	7.7
504	160.85955	-60.258805	16.8	0.2	3.2	16.9	$6.18 \cdot 10^{21}$	11.4	29.1	8.9
505	160.74666	-59.488968	22.2	0.2	4.9	16.9	$6.18 \cdot 10^{21}$	17.3	43.9	13.4
506	160.63547	-59.566067	16.8	0.2	2.7	16.9	$6.18 \cdot 10^{21}$	9.7	24.7	7.5
507	160.99257	-59.491466	16.5	0.2	2.1	17.0	$5.80 \cdot 10^{21}$	7.5	19.2	5.8
508	161.25122	-59.896761	22.5	0.2	6.0	17.0	$5.80 \cdot 10^{21}$	21.0	53.8	16.4
509	160.27442	-59.717294	21.1	0.2	4.4	17.0	$5.80 \cdot 10^{21}$	15.6	40.0	12.2
510	160.50605	-59.545098	16.5	0.2	2.2	17.0	$5.80 \cdot 10^{21}$	7.8	19.9	6.1
511	160.64709	-59.653868	20.6	0.2	4.0	17.0	$5.80 \cdot 10^{21}$	13.9	35.6	10.8
512	161.20816	-59.652086	23.3	0.2	6.0	17.0	$5.80 \cdot 10^{21}$	20.9	53.7	16.4
513	161.71086	-59.796581	17.1	0.2	2.9	17.0	$5.80 \cdot 10^{21}$	10.3	26.5	8.1
514	161.43085	-60.235845	25.0	0.2	7.3	17.0	$5.80 \cdot 10^{21}$	25.7	66.1	20.1
515	161.71875	-59.891045	16.1	0.2	2.5	17.0	$5.80 \cdot 10^{21}$	8.7	22.3	6.8
516	160.67531	-59.573013	21.1	0.2	4.4	17.0	$5.80 \cdot 10^{21}$	15.4	39.6	12.0
517	161.37551	-59.815760	21.7	0.2	5.1	17.0	$5.80 \cdot 10^{21}$	17.8	45.7	13.9
518	161.68691	-59.756159	18.5	0.2	3.1	17.0	$5.80 \cdot 10^{21}$	10.9	28.0	8.5
519	161.43458	-60.315143	20.3	0.2	4.4	17.0	$5.80 \cdot 10^{21}$	15.3	39.4	12.0
520	160.87780	-59.632878	21.4	0.2	4.9	17.0	$5.80 \cdot 10^{21}$	17.1	43.8	13.3
521	160.76668	-59.483990	24.7	0.2	7.2	17.0	$5.80 \cdot 10^{21}$	25.4	65.3	19.9
522	161.06743	-59.721090	22.7	0.2	4.2	17.0	$5.80 \cdot 10^{21}$	14.9	38.3	11.7
523	160.66824	-59.594914	22.2	0.2	4.7	17.0	$5.80 \cdot 10^{21}$	16.6	42.7	13.0
524	160.65832	-59.416009	17.8	0.2	3.6	17.0	$5.80 \cdot 10^{21}$	12.7	32.7	10.0
525	160.59217	-59.565840	18.2	0.2	3.5	17.0	$5.80 \cdot 10^{21}$	12.4	31.8	9.7
526	161.79924	-59.651168	21.7	0.2	4.4	17.0	$5.80 \cdot 10^{21}$	15.3	39.3	12.0
527	161.42294	-59.937207	15.7	0.2	2.3	17.0	$5.80 \cdot 10^{21}$	8.2	21.0	6.4
528	161.75620	-59.678321	21.7	0.2	3.4	17.0	$5.80 \cdot 10^{21}$	11.8	30.4	9.2
529	161.77902	-59.872280	21.7	0.2	4.1	17.0	$5.80 \cdot 10^{21}$	14.4	37.0	11.3

n	R.A. (deg)	Dec. (deg)	R (")	F_{max}	F_{tot}	T	N_{H_2}	M	M (10 K)	M (20 K)
530	161.74426	-59.786349	18.5	0.2	3.0	17.0	$5.80 \cdot 10^{21}$	10.6	27.3	8.3
531	161.24210	-59.338275	21.9	0.2	4.3	17.0	$5.80 \cdot 10^{21}$	15.1	38.8	11.8
532	160.95345	-59.417128	18.5	0.2	3.3	17.0	$5.80 \cdot 10^{21}$	11.5	29.5	9.0
533	161.60732	-59.844107	24.2	0.2	5.0	17.0	$5.80 \cdot 10^{21}$	17.6	45.2	13.7
534	161.33487	-59.461453	17.5	0.2	3.1	17.0	$5.80 \cdot 10^{21}$	10.9	28.0	8.5
535	162.03947	-60.245673	16.5	0.2	2.2	17.0	$5.80 \cdot 10^{21}$	7.8	19.9	6.1
536	161.10611	-59.397197	16.1	0.2	2.3	17.0	$5.80 \cdot 10^{21}$	8.1	20.9	6.4
537	160.90348	-59.719010	17.5	0.2	2.4	17.1	$5.43 \cdot 10^{21}$	8.3	21.5	6.5
538	161.17584	-59.361850	24.2	0.2	5.8	17.1	$5.43 \cdot 10^{21}$	20.2	52.5	16.0
539	160.85385	-59.676669	15.7	0.2	2.0	17.1	$5.43 \cdot 10^{21}$	7.1	18.4	5.6
540	161.15245	-59.412444	19.7	0.2	3.4	17.1	$5.43 \cdot 10^{21}$	11.8	30.6	9.3
541	160.61930	-60.035067	24.7	0.2	5.0	17.1	$5.43 \cdot 10^{21}$	17.3	44.7	13.6
542	160.66189	-59.578010	23.0	0.2	4.9	17.1	$5.43 \cdot 10^{21}$	17.0	44.1	13.4
543	160.38869	-59.576393	18.5	0.2	3.1	17.1	$5.43 \cdot 10^{21}$	10.9	28.1	8.6
544	160.40739	-59.750325	19.4	0.2	3.5	17.1	$5.43 \cdot 10^{21}$	12.2	31.6	9.6
545	161.15593	-59.373640	18.2	0.2	3.0	17.1	$5.43 \cdot 10^{21}$	10.4	27.1	8.2
546	160.46198	-59.576883	16.1	0.2	2.2	17.1	$5.43 \cdot 10^{21}$	7.5	19.6	6.0
547	160.97629	-59.455994	18.5	0.2	3.3	17.1	$5.43 \cdot 10^{21}$	11.4	29.6	9.0
548	161.28503	-59.522198	23.3	0.2	4.9	17.1	$5.43 \cdot 10^{21}$	17.0	44.0	13.4
549	161.40066	-60.365790	16.5	0.2	2.4	17.1	$5.43 \cdot 10^{21}$	8.5	21.9	6.7
550	161.46711	-59.343242	23.5	0.2	4.3	17.1	$5.43 \cdot 10^{21}$	14.9	38.7	11.8
551	160.92445	-59.639769	16.8	0.2	2.5	17.1	$5.43 \cdot 10^{21}$	8.5	22.1	6.7
552	160.46096	-59.484070	19.4	0.2	2.8	17.1	$5.43 \cdot 10^{21}$	9.8	25.4	7.7
553	160.71063	-59.649107	20.0	0.2	3.3	17.1	$5.43 \cdot 10^{21}$	11.5	29.8	9.1
554	161.25060	-60.315201	17.5	0.2	2.5	17.1	$5.43 \cdot 10^{21}$	8.8	22.7	6.9
555	160.89811	-59.609320	19.4	0.2	3.1	17.3	$5.02 \cdot 10^{21}$	10.8	28.4	8.6
556	160.83934	-59.516325	16.1	0.2	2.2	17.3	$5.02 \cdot 10^{21}$	7.4	19.7	6.0
557	161.18803	-59.682441	17.8	0.2	2.6	17.3	$5.02 \cdot 10^{21}$	9.0	23.7	7.2
558	161.72417	-59.788103	17.8	0.2	2.9	17.3	$5.02 \cdot 10^{21}$	10.0	26.3	8.0
559	160.51265	-59.405085	19.1	0.2	3.5	17.3	$5.02 \cdot 10^{21}$	11.9	31.4	9.5
560	162.02565	-60.082075	20.8	0.2	3.9	17.3	$5.02 \cdot 10^{21}$	13.2	34.8	10.6
561	160.48725	-59.634413	17.8	0.2	2.7	17.3	$5.02 \cdot 10^{21}$	9.1	24.0	7.3
562	161.63590	-60.345160	18.5	0.2	2.7	17.3	$5.02 \cdot 10^{21}$	9.3	24.6	7.5
563	160.55939	-59.390173	15.7	0.2	2.2	17.3	$5.02 \cdot 10^{21}$	7.5	19.8	6.0
564	160.43021	-59.387687	19.7	0.2	3.3	17.3	$5.02 \cdot 10^{21}$	11.1	29.4	8.9
565	160.73133	-59.412973	16.5	0.2	2.6	17.3	$5.02 \cdot 10^{21}$	8.8	23.3	7.1
566	160.43051	-59.634050	18.5	0.2	2.8	17.3	$5.02 \cdot 10^{21}$	9.6	25.2	7.7
567	160.37883	-59.571262	20.0	0.2	3.5	17.3	$5.02 \cdot 10^{21}$	12.1	31.9	9.7
568	161.01003	-59.393644	16.1	0.2	2.2	17.3	$5.02 \cdot 10^{21}$	7.5	19.9	6.1
569	161.25207	-59.309596	15.7	0.2	2.2	17.3	$5.02 \cdot 10^{21}$	7.4	19.6	6.0
570	162.36147	-59.688322	17.8	0.2	2.4	17.3	$5.02 \cdot 10^{21}$	8.3	22.0	6.7
571	160.50926	-59.408439	18.5	0.2	2.5	17.3	$5.02 \cdot 10^{21}$	8.6	22.6	6.9

n	R.A. (deg)	Dec. (deg)	R (")	F_{max}	F_{tot}	T	N_{H_2}	M	M (10 K)	M (20 K)
572	160.99620	-59.457729	15.7	0.2	1.8	17.3	$5.02 \cdot 10^{21}$	6.1	16.2	4.9
573	160.46968	-59.399756	18.2	0.2	2.9	17.3	$5.02 \cdot 10^{21}$	9.9	26.2	8.0
574	161.36923	-60.026671	18.2	0.2	2.9	17.3	$5.02 \cdot 10^{21}$	9.7	25.7	7.8
575	161.69952	-59.690317	19.1	0.1	2.9	17.4	$4.66 \cdot 10^{21}$	9.9	26.3	8.0
576	161.28510	-59.375407	17.1	0.1	2.4	17.4	$4.66 \cdot 10^{21}$	8.2	21.8	6.6
577	160.25456	-59.710388	17.8	0.1	3.0	17.4	$4.66 \cdot 10^{21}$	10.0	26.6	8.1
578	161.77928	-59.656304	21.1	0.1	3.7	17.4	$4.66 \cdot 10^{21}$	12.7	33.7	10.3
579	161.44317	-59.942249	21.4	0.1	3.7	17.4	$4.66 \cdot 10^{21}$	12.4	33.0	10.0
580	161.21442	-59.819129	25.4	0.1	5.5	17.4	$4.66 \cdot 10^{21}$	18.7	49.7	15.1
581	160.73706	-59.466992	20.0	0.1	3.1	17.4	$4.66 \cdot 10^{21}$	10.5	28.0	8.5
582	161.59004	-59.788466	17.1	0.1	2.8	17.4	$4.66 \cdot 10^{21}$	9.3	24.9	7.6
583	161.35552	-59.906882	15.7	0.1	2.1	17.4	$4.66 \cdot 10^{21}$	7.1	18.9	5.8
584	161.27111	-60.232531	17.8	0.1	2.5	17.4	$4.66 \cdot 10^{21}$	8.3	22.2	6.8
585	161.17802	-59.677370	20.0	0.1	3.8	17.4	$4.66 \cdot 10^{21}$	12.7	33.9	10.3
586	161.82196	-59.608897	16.5	0.1	2.3	17.4	$4.66 \cdot 10^{21}$	7.9	21.0	6.4
587	160.29263	-59.557127	16.1	0.1	2.2	17.4	$4.66 \cdot 10^{21}$	7.3	19.6	6.0
588	160.82524	-60.278935	19.1	0.1	2.8	17.4	$4.66 \cdot 10^{21}$	9.5	25.4	7.7
589	161.44641	-59.913562	18.5	0.1	3.1	17.4	$4.66 \cdot 10^{21}$	10.4	27.7	8.4
590	160.64522	-59.407507	16.1	0.1	2.3	17.4	$4.66 \cdot 10^{21}$	7.7	20.4	6.2
591	161.32187	-59.898456	25.0	0.1	5.2	17.4	$4.66 \cdot 10^{21}$	17.7	47.1	14.3
592	161.24201	-59.392267	22.2	0.1	4.4	17.4	$4.66 \cdot 10^{21}$	14.9	39.7	12.1
593	160.99898	-59.518478	17.1	0.1	2.5	17.4	$4.66 \cdot 10^{21}$	8.5	22.5	6.9
594	161.33883	-60.023309	17.1	0.1	2.1	17.4	$4.66 \cdot 10^{21}$	7.0	18.7	5.7
595	161.57609	-59.722693	15.7	0.1	2.0	17.4	$4.66 \cdot 10^{21}$	6.9	18.4	5.6
596	161.60510	-60.333422	19.7	0.1	3.4	17.4	$4.66 \cdot 10^{21}$	11.5	30.7	9.4
597	161.32482	-59.343347	15.7	0.1	1.7	17.4	$4.66 \cdot 10^{21}$	5.7	15.1	4.6
598	161.44302	-59.908504	17.8	0.1	2.8	17.4	$4.66 \cdot 10^{21}$	9.4	25.0	7.6
599	160.71372	-59.471951	18.8	0.1	3.0	17.4	$4.66 \cdot 10^{21}$	10.2	27.1	8.3
600	160.22601	-60.078028	16.1	0.1	1.8	17.4	$4.66 \cdot 10^{21}$	6.0	16.0	4.9
601	160.40730	-59.753700	16.1	0.1	2.1	17.4	$4.66 \cdot 10^{21}$	7.1	18.9	5.8
602	161.49555	-60.256013	15.7	0.1	2.2	17.4	$4.66 \cdot 10^{21}$	7.4	19.7	6.0
603	161.22547	-59.377073	18.5	0.1	3.0	17.4	$4.66 \cdot 10^{21}$	10.0	26.7	8.1
604	161.71277	-59.680152	17.8	0.1	2.7	17.4	$4.66 \cdot 10^{21}$	9.0	24.1	7.3
605	161.22744	-60.001360	19.1	0.1	3.0	17.4	$4.66 \cdot 10^{21}$	10.1	27.0	8.2
606	161.73102	-59.799892	15.7	0.1	2.0	17.4	$4.66 \cdot 10^{21}$	6.9	18.5	5.6
607	161.16604	-60.163290	16.1	0.1	1.9	17.4	$4.66 \cdot 10^{21}$	6.4	17.0	5.2
608	160.84264	-60.251999	15.7	0.1	2.0	17.4	$4.66 \cdot 10^{21}$	6.9	18.4	5.6
609	161.34561	-60.041867	21.7	0.1	3.3	17.4	$4.66 \cdot 10^{21}$	11.1	29.7	9.0
610	161.73966	-59.691876	18.2	0.1	2.8	17.4	$4.66 \cdot 10^{21}$	9.4	25.1	7.6
611	161.22441	-59.852880	22.5	0.1	4.6	17.4	$4.66 \cdot 10^{21}$	15.7	41.8	12.7
612	162.00798	-59.731200	17.8	0.1	2.4	17.4	$4.66 \cdot 10^{21}$	8.0	21.3	6.5
613	161.03556	-59.518557	22.5	0.1	4.3	17.4	$4.66 \cdot 10^{21}$	14.7	39.2	11.9

n	R.A. (deg)	Dec. (deg)	R (")	F_{max}	F_{tot}	T	N_{H_2}	M	M (10 K)	M (20 K)
614	161.04559	-59.511828	17.1	0.1	2.4	17.4	$4.66 \cdot 10^{21}$	8.2	21.8	6.6
615	161.55062	-60.341972	17.8	0.1	3.0	17.4	$4.66 \cdot 10^{21}$	10.1	26.9	8.2
616	161.25464	-59.854581	24.2	0.1	4.8	17.4	$4.66 \cdot 10^{21}$	16.2	43.2	13.1
617	161.17492	-59.611564	16.8	0.1	2.7	17.4	$4.66 \cdot 10^{21}$	9.2	24.5	7.5
618	161.23454	-59.824202	25.4	0.1	5.6	17.4	$4.66 \cdot 10^{21}$	19.0	50.5	15.4
619	160.21925	-60.077973	16.1	0.1	2.0	17.6	$4.27 \cdot 10^{21}$	6.8	18.4	5.6
620	161.91657	-59.311515	16.8	0.1	2.2	17.6	$4.27 \cdot 10^{21}$	7.4	19.9	6.1
621	160.40481	-59.721622	15.7	0.1	1.8	17.6	$4.27 \cdot 10^{21}$	5.9	15.9	4.8
622	161.75386	-59.752571	19.7	0.1	3.0	17.6	$4.27 \cdot 10^{21}$	9.8	26.6	8.1
623	161.84813	-60.189226	18.5	0.1	2.6	17.6	$4.27 \cdot 10^{21}$	8.7	23.7	7.2
624	161.77554	-60.098391	17.1	0.1	2.2	17.6	$4.27 \cdot 10^{21}$	7.3	19.8	6.0
625	160.44750	-59.490732	16.1	0.1	2.2	17.6	$4.27 \cdot 10^{21}$	7.3	19.7	6.0
626	161.05636	-59.402176	20.3	0.1	3.7	17.6	$4.27 \cdot 10^{21}$	12.2	33.2	10.1
627	161.57315	-59.773317	16.1	0.1	2.1	17.6	$4.27 \cdot 10^{21}$	6.9	18.7	5.7
628	161.78807	-59.801380	16.1	0.1	2.1	17.6	$4.27 \cdot 10^{21}$	7.1	19.1	5.8
629	161.29503	-59.372033	18.5	0.1	2.5	17.6	$4.27 \cdot 10^{21}$	8.4	22.9	7.0
630	161.13205	-59.513655	16.5	0.1	1.9	17.6	$4.27 \cdot 10^{21}$	6.3	17.1	5.2
631	161.47708	-59.984389	25.2	0.1	5.5	17.6	$4.27 \cdot 10^{21}$	18.2	49.3	15.0
632	161.77510	-60.068021	17.1	0.1	2.0	17.6	$4.27 \cdot 10^{21}$	6.5	17.7	5.4
633	161.59337	-59.785084	16.8	0.1	2.1	17.6	$4.27 \cdot 10^{21}$	7.2	19.4	5.9
634	160.50290	-59.396589	17.5	0.1	2.6	17.6	$4.27 \cdot 10^{21}$	8.8	23.8	7.2
635	160.92433	-59.649893	15.7	0.1	1.9	17.6	$4.27 \cdot 10^{21}$	6.4	17.2	5.2
636	160.90138	-59.614392	18.5	0.1	3.0	17.6	$4.27 \cdot 10^{21}$	10.1	27.3	8.3
637	160.42238	-59.689680	16.8	0.1	2.5	17.6	$4.27 \cdot 10^{21}$	8.3	22.5	6.9
638	160.93751	-59.666803	19.7	0.1	3.5	17.6	$4.27 \cdot 10^{21}$	11.8	32.0	9.7
639	160.49300	-59.394841	15.7	0.1	2.0	17.6	$4.27 \cdot 10^{21}$	6.8	18.4	5.6
640	161.25401	-60.310141	17.1	0.1	2.1	17.6	$4.27 \cdot 10^{21}$	7.2	19.4	5.9
641	160.64735	-59.640370	18.8	0.1	2.9	17.6	$4.27 \cdot 10^{21}$	9.7	26.2	8.0
642	161.01661	-59.398721	16.5	0.1	2.4	17.6	$4.27 \cdot 10^{21}$	8.1	21.9	6.7
643	161.18746	-59.851166	16.1	0.1	1.9	17.6	$4.27 \cdot 10^{21}$	6.4	17.2	5.2
644	161.21521	-59.508673	20.8	0.1	3.1	17.6	$4.27 \cdot 10^{21}$	10.3	27.9	8.5
645	161.15486	-59.623354	17.1	0.1	2.3	17.8	$3.90 \cdot 10^{21}$	7.6	21.0	6.4
646	161.30170	-60.217349	16.8	0.1	1.9	17.8	$3.90 \cdot 10^{21}$	6.3	17.3	5.3
647	160.66785	-59.437990	16.1	0.1	1.8	17.8	$3.90 \cdot 10^{21}$	5.9	16.4	5.0
648	160.26553	-59.680100	15.7	0.1	1.8	17.8	$3.90 \cdot 10^{21}$	5.8	15.9	4.8
649	161.97166	-60.089108	17.5	0.1	2.4	17.8	$3.90 \cdot 10^{21}$	7.8	21.6	6.6
650	161.89875	-59.613630	16.5	0.1	2.1	17.8	$3.90 \cdot 10^{21}$	7.0	19.3	5.9
651	161.41095	-60.379280	16.8	0.1	2.2	17.8	$3.90 \cdot 10^{21}$	7.3	20.1	6.1
652	162.18588	-60.253219	18.2	0.1	2.3	17.8	$3.90 \cdot 10^{21}$	7.6	21.0	6.4
653	160.78650	-59.927831	18.5	0.1	2.4	17.8	$3.90 \cdot 10^{21}$	7.9	21.9	6.7
654	161.33169	-59.616682	17.8	0.1	2.3	17.8	$3.90 \cdot 10^{21}$	7.4	20.5	6.2
655	161.32814	-59.355157	15.7	0.1	1.8	17.8	$3.90 \cdot 10^{21}$	5.9	16.2	4.9

n	R.A. (deg)	Dec. (deg)	R (")	F_{max}	F_{tot}	T	N_{H_2}	M	M (10 K)	M (20 K)
656	160.95477	-59.936814	18.8	0.1	2.4	17.8	$3.90 \cdot 10^{21}$	7.9	21.9	6.7
657	161.38698	-60.353989	16.5	0.1	1.8	17.8	$3.90 \cdot 10^{21}$	5.9	16.1	4.9
658	161.85735	-59.731925	16.8	0.1	1.9	17.9	$3.57 \cdot 10^{21}$	6.1	16.9	5.1
659	161.43035	-60.109301	16.8	0.1	1.9	17.9	$3.57 \cdot 10^{21}$	6.2	17.2	5.2
660	161.39596	-59.927106	17.5	0.1	2.1	17.9	$3.57 \cdot 10^{21}$	6.7	18.8	5.7
661	160.85977	-60.241932	16.1	0.1	1.7	17.9	$3.57 \cdot 10^{21}$	5.6	15.6	4.7
662	161.45927	-59.788689	16.1	0.1	1.8	17.9	$3.57 \cdot 10^{21}$	5.7	15.9	4.8
663	160.54399	-59.486265	16.5	0.1	2.0	17.9	$3.57 \cdot 10^{21}$	6.4	17.7	5.4
664	160.17196	-60.273331	15.7	0.1	1.7	17.9	$3.57 \cdot 10^{21}$	5.6	15.6	4.7
665	162.17251	-59.878703	18.2	0.1	2.5	17.9	$3.57 \cdot 10^{21}$	8.3	23.0	7.0
666	161.12866	-59.527148	19.1	0.1	2.5	17.9	$3.57 \cdot 10^{21}$	8.2	22.7	6.9
667	161.28132	-60.212286	16.5	0.1	1.9	17.9	$3.57 \cdot 10^{21}$	6.1	17.0	5.2
668	162.05504	-59.887864	16.1	0.1	1.7	17.9	$3.57 \cdot 10^{21}$	5.5	15.4	4.7
669	161.16269	-60.154850	18.5	0.1	2.2	17.9	$3.57 \cdot 10^{21}$	7.3	20.3	6.2
670	161.27794	-60.181915	19.4	0.1	2.5	17.9	$3.57 \cdot 10^{21}$	8.1	22.6	6.9
671	161.08384	-59.770048	16.5	0.1	1.8	17.9	$3.57 \cdot 10^{21}$	5.9	16.4	5.0
672	161.19485	-59.638578	16.5	0.1	1.9	17.9	$3.57 \cdot 10^{21}$	6.1	17.0	5.2
673	161.35908	-60.014865	17.5	0.1	1.9	18.1	$3.22 \cdot 10^{21}$	6.2	17.5	5.3
674	161.14304	-60.009724	17.1	0.1	2.0	18.1	$3.22 \cdot 10^{21}$	6.5	18.5	5.6
675	161.54717	-60.336916	15.7	0.1	1.6	18.1	$3.22 \cdot 10^{21}$	5.2	14.7	4.5
676	161.00666	-60.163034	18.5	0.1	2.3	18.1	$3.22 \cdot 10^{21}$	7.2	20.5	6.2
677	161.30497	-59.361909	16.1	0.1	1.7	18.1	$3.22 \cdot 10^{21}$	5.5	15.6	4.7
678	161.79468	-59.794606	18.2	0.1	2.1	18.1	$3.22 \cdot 10^{21}$	6.7	18.8	5.7
679	161.19831	-59.599773	16.1	0.1	1.7	18.1	$3.22 \cdot 10^{21}$	5.5	15.7	4.8
680	161.10874	-59.518684	15.7	0.1	1.7	18.1	$3.22 \cdot 10^{21}$	5.4	15.4	4.7
681	160.78303	-59.934567	16.1	0.1	1.6	18.1	$3.22 \cdot 10^{21}$	5.3	14.9	4.5
682	161.37450	-59.363575	17.8	0.1	2.1	18.4	$2.85 \cdot 10^{21}$	6.5	18.8	5.7
683	160.54705	-59.498094	16.8	0.1	2.0	18.4	$2.85 \cdot 10^{21}$	6.2	17.9	5.4
684	160.80480	-60.280548	17.5	0.1	2.1	18.4	$2.85 \cdot 10^{21}$	6.5	18.8	5.7
685	160.93786	-59.943518	16.1	0.1	1.7	18.4	$2.85 \cdot 10^{21}$	5.2	15.1	4.6
686	161.22842	-59.550863	21.9	0.1	3.0	18.4	$2.85 \cdot 10^{21}$	9.5	27.5	8.4
687	160.91582	-60.100373	16.5	0.1	1.7	18.4	$2.85 \cdot 10^{21}$	5.3	15.3	4.7
688	161.42182	-59.631814	18.5	0.1	2.2	18.4	$2.85 \cdot 10^{21}$	6.7	19.6	6.0

Table A.2: Properties of the GAUSSCLUMPS sample

n	R.A. (deg) (J2000)	Dec. (deg) (J2000)	F_{max} [Jy/beam]	F_{tot} [Jy/beam]	T [K]	N_{H_2} [cm^{-2}]	M [$M_\odot$]	M (10 K) [$M_\odot$]	M (20 K) [$M_\odot$]
2	160.8319269510	-59.5719832902	4.0	357.7	8.6	$4.55\cdot10^{23}$	4458.2	3225.9	981.7
3	160.8719246793	-59.5704326418	4.1	97.9	8.5	$4.79\cdot10^{23}$	1253.1	883.0	268.7
4	161.4802397983	-59.9455776270	3.4	148.4	9.2	$3.36\cdot10^{23}$	1594.0	1338.1	407.2
5	160.6980078339	-59.4229592369	2.7	49.2	10.0	$2.22\cdot10^{23}$	443.4	443.4	134.9
6	160.8817290940	-59.5856495158	2.2	223.6	10.5	$1.67\cdot10^{23}$	1827.6	2016.5	613.6
7	160.8486743923	-59.5652929655	3.7	21.2	8.9	$3.92\cdot10^{23}$	244.6	191.0	58.1
8	161.5162757667	-59.7886082300	1.9	135.2	11.0	$1.31\cdot10^{23}$	1008.6	1219.0	371.0
9	160.8383343724	-59.5905658047	1.7	202.9	11.3	$1.12\cdot10^{23}$	1437.6	1829.5	556.8
10	161.1252169070	-59.5490806353	1.7	85.3	11.3	$1.12\cdot10^{23}$	604.5	769.3	234.1
11	160.6943882720	-59.4398147949	1.8	60.0	11.1	$1.23\cdot10^{23}$	439.9	541.0	164.6
12	160.8230118259	-59.4960251845	1.6	35.5	11.5	$9.95\cdot10^{22}$	243.1	319.9	97.3
13	161.2849025200	-59.8073447006	1.2	111.9	12.3	$6.64\cdot10^{22}$	677.1	1008.9	307.0
14	160.7952824894	-59.5718474374	1.2	132.9	12.4	$6.41\cdot10^{22}$	792.4	1198.3	364.6
15	160.8887460814	-59.5569884851	1.3	36.1	12.1	$7.40\cdot10^{22}$	225.3	325.8	99.2
16	161.4310645133	-60.2898262894	1.1	156.1	12.5	$6.09\cdot10^{22}$	917.2	1407.2	428.2
17	161.1871852137	-59.9321543551	1.5	19.6	11.7	$9.15\cdot10^{22}$	130.0	176.6	53.8
18	160.7910500924	-59.4115438487	1.3	39.1	12.2	$7.09\cdot10^{22}$	240.4	352.9	107.4
19	161.4950440363	-60.1716456203	1.1	107.8	12.5	$5.95\cdot10^{22}$	633.6	972.1	295.8
20	160.9650287482	-59.9216543352	1.3	25.1	12.0	$7.70\cdot10^{22}$	158.8	226.2	68.8
21	161.4377244842	-60.2543893027	1.1	67.5	12.6	$5.78\cdot10^{22}$	390.8	608.3	185.1
22	161.4836927761	-59.9607581518	1.1	101.8	12.6	$5.72\cdot10^{22}$	590.0	918.4	279.5
23	161.4894990085	-59.7970857722	1.2	52.4	12.3	$6.55\cdot10^{22}$	316.9	472.2	143.7
24	161.2580837796	-59.7904663206	1.0	68.0	12.7	$5.45\cdot10^{22}$	388.4	613.2	186.6
25	162.0570614585	-59.9772787028	1.2	20.8	12.4	$6.41\cdot10^{22}$	123.8	187.1	56.9
26	161.2319937145	-59.4293881502	1.1	32.0	12.6	$5.70\cdot10^{22}$	185.1	288.1	87.7
27	161.6850547774	-60.1762921885	1.1	25.9	12.5	$6.05\cdot10^{22}$	152.3	233.7	71.1
28	160.3265925150	-59.5354602510	1.0	44.6	12.7	$5.32\cdot10^{22}$	254.6	401.9	122.3
29	160.7791234770	-59.5397264096	0.9	84.5	13.1	$4.42\cdot10^{22}$	456.9	762.1	231.9
30	161.9065281375	-60.0438588941	1.0	52.9	12.9	$4.89\cdot10^{22}$	293.9	477.0	145.2
31	161.0090763815	-59.5050065836	1.0	38.8	12.8	$5.09\cdot10^{22}$	218.3	349.5	106.4
32	161.4194104355	-59.8933416868	0.9	41.7	13.0	$4.64\cdot10^{22}$	228.7	376.3	114.5
33	160.8614682319	-59.6058304531	0.9	74.5	13.1	$4.33\cdot10^{22}$	402.7	671.8	204.4
34	161.3455205454	-59.9743758993	0.9	40.1	13.0	$4.62\cdot10^{22}$	219.8	361.7	110.1
35	161.1499511062	-59.9742986120	0.8	49.3	13.3	$3.98\cdot10^{22}$	259.5	444.5	135.3
36	161.4948844566	-60.1446505894	0.8	92.0	13.5	$3.62\cdot10^{22}$	471.7	829.2	252.3
37	161.5262434375	-59.7750933818	0.8	49.2	13.5	$3.58\cdot10^{22}$	252.5	443.9	135.1
38	160.8624588715	-59.5299075433	0.7	31.5	13.6	$3.35\cdot10^{22}$	159.7	284.3	86.5
39	160.9866987605	-59.4087844647	0.7	42.5	13.7	$3.19\cdot10^{22}$	212.3	382.9	116.5
40	161.2484412525	-59.5205042918	0.7	52.6	13.8	$3.08\cdot10^{22}$	259.5	473.9	144.2
41	161.2382669623	-59.6267951834	0.7	16.6	13.6	$3.40\cdot10^{22}$	83.9	149.4	45.5
42	161.0224590678	-59.4949123231	0.7	20.3	13.5	$3.51\cdot10^{22}$	104.2	183.2	55.8

n	R.A. (deg)	Dec. (deg)	F_{max}	F_{tot}	T	N_{H_2}	M	M (10 K)	M (20 K)
43	160.8651311421	-59.5805338061	0.8	11.4	13.2	$4.12 \cdot 10^{22}$	61.1	103.2	31.4
44	161.4667979175	-59.9523442856	0.9	9.8	13.1	$4.40 \cdot 10^{22}$	53.0	88.4	26.9
45	161.5431249631	-59.7919359534	0.7	22.9	13.8	$3.04 \cdot 10^{22}$	113.2	206.6	62.9
46	161.3586826985	-59.7904599203	0.6	30.2	14.0	$2.79 \cdot 10^{22}$	145.4	272.1	82.8
47	160.9851554060	-59.5741277130	0.6	44.0	13.9	$2.86 \cdot 10^{22}$	214.8	397.1	120.8
48	161.0886809059	-59.5355290600	0.6	62.1	14.1	$2.57 \cdot 10^{22}$	295.8	560.3	170.5
49	161.4912506931	-60.1024754946	0.6	22.6	13.9	$2.89 \cdot 10^{22}$	110.5	204.2	62.1
50	161.4651155556	-60.2914755519	0.6	48.5	14.3	$2.38 \cdot 10^{22}$	225.4	437.3	133.1
51	161.1937422479	-59.9878390153	0.6	71.1	14.1	$2.64 \cdot 10^{22}$	338.5	641.2	195.1
52	160.8918914277	-59.5721835187	0.7	10.4	13.5	$3.50 \cdot 10^{22}$	53.3	93.6	28.5
53	160.8512834975	-59.6192941285	0.6	36.1	14.1	$2.62 \cdot 10^{22}$	171.7	325.3	99.0
54	160.2985255045	-59.6955482404	0.6	62.2	14.3	$2.38 \cdot 10^{22}$	289.2	561.0	170.7
55	160.8323265613	-59.5433014626	0.6	40.5	14.3	$2.40 \cdot 10^{22}$	188.2	365.2	111.1
56	161.4858629121	-59.7464731183	0.5	53.9	14.4	$2.22 \cdot 10^{22}$	247.5	485.8	147.8
57	160.4020301198	-59.7013577842	0.6	44.0	14.2	$2.43 \cdot 10^{22}$	206.7	396.3	120.6
58	161.4649969060	-60.2678555586	0.6	49.2	14.3	$2.37 \cdot 10^{22}$	228.7	443.6	135.0
59	161.7583975653	-60.0832613190	0.6	24.3	14.1	$2.58 \cdot 10^{22}$	115.7	219.1	66.7
60	160.7965477217	-59.4874899837	0.5	33.6	14.3	$2.34 \cdot 10^{22}$	156.2	303.1	92.2
61	160.7720696390	-59.5650070417	0.5	30.9	14.3	$2.32 \cdot 10^{22}$	143.8	279.0	84.9
62	161.4788251008	-60.3083292771	0.6	23.2	14.3	$2.35 \cdot 10^{22}$	107.9	209.4	63.7
63	161.3251586451	-59.8022813903	0.5	29.0	14.5	$2.15 \cdot 10^{22}$	131.8	261.7	79.6
64	160.6815490871	-59.4161335688	0.5	19.3	14.4	$2.25 \cdot 10^{22}$	88.8	174.3	53.0
65	161.3318482734	-59.7820328510	0.6	18.6	14.2	$2.44 \cdot 10^{22}$	87.6	167.8	51.1
66	161.8214205572	-60.0037268204	0.5	28.7	14.5	$2.15 \cdot 10^{22}$	130.2	258.5	78.7
67	161.4534207631	-59.9742947434	0.5	33.6	14.4	$2.22 \cdot 10^{22}$	154.2	302.6	92.1
68	162.1012322790	-60.1305637797	0.6	17.7	14.3	$2.40 \cdot 10^{22}$	82.1	159.3	48.5
69	161.4162828218	-59.9608346237	0.6	11.4	14.0	$2.75 \cdot 10^{22}$	54.7	102.4	31.1
70	161.0247614606	-59.6197723061	0.6	17.9	14.2	$2.46 \cdot 10^{22}$	84.3	161.7	49.2
71	161.1351878988	-59.5524679936	0.6	8.8	14.1	$2.62 \cdot 10^{22}$	41.9	79.4	24.2
72	161.2148871199	-59.6352183163	0.5	19.5	14.6	$1.98 \cdot 10^{22}$	87.6	176.0	53.5
74	160.2761050343	-59.6633153581	0.5	34.7	14.7	$1.89 \cdot 10^{22}$	154.2	313.3	95.3
75	161.5047068179	-60.0889576085	0.6	12.2	14.2	$2.52 \cdot 10^{22}$	57.3	109.8	33.4
76	161.2478947200	-59.8731383265	0.5	81.2	14.7	$1.90 \cdot 10^{22}$	360.6	732.6	222.9
77	161.2647547098	-59.8242134344	0.5	48.9	14.6	$2.01 \cdot 10^{22}$	219.5	440.9	134.2
78	160.7684452106	-59.5835522938	0.5	32.0	14.6	$2.00 \cdot 10^{22}$	143.5	288.2	87.7
79	160.9212648411	-59.6262636288	0.5	79.7	14.8	$1.83 \cdot 10^{22}$	349.7	718.6	218.7
80	160.9713109288	-59.9672262355	0.5	13.6	14.6	$2.02 \cdot 10^{22}$	61.3	123.0	37.4
81	161.4991577065	-59.7295810820	0.4	24.7	14.9	$1.76 \cdot 10^{22}$	107.4	223.1	67.9
82	160.6808676385	-59.4532494001	0.4	23.3	14.9	$1.76 \cdot 10^{22}$	101.2	210.3	64.0
83	161.4883852802	-60.1935887690	0.5	29.1	14.8	$1.84 \cdot 10^{22}$	127.6	262.2	79.8
84	160.4509890565	-59.7489285838	0.5	24.4	14.7	$1.88 \cdot 10^{22}$	108.2	219.7	66.9
85	161.3719902504	-59.7415228671	0.5	16.7	14.6	$2.00 \cdot 10^{22}$	75.0	150.8	45.9
86	161.2114289370	-59.6807716563	0.5	9.4	14.4	$2.24 \cdot 10^{22}$	43.0	84.3	25.7
87	161.5123961754	-59.7059387662	0.4	63.2	14.9	$1.75 \cdot 10^{22}$	274.5	570.3	173.6

n	R.A. (deg)	Dec. (deg)	F_{max}	F_{tot}	T	N_{H_2}	M	M (10 K)	M (20 K)
88	160.4049612213	-59.3419812412	0.5	8.4	14.4	$2.23 \cdot 10^{22}$	38.4	75.4	22.9
89	161.3992536198	-59.9017946584	0.4	42.9	15.0	$1.65 \cdot 10^{22}$	184.1	386.8	117.7
90	161.0152688974	-59.5590114011	0.6	5.3	13.9	$2.90 \cdot 10^{22}$	25.9	47.8	14.6
92	161.8053779478	-59.6157137552	0.4	22.3	14.9	$1.71 \cdot 10^{22}$	96.9	201.2	61.2
93	161.4928064762	-60.3690462436	0.4	16.4	14.9	$1.72 \cdot 10^{22}$	71.4	148.3	45.1
94	161.8938305301	-60.0894727780	0.4	14.4	14.9	$1.73 \cdot 10^{22}$	62.4	129.6	39.4
95	160.5230668715	-59.5300226654	0.4	27.7	15.2	$1.50 \cdot 10^{22}$	116.2	249.6	75.9
96	160.3130929503	-59.6551614801	0.4	48.8	15.1	$1.53 \cdot 10^{22}$	207.2	440.1	133.9
97	160.8822332544	-59.5451572028	0.4	28.1	15.1	$1.54 \cdot 10^{22}$	119.1	253.1	77.0
98	161.1227513229	-59.3854192318	0.4	37.8	15.2	$1.50 \cdot 10^{22}$	158.9	341.1	103.8
99	160.9576593022	-59.6567341502	0.4	24.1	15.1	$1.53 \cdot 10^{22}$	102.3	217.4	66.2
100	160.5070691481	-59.5029302365	0.4	24.8	15.2	$1.49 \cdot 10^{22}$	104.2	223.7	68.1
101	161.2223563638	-59.2927236605	0.4	29.2	15.1	$1.53 \cdot 10^{22}$	124.0	263.5	80.2
102	161.5174749879	-59.9725176712	0.4	21.9	15.1	$1.57 \cdot 10^{22}$	93.0	197.6	60.1
103	161.2154618431	-59.4074452253	0.4	23.0	15.2	$1.47 \cdot 10^{22}$	96.7	207.6	63.2
104	161.5359763944	-59.7295202148	0.4	30.5	15.1	$1.53 \cdot 10^{22}$	129.6	275.3	83.8
105	161.6128338735	-59.7158618392	0.4	11.2	15.0	$1.66 \cdot 10^{22}$	48.3	101.4	30.9
106	161.0555008932	-59.5219736069	0.4	24.6	15.2	$1.49 \cdot 10^{22}$	103.1	221.4	67.4
107	160.8016695693	-59.5904317129	0.4	18.1	15.1	$1.57 \cdot 10^{22}$	77.0	163.6	49.8
108	160.7830689781	-59.2832871746	0.4	21.4	15.3	$1.40 \cdot 10^{22}$	89.1	193.4	58.8
109	161.0169329149	-59.3616126135	0.4	16.7	15.1	$1.59 \cdot 10^{22}$	70.8	150.3	45.7
110	161.3319354997	-59.8731447481	0.4	22.5	15.2	$1.50 \cdot 10^{22}$	94.5	202.9	61.8
111	160.9694941219	-59.4728556296	0.4	49.6	15.4	$1.35 \cdot 10^{22}$	203.7	446.9	136.0
112	160.6251467788	-59.4175419597	0.3	25.2	15.5	$1.27 \cdot 10^{22}$	102.5	227.3	69.2
113	160.4277688954	-59.7403400288	0.4	22.5	15.2	$1.50 \cdot 10^{22}$	94.6	203.2	61.8
114	161.5093683556	-59.7565614021	0.4	29.2	15.3	$1.38 \cdot 10^{22}$	121.3	263.4	80.1
115	160.3683973723	-59.5880713161	0.4	36.5	15.3	$1.37 \cdot 10^{22}$	151.7	329.4	100.2
116	160.3974435749	-59.3756745224	0.4	8.1	14.9	$1.74 \cdot 10^{22}$	35.3	73.3	22.3
117	161.5698975464	-59.7851347690	0.4	16.8	15.3	$1.43 \cdot 10^{22}$	70.0	151.9	46.2
118	160.8021452756	-59.5583756121	0.4	17.4	15.3	$1.39 \cdot 10^{22}$	72.4	157.2	47.9
119	160.8180929877	-59.6073656656	0.5	10.0	14.7	$1.93 \cdot 10^{22}$	44.4	90.3	27.5
120	161.2649482031	-59.6403029362	0.3	56.6	15.5	$1.28 \cdot 10^{22}$	230.3	510.5	155.3
121	160.4538108967	-59.6375823203	0.4	34.2	15.4	$1.34 \cdot 10^{22}$	140.4	308.0	93.7
122	161.4171886428	-60.2172912235	0.4	7.5	14.9	$1.74 \cdot 10^{22}$	32.8	68.1	20.7
123	161.2553895193	-59.2978004838	0.4	12.5	15.2	$1.50 \cdot 10^{22}$	52.7	113.1	34.4
124	161.0164939182	-59.4139139919	0.3	37.2	15.4	$1.31 \cdot 10^{22}$	152.8	335.2	102.0
125	161.3620611119	-59.8039564381	0.4	11.8	15.3	$1.42 \cdot 10^{22}$	48.9	106.2	32.3
126	160.8758953534	-59.5198282857	0.4	20.6	15.4	$1.32 \cdot 10^{22}$	84.8	186.1	56.6
127	160.9073840753	-59.6717789521	0.3	48.8	15.5	$1.26 \cdot 10^{22}$	198.6	440.2	134.0
128	161.4576911235	-60.1632592393	0.3	37.4	15.5	$1.27 \cdot 10^{22}$	152.1	337.3	102.6
129	161.1947917250	-59.6571379291	0.3	39.5	15.6	$1.19 \cdot 10^{22}$	158.8	355.8	108.3
130	161.0842481464	-59.7076205626	0.4	7.3	15.0	$1.63 \cdot 10^{22}$	31.3	65.7	20.0
131	160.4012825282	-59.4803123360	0.3	31.1	15.6	$1.22 \cdot 10^{22}$	125.0	280.1	85.2
132	160.6889899755	-59.5545227584	0.4	19.8	15.4	$1.32 \cdot 10^{22}$	81.4	178.6	54.3

n	R.A. (deg)	Dec. (deg)	F_{max}	F_{tot}	T	N_{H_2}	M	M (10 K)	M (20 K)
133	161.3413844063	-59.3619126601	0.4	14.7	15.3	$1.39 \cdot 10^{22}$	61.1	132.7	40.4
134	161.5779668699	-59.9487827502	0.4	11.7	15.2	$1.49 \cdot 10^{22}$	49.0	105.3	32.0
135	161.1352706494	-59.5355958749	0.4	17.5	15.4	$1.35 \cdot 10^{22}$	72.1	158.2	48.2
136	161.5058945425	-60.2796086557	0.3	27.2	15.5	$1.24 \cdot 10^{22}$	110.6	245.1	74.6
137	160.2890061059	-59.6786016185	0.3	15.8	15.5	$1.28 \cdot 10^{22}$	64.4	142.8	43.5
138	160.3097077699	-59.5437704975	0.4	11.4	15.4	$1.34 \cdot 10^{22}$	47.0	103.1	31.4
139	161.6852322383	-60.1914765548	0.4	10.4	15.3	$1.43 \cdot 10^{22}$	43.3	94.0	28.6
140	160.9648329760	-59.2737579785	0.3	8.1	15.5	$1.27 \cdot 10^{22}$	33.1	73.4	22.3
141	160.7292883408	-59.5344571872	0.3	19.2	15.6	$1.20 \cdot 10^{22}$	77.4	173.3	52.7
142	160.5582484728	-59.5943435960	0.4	8.3	15.2	$1.48 \cdot 10^{22}$	34.7	74.6	22.7
143	160.8557777222	-59.2801807189	0.4	10.0	15.2	$1.46 \cdot 10^{22}$	42.2	90.6	27.6
144	161.8924128576	-60.1991502723	0.3	14.3	15.6	$1.18 \cdot 10^{22}$	57.6	129.1	39.3
145	160.6396572161	-59.6926416263	0.3	12.3	15.5	$1.28 \cdot 10^{22}$	50.1	111.0	33.8
146	161.3083900371	-59.8174688460	0.4	8.1	15.2	$1.47 \cdot 10^{22}$	34.1	73.2	22.3
147	161.2915530787	-60.0418730486	0.4	9.1	15.2	$1.50 \cdot 10^{22}$	38.3	82.2	25.0
148	161.4758963193	-59.7616721488	0.3	11.5	15.5	$1.26 \cdot 10^{22}$	46.6	103.4	31.5
149	161.8586089703	-60.2077328233	0.3	8.1	15.6	$1.21 \cdot 10^{22}$	32.5	72.7	22.1
150	161.9104670426	-60.0742117691	0.3	20.4	15.7	$1.15 \cdot 10^{22}$	81.2	183.9	56.0
151	161.1736249395	-59.9557636117	0.4	7.5	15.4	$1.35 \cdot 10^{22}$	31.0	67.9	20.7
152	161.7316085547	-60.3634256294	0.3	10.8	15.6	$1.19 \cdot 10^{22}$	43.3	97.0	29.5
153	161.2188176665	-59.3905756741	0.3	19.6	15.7	$1.12 \cdot 10^{22}$	78.2	176.9	53.8
154	161.4275816176	-60.2695838558	0.4	10.8	15.4	$1.33 \cdot 10^{22}$	44.6	97.8	29.8
155	160.5400830470	-59.5132495634	0.3	39.3	15.7	$1.13 \cdot 10^{22}$	156.8	354.8	108.0
156	160.5622497061	-59.5639948047	0.3	13.1	15.6	$1.19 \cdot 10^{22}$	52.6	117.8	35.8
157	162.0085744673	-60.0754107675	0.3	10.0	15.5	$1.26 \cdot 10^{22}$	40.9	90.6	27.6
158	161.2881179790	-60.1987833712	0.3	24.4	15.9	$1.03 \cdot 10^{22}$	95.3	220.2	67.0
159	161.2124967680	-59.2724720957	0.3	13.9	15.8	$1.09 \cdot 10^{22}$	54.7	125.1	38.1
160	160.9253184173	-59.5621597804	0.3	6.7	15.5	$1.28 \cdot 10^{22}$	27.3	60.5	18.4
161	161.6368321768	-59.7731697467	0.3	21.0	15.8	$1.10 \cdot 10^{22}$	82.7	189.1	57.5
162	160.4012709310	-59.6051739078	0.3	18.0	15.8	$1.06 \cdot 10^{22}$	70.9	162.1	49.3
163	161.1312990589	-59.6638207566	0.4	5.1	15.1	$1.58 \cdot 10^{22}$	21.8	46.4	14.1
164	161.5187995070	-60.1732958005	0.3	12.8	15.6	$1.19 \cdot 10^{22}$	51.4	115.0	35.0
165	161.4812532226	-60.1311722251	0.3	9.8	15.9	$1.05 \cdot 10^{22}$	38.3	88.4	26.9
166	160.7568904504	-59.4738336649	0.3	19.5	15.9	$1.02 \cdot 10^{22}$	76.3	176.2	53.6
168	161.4937549655	-59.9523075229	1.0	2.2	12.8	$5.16 \cdot 10^{22}$	12.3	19.7	6.0
169	160.6108832717	-59.4663976715	0.3	10.7	15.7	$1.14 \cdot 10^{22}$	42.5	96.3	29.3
170	160.9477312310	-59.9654782574	0.3	21.4	16.0	$9.83 \cdot 10^{21}$	82.8	193.3	58.8
171	161.0501645221	-59.3448088385	0.4	4.3	15.4	$1.35 \cdot 10^{22}$	17.6	38.6	11.8
172	161.0105284614	-59.3362912663	0.4	6.8	15.3	$1.38 \cdot 10^{22}$	28.4	61.6	18.7
173	161.5097284751	-60.3470882040	0.3	6.1	15.6	$1.21 \cdot 10^{22}$	24.4	54.7	16.7
174	161.4345171374	-60.3016328530	0.7	2.3	13.6	$3.33 \cdot 10^{22}$	11.9	21.1	6.4
175	161.5613464834	-59.9775000111	0.3	11.4	15.7	$1.15 \cdot 10^{22}$	45.4	102.9	31.3
176	161.6153785831	-60.3401315279	0.3	9.0	15.9	$1.04 \cdot 10^{22}$	35.2	81.2	24.7
177	161.6427950115	-60.3535608569	0.3	13.2	15.8	$1.09 \cdot 10^{22}$	52.2	119.4	36.3

n	R.A. (deg)	Dec. (deg)	F_{max}	F_{tot}	T	N_{H_2}	M	M (10 K)	M (20 K)
178	160.6739464736	-59.4684016487	0.3	16.5	16.1	$9.44 \cdot 10^{21}$	63.0	148.6	45.2
179	160.7145904696	-59.4230344941	0.3	13.7	15.8	$1.10 \cdot 10^{22}$	54.2	123.9	37.7
180	161.7284327489	-60.1204808610	0.3	7.6	15.7	$1.16 \cdot 10^{22}$	30.4	68.9	21.0
181	160.7380312924	-59.4096395786	0.3	9.6	15.8	$1.07 \cdot 10^{22}$	37.9	86.6	26.4
182	161.5599182804	-59.7952784307	0.4	6.1	15.0	$1.61 \cdot 10^{22}$	26.0	54.7	16.6
183	160.6971918271	-59.6541102059	0.3	27.4	16.0	$9.61 \cdot 10^{21}$	105.8	246.9	75.1
184	160.7767760866	-59.2630164284	0.3	7.8	15.6	$1.22 \cdot 10^{22}$	31.5	70.5	21.5
185	161.8182833577	-60.0189246068	0.3	7.0	15.8	$1.07 \cdot 10^{22}$	27.6	63.1	19.2
186	161.4240330190	-60.2307824208	0.3	12.7	15.8	$1.07 \cdot 10^{22}$	50.2	114.8	34.9
187	161.1364220268	-59.9827188127	0.3	6.9	15.7	$1.14 \cdot 10^{22}$	27.5	62.3	19.0
188	161.9602378444	-60.1954560265	0.3	19.4	15.9	$1.01 \cdot 10^{22}$	75.7	174.9	53.2
189	160.9880096433	-59.2670670078	0.3	7.0	15.6	$1.19 \cdot 10^{22}$	28.1	62.9	19.1
190	161.4478579794	-60.2391939190	0.3	11.4	15.8	$1.10 \cdot 10^{22}$	44.9	102.7	31.3
191	161.4692725561	-59.7768661722	0.3	19.6	15.8	$1.09 \cdot 10^{22}$	77.4	177.0	53.9
192	161.0213411306	-59.6298885823	0.4	4.4	15.3	$1.43 \cdot 10^{22}$	18.4	39.8	12.1
193	161.5191742391	-59.7194257129	0.3	9.6	15.8	$1.09 \cdot 10^{22}$	37.8	86.4	26.3
194	160.7646068680	-59.4063766557	0.3	5.2	15.4	$1.31 \cdot 10^{22}$	21.4	46.9	14.3
195	160.9763410827	-60.1427117816	0.3	16.2	16.0	$9.81 \cdot 10^{21}$	62.7	146.3	44.5
196	160.8078408521	-59.6242003055	0.3	6.8	15.7	$1.12 \cdot 10^{22}$	27.2	61.6	18.8
197	161.1518355074	-59.5524878572	0.4	4.0	15.1	$1.53 \cdot 10^{22}$	17.1	36.4	11.1
198	161.8960576667	-60.0253463570	0.4	5.3	15.4	$1.35 \cdot 10^{22}$	21.7	47.6	14.5
199	160.3952396874	-59.5815097902	0.3	5.6	15.6	$1.19 \cdot 10^{22}$	22.6	50.7	15.4
200	161.4823482135	-59.7161073870	0.3	8.4	15.9	$1.05 \cdot 10^{22}$	33.0	76.1	23.2
201	160.7035066347	-59.4870993202	0.3	27.8	16.1	$9.30 \cdot 10^{21}$	106.3	250.6	76.2
202	161.7451614606	-60.1052406175	0.3	6.8	15.9	$1.04 \cdot 10^{22}$	26.6	61.4	18.7
203	161.1681718928	-59.6318052577	0.3	7.4	16.1	$9.40 \cdot 10^{21}$	28.5	67.1	20.4
204	160.8292344911	-59.5264179567	0.3	9.5	15.9	$1.02 \cdot 10^{22}$	37.1	85.7	26.1
205	161.4206905543	-60.2459700264	0.4	4.4	15.3	$1.38 \cdot 10^{22}$	18.4	40.0	12.2
206	160.8195675555	-59.5044487712	0.5	3.6	14.6	$1.99 \cdot 10^{22}$	16.3	32.8	10.0
207	160.6039628400	-59.4798591204	0.3	13.7	16.0	$9.63 \cdot 10^{21}$	53.1	124.0	37.7
208	161.1383712709	-59.5828420688	0.4	3.4	15.0	$1.65 \cdot 10^{22}$	14.4	30.4	9.2
209	161.7362066201	-59.6834524347	0.3	21.1	16.1	$9.29 \cdot 10^{21}$	80.8	190.6	58.0
210	160.8595391434	-60.2604800237	0.3	17.3	16.0	$9.62 \cdot 10^{21}$	66.8	156.0	47.5
211	160.2847801966	-59.5975752444	0.3	25.3	16.2	$8.95 \cdot 10^{21}$	95.8	228.1	69.4
212	160.7898781444	-59.2698168650	0.3	5.6	15.7	$1.13 \cdot 10^{22}$	22.3	50.4	15.3
213	162.1133058161	-59.9330741154	0.3	8.2	16.0	$9.85 \cdot 10^{21}$	31.8	74.3	22.6
214	160.3642262212	-59.4986132194	0.3	9.5	16.1	$9.30 \cdot 10^{21}$	36.3	85.6	26.1
215	161.1546905632	-59.6621614503	0.3	13.3	16.2	$8.97 \cdot 10^{21}$	50.5	120.1	36.5
217	161.8721572265	-60.0102662949	0.3	4.1	15.6	$1.19 \cdot 10^{22}$	16.6	37.1	11.3
218	161.3654455755	-59.8191401275	0.3	19.3	16.2	$8.84 \cdot 10^{21}$	73.2	174.2	53.0
219	161.4345932073	-60.3201912772	0.3	8.5	15.9	$1.02 \cdot 10^{22}$	33.2	76.8	23.4
220	161.4722585856	-59.7059974496	0.4	3.9	15.3	$1.42 \cdot 10^{22}$	16.3	35.4	10.8
221	161.4689712944	-60.3792012061	0.3	8.9	16.0	$9.92 \cdot 10^{21}$	34.4	80.3	24.4
222	160.9608966079	-59.6668661015	0.3	5.3	15.8	$1.06 \cdot 10^{22}$	20.9	47.9	14.6

n	R.A. (deg)	Dec. (deg)	F_{max}	F_{tot}	T	N_{H_2}	M	M (10 K)	M (20 K)
223	161.6968976399	-59.7510678606	0.3	15.2	16.1	$9.11 \cdot 10^{21}$	58.0	136.8	41.6
224	160.2928653018	-59.5503915987	0.3	6.4	15.9	$1.02 \cdot 10^{22}$	25.1	58.0	17.7
225	161.0011224591	-59.6517784179	0.3	6.6	15.8	$1.06 \cdot 10^{22}$	26.2	59.9	18.2
226	161.2379357469	-59.8056436950	0.3	7.4	16.2	$8.77 \cdot 10^{21}$	28.0	66.7	20.3
227	161.9075812407	-60.1012213271	0.3	5.1	15.8	$1.07 \cdot 10^{22}$	20.3	46.4	14.1
228	161.1803953289	-59.9473336558	0.3	4.1	15.5	$1.25 \cdot 10^{22}$	16.8	37.3	11.4
229	161.2816312068	-59.6554915133	0.4	3.5	15.2	$1.48 \cdot 10^{22}$	14.6	31.2	9.5
230	162.1674899757	-59.9445409134	0.3	5.2	15.9	$1.02 \cdot 10^{22}$	20.3	46.9	14.3
231	161.2284650950	-59.5289309807	0.2	13.0	16.3	$8.44 \cdot 10^{21}$	48.6	116.8	35.5
232	160.2643107801	-59.7205940390	0.3	9.4	16.1	$9.19 \cdot 10^{21}$	36.1	85.1	25.9
233	160.7072215202	-59.2762160100	0.3	7.5	16.2	$8.80 \cdot 10^{21}$	28.3	67.3	20.5
234	161.2949555054	-59.8866465646	0.2	42.4	16.4	$8.05 \cdot 10^{21}$	157.5	382.4	116.4
235	161.2585969806	-59.3770970393	0.3	11.3	16.1	$9.42 \cdot 10^{21}$	43.4	102.3	31.1
236	160.9470743057	-59.3934988906	0.2	12.0	16.4	$7.91 \cdot 10^{21}$	44.7	108.5	33.0
237	161.4955644801	-60.2593783287	0.3	9.7	16.2	$8.92 \cdot 10^{21}$	36.8	87.7	26.7
238	160.9743985200	-59.3092118852	0.3	7.0	16.1	$9.25 \cdot 10^{21}$	26.7	63.0	19.2
239	160.9242304921	-59.9569772304	0.3	4.1	15.6	$1.18 \cdot 10^{22}$	16.4	36.8	11.2
240	161.5965991788	-59.7715792176	0.3	11.6	16.1	$9.09 \cdot 10^{21}$	44.4	104.7	31.9
241	160.8990177620	-59.5333989375	0.3	5.3	15.7	$1.14 \cdot 10^{22}$	21.0	47.6	14.5
242	160.7893642079	-59.5228942123	0.2	6.3	16.4	$7.85 \cdot 10^{21}$	23.4	56.7	17.3
243	161.5095667373	-60.3217815441	0.2	11.6	16.3	$8.50 \cdot 10^{21}$	43.6	104.8	31.9
244	160.9472843550	-59.6904519675	0.3	5.3	15.9	$1.02 \cdot 10^{22}$	20.5	47.4	14.4
245	161.3955785822	-59.7938128404	0.3	7.5	16.1	$9.42 \cdot 10^{21}$	28.6	67.5	20.5
246	162.0839161950	-59.9720602747	0.2	9.6	16.3	$8.42 \cdot 10^{21}$	36.0	86.6	26.3
247	160.4445078629	-59.7404498869	0.6	2.2	14.3	$2.38 \cdot 10^{22}$	10.4	20.2	6.1
248	160.7102592295	-59.2914141614	0.3	6.3	16.0	$9.56 \cdot 10^{21}$	24.4	56.9	17.3
249	160.8060908678	-59.2901249257	0.2	7.0	16.4	$8.09 \cdot 10^{21}$	26.1	63.3	19.3
250	161.0447528380	-59.6231871760	0.4	3.6	15.4	$1.34 \cdot 10^{22}$	14.8	32.5	9.9
251	161.3972716623	-60.3742114834	0.3	4.3	15.8	$1.08 \cdot 10^{22}$	16.8	38.4	11.7
252	161.7186856025	-59.8859827369	0.3	7.6	16.2	$8.76 \cdot 10^{21}$	28.7	68.2	20.8
253	161.5310321831	-59.9826181940	0.3	5.4	15.9	$1.01 \cdot 10^{22}$	21.0	48.4	14.7
254	161.2815540607	-59.7955334695	0.3	4.3	15.7	$1.15 \cdot 10^{22}$	17.0	38.6	11.7
255	160.2164795554	-59.6476507592	0.4	2.9	15.3	$1.40 \cdot 10^{22}$	12.2	26.6	8.1
256	160.9581096229	-59.2855503886	0.4	1.9	14.9	$1.72 \cdot 10^{22}$	8.2	17.1	5.2
257	160.4181710276	-59.7234025517	0.2	11.3	16.3	$8.39 \cdot 10^{21}$	42.5	102.1	31.1
258	161.1363554089	-59.9962167035	0.2	10.6	16.4	$7.94 \cdot 10^{21}$	39.5	95.9	29.2
259	161.2543936089	-60.0368037644	0.5	2.3	14.7	$1.94 \cdot 10^{22}$	10.4	21.0	6.4
260	160.3330303881	-59.6586844340	0.3	5.0	15.7	$1.12 \cdot 10^{22}$	19.9	45.2	13.7
261	160.6536821446	-59.6589653004	0.2	9.3	16.3	$8.27 \cdot 10^{21}$	34.8	83.8	25.5
262	161.7985336806	-60.0527457798	0.3	6.9	16.2	$8.89 \cdot 10^{21}$	26.3	62.6	19.1
263	160.7550058687	-59.5902462379	0.3	3.8	15.5	$1.24 \cdot 10^{22}$	15.5	34.4	10.5
264	161.2353369829	-59.4158924263	0.3	6.6	16.1	$9.31 \cdot 10^{21}$	25.2	59.4	18.1
265	160.9568955537	-59.4053353049	0.2	6.3	16.4	$7.90 \cdot 10^{21}$	23.4	56.8	17.3
266	161.1682249752	-59.6183073857	0.2	27.1	16.6	$7.14 \cdot 10^{21}$	98.8	244.5	74.4

n	R.A. (deg)	Dec. (deg)	F_{max}	F_{tot}	T	N_{H_2}	M	M (10 K)	M (20 K)
267	161.0369546521	-59.3414086061	0.3	3.3	15.5	$1.28 \cdot 10^{22}$	13.2	29.4	8.9
268	161.2711081492	-60.2392729899	0.2	7.2	16.3	$8.31 \cdot 10^{21}$	27.1	65.1	19.8
269	161.2574158993	-60.3135039513	0.2	9.4	16.4	$8.03 \cdot 10^{21}$	34.9	84.8	25.8
270	160.9481008627	-59.6128402487	0.3	4.2	16.0	$9.92 \cdot 10^{21}$	16.3	38.1	11.6
271	160.9948742043	-59.6045210369	0.3	4.4	15.9	$1.01 \cdot 10^{22}$	17.1	39.5	12.0
272	160.6504719354	-59.4800980486	0.3	6.7	16.2	$8.72 \cdot 10^{21}$	25.5	60.6	18.4
273	160.6110281424	-59.6216279768	0.2	15.8	16.6	$7.01 \cdot 10^{21}$	57.4	142.1	43.2
274	160.3818745041	-59.7045933435	0.2	7.9	16.3	$8.21 \cdot 10^{21}$	29.6	71.2	21.7
275	160.8220045057	-60.2687863709	0.2	5.3	16.5	$7.58 \cdot 10^{21}$	19.6	48.1	14.6
276	161.0929650756	-59.3803139575	0.3	5.1	16.2	$8.88 \cdot 10^{21}$	19.4	46.1	14.0
277	161.4927164204	-59.7734594374	0.3	3.6	15.6	$1.19 \cdot 10^{22}$	14.4	32.2	9.8
278	161.0290115276	-59.5067365452	0.4	2.2	15.3	$1.40 \cdot 10^{22}$	9.0	19.5	5.9
279	161.4195499785	-59.9321484332	0.2	21.0	16.7	$6.65 \cdot 10^{21}$	76.0	189.8	57.8
280	161.7585145783	-60.0916971551	0.3	3.5	15.9	$1.04 \cdot 10^{22}$	13.8	31.8	9.7
281	160.3925022656	-59.6827314960	0.2	8.0	16.4	$8.07 \cdot 10^{21}$	29.5	71.7	21.8
282	161.0553412653	-59.5439072102	0.2	5.8	16.3	$8.48 \cdot 10^{21}$	21.8	52.3	15.9
283	161.0142639445	-59.6771164887	0.7	1.8	13.6	$3.37 \cdot 10^{22}$	8.9	15.9	4.8
284	160.2849905725	-59.2601160989	0.3	3.0	15.5	$1.24 \cdot 10^{22}$	12.3	27.3	8.3
285	161.6567646514	-60.0700759328	0.2	6.5	16.3	$8.39 \cdot 10^{21}$	24.6	59.0	18.0
286	160.4203029006	-59.6424242133	0.2	9.0	16.5	$7.59 \cdot 10^{21}$	33.1	81.0	24.7
287	161.4211192250	-60.3623822157	0.2	8.6	16.4	$7.85 \cdot 10^{21}$	31.9	77.4	23.5
288	160.9769952472	-59.3834531792	0.2	8.3	16.3	$8.20 \cdot 10^{21}$	31.0	74.6	22.7
289	160.5167035399	-59.3747564525	0.2	18.3	16.7	$6.85 \cdot 10^{21}$	66.1	165.2	50.3
290	160.6620977274	-59.5678929147	0.2	14.0	16.8	$6.51 \cdot 10^{21}$	49.9	125.9	38.3
291	161.8185475091	-60.0357962750	0.2	12.2	16.5	$7.40 \cdot 10^{21}$	44.9	109.9	33.5
292	160.8472866392	-59.6682111778	0.2	9.5	16.5	$7.65 \cdot 10^{21}$	35.1	85.9	26.2
293	162.1141330920	-59.9668156978	0.2	6.4	16.4	$7.85 \cdot 10^{21}$	23.7	57.6	17.5
294	162.3132208046	-59.8625095031	0.3	4.0	16.0	$9.95 \cdot 10^{21}$	15.4	36.0	11.0
295	161.4228426756	-59.9118983585	0.2	9.9	16.5	$7.54 \cdot 10^{21}$	36.4	89.3	27.2
296	161.2076395222	-59.8427456457	0.2	5.7	16.5	$7.62 \cdot 10^{21}$	21.1	51.6	15.7
297	160.9080953275	-59.6110396834	0.3	4.7	16.1	$9.34 \cdot 10^{21}$	18.0	42.4	12.9
298	160.5668326391	-59.5066528462	0.3	3.6	15.8	$1.09 \cdot 10^{22}$	14.1	32.3	9.8
299	160.6717587594	-59.4076508026	0.3	5.5	16.2	$8.71 \cdot 10^{21}$	20.7	49.3	15.0
300	161.1072640875	-59.7768339323	0.2	9.4	16.6	$7.23 \cdot 10^{21}$	34.4	85.2	25.9
301	161.8454044099	-60.0255647346	0.2	9.0	16.4	$7.77 \cdot 10^{21}$	33.3	80.9	24.6
302	161.8346743273	-59.9884884235	0.3	2.5	15.6	$1.19 \cdot 10^{22}$	10.0	22.5	6.8
303	161.9941444455	-60.1935959283	0.2	5.9	16.4	$7.91 \cdot 10^{21}$	22.1	53.6	16.3
304	161.4891505323	-60.3268734986	0.2	5.2	16.3	$8.47 \cdot 10^{21}$	19.4	46.6	14.2
305	161.6851550030	-59.8945211930	0.2	10.7	16.5	$7.52 \cdot 10^{21}$	39.4	96.5	29.4
306	161.0976586263	-59.7025801040	0.3	3.8	16.0	$9.94 \cdot 10^{21}$	14.8	34.6	10.5
307	161.5530187594	-59.7699828779	0.3	4.0	16.0	$9.89 \cdot 10^{21}$	15.5	36.3	11.0
308	160.2528315051	-59.6597572076	0.3	3.3	15.8	$1.06 \cdot 10^{22}$	13.1	30.1	9.1
309	160.3622828965	-59.6875815151	0.3	5.3	16.0	$9.73 \cdot 10^{21}$	20.4	47.5	14.5
310	160.9574694398	-59.6752935225	0.2	7.0	16.4	$7.82 \cdot 10^{21}$	26.1	63.3	19.3

n	R.A. (deg)	Dec. (deg)	F_{max}	F_{tot}	T	N_{H_2}	M	M (10 K)	M (20 K)
311	161.5524953306	-59.7008061323	0.3	6.5	16.0	$9.67 \cdot 10^{21}$	25.2	58.9	17.9
312	160.7895947586	-59.5077099226	0.2	11.5	16.6	$7.24 \cdot 10^{21}$	41.9	103.6	31.5
313	161.2187364137	-59.4243190497	0.4	2.6	15.0	$1.62 \cdot 10^{22}$	10.9	23.0	7.0
314	161.6829588051	-59.7038655233	0.2	11.4	16.6	$7.01 \cdot 10^{21}$	41.6	103.1	31.4
315	160.8023952828	-59.5415040437	0.2	4.3	16.3	$8.41 \cdot 10^{21}$	16.1	38.6	11.7
316	160.7558815012	-59.5362575086	0.3	3.2	15.8	$1.08 \cdot 10^{22}$	12.8	29.3	8.9
317	161.9063426746	-60.0337360608	0.3	3.3	15.7	$1.12 \cdot 10^{22}$	13.1	29.7	9.0
318	161.9828084755	-60.1379752250	0.3	4.3	16.2	$8.97 \cdot 10^{21}$	16.4	38.9	11.9
319	161.3387925512	-59.9878760027	0.2	8.7	16.4	$8.02 \cdot 10^{21}$	32.4	78.8	24.0
320	161.6890392651	-59.6515424149	0.3	3.5	15.6	$1.21 \cdot 10^{22}$	14.2	31.9	9.7
321	161.4816897144	-60.2104699677	0.2	6.7	16.5	$7.59 \cdot 10^{21}$	24.6	60.3	18.3
322	161.1985610417	-59.5154135422	0.2	8.7	16.6	$7.13 \cdot 10^{21}$	31.7	78.4	23.9
323	161.7887488260	-59.6191512373	0.2	6.6	16.2	$8.67 \cdot 10^{21}$	25.2	59.9	18.2
324	160.2449396067	-59.5921989194	0.3	3.0	15.7	$1.12 \cdot 10^{22}$	11.8	26.8	8.2
325	160.6221624239	-59.5660053638	0.2	8.4	16.4	$7.96 \cdot 10^{21}$	31.1	75.6	23.0
326	162.3448820273	-59.6935231187	0.2	6.0	16.5	$7.68 \cdot 10^{21}$	22.2	54.5	16.6
327	161.1947333751	-59.6756976023	0.2	8.3	16.7	$6.83 \cdot 10^{21}$	29.9	74.8	22.8
328	161.4905112503	-59.9742465142	0.2	5.0	16.5	$7.64 \cdot 10^{21}$	18.6	45.5	13.8
329	161.7924419700	-59.8705426278	0.2	7.8	16.5	$7.64 \cdot 10^{21}$	28.7	70.4	21.4
330	161.2646670288	-59.9068889941	0.2	7.9	16.5	$7.40 \cdot 10^{21}$	29.0	71.1	21.6
331	160.3760254343	-59.6741799545	0.2	3.9	16.2	$8.63 \cdot 10^{21}$	14.6	34.8	10.6
332	161.7025114518	-60.2167333637	0.3	3.0	15.9	$1.03 \cdot 10^{22}$	11.7	27.1	8.2
333	160.6549902873	-59.4176925248	0.2	14.0	16.7	$6.85 \cdot 10^{21}$	50.6	126.5	38.5
334	161.3455994186	-60.0317420628	0.2	23.4	16.9	$6.14 \cdot 10^{21}$	82.8	210.7	64.1
335	161.8552239530	-60.0069638613	0.2	5.5	16.7	$6.85 \cdot 10^{21}$	19.7	49.3	15.0
336	160.6181396795	-59.4360652264	0.2	5.6	16.6	$7.04 \cdot 10^{21}$	20.4	50.5	15.4
337	161.4297912453	-59.9675710508	0.3	3.9	16.1	$9.35 \cdot 10^{21}$	15.1	35.6	10.8
338	160.7700158946	-59.2731119518	0.2	2.4	16.2	$8.61 \cdot 10^{21}$	9.2	21.8	6.6
339	160.5027852459	-59.5433992643	0.4	2.9	14.9	$1.70 \cdot 10^{22}$	12.7	26.5	8.1
340	161.1633482186	-59.9962473358	0.2	4.8	16.2	$8.66 \cdot 10^{21}$	18.1	43.0	13.1
341	161.7074807131	-59.7949047564	0.2	5.5	16.5	$7.44 \cdot 10^{21}$	20.2	49.4	15.0
342	161.2377688028	-59.8950682731	0.3	5.1	16.2	$8.72 \cdot 10^{21}$	19.4	46.3	14.1
343	161.4689017043	-60.3657044557	0.3	2.5	15.7	$1.15 \cdot 10^{22}$	9.8	22.1	6.7
344	160.4906151482	-59.3577251500	0.2	6.8	16.3	$8.25 \cdot 10^{21}$	25.6	61.6	18.7
345	160.8775701192	-59.3865440640	0.2	4.6	16.4	$8.03 \cdot 10^{21}$	17.2	41.9	12.7
346	160.3558088267	-59.3247626840	0.3	4.6	16.2	$8.92 \cdot 10^{21}$	17.2	41.1	12.5
347	161.1227070124	-59.3938550054	0.3	2.7	15.5	$1.26 \cdot 10^{22}$	11.1	24.6	7.5
348	160.9734212783	-59.4104391692	1.3	1.6	12.1	$7.27 \cdot 10^{22}$	10.1	14.6	4.5
349	161.1433269255	-59.9489821685	0.6	1.8	14.2	$2.43 \cdot 10^{22}$	8.7	16.7	5.1
350	160.8844977065	-59.6312142418	0.2	4.3	16.4	$7.90 \cdot 10^{21}$	16.1	39.2	11.9
351	161.0640950853	-59.7193967808	0.3	3.6	16.1	$9.18 \cdot 10^{21}$	13.7	32.2	9.8
352	160.6649498134	-59.5932159430	0.2	9.8	16.8	$6.42 \cdot 10^{21}$	35.0	88.1	26.8
353	161.7958700916	-59.6494954236	0.2	15.0	16.9	$6.14 \cdot 10^{21}$	53.0	135.0	41.1
354	160.6657154243	-59.5527249897	0.2	3.5	16.2	$8.65 \cdot 10^{21}$	13.2	31.4	9.6

n	R.A. (deg)	Dec. (deg)	F_{max}	F_{tot}	T	N_{H_2}	M	M (10 K)	M (20 K)
355	161.5328291338	-59.7582092720	0.2	3.2	16.2	$8.68 \cdot 10^{21}$	12.0	28.6	8.7
356	160.8790314081	-59.5350235227	0.2	3.3	16.3	$8.23 \cdot 10^{21}$	12.4	29.8	9.1
357	160.4273721798	-59.7555235664	0.2	8.4	16.5	$7.67 \cdot 10^{21}$	30.7	75.3	22.9
358	160.3777983620	-59.4885856020	0.2	3.6	16.3	$8.44 \cdot 10^{21}$	13.4	32.1	9.8
359	161.2353628538	-59.4023950650	0.3	3.2	16.2	$8.94 \cdot 10^{21}$	12.1	28.7	8.7
360	160.7599684473	-59.4890315166	0.2	6.8	16.7	$6.65 \cdot 10^{21}$	24.6	61.3	18.7
361	161.4487623306	-59.6874663366	0.3	3.2	16.1	$9.32 \cdot 10^{21}$	12.2	28.7	8.7
362	161.7408830977	-59.7846735414	0.2	7.5	17.0	$5.89 \cdot 10^{21}$	26.2	67.4	20.5
363	160.8989682746	-60.0952579974	0.3	2.4	15.5	$1.27 \cdot 10^{22}$	9.9	22.0	6.7
364	161.6039473482	-59.8424277822	0.2	5.0	16.7	$6.84 \cdot 10^{21}$	18.1	45.1	13.7
365	162.0360029973	-60.2439879698	0.6	2.1	14.3	$2.37 \cdot 10^{22}$	10.0	19.3	5.9
366	161.2388000034	-59.3349105758	0.2	4.7	16.5	$7.58 \cdot 10^{21}$	17.1	42.0	12.8
367	161.8416865057	-60.2111773238	0.2	3.6	16.5	$7.63 \cdot 10^{21}$	13.2	32.3	9.8
368	160.9001572222	-59.7173134608	0.4	3.2	15.4	$1.32 \cdot 10^{22}$	13.0	28.6	8.7
369	161.1725425834	-59.3601699003	0.2	11.6	16.9	$6.07 \cdot 10^{21}$	41.2	104.9	31.9
370	160.6017956859	-59.4241683500	0.2	4.3	16.3	$8.19 \cdot 10^{21}$	16.2	38.9	11.8
371	161.1491425541	-59.4107598904	0.2	3.5	16.3	$8.44 \cdot 10^{21}$	13.1	31.4	9.6
372	161.4576024230	-60.1447001023	0.2	3.7	16.4	$7.94 \cdot 10^{21}$	13.6	33.0	10.0
373	160.6159713551	-60.0333575052	0.2	5.4	16.6	$7.03 \cdot 10^{21}$	19.7	48.8	14.8
374	160.5007382436	-59.6294396253	0.3	3.4	16.2	$8.75 \cdot 10^{21}$	13.0	30.9	9.4
375	161.9309189262	-60.0825523450	0.2	5.4	16.6	$7.01 \cdot 10^{21}$	19.8	48.9	14.9
376	161.4582498032	-60.2796738429	0.3	2.7	16.0	$9.56 \cdot 10^{21}$	10.2	23.9	7.3

Table A.3: Properties of the SExtractor sample

n	R.A. (deg) (J2000)	Dec. (deg) (J2000)	F_{max} [Jy/beam]	F_{tot} [Jy/beam]	T [K]	N_{H_2} [cm^{-2}]	M [$M_\odot$]	M (10 K) [$M_\odot$]	M (20 K) [$M_\odot$]
1	161.2583713	-60.3135969	0.2	36.3	16.6	$7.09 \cdot 10^{21}$	132.3	327.3	99.6
3	160.7103927	-59.3007908	0.2	4.7	17.1	$5.43 \cdot 10^{21}$	16.3	42.2	12.8
4	160.7110847	-59.2766102	0.3	5.2	15.9	$1.02 \cdot 10^{22}$	20.2	46.6	14.2
5	160.7093309	-59.2906850	0.2	2.6	16.6	$7.27 \cdot 10^{21}$	9.5	23.4	7.1
7	160.8550469	-59.2803736	0.3	11.4	15.7	$1.14 \cdot 10^{22}$	45.5	102.9	31.3
8	160.8368353	-59.2825129	0.3	3.1	16.1	$9.10 \cdot 10^{21}$	11.8	27.9	8.5
9	160.7793888	-59.2649686	0.3	8.7	16.0	$9.56 \cdot 10^{21}$	33.7	78.6	23.9
10	160.7860705	-59.2807285	0.4	39.2	15.2	$1.48 \cdot 10^{22}$	164.5	353.2	107.5
11	160.9604049	-59.2880091	0.2	5.3	16.5	$7.48 \cdot 10^{21}$	19.5	47.7	14.5
12	160.9741944	-59.3018092	0.2	2.8	16.7	$6.84 \cdot 10^{21}$	10.1	25.1	7.7
13	160.9765677	-59.3085106	0.2	8.4	16.4	$7.87 \cdot 10^{21}$	31.4	76.2	23.2
14	160.9592946	-59.2796550	0.2	4.5	16.3	$8.48 \cdot 10^{21}$	16.9	40.7	12.4

n	R.A. (deg)	Dec. (deg)	F_{max}	F_{tot}	T	N_{H_2}	M	M (10 K)	M (20 K)
15	160.9770684	-59.2678106	0.3	9.3	15.9	$1.04 \cdot 10^{22}$	36.1	83.5	25.4
16	160.9688258	-59.2736774	0.3	6.0	15.7	$1.15 \cdot 10^{22}$	23.9	54.2	16.5
17	161.0826572	-59.2615628	0.2	2.4	16.9	$6.07 \cdot 10^{21}$	8.4	21.4	6.5
18	161.2520398	-59.2993369	0.3	27.6	15.5	$1.26 \cdot 10^{22}$	112.4	249.2	75.8
19	161.2247867	-59.2674146	0.3	2.2	16.0	$9.79 \cdot 10^{21}$	8.7	20.2	6.1
20	161.2256636	-59.2826126	0.2	4.1	16.4	$8.03 \cdot 10^{21}$	15.2	36.9	11.2
21	161.2206059	-59.3012368	0.3	3.6	15.8	$1.09 \cdot 10^{22}$	14.2	32.4	9.9
22	161.2133642	-59.2723309	0.3	16.9	15.5	$1.26 \cdot 10^{22}$	68.9	152.8	46.5
23	161.2191900	-59.2887609	0.3	4.1	15.6	$1.18 \cdot 10^{22}$	16.5	37.0	11.2
24	161.2228982	-59.2931319	0.4	4.1	15.3	$1.43 \cdot 10^{22}$	17.2	37.4	11.4
28	161.9291256	-59.3146420	0.1	10.4	17.5	$4.51 \cdot 10^{21}$	34.8	93.4	28.4
29	160.3558754	-59.3262302	0.2	5.1	16.5	$7.51 \cdot 10^{21}$	18.8	46.1	14.0
30	161.4633466	-59.3401202	0.2	3.5	17.2	$5.30 \cdot 10^{21}$	11.9	31.2	9.5
31	161.2816166	-59.3344839	0.2	4.2	17.4	$4.80 \cdot 10^{21}$	14.2	37.7	11.5
32	161.4948136	-59.3364283	0.2	2.6	17.3	$4.88 \cdot 10^{21}$	8.9	23.4	7.1
33	160.4051089	-59.3416987	0.4	14.5	15.1	$1.59 \cdot 10^{22}$	61.8	131.2	39.9
34	161.0134039	-59.3368591	0.3	7.9	16.0	$9.58 \cdot 10^{21}$	30.5	71.1	21.6
35	161.0392864	-59.3414265	0.2	2.9	16.4	$7.98 \cdot 10^{21}$	10.7	26.0	7.9
36	161.0487939	-59.3456703	0.3	4.0	15.7	$1.14 \cdot 10^{22}$	15.8	35.7	10.9
37	161.2409257	-59.3386516	0.2	4.2	17.1	$5.62 \cdot 10^{21}$	14.8	38.3	11.7
38	160.5479670	-59.3903382	0.2	4.6	17.3	$5.01 \cdot 10^{21}$	15.8	41.8	12.7
39	160.4181666	-59.3900423	0.2	5.3	17.2	$5.28 \cdot 10^{21}$	18.4	48.2	14.7
40	160.4427905	-59.3539742	0.2	6.1	17.2	$5.32 \cdot 10^{21}$	21.0	54.9	16.7
41	160.4674008	-59.3977558	0.2	7.9	17.3	$4.92 \cdot 10^{21}$	27.1	71.4	21.7
42	160.4751444	-59.3576383	0.2	4.5	17.4	$4.77 \cdot 10^{21}$	15.2	40.4	12.3
43	160.4924209	-59.3602969	0.2	3.5	16.7	$6.70 \cdot 10^{21}$	12.8	31.9	9.7
44	160.5151260	-59.3750952	0.2	8.1	16.7	$6.78 \cdot 10^{21}$	29.3	73.2	22.3
45	160.5318749	-59.3772591	0.2	2.8	17.1	$5.42 \cdot 10^{21}$	9.9	25.7	7.8
46	160.3981364	-59.3753776	0.4	14.4	15.4	$1.34 \cdot 10^{22}$	59.0	129.5	39.4
47	161.0914998	-59.3977106	0.2	4.3	17.1	$5.60 \cdot 10^{21}$	14.9	38.7	11.8
48	161.1673508	-59.3612692	0.2	18.4	16.7	$6.68 \cdot 10^{21}$	66.4	166.0	50.5
49	161.0928988	-59.3786267	0.2	3.0	16.7	$6.81 \cdot 10^{21}$	10.8	26.9	8.2
50	161.1061312	-59.3853956	0.2	4.6	16.4	$7.81 \cdot 10^{21}$	17.0	41.2	12.5
51	161.1244619	-59.3843678	0.4	15.0	15.0	$1.61 \cdot 10^{22}$	64.2	134.9	41.1
52	161.1211856	-59.3918911	0.4	11.2	15.3	$1.42 \cdot 10^{22}$	46.6	101.2	30.8
53	161.3427933	-59.3601283	0.3	27.3	15.6	$1.18 \cdot 10^{22}$	109.9	246.1	74.9
54	161.2556951	-59.3792351	0.2	15.5	16.4	$7.86 \cdot 10^{21}$	57.4	139.3	42.4
55	161.2347173	-59.4011091	0.2	6.5	16.6	$7.29 \cdot 10^{21}$	23.6	58.5	17.8
56	161.2159255	-59.3881825	0.3	16.4	15.7	$1.15 \cdot 10^{22}$	65.5	148.2	45.1
57	161.2325622	-59.4282015	0.9	39.8	12.9	$4.81 \cdot 10^{22}$	221.3	359.2	109.3
58	161.2121713	-59.3985297	0.3	2.2	15.9	$1.02 \cdot 10^{22}$	8.7	20.1	6.1
59	161.2130315	-59.4083559	0.4	20.2	15.3	$1.43 \cdot 10^{22}$	84.1	182.5	55.5

n	R.A. (deg)	Dec. (deg)	F_{max}	F_{tot}	T	N_{H_2}	M	M (10 K)	M (20 K)
60	161.0180805	-59.3605824	0.4	15.7	15.4	$1.35 \cdot 10^{22}$	64.4	141.3	43.0
61	160.9012841	-59.3723548	0.2	8.3	16.3	$8.47 \cdot 10^{21}$	31.0	74.5	22.7
62	161.0035733	-59.3905368	0.2	16.1	16.4	$8.02 \cdot 10^{21}$	59.7	145.0	44.1
63	160.9506423	-59.4137588	0.2	5.0	17.0	$5.77 \cdot 10^{21}$	17.5	44.9	13.7
64	160.8702418	-59.3788999	0.2	4.3	16.9	$6.15 \cdot 10^{21}$	15.4	39.2	11.9
65	160.9788823	-59.3849351	0.2	9.4	16.5	$7.62 \cdot 10^{21}$	34.5	84.4	25.7
66	160.9508482	-59.3971494	0.2	9.3	16.4	$8.04 \cdot 10^{21}$	34.5	83.7	25.5
67	161.0277579	-59.4043421	0.2	4.9	16.3	$8.46 \cdot 10^{21}$	18.3	44.1	13.4
68	161.0175719	-59.4154470	0.4	26.6	15.3	$1.40 \cdot 10^{22}$	110.5	239.7	73.0
69	160.9857690	-59.4080674	0.7	58.0	13.8	$3.10 \cdot 10^{22}$	286.6	523.3	159.2
70	160.9942633	-59.4170121	0.4	9.5	14.9	$1.75 \cdot 10^{22}$	41.2	85.5	26.0
71	160.6680141	-59.4925710	0.2	5.3	17.4	$4.81 \cdot 10^{21}$	17.9	47.7	14.5
72	160.6341060	-59.4443663	0.3	29.8	16.0	$9.68 \cdot 10^{21}$	115.3	269.0	81.8
73	160.8379888	-59.5147524	0.2	3.0	17.2	$5.32 \cdot 10^{21}$	10.4	27.2	8.3
74	160.9322469	-59.6033224	0.2	4.1	16.9	$6.22 \cdot 10^{21}$	14.6	37.0	11.3
75	160.6519867	-59.4803209	0.2	14.9	16.3	$8.51 \cdot 10^{21}$	55.8	134.1	40.8
76	160.7826664	-59.5085807	0.2	11.3	16.5	$7.45 \cdot 10^{21}$	41.5	101.8	31.0
77	160.7311131	-59.5338799	0.7	83.4	13.8	$2.99 \cdot 10^{22}$	411.9	752.1	228.9
78	160.7084698	-59.4867804	0.3	27.7	16.0	$9.92 \cdot 10^{21}$	107.2	250.2	76.1
79	160.9247499	-59.5627250	0.3	7.7	15.9	$1.02 \cdot 10^{22}$	29.9	69.1	21.0
80	160.6254196	-59.4180848	0.4	108.5	15.4	$1.34 \cdot 10^{22}$	446.0	978.3	297.7
81	160.6930574	-59.4741332	0.2	10.8	16.3	$8.39 \cdot 10^{21}$	40.6	97.6	29.7
82	160.7417310	-59.4081150	0.3	19.8	15.7	$1.13 \cdot 10^{22}$	78.9	178.6	54.3
83	160.7889249	-59.4116702	1.1	44.3	12.6	$5.78 \cdot 10^{22}$	256.9	399.8	121.7
84	160.8066205	-59.6252929	0.3	10.3	16.1	$9.26 \cdot 10^{21}$	39.3	92.7	28.2
85	160.6121635	-59.4684550	0.3	10.7	16.0	$9.69 \cdot 10^{21}$	41.4	96.7	29.4
86	160.6061104	-59.4805198	0.3	12.2	16.1	$9.17 \cdot 10^{21}$	46.8	110.2	33.5
87	160.7551131	-59.4747121	0.3	16.9	16.0	$9.80 \cdot 10^{21}$	65.2	152.1	46.3
88	160.8102521	-59.4925519	1.3	89.5	12.0	$7.69 \cdot 10^{22}$	566.4	806.7	245.5
89	160.9209773	-59.6252044	1.1	122.0	12.5	$5.89 \cdot 10^{22}$	717.1	1100.2	334.8
90	160.8672338	-59.5285015	0.7	76.3	13.7	$3.27 \cdot 10^{22}$	381.4	687.7	209.3
91	160.8996050	-59.5340923	0.3	4.5	15.6	$1.18 \cdot 10^{22}$	18.2	40.7	12.4
92	160.8346055	-59.5437563	1.1	56.5	12.6	$5.76 \cdot 10^{22}$	327.4	509.6	155.1
93	160.8871042	-59.5553415	1.2	67.8	12.4	$6.33 \cdot 10^{22}$	404.2	611.2	186.0
94	160.7803716	-59.5403279	1.9	296.9	11.0	$1.31 \cdot 10^{23}$	2214.8	2676.9	814.6
95	160.8467194	-59.6162022	1.0	116.7	12.9	$4.90 \cdot 10^{22}$	648.5	1052.6	320.3
96	160.6968679	-59.4231485	2.3	81.4	10.5	$1.71 \cdot 10^{23}$	665.5	734.3	223.4
97	160.6942962	-59.4391077	1.7	92.1	11.4	$1.07 \cdot 10^{23}$	641.8	830.5	252.7
98	160.8593640	-59.5970842	1.4	29.8	11.9	$8.24 \cdot 10^{22}$	191.7	268.9	81.8
99	160.8858147	-59.5842622	2.2	269.0	10.5	$1.67 \cdot 10^{23}$	2198.8	2426.0	738.3
100	160.8720230	-59.5704743	3.7	160.8	8.8	$4.06 \cdot 10^{23}$	1903.1	1449.6	441.1
101	160.8383576	-59.5888808	1.9	60.3	11.0	$1.30 \cdot 10^{23}$	450.1	544.0	165.6

n	R.A. (deg)	Dec. (deg)	F_{max}	F_{tot}	T	N_{H_2}	M	M (10 K)	M (20 K)
102	160.8459761	-59.5662931	3.8	56.7	8.8	$4.15 \cdot 10^{23}$	671.5	511.5	155.7
103	160.8316410	-59.5726098	4.0	232.3	8.5	$4.73 \cdot 10^{23}$	2972.8	2094.9	637.5
104	161.1474406	-59.4103921	0.2	4.6	17.1	$5.54 \cdot 10^{21}$	16.1	41.8	12.7
105	160.9758709	-59.4936763	0.2	2.9	16.4	$7.95 \cdot 10^{21}$	10.7	26.0	7.9
106	160.9908888	-59.4896155	0.2	3.4	16.4	$7.77 \cdot 10^{21}$	12.6	30.6	9.3
107	160.9354519	-59.4896923	0.2	4.2	17.2	$5.27 \cdot 10^{21}$	14.3	37.5	11.4
108	161.1226495	-59.5240655	0.4	24.6	15.3	$1.41 \cdot 10^{22}$	102.0	221.4	67.4
109	160.9968453	-59.5170257	0.2	4.0	16.5	$7.46 \cdot 10^{21}$	14.6	35.9	10.9
110	161.0079572	-59.4783993	0.3	16.7	15.8	$1.09 \cdot 10^{22}$	65.7	150.2	45.7
111	160.9736642	-59.4539611	0.2	13.4	16.9	$6.01 \cdot 10^{21}$	47.4	120.7	36.7
112	160.9733361	-59.4721499	0.4	42.9	15.4	$1.36 \cdot 10^{22}$	176.5	387.2	117.8
113	160.9597789	-59.4779808	0.3	13.4	15.5	$1.28 \cdot 10^{22}$	54.3	120.5	36.7
114	161.0636344	-59.5258118	0.5	70.7	14.6	$1.98 \cdot 10^{22}$	317.4	637.6	194.0
115	161.1030443	-59.5374083	0.7	37.4	13.7	$3.19 \cdot 10^{22}$	186.9	337.0	102.5
116	161.0210235	-59.4972900	0.7	24.7	13.6	$3.34 \cdot 10^{22}$	125.2	222.9	67.8
117	161.0076585	-59.5057184	0.9	36.3	13.0	$4.56 \cdot 10^{22}$	199.1	327.6	99.7
118	161.1202301	-59.5465317	1.7	36.3	11.4	$1.07 \cdot 10^{23}$	252.6	326.9	99.5
119	161.1302035	-59.5516498	1.7	51.9	11.4	$1.06 \cdot 10^{23}$	361.5	467.9	142.4
120	161.1939901	-59.4593075	0.2	4.6	17.3	$4.99 \cdot 10^{21}$	15.6	41.1	12.5
121	161.3359954	-59.4590481	0.2	6.0	17.1	$5.57 \cdot 10^{21}$	20.9	54.1	16.5
122	160.9112272	-59.4765407	0.2	9.4	17.1	$5.44 \cdot 10^{21}$	32.6	84.6	25.7
123	160.4588748	-59.4821922	0.2	4.2	17.2	$5.31 \cdot 10^{21}$	14.5	38.0	11.6
124	160.4491812	-59.4915501	0.2	4.8	17.1	$5.54 \cdot 10^{21}$	16.7	43.4	13.2
125	160.3749266	-59.4892138	0.2	6.2	16.4	$7.93 \cdot 10^{21}$	22.9	55.5	16.9
126	160.3654301	-59.4964445	0.3	6.8	16.2	$8.94 \cdot 10^{21}$	25.8	61.5	18.7
127	160.3960266	-59.4789662	0.3	38.9	15.6	$1.21 \cdot 10^{22}$	156.7	350.9	106.8
128	160.4192411	-59.4879876	0.3	7.5	16.2	$8.97 \cdot 10^{21}$	28.2	67.2	20.5
129	161.0845333	-59.5351170	0.6	8.8	14.1	$2.59 \cdot 10^{22}$	41.9	79.4	24.2
130	160.5401853	-59.4836449	0.1	20.1	17.5	$4.52 \cdot 10^{21}$	67.3	180.9	55.0
131	160.5668775	-59.5066129	0.2	4.5	16.6	$7.14 \cdot 10^{21}$	16.4	40.5	12.3
132	160.5593413	-59.5126228	0.2	5.6	16.7	$6.89 \cdot 10^{21}$	20.1	50.2	15.3
133	160.5437055	-59.5183507	0.3	7.6	15.9	$1.01 \cdot 10^{22}$	29.5	68.1	20.7
134	160.5217023	-59.5139524	0.3	3.0	15.9	$1.04 \cdot 10^{22}$	11.8	27.3	8.3
135	160.5253114	-59.5286669	0.4	38.7	15.3	$1.42 \cdot 10^{22}$	160.6	348.5	106.1
136	160.5220186	-59.5069466	0.3	8.9	15.7	$1.16 \cdot 10^{22}$	35.6	80.6	24.5
137	160.5051066	-59.5037553	0.4	18.4	15.3	$1.41 \cdot 10^{22}$	76.6	166.3	50.6
138	162.1345538	-59.4869872	0.2	2.4	16.6	$7.10 \cdot 10^{21}$	8.9	22.0	6.7
140	161.2441625	-59.5221501	0.7	77.4	13.9	$2.92 \cdot 10^{22}$	377.6	698.0	212.4
141	161.1976299	-59.5147221	0.2	7.4	16.8	$6.42 \cdot 10^{21}$	26.5	66.7	20.3
142	160.5202745	-59.5030095	0.3	4.5	15.5	$1.24 \cdot 10^{22}$	18.4	40.9	12.4
143	160.3706415	-59.5374937	0.2	2.7	16.8	$6.54 \cdot 10^{21}$	9.6	24.3	7.4
144	160.3221190	-59.5373602	0.9	66.6	13.0	$4.61 \cdot 10^{22}$	364.7	600.2	182.6

n	R.A. (deg)	Dec. (deg)	F_{max}	F_{tot}	T	N_{H_2}	M	M (10 K)	M (20 K)
145	160.2782571	-59.5532965	0.2	2.2	16.4	$7.94 \cdot 10^{21}$	8.3	20.0	6.1
146	160.6257814	-59.5649638	0.2	7.4	16.8	$6.37 \cdot 10^{21}$	26.3	66.4	20.2
147	160.6820647	-59.5558210	0.3	26.2	15.6	$1.18 \cdot 10^{22}$	105.3	236.0	71.8
148	160.6550989	-59.5758010	0.2	4.9	17.0	$5.70 \cdot 10^{21}$	17.3	44.4	13.5
149	160.6737149	-59.5878225	0.2	6.9	17.0	$5.71 \cdot 10^{21}$	24.3	62.4	19.0
150	160.6657428	-59.5940960	0.2	5.8	16.9	$6.08 \cdot 10^{21}$	20.6	52.4	15.9
151	160.6820592	-59.5706651	0.2	2.4	17.1	$5.41 \cdot 10^{21}$	8.4	21.8	6.6
152	160.6621228	-59.5685169	0.2	3.9	16.7	$6.75 \cdot 10^{21}$	14.3	35.6	10.8
153	160.5645930	-59.5637454	0.3	13.5	15.9	$1.02 \cdot 10^{22}$	52.5	121.4	36.9
154	160.5882914	-59.5641620	0.2	2.6	17.0	$5.89 \cdot 10^{21}$	9.1	23.5	7.1
155	161.0162445	-59.5596887	0.4	5.5	15.1	$1.55 \cdot 10^{22}$	23.5	49.8	15.2
156	160.9842131	-59.5731976	0.6	49.7	14.0	$2.74 \cdot 10^{22}$	239.4	448.0	136.3
157	160.9866122	-59.5859125	0.2	2.2	16.8	$6.50 \cdot 10^{21}$	7.7	19.5	5.9
158	160.3719181	-59.5676607	0.2	3.1	17.3	$4.91 \cdot 10^{21}$	10.7	28.3	8.6
159	160.3872540	-59.5733491	0.2	5.2	17.1	$5.41 \cdot 10^{21}$	18.3	47.3	14.4
160	160.4976265	-59.6287134	0.2	5.3	16.9	$6.02 \cdot 10^{21}$	18.8	47.7	14.5
161	160.4542351	-59.6375833	0.3	30.1	15.5	$1.27 \cdot 10^{22}$	122.6	271.8	82.7
162	160.4265118	-59.6439001	0.2	13.4	16.3	$8.34 \cdot 10^{21}$	50.4	121.2	36.9
163	160.3924426	-59.5835644	0.3	10.5	16.0	$9.92 \cdot 10^{21}$	40.6	94.7	28.8
164	160.3969132	-59.6003971	0.3	6.0	16.0	$9.79 \cdot 10^{21}$	23.3	54.5	16.6
165	160.4012250	-59.6055126	0.3	10.2	16.0	$9.72 \cdot 10^{21}$	39.4	91.9	28.0
166	160.3615533	-59.5874933	0.3	23.0	15.4	$1.31 \cdot 10^{22}$	94.6	207.6	63.2
167	160.3784258	-59.5892854	0.3	2.5	15.6	$1.18 \cdot 10^{22}$	10.0	22.5	6.8
169	161.1392501	-59.5837477	0.2	3.5	16.2	$8.68 \cdot 10^{21}$	13.2	31.4	9.6
170	160.2476482	-59.5932162	0.2	5.5	16.7	$6.80 \cdot 10^{21}$	20.0	50.0	15.2
171	160.2821238	-59.5971115	0.2	22.4	16.2	$8.65 \cdot 10^{21}$	84.8	201.8	61.4
172	161.2820478	-59.6545877	0.2	3.9	16.3	$8.18 \cdot 10^{21}$	14.5	34.8	10.6
173	161.1452400	-59.6211572	0.1	5.2	17.7	$4.10 \cdot 10^{21}$	17.3	47.2	14.4
174	161.1320125	-59.6639623	0.4	9.4	15.3	$1.39 \cdot 10^{22}$	39.3	85.2	25.9
175	161.1616931	-59.6817004	0.1	5.9	17.6	$4.33 \cdot 10^{21}$	19.8	53.5	16.3
176	161.1781745	-59.6060626	0.2	8.9	16.7	$6.86 \cdot 10^{21}$	32.2	80.4	24.5
177	161.3071876	-59.6250683	0.2	2.9	17.2	$5.21 \cdot 10^{21}$	10.1	26.3	8.0
178	161.1933494	-59.6741528	0.2	8.3	16.7	$6.88 \cdot 10^{21}$	30.0	74.8	22.8
179	161.2119622	-59.6800345	0.4	14.0	14.9	$1.72 \cdot 10^{22}$	60.8	126.4	38.5
180	161.1649059	-59.6305403	0.3	8.3	16.2	$8.81 \cdot 10^{21}$	31.4	74.7	22.7
181	161.2064643	-59.6495894	0.2	2.6	16.9	$6.08 \cdot 10^{21}$	9.1	23.3	7.1
182	161.1783493	-59.6183636	0.2	12.0	16.5	$7.54 \cdot 10^{21}$	44.1	108.0	32.9
183	161.2946076	-59.6282648	0.2	5.6	16.4	$7.97 \cdot 10^{21}$	20.6	50.1	15.3
184	161.2315607	-59.6544335	0.3	3.5	16.2	$8.94 \cdot 10^{21}$	13.3	31.7	9.7
185	161.2392490	-59.6273054	0.7	23.8	13.9	$2.92 \cdot 10^{22}$	116.1	214.6	65.3
186	161.2168713	-59.6344169	0.5	27.3	14.7	$1.94 \cdot 10^{22}$	121.3	246.6	75.0
187	161.2635649	-59.6411192	0.3	49.1	15.4	$1.30 \cdot 10^{22}$	201.9	442.9	134.8

n	R.A. (deg)	Dec. (deg)	F_{max}	F_{tot}	T	N_{H_2}	M	M (10 K)	M (20 K)
188	161.1935554	-59.6577560	0.3	26.4	15.6	$1.22 \cdot 10^{22}$	106.1	237.7	72.3
189	161.1714302	-59.6607923	0.3	20.0	15.8	$1.10 \cdot 10^{22}$	78.7	180.1	54.8
190	160.5547289	-59.5952280	0.3	9.6	15.8	$1.09 \cdot 10^{22}$	37.8	86.3	26.3
191	160.9957846	-59.6030723	0.2	4.4	16.6	$7.01 \cdot 10^{21}$	15.9	39.3	12.0
192	161.8010847	-59.6175540	0.4	31.7	15.0	$1.61 \cdot 10^{22}$	136.2	286.2	87.1
193	160.6115967	-59.6520967	0.1	5.2	17.6	$4.22 \cdot 10^{21}$	17.4	47.3	14.4
194	160.6174223	-59.6261179	0.2	50.1	16.6	$7.15 \cdot 10^{21}$	182.5	451.5	137.4
195	160.7074503	-59.6469055	0.2	3.1	17.1	$5.51 \cdot 10^{21}$	10.6	27.6	8.4
196	160.6448894	-59.6516586	0.2	2.3	16.9	$6.17 \cdot 10^{21}$	8.2	20.9	6.4
197	160.6595579	-59.6531752	0.2	2.4	16.8	$6.36 \cdot 10^{21}$	8.5	21.3	6.5
198	160.6525788	-59.6596307	0.2	5.4	16.6	$7.17 \cdot 10^{21}$	19.7	48.8	14.8
199	160.7096434	-59.6583320	0.2	4.9	16.6	$7.22 \cdot 10^{21}$	18.0	44.5	13.5
200	160.6822732	-59.6472918	0.2	3.5	16.3	$8.29 \cdot 10^{21}$	13.2	31.7	9.7
201	160.6851669	-59.6519936	0.3	9.8	16.2	$8.91 \cdot 10^{21}$	37.1	88.3	26.9
202	161.8987376	-59.6142325	0.1	4.0	17.8	$3.92 \cdot 10^{21}$	13.0	35.8	10.9
203	160.6979993	-59.6550384	0.3	6.4	16.0	$9.65 \cdot 10^{21}$	24.9	58.0	17.7
204	161.0240641	-59.6193975	0.5	19.7	14.6	$2.00 \cdot 10^{22}$	88.3	177.4	54.0
205	161.0185030	-59.6300203	0.3	5.5	15.6	$1.18 \cdot 10^{22}$	22.2	49.8	15.2
206	161.3841235	-59.6297583	0.1	5.7	17.5	$4.39 \cdot 10^{21}$	19.0	51.1	15.6
207	160.9013211	-59.6420395	0.3	3.7	16.2	$8.75 \cdot 10^{21}$	14.1	33.6	10.2
209	161.7910199	-59.6520654	0.2	7.5	17.0	$5.89 \cdot 10^{21}$	26.4	67.9	20.7
210	161.7713153	-59.6573148	0.2	2.5	17.3	$4.90 \cdot 10^{21}$	8.5	22.4	6.8
211	160.2675193	-59.7180709	0.4	24.4	15.2	$1.47 \cdot 10^{22}$	102.6	220.3	67.0
212	160.3300806	-59.6597072	0.3	12.8	15.9	$1.01 \cdot 10^{22}$	49.9	115.3	35.1
213	160.2711840	-59.6632042	0.5	47.0	14.7	$1.90 \cdot 10^{22}$	208.7	424.1	129.1
214	160.2857877	-59.6767092	0.4	18.4	15.4	$1.35 \cdot 10^{22}$	75.8	166.3	50.6
215	160.3030878	-59.6959192	0.6	52.2	14.3	$2.35 \cdot 10^{22}$	242.7	470.7	143.2
216	160.2873060	-59.6959798	0.5	3.8	14.6	$1.98 \cdot 10^{22}$	17.2	34.6	10.5
217	160.2158063	-59.6477787	0.2	2.7	16.4	$7.80 \cdot 10^{21}$	10.2	24.7	7.5
218	160.9483099	-59.6896456	0.2	6.3	16.5	$7.44 \cdot 10^{21}$	23.0	56.5	17.2
219	160.8462574	-59.6659095	0.2	13.7	16.7	$6.82 \cdot 10^{21}$	49.5	123.6	37.6
220	161.0015898	-59.6513402	0.2	4.1	16.4	$8.01 \cdot 10^{21}$	15.2	36.9	11.2
221	160.9883054	-59.6552826	0.2	8.4	16.9	$6.05 \cdot 10^{21}$	29.7	75.5	23.0
222	160.9569279	-59.6764340	0.2	3.3	16.7	$6.92 \cdot 10^{21}$	11.9	29.7	9.0
223	160.9127800	-59.6737544	0.3	72.7	15.6	$1.22 \cdot 10^{22}$	292.6	655.6	199.5
224	160.8776450	-59.6672018	0.2	3.3	16.4	$8.04 \cdot 10^{21}$	12.2	29.7	9.0
225	160.9577665	-59.6559990	0.4	13.0	15.2	$1.45 \cdot 10^{22}$	54.6	117.3	35.7
226	160.9625816	-59.6643368	0.4	4.7	15.4	$1.35 \cdot 10^{22}$	19.4	42.6	13.0
227	161.6911400	-59.6509708	0.2	2.4	16.9	$6.23 \cdot 10^{21}$	8.6	21.9	6.7
228	160.3619095	-59.6852300	0.2	7.4	16.8	$6.39 \cdot 10^{21}$	26.4	66.6	20.3
229	160.4428003	-59.7233622	0.2	3.3	16.5	$7.40 \cdot 10^{21}$	12.0	29.4	8.9
230	160.4074194	-59.7487103	0.2	4.8	16.9	$6.08 \cdot 10^{21}$	16.8	42.8	13.0

n	R.A. (deg)	Dec. (deg)	F_{max}	F_{tot}	T	N_{H_2}	M	M (10 K)	M (20 K)
231	160.4088631	-59.7240125	0.2	3.9	17.0	$5.92 \cdot 10^{21}$	13.6	35.0	10.6
232	160.3908748	-59.6824434	0.2	4.3	16.7	$6.69 \cdot 10^{21}$	15.5	38.7	11.8
233	160.3989091	-59.7007439	0.5	61.4	14.4	$2.28 \cdot 10^{22}$	281.9	553.4	168.4
234	160.4267000	-59.7408097	0.4	17.0	15.4	$1.35 \cdot 10^{22}$	69.8	153.1	46.6
235	160.4427513	-59.7415922	0.3	4.8	15.6	$1.19 \cdot 10^{22}$	19.3	43.3	13.2
236	160.4551706	-59.7476919	0.4	6.2	14.9	$1.69 \cdot 10^{22}$	26.7	55.5	16.9
237	160.4411673	-59.7530915	0.4	17.4	15.2	$1.51 \cdot 10^{22}$	72.9	156.6	47.7
238	161.7304962	-59.6838637	0.2	23.3	16.2	$8.67 \cdot 10^{21}$	88.3	210.1	63.9
239	161.6861403	-59.7044880	0.2	8.9	16.8	$6.33 \cdot 10^{21}$	31.7	80.0	24.3
241	160.4235563	-59.7255912	0.3	6.6	16.2	$8.83 \cdot 10^{21}$	24.9	59.2	18.0
242	160.6391192	-59.6921658	0.3	21.1	15.8	$1.08 \cdot 10^{22}$	83.1	190.1	57.8
243	161.4486826	-59.6882172	0.2	3.3	16.6	$7.05 \cdot 10^{21}$	12.0	29.6	9.0
244	161.0885947	-59.7060381	0.3	11.9	15.5	$1.28 \cdot 10^{22}$	48.6	107.7	32.8
245	161.6027861	-59.7942850	0.2	5.1	16.7	$6.87 \cdot 10^{21}$	18.3	45.6	13.9
246	161.4564164	-59.7877900	0.2	4.0	16.6	$7.03 \cdot 10^{21}$	14.6	36.1	11.0
247	161.6139801	-59.7169006	0.4	13.0	15.4	$1.36 \cdot 10^{22}$	53.3	117.0	35.6
248	161.5779222	-59.7193817	0.2	6.9	17.0	$5.91 \cdot 10^{21}$	24.1	61.8	18.8
249	161.6294915	-59.7736047	0.4	45.5	15.2	$1.48 \cdot 10^{22}$	190.9	410.0	124.8
250	161.5484447	-59.7021983	0.3	8.4	16.1	$9.19 \cdot 10^{21}$	32.3	76.2	23.2
251	161.4685038	-59.7697335	0.3	18.4	15.9	$1.03 \cdot 10^{22}$	71.8	165.9	50.5
252	161.4829134	-59.7164091	0.3	8.3	15.7	$1.14 \cdot 10^{22}$	33.1	74.9	22.8
253	161.4795563	-59.7588672	0.4	8.4	15.4	$1.33 \cdot 10^{22}$	34.4	75.4	22.9
254	161.5005964	-59.7318519	0.5	36.0	14.8	$1.85 \cdot 10^{22}$	157.9	324.5	98.8
255	161.5338685	-59.7312074	0.4	21.9	14.9	$1.72 \cdot 10^{22}$	95.2	197.8	60.2
256	161.5056881	-59.7467816	0.5	41.5	14.7	$1.92 \cdot 10^{22}$	184.1	373.9	113.8
257	161.4827450	-59.7468610	0.5	33.4	14.3	$2.32 \cdot 10^{22}$	155.2	301.1	91.6
258	161.5089948	-59.7034004	0.4	7.4	15.0	$1.66 \cdot 10^{22}$	31.8	66.8	20.3
259	161.5194002	-59.7079336	0.4	35.6	15.0	$1.62 \cdot 10^{22}$	153.0	321.4	97.8
260	161.5005034	-59.7707116	0.5	20.6	14.7	$1.95 \cdot 10^{22}$	91.3	185.6	56.5
261	161.5191466	-59.7879315	1.9	190.7	11.0	$1.29 \cdot 10^{23}$	1422.5	1719.2	523.2
262	161.4920299	-59.7957091	1.1	52.5	12.4	$6.28 \cdot 10^{22}$	313.0	473.3	144.0
263	160.8975275	-59.7199724	0.2	3.0	17.1	$5.51 \cdot 10^{21}$	10.5	27.1	8.2
265	161.0630946	-59.7220416	0.2	6.1	16.8	$6.53 \cdot 10^{21}$	21.7	54.6	16.6
266	161.5987508	-59.7731393	0.2	9.4	16.3	$8.35 \cdot 10^{21}$	35.4	85.2	25.9
267	162.3450867	-59.6934324	0.2	8.6	16.9	$6.21 \cdot 10^{21}$	30.3	77.2	23.5
268	161.7480736	-59.7483969	0.1	3.0	17.5	$4.49 \cdot 10^{21}$	10.1	27.3	8.3
269	161.6971884	-59.7509680	0.2	21.7	16.3	$8.20 \cdot 10^{21}$	81.5	195.9	59.6
270	161.3735485	-59.7415065	0.4	17.7	14.9	$1.73 \cdot 10^{22}$	76.7	159.4	48.5
272	161.1024619	-59.7764822	0.2	15.9	16.6	$7.21 \cdot 10^{21}$	58.0	143.5	43.7
273	161.7419142	-59.7857374	0.2	6.7	17.0	$5.77 \cdot 10^{21}$	23.4	60.2	18.3
274	161.7236462	-59.7890362	0.2	3.7	17.2	$5.14 \cdot 10^{21}$	12.7	33.1	10.1
275	161.7087251	-59.7953835	0.2	9.2	16.9	$6.04 \cdot 10^{21}$	32.7	83.3	25.3

n	R.A. (deg)	Dec. (deg)	F_{max}	F_{tot}	T	N_{H_2}	M	M (10 K)	M (20 K)
276	161.2402607	-59.8950776	0.3	14.8	16.0	$9.59 \cdot 10^{21}$	57.3	133.7	40.7
277	161.2625754	-59.9059388	0.2	9.3	16.8	$6.58 \cdot 10^{21}$	33.3	84.0	25.6
278	161.3966478	-59.7933428	0.2	8.5	16.5	$7.61 \cdot 10^{21}$	31.4	76.9	23.4
279	161.1966235	-59.8403438	0.2	5.9	16.9	$6.14 \cdot 10^{21}$	20.8	52.8	16.1
280	161.2077934	-59.8435465	0.2	3.1	16.9	$6.21 \cdot 10^{21}$	10.9	27.8	8.5
281	161.2246119	-59.8123229	0.2	6.9	16.6	$7.07 \cdot 10^{21}$	25.3	62.6	19.1
282	161.3642876	-59.8211456	0.2	23.4	16.2	$8.67 \cdot 10^{21}$	88.6	210.9	64.2
283	161.3317661	-59.8738676	0.4	23.8	15.3	$1.40 \cdot 10^{22}$	98.9	214.8	65.4
284	161.3044428	-59.8868440	0.3	57.7	15.5	$1.26 \cdot 10^{22}$	234.9	520.7	158.5
285	161.3332384	-59.7844185	0.5	25.6	14.4	$2.27 \cdot 10^{22}$	117.8	231.2	70.3
286	161.3273789	-59.8007193	0.5	31.6	14.5	$2.11 \cdot 10^{22}$	143.4	284.8	86.7
287	161.2469276	-59.8714571	0.5	36.0	14.8	$1.85 \cdot 10^{22}$	157.9	324.4	98.7
288	161.2579828	-59.8769384	0.5	10.8	14.8	$1.82 \cdot 10^{22}$	47.2	97.0	29.5
289	161.2590250	-59.7896484	1.0	66.9	12.8	$5.10 \cdot 10^{22}$	377.1	603.7	183.7
290	161.2836828	-59.8083769	1.2	207.7	12.2	$6.87 \cdot 10^{22}$	1275.5	1872.6	569.9
291	161.3584737	-59.7905730	0.6	29.9	14.0	$2.72 \cdot 10^{22}$	143.9	269.3	81.9
292	161.7902694	-59.7994275	0.1	11.0	17.4	$4.63 \cdot 10^{21}$	37.3	99.2	30.2
294	161.3632071	-59.8003030	0.3	9.2	15.5	$1.29 \cdot 10^{22}$	37.6	83.4	25.4
295	160.3105256	-59.6545777	0.4	45.5	15.2	$1.45 \cdot 10^{22}$	190.9	410.0	124.8
296	160.2069896	-59.8357611	0.2	5.5	16.5	$7.39 \cdot 10^{21}$	20.4	50.0	15.2
297	161.4731294	-59.7053962	0.4	26.9	15.4	$1.34 \cdot 10^{22}$	110.7	242.7	73.9
298	162.3092525	-59.8631442	0.2	4.5	16.8	$6.50 \cdot 10^{21}$	16.2	40.8	12.4
299	161.6034913	-59.8422433	0.2	8.0	16.6	$7.18 \cdot 10^{21}$	29.2	72.2	22.0
300	161.7752529	-59.8703932	0.2	4.0	17.0	$5.79 \cdot 10^{21}$	14.0	36.0	11.0
301	161.7915419	-59.8694636	0.2	7.7	16.9	$6.14 \cdot 10^{21}$	27.1	69.0	21.0
302	161.5606425	-59.9775934	0.3	20.1	15.5	$1.26 \cdot 10^{22}$	81.6	181.0	55.1
303	161.4105768	-59.8985780	0.9	105.2	13.1	$4.35 \cdot 10^{22}$	568.7	948.5	288.6
304	161.4150783	-59.9276231	0.2	9.8	16.6	$7.01 \cdot 10^{21}$	35.6	88.1	26.8
305	161.4224347	-59.9372507	0.2	5.7	16.7	$6.78 \cdot 10^{21}$	20.4	51.0	15.5
306	161.4170675	-59.9600600	0.5	22.2	14.6	$2.04 \cdot 10^{22}$	99.8	200.4	61.0
307	161.5208090	-59.9746234	0.4	6.4	15.3	$1.38 \cdot 10^{22}$	26.5	57.6	17.5
308	161.4819703	-59.9491476	3.1	283.7	9.5	$2.85 \cdot 10^{23}$	2846.1	2558.4	778.6
309	161.4646862	-59.9680773	0.8	24.2	13.5	$3.62 \cdot 10^{22}$	124.0	218.1	66.4
310	161.7214997	-59.8864320	0.2	9.8	16.5	$7.45 \cdot 10^{21}$	36.0	88.1	26.8
311	161.6957267	-59.8924741	0.3	5.4	16.2	$8.86 \cdot 10^{21}$	20.5	48.8	14.8
312	161.6822501	-59.8943708	0.2	8.4	16.5	$7.51 \cdot 10^{21}$	31.0	76.0	23.1
313	161.3503671	-59.9039666	0.2	4.2	17.4	$4.79 \cdot 10^{21}$	14.4	38.2	11.6
314	160.9625005	-59.9227052	1.1	28.8	12.6	$5.74 \cdot 10^{22}$	166.7	259.5	79.0
315	160.9635559	-59.9742626	0.2	3.9	16.3	$8.39 \cdot 10^{21}$	14.5	34.9	10.6
316	160.9296647	-59.9562056	0.2	7.6	16.3	$8.47 \cdot 10^{21}$	28.5	68.5	20.8
317	160.9475061	-59.9633227	0.3	12.5	15.9	$1.01 \cdot 10^{22}$	48.7	112.4	34.2
318	160.9714940	-59.9658602	0.4	30.0	14.8	$1.80 \cdot 10^{22}$	131.8	270.9	82.4

n	R.A. (deg)	Dec. (deg)	F_{max}	F_{tot}	T	N_{H_2}	M	M (10 K)	M (20 K)
319	161.1881612	-59.9330439	1.1	22.5	12.5	$6.08 \cdot 10^{22}$	132.0	202.5	61.6
320	161.1814456	-59.9467969	0.3	2.6	16.1	$9.20 \cdot 10^{21}$	10.0	23.5	7.2
321	161.1901649	-59.9883236	0.6	104.1	14.3	$2.40 \cdot 10^{22}$	483.7	938.3	285.5
322	161.1581051	-59.9605038	0.4	7.7	15.2	$1.48 \cdot 10^{22}$	32.2	69.1	21.0
323	161.1537868	-59.9711484	0.8	17.3	13.4	$3.74 \cdot 10^{22}$	89.7	155.7	47.4
324	161.1474540	-59.9786546	0.7	13.8	13.7	$3.26 \cdot 10^{22}$	69.2	124.7	38.0
325	162.1148258	-59.9321547	0.2	11.7	16.3	$8.38 \cdot 10^{21}$	44.0	105.8	32.2
327	162.1637626	-59.9457053	0.2	9.8	16.4	$8.01 \cdot 10^{21}$	36.6	88.8	27.0
328	162.1487501	-59.9539576	0.2	3.8	17.1	$5.40 \cdot 10^{21}$	13.2	34.1	10.4
329	161.5781251	-59.9482286	0.3	12.0	15.6	$1.19 \cdot 10^{22}$	48.4	108.4	33.0
330	161.1713420	-59.9574674	0.4	6.7	15.3	$1.40 \cdot 10^{22}$	27.8	60.2	18.3
331	162.0844109	-59.9729566	0.2	3.7	16.5	$7.57 \cdot 10^{21}$	13.6	33.4	10.2
332	162.1142838	-59.9670645	0.2	18.1	16.4	$7.79 \cdot 10^{21}$	67.2	163.1	49.6
333	162.0572848	-59.9763607	0.9	28.6	12.9	$4.83 \cdot 10^{22}$	159.1	258.3	78.6
334	161.7290101	-60.1192115	0.3	8.5	15.8	$1.07 \cdot 10^{22}$	33.6	76.9	23.4
335	161.8469341	-60.0235988	0.2	8.2	16.7	$6.65 \cdot 10^{21}$	29.6	74.0	22.5
336	161.8722590	-60.0102650	0.2	5.8	16.3	$8.39 \cdot 10^{21}$	21.7	52.1	15.9
338	161.8150792	-60.0389062	0.2	11.9	16.7	$6.70 \cdot 10^{21}$	42.8	106.9	32.5
339	161.7986391	-60.0533176	0.2	5.5	16.6	$7.07 \cdot 10^{21}$	20.1	49.7	15.1
340	161.7591172	-60.0843713	0.5	32.3	14.4	$2.24 \cdot 10^{22}$	148.6	291.7	88.8
341	161.7481001	-60.1038233	0.3	6.2	16.2	$8.91 \cdot 10^{21}$	23.6	56.2	17.1
342	161.8548161	-60.0065618	0.2	5.0	16.9	$6.14 \cdot 10^{21}$	17.7	45.1	13.7
343	161.8231334	-60.0038545	0.5	34.1	14.6	$2.03 \cdot 10^{22}$	153.3	307.9	93.7
344	161.8200193	-60.0195641	0.3	8.0	16.1	$9.29 \cdot 10^{21}$	30.8	72.5	22.1
345	161.8388594	-59.9874577	0.2	5.2	16.8	$6.56 \cdot 10^{21}$	18.8	47.3	14.4
346	161.3448506	-59.9774613	0.8	47.8	13.4	$3.81 \cdot 10^{22}$	248.6	431.4	131.3
347	162.1770296	-59.9896502	0.1	3.1	17.8	$3.86 \cdot 10^{21}$	10.2	28.1	8.5
348	161.3515642	-60.0215053	0.2	4.6	16.8	$6.45 \cdot 10^{21}$	16.5	41.7	12.7
349	161.3510944	-60.0297442	0.2	21.6	16.8	$6.57 \cdot 10^{21}$	77.1	194.5	59.2
350	161.9087084	-60.0048360	0.1	3.4	17.5	$4.54 \cdot 10^{21}$	11.3	30.5	9.3
351	161.9551454	-60.0158914	0.2	6.9	16.9	$6.20 \cdot 10^{21}$	24.5	62.3	19.0
352	161.9674313	-60.0885239	0.2	9.7	17.1	$5.61 \cdot 10^{21}$	33.7	87.4	26.6
353	161.9114179	-60.1017361	0.2	16.5	16.3	$8.26 \cdot 10^{21}$	61.9	148.8	45.3
354	161.9440129	-60.1014236	0.2	2.7	17.2	$5.19 \cdot 10^{21}$	9.3	24.2	7.4
355	161.9112533	-60.0658138	0.2	3.2	16.6	$7.21 \cdot 10^{21}$	11.6	28.7	8.7
356	161.9083243	-60.0745452	0.3	11.6	15.8	$1.09 \cdot 10^{22}$	45.8	104.7	31.9
357	161.9252678	-60.0817227	0.2	6.9	16.4	$7.78 \cdot 10^{21}$	25.4	61.8	18.8
358	161.9128908	-60.0843269	0.2	2.0	16.4	$7.92 \cdot 10^{21}$	7.6	18.4	5.6
359	161.8941038	-60.0891131	0.4	17.5	15.2	$1.51 \cdot 10^{22}$	73.5	157.8	48.0
360	161.8956428	-60.0248716	0.3	4.7	15.4	$1.31 \cdot 10^{22}$	19.4	42.6	12.9
361	161.9052073	-60.0424453	0.9	66.2	13.0	$4.56 \cdot 10^{22}$	363.0	597.4	181.8
362	160.6126293	-60.0338306	0.2	4.9	17.1	$5.52 \cdot 10^{21}$	17.0	44.1	13.4

n	R.A. (deg)	Dec. (deg)	F_{max}	F_{tot}	T	N_{H_2}	M	M (10 K)	M (20 K)
363	161.2547272	-60.0364229	0.2	3.2	16.4	$7.91 \cdot 10^{21}$	12.0	29.1	8.9
364	161.2927925	-60.0418043	0.3	13.6	15.8	$1.08 \cdot 10^{22}$	53.6	122.6	37.3
365	161.6556948	-60.0716082	0.2	11.9	16.7	$6.82 \cdot 10^{21}$	43.1	107.6	32.7
366	160.2161690	-60.0761555	0.1	4.3	17.4	$4.62 \cdot 10^{21}$	14.5	38.5	11.7
367	162.0097985	-60.0772375	0.3	20.4	15.5	$1.26 \cdot 10^{22}$	83.0	184.0	56.0
368	161.5030788	-60.0889973	0.5	8.0	14.6	$2.01 \cdot 10^{22}$	35.8	71.9	21.9
369	161.4979703	-60.0940771	0.5	4.9	14.6	$2.04 \cdot 10^{22}$	22.0	44.1	13.4
370	161.4891733	-60.1031189	0.6	24.5	14.2	$2.50 \cdot 10^{22}$	115.2	220.8	67.2
371	162.0967619	-60.1302611	0.5	30.7	14.6	$2.03 \cdot 10^{22}$	137.8	276.7	84.2
372	161.4664987	-60.1575057	0.3	20.2	15.5	$1.29 \cdot 10^{22}$	82.2	182.3	55.5
373	161.4835142	-60.1305937	0.4	7.1	15.0	$1.61 \cdot 10^{22}$	30.5	64.0	19.5
374	161.4990439	-60.1490451	0.9	129.5	13.0	$4.54 \cdot 10^{22}$	709.8	1168.0	355.4
375	161.4906847	-60.1907790	0.7	9.4	13.6	$3.37 \cdot 10^{22}$	47.4	84.4	25.7
376	161.4943028	-60.1726342	1.1	119.3	12.5	$5.89 \cdot 10^{22}$	701.1	1075.7	327.3
377	161.4786349	-60.2125924	0.3	13.8	15.6	$1.21 \cdot 10^{22}$	55.4	124.1	37.8
378	160.9792026	-60.1430312	0.3	25.8	16.2	$8.92 \cdot 10^{21}$	97.7	232.6	70.8
380	161.6861794	-60.1796146	0.9	36.1	13.0	$4.64 \cdot 10^{22}$	197.9	325.7	99.1
381	161.8449080	-60.1841095	0.2	4.7	17.4	$4.67 \cdot 10^{21}$	15.8	42.1	12.8
382	161.8415068	-60.1956357	0.2	4.3	17.2	$5.21 \cdot 10^{21}$	14.7	38.4	11.7
383	161.8460597	-60.2212585	0.1	4.2	17.7	$4.11 \cdot 10^{21}$	13.9	37.9	11.5
384	161.8585239	-60.1903435	0.2	1.7	17.4	$4.78 \cdot 10^{21}$	5.8	15.4	4.7
385	161.8598578	-60.2082087	0.3	15.8	15.8	$1.07 \cdot 10^{22}$	62.4	142.6	43.4
386	161.8891279	-60.1997357	0.3	7.3	15.8	$1.09 \cdot 10^{22}$	28.7	65.7	20.0
387	161.8834781	-60.2048025	0.2	4.4	16.3	$8.41 \cdot 10^{21}$	16.5	39.6	12.1
388	161.2723614	-60.2371002	0.2	9.7	16.6	$7.24 \cdot 10^{21}$	35.3	87.2	26.5
389	161.2839940	-60.1972468	0.3	43.7	15.8	$1.07 \cdot 10^{22}$	172.4	394.4	120.0
390	161.9427230	-60.2002436	0.2	3.5	16.6	$7.26 \cdot 10^{21}$	12.8	31.6	9.6
391	161.9632119	-60.1942244	0.3	13.6	16.1	$9.23 \cdot 10^{21}$	52.2	122.9	37.4
392	161.9875647	-60.1953820	0.2	19.1	16.3	$8.28 \cdot 10^{21}$	71.5	171.9	52.3
393	161.5213683	-60.2455907	0.2	7.8	17.0	$5.72 \cdot 10^{21}$	27.3	70.2	21.4
394	161.5065419	-60.3453582	0.3	8.9	16.1	$9.44 \cdot 10^{21}$	34.1	80.4	24.5
395	161.4927645	-60.3277809	0.2	7.9	16.6	$7.19 \cdot 10^{21}$	28.9	71.6	21.8
396	161.4356326	-60.3644316	0.2	6.7	16.7	$6.69 \cdot 10^{21}$	24.1	60.1	18.3
398	161.3960444	-60.3718785	0.2	4.5	16.6	$7.22 \cdot 10^{21}$	16.3	40.3	12.3
399	161.5146805	-60.3218249	0.2	12.6	16.4	$7.80 \cdot 10^{21}$	46.9	114.0	34.7
400	161.5067873	-60.2783550	0.3	33.6	15.6	$1.21 \cdot 10^{22}$	135.2	302.8	92.1
401	161.4191936	-60.3198189	0.2	9.4	16.3	$8.28 \cdot 10^{21}$	35.3	84.9	25.8
402	161.4345707	-60.3205053	0.2	4.9	16.3	$8.38 \cdot 10^{21}$	18.5	44.5	13.5
403	161.4922034	-60.3696695	0.4	27.2	15.2	$1.48 \cdot 10^{22}$	114.0	244.9	74.5
404	161.4665526	-60.3772560	0.2	5.8	16.2	$8.67 \cdot 10^{21}$	22.0	52.4	16.0
405	161.4150791	-60.2170899	0.3	7.9	15.5	$1.28 \cdot 10^{22}$	32.0	70.9	21.6
406	161.4245628	-60.2271616	0.3	9.7	16.1	$9.37 \cdot 10^{21}$	37.1	87.5	26.6

n	R.A. (deg)	Dec. (deg)	F_{max}	F_{tot}	T	N_{H_2}	M	M (10 K)	M (20 K)
407	161.4492008	-60.2386611	0.7	18.9	13.6	$3.38 \cdot 10^{22}$	95.8	170.5	51.9
408	161.4883138	-60.2611048	0.3	14.0	15.9	$1.04 \cdot 10^{22}$	54.8	126.7	38.5
409	161.4741798	-60.3074168	0.6	43.1	13.9	$2.89 \cdot 10^{22}$	210.1	388.4	118.2
410	161.4363863	-60.2539403	1.1	131.8	12.6	$5.67 \cdot 10^{22}$	763.5	1188.4	361.6
411	161.4638889	-60.2905485	0.7	59.9	13.8	$3.03 \cdot 10^{22}$	295.9	540.2	164.4
412	161.4589057	-60.2651675	0.6	8.0	14.1	$2.61 \cdot 10^{22}$	38.1	72.1	21.9
413	161.4351797	-60.2989190	0.9	19.9	13.1	$4.41 \cdot 10^{22}$	107.7	179.6	54.7
414	161.4388986	-60.2847717	1.0	26.3	12.8	$5.08 \cdot 10^{22}$	148.4	237.5	72.3
415	161.4248345	-60.2920725	1.1	69.8	12.4	$6.25 \cdot 10^{22}$	416.2	629.3	191.5
416	161.7012316	-60.2192464	0.2	6.2	16.9	$6.15 \cdot 10^{21}$	22.0	56.1	17.1
417	161.7135394	-60.2373620	0.2	17.9	16.5	$7.46 \cdot 10^{21}$	66.0	161.7	49.2
418	160.8449861	-60.2501346	0.2	10.4	17.0	$5.89 \cdot 10^{21}$	36.4	93.5	28.4
419	160.8527166	-60.2609520	0.2	19.8	16.2	$8.63 \cdot 10^{21}$	74.9	178.2	54.2
420	160.8217443	-60.2671003	0.2	4.8	16.7	$6.86 \cdot 10^{21}$	17.4	43.6	13.3
421	162.0343283	-60.2444726	0.2	7.0	17.1	$5.55 \cdot 10^{21}$	24.3	63.1	19.2
423	162.1858677	-60.2497382	0.1	2.3	17.8	$3.80 \cdot 10^{21}$	7.5	20.6	6.3
424	160.3026504	-60.2719423	0.1	3.0	18.1	$3.26 \cdot 10^{21}$	9.7	27.4	8.3
425	160.2924437	-59.2624656	0.2	5.6	16.7	$6.72 \cdot 10^{21}$	20.1	50.2	15.3
427	162.0538825	-60.3157726	0.1	6.0	17.7	$3.96 \cdot 10^{21}$	19.8	54.1	16.5
428	161.6112490	-60.3397393	0.3	21.4	16.1	$9.40 \cdot 10^{21}$	81.9	193.1	58.8
429	161.6374435	-60.3519309	0.3	26.0	16.1	$9.41 \cdot 10^{21}$	99.3	234.0	71.2
430	161.6371044	-60.3605859	0.2	6.4	16.4	$7.79 \cdot 10^{21}$	23.6	57.3	17.4
431	161.8259386	-60.3347630	0.1	2.6	18.1	$3.24 \cdot 10^{21}$	8.2	23.2	7.1
432	161.7318249	-60.3623501	0.3	23.3	15.9	$1.04 \cdot 10^{22}$	90.9	209.9	63.9

Acknowledgements/Danksagung